Optimization Problems and Forecast Models in Construction

Lead Guest Editor: Milos Knezevic
Guest Editors: Tomas Hanak, Nenad Ivanisevic, and Igor Peško

Optimization Problems and Forecast Models in Construction

Optimization Problems and Forecast Models in Construction

Lead Guest Editor: Milos Knezevic
Guest Editors: Tomas Hanak, Nenad Ivanisevic, and
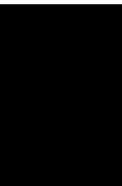Igor Peško

Zhaofei Chu (iD), China
Wonseok Chung (iD), Republic of Korea
Donato Ciampa (iD), Italy
Gian Paolo Cimellaro, Italy
Francesco Colangelo, Italy
Romulus Costache (iD), Romania
Liviu-Adrian Cotfas (iD), Romania
Antonio Maria D'Altri, Italy
Bruno Dal Lago (iD), Italy
Amos Darko (iD), Hong Kong
Arka Jyoti Das (iD), India
Dario De Domenico (iD), Italy
Gianmarco De Felice (iD), Italy
Stefano De Miranda (iD), Italy
Maria T. De Risi (iD), Italy
Tayfun Dede, Turkey
Sadik O. Degertekin (iD), Turkey
Camelia Delcea (iD), Romania
Cristoforo Demartino, China
Giuseppe Di Filippo (iD), Italy
Luigi Di Sarno, Italy
Fabio Di Trapani (iD), Italy
Aboelkasim Diab (iD), Egypt
Thi My Dung Do, Vietnam
Giulio Dondi (iD), Italy
Jiangfeng Dong (iD), China
Chao Dou (iD), China
Mario D'Aniello (iD), Italy
Jingtao Du (iD), China
Ahmed Elghazouli, United Kingdom
Francesco Fabbrocino (iD), Italy
Flora Faleschini (iD), Italy
Dingqiang Fan, Hong Kong
Xueping Fan, China
Qian Fang (iD), China
Salar Farahmand-Tabar (iD), Iran
Ilenia Farina, Italy
Roberto Fedele, Italy
Guang-Liang Feng (iD), China
Luigi Fenu (iD), Italy
Tiago Ferreira (iD), Portugal
Marco Filippo Ferrotto, Italy
Antonio Formisano (iD), Italy
Guoyang Fu, Australia
Stefano Galassi (iD), Italy

Junfeng Gao (iD), China
Meng Gao (iD), China
Giovanni Garcea (iD), Italy
Enrique García-Macías, Spain
Emilio García-Taengua (iD), United Kingdom
DongDong Ge (iD), USA
Khaled Ghaedi, Malaysia
Khaled Ghaedi (iD), Malaysia
Gian Felice Giaccu, Italy
Agathoklis Giaralis (iD), United Kingdom
Ravindran Gobinath, India
Rodrigo Gonçalves, Portugal
Peilin Gong (iD), China
Belén González-Fonteboa (iD), Spain
Salvatore Grasso (iD), Italy
Fan Gu, USA
Erhan Güneyisi (iD), Turkey
Esra Mete Güneyisi, Turkey
Pingye Guo (iD), China
Ankit Gupta (iD), India
Federico Gusella (iD), Italy
Kemal Hacıefendioğlu, Turkey
Jianyong Han (iD), China
Song Han (iD), China
Asad Hanif (iD), Macau
Hadi Hasanzadehshooiili (iD), Canada
Mostafa Fahmi Hassanein, Egypt
Amir Ahmad Hedayat (iD), Iran
Khandaker Hossain (iD), Canada
Zahid Hossain (iD), USA
Chao Hou, China
Biao Hu, China
Jiang Hu (iD), China
Xiaodong Hu, China
Lei Huang (iD), China
Cun Hui (iD), China
Bon-Gang Hwang, Singapore
Jijo James (iD), India
Abbas Fadhil Jasim (iD), Iraq
Ahad Javanmardi (iD), China
Krishnan Prabhakan Jaya, India
Dong-Sheng Jeng (iD), Australia
Han-Yong Jeon, Republic of Korea
Pengjiao Jia, China
Shaohua Jiang (iD), China

Chayut Ngamkhanong (iD), Thailand
Trung Ngo, Australia
Tengfei Nian, China
Mehdi Nikoo (iD), Canada
Youjun Ning (iD), China
Olugbenga Timo Oladinrin (iD), United Kingdom
Oladimeji Benedict Olalusi, South Africa
Timothy O. Olawumi (iD), Hong Kong
Alejandro Orfila (iD), Spain
Maurizio Orlando (iD), Italy
Siti Aminah Osman, Malaysia
Walid Oueslati (iD), Tunisia
SUVASH PAUL (iD), Bangladesh
John-Paris Pantouvakis (iD), Greece
Fabrizio Paolacci (iD), Italy
Giuseppina Pappalardo (iD), Italy
Fulvio Parisi (iD), Italy
Dimitrios G. Pavlou (iD), Norway
Daniele Pellegrini (iD), Italy
Gatheeshgar Perampalam (iD), United Kingdom
Daniele Perrone (iD), Italy
Giuseppe Piccardo (iD), Italy
Vagelis Plevris (iD), Qatar
Andrea Pranno (iD), Italy
Adolfo Preciado (iD), Mexico
Chongchong Qi (iD), China
Yu Qian, USA
Ying Qin (iD), China
Giuseppe Quaranta (iD), Italy
Krishanu ROY (iD), New Zealand
Vlastimir Radonjanin, Serbia
Carlo Rainieri (iD), Italy
Rahul V. Ralegaonkar, India
Raizal Saifulnaz Muhammad Rashid, Malaysia
Alessandro Rasulo (iD), Italy
Chonghong Ren (iD), China
Qing-Xin Ren, China
Dimitris Rizos (iD), USA
Geoffrey W. Rodgers (iD), New Zealand
Pier Paolo Rossi, Italy
Nicola Ruggieri (iD), Italy
JUNLONG SHANG, Singapore

Nikhil Saboo, India
Anna Saetta, Italy
Juan Sagaseta (iD), United Kingdom
Timo Saksala, Finland
Mostafa Salari, Canada
Ginevra Salerno (iD), Italy
Evangelos J. Sapountzakis (iD), Greece
Vassilis Sarhosis (iD), United Kingdom
Navaratnarajah Sathiparan (iD), Sri Lanka
Fabrizio Scozzese (iD), Italy
Halil Sezen (iD), USA
Payam Shafigh (iD), Malaysia
M. Shahria Alam, Canada
Yi Shan, China
Hussein Sharaf, Iraq
Mostafa Sharifzadeh, Australia
Sanjay Kumar Shukla, Australia
Amir Si Larbi (iD), France
Okan Sirin (iD), Qatar
Piotr Smarzewski (iD), Poland
Francesca Sollecito (iD), Italy
Rui Song (iD), China
Tian-Yi Song, Australia
Flavio Stochino (iD), Italy
Mayank Sukhija (iD), USA
Piti Sukontasukkul (iD), Thailand
Jianping Sun, Singapore
Xiao Sun (iD), China
T. Tafsirojjaman (iD), Australia
Fujiao Tang (iD), China
Patrick W.C. Tang (iD), Australia
Zhi Cheng Tang (iD), China
Weerachart Tangchirapat (iD), Thailand
Xiaxin Tao, China
Piergiorgio Tataranni (iD), Italy
Elisabete Teixeira (iD), Portugal
Jorge Iván Tobón (iD), Colombia
Jing-Zhong Tong, China
Francesco Trentadue (iD), Italy
Antonello Troncone, Italy
Majbah Uddin (iD), USA
Tariq Umar (iD), United Kingdom
Muahmmad Usman, United Kingdom
Muhammad Usman (iD), Pakistan
Mucteba Uysal (iD), Turkey

Ilaria Venanzi , Italy
Castorina S. Vieira , Portugal
Valeria Vignali , Italy
Claudia Vitone , Italy
Liwei WEN , China
Chunfeng Wan , China
Hua-Ping Wan, China
Roman Wan-Wendner , Austria
Chaohui Wang , China
Hao Wang , USA
Shiming Wang , China
Wayne Yu Wang , United Kingdom
Wen-Da Wang, China
Xing Wang , China
Xiuling Wang , China
Zhenjun Wang , China
Xin-Jiang Wei , China
Tao Wen , China
Weiping Wen , China
Lei Weng , China
Chao Wu , United Kingdom
Jiangyu Wu, China
Wangjie Wu , China
Wenbing Wu , China
Zhixing Xiao, China
Gang Xu, China
Jian Xu , China
Panpan , China
Rongchao Xu , China
HE YONGLIANG, China
Michael Yam, Hong Kong
Hailu Yang , China
Xu-Xu Yang , China
Hui Yao , China
Xinyu Ye , China
Zhoujing Ye , China
Gürol Yildirim , Turkey
Dawei Yin , China
Doo-Yeol Yoo , Republic of Korea
Zhanping You , USA
Afshar A. Yousefi , Iran
Xinbao Yu , USA
Dongdong Yuan , China
Geun Y. Yun , Republic of Korea

Hyun-Do Yun , Republic of Korea
Cemal YİĞİT , Turkey
Paolo Zampieri, Italy
Giulio Zani , Italy
Mariano Angelo Zanini , Italy
Zhixiong Zeng , Hong Kong
Mustafa Zeybek, Turkey
Henglong Zhang , China
Jiupeng Zhang, China
Tingting Zhang , China
Zengping Zhang, China
Zetian Zhang , China
Zhigang Zhang , China
Zhipeng Zhao , Japan
Jun Zhao , China
Annan Zhou , Australia
Jia-wen Zhou , China
Hai-Tao Zhu , China
Peng Zhu , China
QuanJie Zhu , China
Wenjun Zhu , China
Marco Zucca, Italy
Haoran Zuo, Australia
Junqing Zuo , China
Robert Černý , Czech Republic
Süleyman İpek , Turkey

Contents

Research Article

Research on Numerical Simulation of Top-Down Construction Effect of Diaphragm Wall of Deep and Large Foundation Pit under Different Working Conditions in Complex Stratum

Fuxue Sun [ID],[1] Mingqing Liu [ID],[2] Yunhui Zhu,[2] Xiaochun Li,[3] and Gang Ge[3]

[1]*Wenzhou University, Wenzhou 325035, China*
[2]*Wenzhou University of Technology, Wenzhou 325035, China*
[3]*Shanghai Tunnel Engineering Co., Ltd, Shanghai 200000, China*

Correspondence should be addressed to Mingqing Liu; 846765019@qq.com

In order to study the construction effect of deep and large foundation pit excavation and its impact on the surrounding environment under complex stratum conditions, the deep and large foundation pit of the top-down construction method of shield exit shaft of S2 line of Wenzhou City railway is taken as the research object in this paper. According to the complex geological conditions of deep soft soil layer with underlying inclined rock surface in Wenzhou, the numerical simulation method is used to carry out the related research. The simulation results of the deformation characteristics of the diaphragm wall under two different working conditions which are the same length diaphragm wall and the suspended foot diaphragm wall are compared and analyzed. According to the analysis results, the suspended foot diaphragm wall is determined as the final construction scheme of the diaphragm wall, and it is verified by field measurement. The research results can provide technical support for the construction of similar projects. At the same time, it can also provide basic accumulation for the construction of major projects in Wenzhou.

1. Introduction

With the construction of the urban underground track, a large number of foundation pit projects appear. Foundation pit engineering is a multidisciplinary system engineering involving structural engineering, engineering mechanics, soil mechanics, foundation engineering, engineering monitoring technology, and construction organization management. It is a complex technology with two branches of civil engineering, which are architectural engineering and geotechnical engineering [1]. Generally, the regional geological conditions of foundation pit engineering are relatively poor, generally weak, or weak soil layers, and the occurrence and change forms of groundwater are diverse, such as the southeast coast of China. In this case, the key links of foundation pit engineering construction, including excavation, support, and dewatering, are often complex, which is a highly risky and challenging topic in the field of

geotechnical engineering [2]. The traditional excavation method of foundation pit is sloping excavation; that is, large open excavation without support structure or vertical excavation after certain support measures (such as anchor support, retaining wall support, and pile wall support) is adopted. After reaching the predetermined excavation depth, the concrete bottom plate is poured, and then the construction method is from bottom to top, or a combination of the two, and the sloping excavation is adopted for the upper part, the lower part adopts the construction method of support and excavation [3]. Although the above excavation methods are simple and fast, they have high requirements for engineering geological conditions, hydrogeological conditions, sloping excavation space, and excavation depth and are not suitable for the construction of underground space in large cities with poor hydrogeological conditions and dense populations. Under this background, the top-down construction method of the foundation pit

came into being. Its important feature is how to deal with the sliding resistance, horizontal resistance, and vertical load capacity of the basement structure. The common method to transfer the vertical load to the foundation is to use the frame column or Qiao. At this time, the outer wall of the basement can be served by the diaphragm wall. Italy is the first country in the world to have the reverse practice, and then, it has gradually developed in western developed countries such as the United States and Japan. So far, many engineering practices show that the top-down construction method of foundation pit is an effective construction method for multistorey underground space structures of buildings and roads in big cities [4,5].

So far, the pace of theoretical research on the top-down construction method is relatively slow, showing the phenomenon that theoretical research lags behind engineering practice [6–10]. There are three main research methods: (1) using many engineering practices and the basic theory of soil mechanics to summarize the engineering experience and practical methods, (2) using engineering monitoring technology and field test to capture the information of monitoring points during construction, and (3) the finite element simulation of the project carried out by using computer technology. The research contents mainly include the following: research on water and soil pressure and deformation around foundation pit; research on stress, strain, and displacement of foundation pit support structure; and study on the settlement difference between intermediate pile (column) and diaphragm wall.

In the study of soil displacement, Hsieh and Ou [11] fitted and analyzed 9 foundation pit engineering examples with different support methods of top-down construction method and down-top construction method and considered that the conclusion of soil deformation law caused by down-top construction method can be applied to the top-down construction method. Yoo and Lee [12] used the hardening soil constitutive model to establish a two-dimensional numerical model to study the characteristics of surface soil displacement. In the study of internal force and deformation of foundation pit retaining structure, Bose and Som [13] used numerical simulation to study the influence of diaphragm wall height, excavation width, and support structure prestress on foundation pit excavation; Ng et al. [14] used the Cambridge model to study the excavation process and results of multisupport foundation pit in cohesive soil, compared with the actual project, and obtained some meaningful conclusions; Finno et al. [15] studied the influence of foundation pit excavation on soil deformation and the influence of foundation pit support structure on pore water pressure by means of a test. The focus or foundation of the research on the differential settlement of top-down construction method lies in the research on pile foundation settlement theory. Poulos has made outstanding contributions in this regard. The Poulos elastic theory model established by Poulos has been used for reference by many scholars [16]. Because the elastic theory method assumes that the soil layer is uniform and the stiffness is constant, it can not reflect the anisotropy

and stratification characteristics of the actual foundation soil. On this basis, scholars at home and abroad introduce correction factors to modify and supplement Poulos's elastic theory model in varying degrees according to the actual formation conditions.

In addition, as an important retaining structure of the foundation pit, the diaphragm wall has the advantages of good overall, large stiffness, and convenient construction. It is still loved by builders. Bolton and Powrie [17] described the construction and foundation pit design mechanism by using an indoor centrifuge test and studied the behavior of diaphragm wall before foundation pit instability, including surface settlement outside the foundation pit and bending moment of the diaphragm wall. Ou et al. [18] conducted field measurement on the foundation pit excavated by the top-down construction method, analyzed the data, and concluded that the horizontal displacement of soil close to the diaphragm wall is similar to that of the wall. Graham [19] simulated and studied the deformation of diaphragm walls during foundation pit construction and analyzed the law of wall displacement and internal force. Wang et al. [20] analyzed a large number of field-measured data of ground connecting wall deformation in foundation pit and pointed out that the deformation of ground connecting wall in top-down construction method is smaller than that in the forward method. Xu et al. [21] analyzed the deformation law of diaphragm walls in different foundation pit projects by studying a large number of practical projects using diaphragm walls as a support structure in the deep foundation pit in Shanghai. Qiu et al. [22] established a practical engineering numerical model through the finite element numerical simulation research method to simulate the excavation process of the foundation pit and found that the greater the excavation depth of the foundation pit, the greater the deformation of the diaphragm wall.

To sum up, although the construction technology and relevant theories of the top-down construction method have achieved certain results and the application has been popularized, it is still applied as a special construction method, which is mainly used when there are special requirements for the project, or when the traditional method can not meet the requirements and is very uneconomic. At the same time, the combined action of the diaphragm wall and top-down construction method can reduce the deformation of the foundation pit. The deformation law of the diaphragm wall provides guidance for subsequent foundation pit design and construction and ensures the safety of foundation pit construction. In this paper, based on the top-down construction method of deep foundation pit for shield exit shaft of S2 line of Wenzhou City railway, aiming at the complex geological conditions of deep soft soil layer with underlying inclined rock surface in Wenzhou, the deformation characteristics of different diaphragm walls (diaphragm wall with the same length and suspended foot diaphragm wall) are compared and analyzed by using numerical simulation method, and the suitable construction scheme of diaphragm wall is determined, It can provide a reference for foundation pit engineering under similar geological conditions.

2. Project Overview

The project is located at the mouth of Oujiang River, connecting Qitoushan, Huanghua Town, Yueqing City, and Lingkun Town, Longwan District. It is an important part of line S2 of the Wenzhou City railway. The shield tunneling method is used for construction. The tunnel location is shown in Figure 1. Jiangbei's working shaft is the exit shaft of the shield tunnel, and foundation pit engineering is an important construction item of the Oujiang North portal tunnel. The length of the foundation pit is 43 m, the width is 21.9 m or 27.6 m, the excavation depth is 51.63 m (as shown in Figure 2), and the excavation depth is 51.63 m. Jiangbei working well is located in the deep muddy soil layer of the Oujiang shoal area. The upper part is the muddy soil and clay layer, and its thickness is about 46 m. There is a deep riprap layer in the middle and a weakly weathered tuff layer in the lower part. The rock surface is horizontally extroverted, and the geological conditions are complex (as shown in Figure 3). The foundation pit is protected by diaphragm wall, the thickness of the diaphragm wall is 1.5 m, the width of the standard section is generally 5.5 m, the length of the local special-shaped diaphragm wall is adjusted appropriately (as shown in Figure 4), and the reinforced concrete ring frame beam and each floor plate are used as support (as shown in Figure 5).

To sum up, the deep foundation pit engineering of Jiangbei working well is the deepest foundation pit in Zhejiang Province, and it faces multiple complex geology. Therefore, how to carry out diaphragm wall construction and foundation pit excavation and support under complex geological conditions and effectively control the deformation of foundation pit to ensure construction safety has become a construction difficulty of this project, which is also the research focus of this paper. In this paper, the numerical simulation method is used to compare and analyze the construction effect of the top-down method of diaphragm wall foundation pit under different working conditions and, finally, determine the best design scheme of diaphragm wall construction and foundation pit excavation and support suitable for the project.

3. Research on Numerical Simulation

Midas GTS software is used in numerical simulation, which can carry out two-dimensional and three-dimensional finite element numerical modeling for geotechnical engineering and analyze the stress and deformation of structural components and soil materials in engineering. The simulation results are very similar to the measured data.

3.1. Numerical Model

3.1.1. Model Size. According to the actual size of the foundation pit, the calculation model diagram is established, as shown in Figure 3. The length of the foundation pit relying on the project is 43 m, the left width is 21.9 m, the right width is 27.6 m, and the excavation depth is 51.63 m. According to the previous modeling experience, the size of the foundation

FIGURE 1: Schematic diagram of the location of Oujiang Beikou tunnel.

pit model can generally be 3–5 times the excavation depth of the foundation pit [23]. Finally, the overall size of the foundation pit model is determined as the length is 287 m, the width is 227.6 m, and the height is 100 m.

3.1.2. Formation Treatment Method. According to the detailed investigation report of the Oujiang North portal tunnel, the stratum is fine layered. Through sorting out and merging the soil materials with similar properties, the soil materials are divided into five different layers, and the modified Mohr-Coulomb constitutive model is adopted for the soil materials. The material parameters of each layer are shown in Table 1. (Note: the parameters that cannot be provided in the geological survey report are calculated by the empirical method. The other two stiffness properties can be selected according to the compression modulus of a certain ratio. Generally, the secant modulus is equal to the tangent modulus and three times the compression modulus.)

For the inclined rock surface, according to the geological survey data, the inclined rock surface is diagonally inclined, and the slope of the rock surface is not uniform. It is difficult to model and simulate according to the actual trend, and there are many irregular grid cells, which lead to poor quality of the grid and reduce the simulation speed. In order to meet the needs of simulation calculation, according to the depth of the rock surface around the foundation pit determined by the survey, after determining the depth of the weathered rock at the interface between the rock surface and the foundation pit, the rock surface trend inside the foundation pit is determined by the slope average method, and the rock surface trend outside the foundation pit is extended according to the slope inside the foundation pit to form the internal rock surface trend of the model. The size of the completed model is shown in Figure 6.

3.2. Selection of Structural Elements and Material Parameters. The supporting structure of the deep foundation pit in Beikou well is mainly the diaphragm wall, supporting plate, and reinforced concrete ring frame beam, as shown in Figure 5. The elastic constitutive model is selected for all supporting structures, in which the diaphragm wall and each floor structure adopt a two-dimensional plate element,
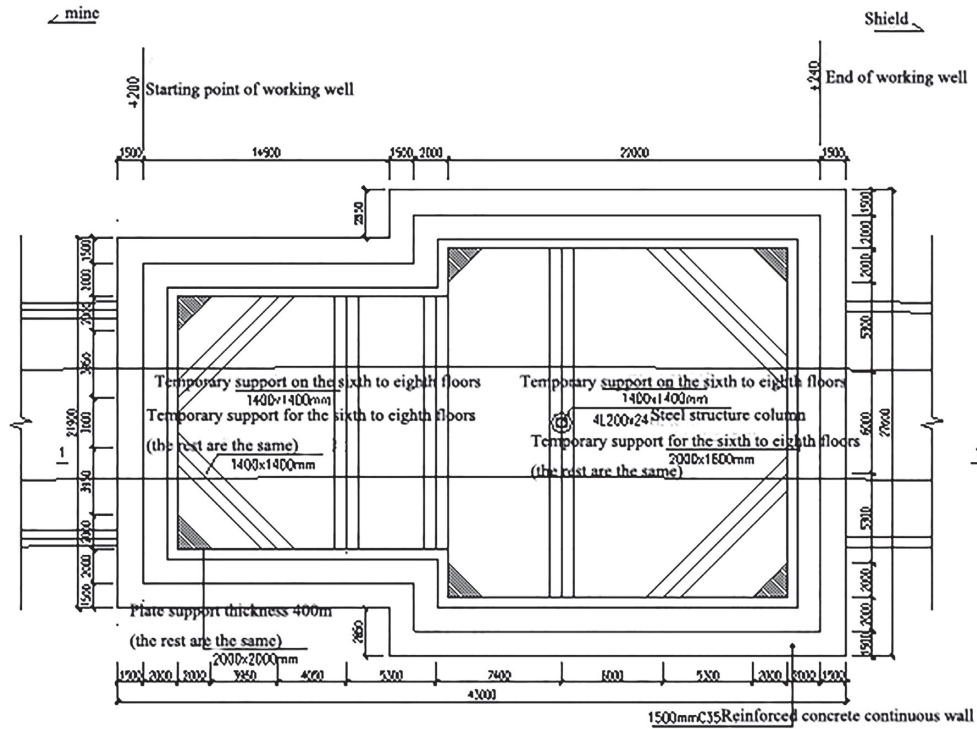
Figure 2: Layout map of Jiangbei working well.
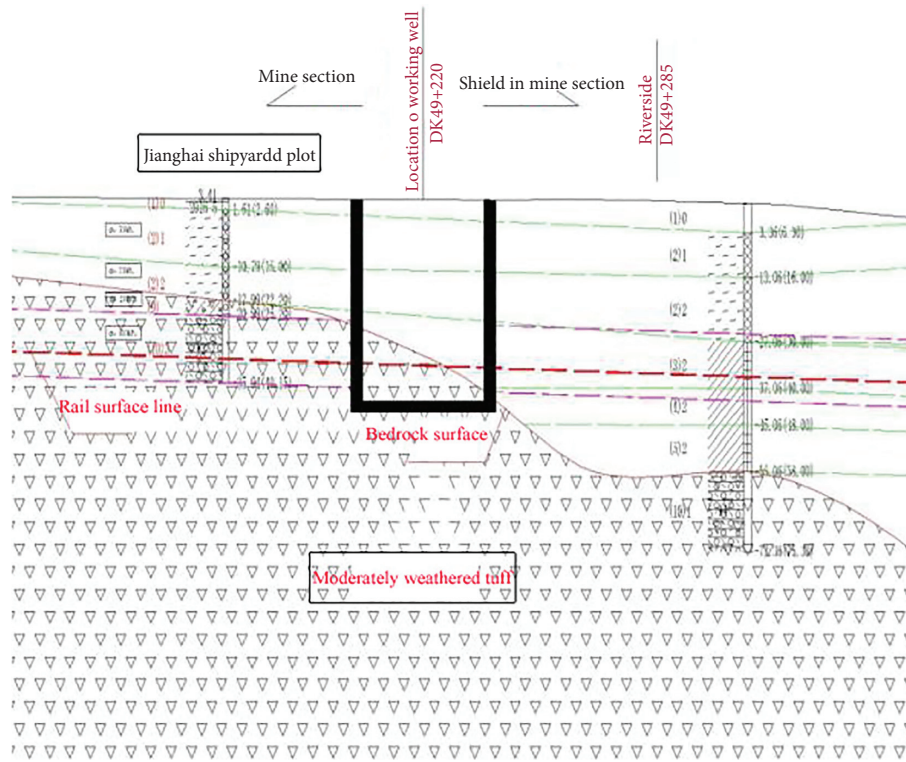
Figure 3: Geological profile of Jiangbei working well.

which is extracted from the three-dimensional solid element. The reinforced concrete ring frame beam is mainly flexural, and its length is larger than the cross-sectional area, so a one-dimensional beam element is adopted, which is extracted from the three-dimensional solid element. The material parameters of the supporting structure are shown in Table 2.
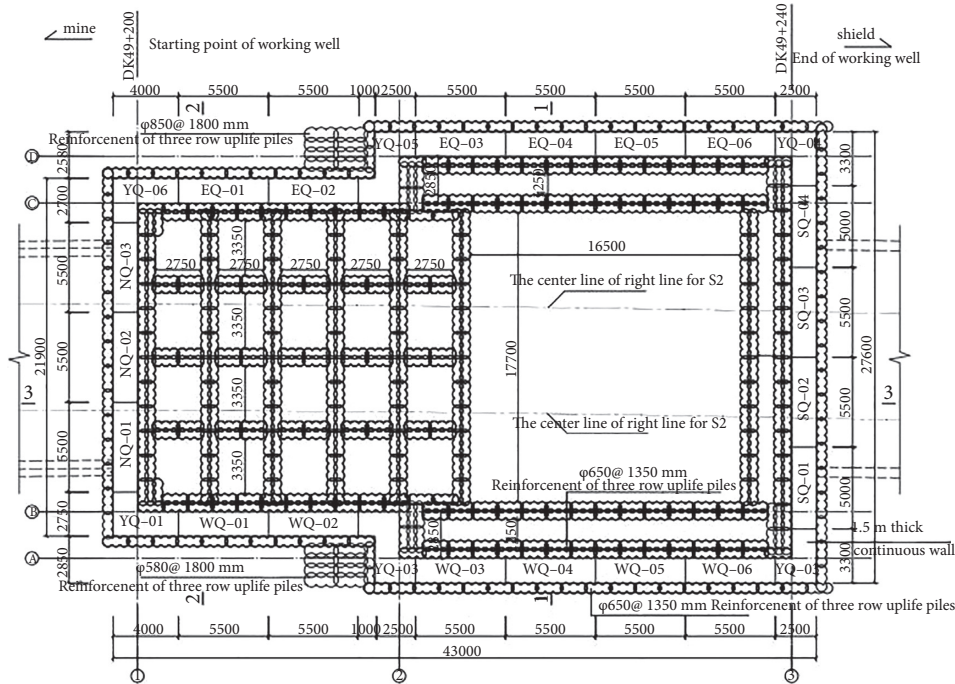
FIGURE 4: Division map of ground connecting wall in Jiangbei working well.

3.3. Boundary Conditions and Mesh Generation. In the length direction (*X* direction) of the model, the displacement of the *X*-axis is limited, that is, $u = 0$, $v \neq 0$, and $w \neq 0$. In the width direction (*Y* direction), the displacement of the *Y*-axis is limited, that is, $u \neq 0$, $v = 0$, and $w \neq 0$. In the height direction (*z* direction), the upper boundary of the model is free, i.e., unrestricted, and the lower boundary of the model is fully constrained, i.e., $u = 0$, $v = 0$, and $w = 0$ (U is the displacement in the *X* direction, *V* is displacement in the *Y* direction, and *W* is displacement in the *Z* direction). In this model, a hybrid grid is used.

3.4. Determination of Simulated Construction Process of Top-Down Method. The deep foundation pit is constructed by the top-down method. According to the design and construction technology of the foundation pit, the foundation pit excavation is simulated according to the actual technology. The foundation pit excavation is divided into 12 steps, and the specific construction process is shown in Table 3.

3.5. Determination of Simulation Conditions. According to the needs of the project, the following two comparative conditions are determined for research: ① the bottom of the diaphragm wall is at the same elevation and ② suspended foot diaphragm wall. The construction procedures of the two conditions are shown in Table 3. According to the needs of simulation, the horizontal displacement, bending moment deformation and surrounding ground settlement of diaphragm wall are selected as the construction effect indexes.

3.6. Calculation Assumption. In this paper, based on the foundation pit of the exit well of the project, the calculation model is established considering the surrounding soil. According to the actual stratum situation and the calculation needs of the model, the following assumptions are made. ① The soil is isotropic and evenly distributed, and the soil is isotropic and uniformly distributed. ② The influence of the surrounding environment induced by diaphragm wall construction is not considered. ③ The influence of soil drainage consolidation and groundwater seepage is not considered.

4. Numerical Simulation of Construction Effect of Diaphragm Wall Foundation Pit with Top-Down Method under Different Working Conditions

4.1. Numerical Simulation Study on Construction Effect of Top-Down Construction Method for Foundation Pit with Diaphragm Wall of the Same Length. The foundation pit construction is divided into 12 steps, and there are many excavation conditions. In the simulation, the first, third, fifth, seventh, and tenth excavation is selected (corresponding to the process number in Table 3 is third, fifth, seventh, ninth, and twelfth). These five excavation conditions are used to study and analyze the foundation pit construction effect.

4.1.1. Design of Diaphragm Wall with the Same Length. The excavation depth of the foundation pit is 51.63 m, which belongs to a super deep foundation pit with a weak stratum. The original design diaphragm wall of the foundation pit is
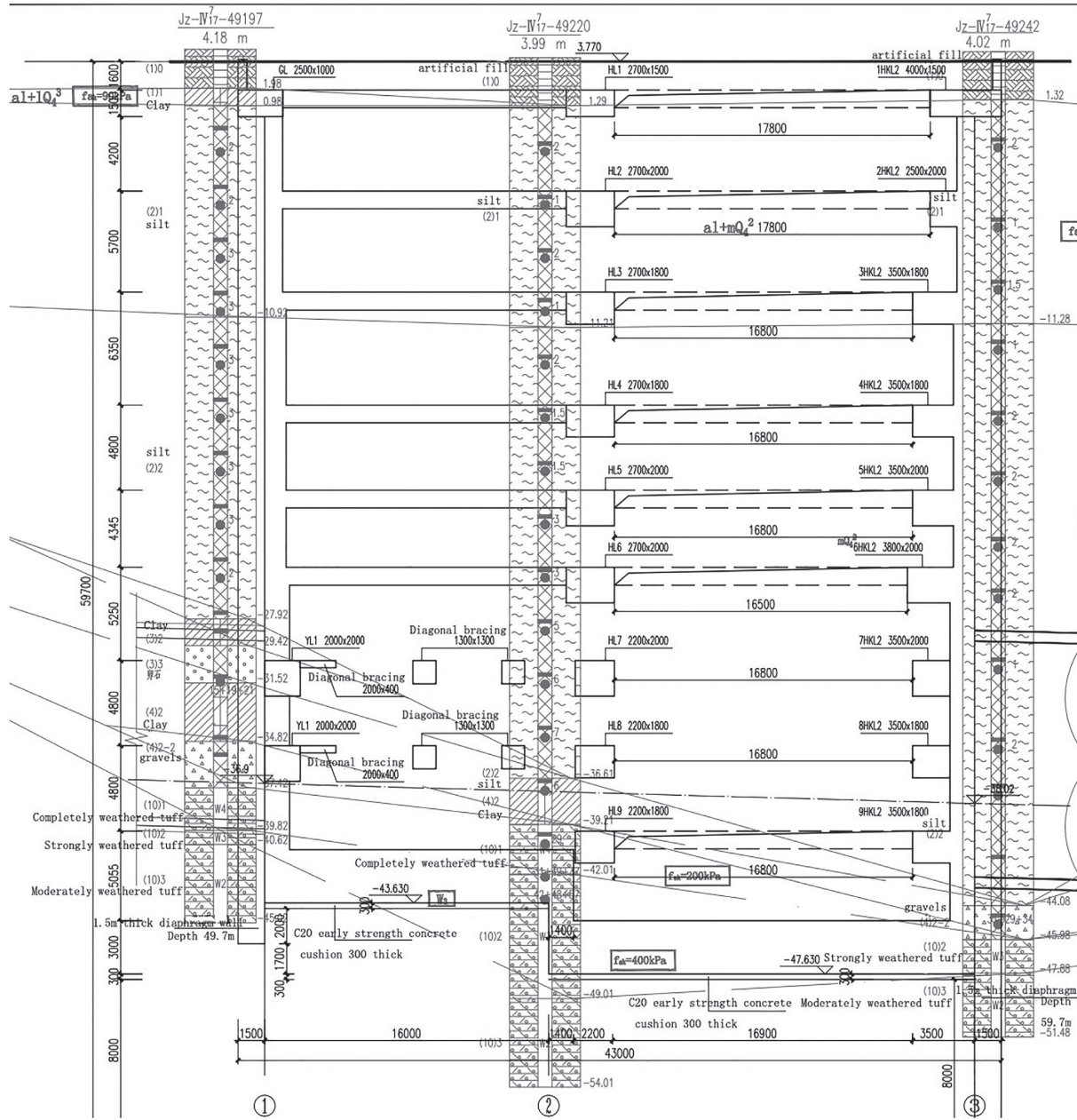
FIGURE 5: Section diagram of foundation pit supporting structure.

TABLE 1: Material parameters of soil layer.

Number	Layer	Layer thickness (m)	Compression modulus (MPa)	Poisson's ratio	Unit weight (kN/m³)	Cohesion (kPa)	Internal friction angle (°)
①	Silt 1	18	1.97	0.30	18	6.05	2.93
②	Silt 2	14	2.09	0.30	15	6.38	3.11
③	Clay 1	14.8	2.98	0.40	20	10.23	3.10
④	Clay 2	3.18	3.80	0.35	18	12.45	7.58
⑤	Tuff	1.65	500.00	0.30	23	20.00	33.00

the same length diaphragm wall. The diaphragm wall is made of C45 waterproof concrete, with the bottom at the same elevation, the depth of 59.80 m, and the thickness is 1.5 m, as shown in Figure 7.

4.1.2. Analysis of Horizontal Displacement Simulation Results of Diaphragm Wall with the Same Length. The horizontal displacement contour plot of the diaphragm wall with the same length under five excavation conditions is shown in
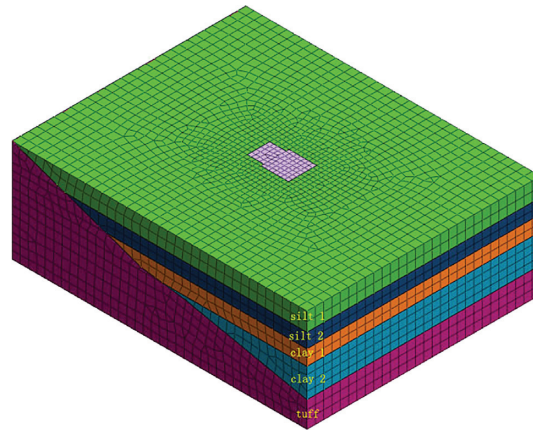
Figure 6: Overall calculation model of foundation pit.

Table 2: Material parameters of supporting structure.

Structure name	Element type	Constitutive model	Modulus of elasticity (kN/m^2)	Poisson's ratio	Unit weight (kN/m^3)	Thickness/diameter (m)
Diaphragm wall	Plate	Elastic	32500000	0.2	24.5	1.5
Ring frame beam	Beam	Elastic	32500000	0.2	24.5	3.5×1.8
Top plate/middle plate	Plate	Elastic	32500000	0.2	24.5	0.4
Floor	Plate	Elastic	32500000	0.2	24.5	3

Table 3: Details of construction procedures.

Process number	Process node
1	The original stratum is established, and the initial stress is analyzed by applying boundary constraint and self-weight load
2	Activate diaphragm wall and clear displacement
3	The first excavation to −2.000 m activates the first ring frame beam and roof
4	The second excavation was to −7.700 m, and the second ring frame beam and the middle slab of the negative first floor were activated
5	After the third excavation to −13.400 m, the third ring frame beam and the middle slab of the second floor were activated
6	The fourth excavation to −19.750 m, the fourth ring frame beam and the negative third floor slab were activated
7	The fifth excavation to −24.550 m, the fifth ring frame beam and the negative fourth floor slab were activated
8	The sixth excavation was to −28.895 m, and the sixth ring frame beam and the middle slab of the fifth floor were activated
9	The seventh excavation was carried out to −34.145 m, and the seventh ring frame beam and the middle slab of the sixth floor were activated
10	The eighth excavation to −38.945 m, the eighth ring frame beam and the negative seventh floor middle plate were activated
11	The ninth excavation was carried out to −43.575 m, and the ninth ring frame beam and the middle slab of the eighth floor were activated
12	The tenth excavation to −51.630 m, the floor was activated

Figure 8. In the contour plot, the one on the left is the west wall, and the one on the right is the east wall (the same below).

The horizontal displacement data of the diaphragm wall under five excavation conditions obtained from Figure 8 are sorted and analyzed, and the depth-displacement curve of the diaphragm wall can be obtained, as shown in Figure 9, and the maximum horizontal displacement and depth data of diaphragm wall can be summarized into a table, as shown in Table 4.

It can be seen from the above that the horizontal displacement of the diaphragm wall is small in the first excavation. With the excavation of the foundation pit, the pouring of intermediate plate structure, and the support of ring frame beam, the horizontal displacement curve of diaphragm wall forms the deformation law of "small at both ends, large in the middle." The maximum horizontal displacement of the east wall is larger than that of the west wall, which is due to the existence of an inclined rock surface, and the displacement and deformation laws of the east and west walls are basically the same. With the increase of the excavation depth of the foundation pit, the maximum horizontal displacement of the diaphragm wall increases continuously, and the position of the maximum
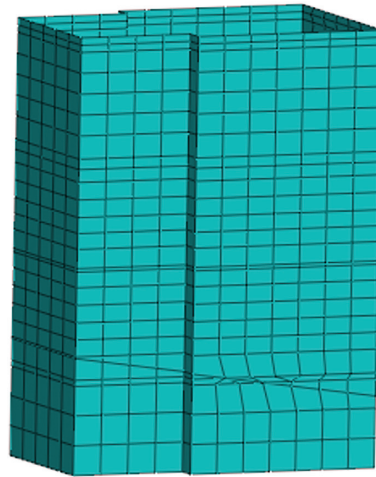
FIGURE 7: Schematic diagram of the bottom-level wall-to-wall model.

(a)

(b)

(c)

(d)

(e)
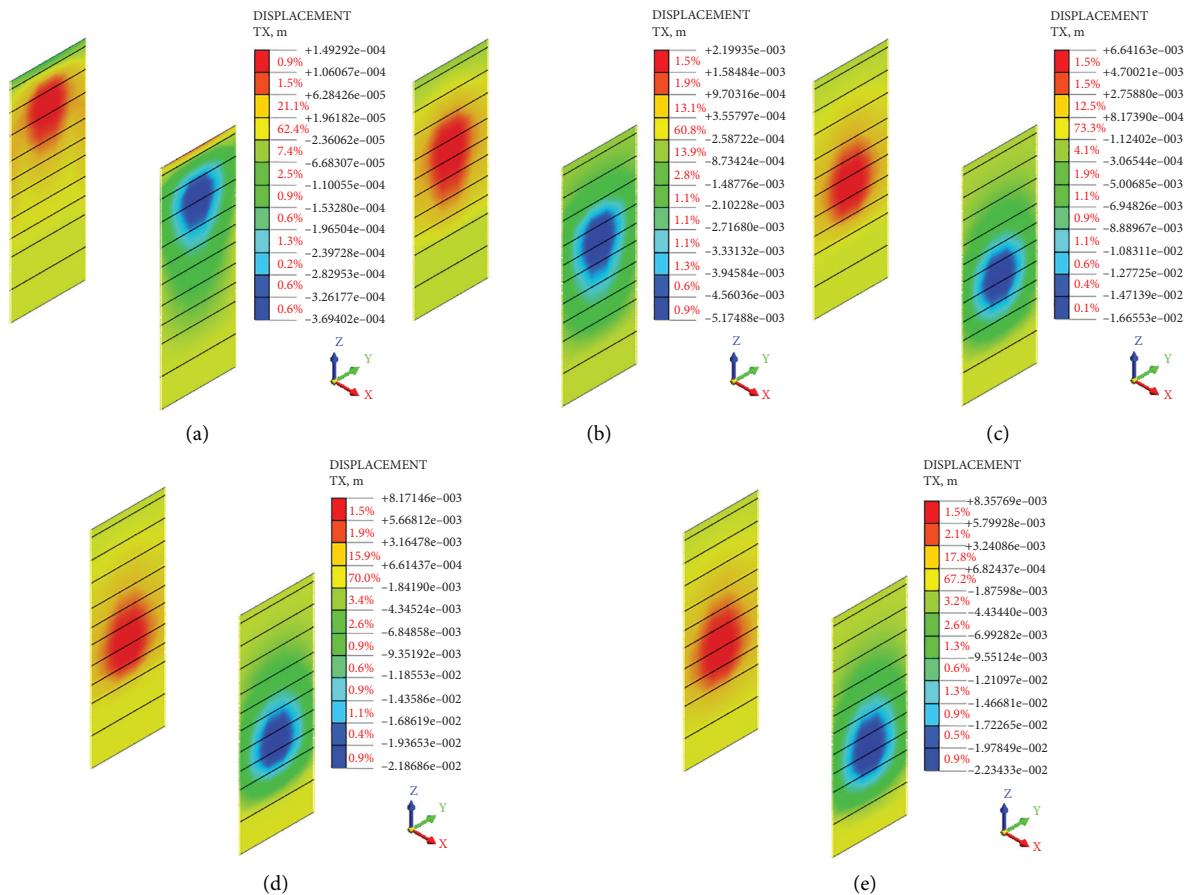
FIGURE 8: The horizontal displacement contour plot of the diaphragm wall with the same length under five excavation step conditions. (a) The first excavation step. (b) The third excavation step. (c) The fifth excavation step. (d) The seventh excavation step. (e) The tenth excavation step.

horizontal displacement moves downward. Due to the constraint of rock on the diaphragm wall, the final maximum horizontal displacement is above the excavation surface, and the maximum horizontal displacement is about 3/5~3/4 times of the final excavation depth of the foundation pit.
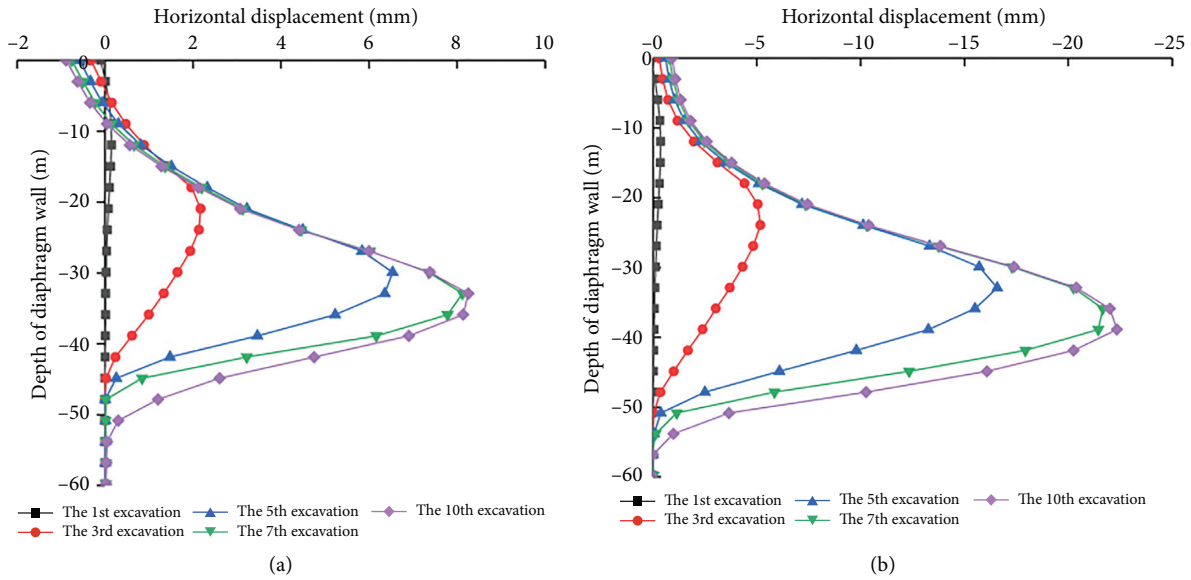
Figure 9: The horizontal displacement curve of the diaphragm wall. (a) West wall. (b) East wall.

Table 4: Summary of the corresponding depth of the maximum horizontal displacement of the ground connecting wall.

Working procedure	Diaphragm wall (west)		Diaphragm wall (east)	
	Maximum horizontal displacement (mm)	The depth of diaphragm wall (m)	Maximum horizontal displacement (mm)	The depth of diaphragm wall (m)
The first excavation step (−2.000 m)	0.145	−11.96	−0.364	−11.96
The third excavation step (−13.400 m)	2.171	−20.93	−5.171	−23.92
The fifth excavation step (−24.550 m)	6.537	−29.90	−16.581	−32.89
The seventh excavation step (−34.145 m)	8.126	−32.89	−21.666	−35.88
The tenth excavation step (−51.630 m)	8.256	−32.89	−22.341	−38.87

4.1.3. Analysis of the Bending Moment Simulation Results of Diaphragm Wall with the Same Length. The bending moment contour plot of the diaphragm wall under five excavation conditions is shown in Figure 10.

The depth-bending moment curve of the diaphragm wall can be obtained by sorting and analyzing the bending moment data of the diaphragm wall under five excavation step conditions, as shown in Figure 11, and the maximum bending moment and depth data of the diaphragm wall can be summarized into a table, as shown in Table 5.

It can be seen from the above that the bending moment of the diaphragm wall is small in the first excavation, and there is a reverse bending point. With the progress of excavation, the bending moment of the diaphragm wall increases gradually, and the bending moment in the final excavation stage decreases slightly compared with that in the previous stage. The maximum positive moment is larger than the maximum negative moment at each excavation stage. Due to the existence of inclined strata, the maximum bending moment of the east wall is larger than

that of the west wall in each excavation stage, and the deformation law of the east wall and the west wall is basically the same, but asymmetric. With the increase of the excavation depth of the foundation pit, the maximum positive (negative) bending moment of the diaphragm wall increases continuously (except for the tenth excavation). During the tenth excavation, the maximum positive bending moment of the diaphragm wall decreases, the position of the maximum positive bending moment first moves down and then rises, the original position remains unchanged, and the position of the maximum negative bending moment does not change with the change of excavation stage. In each excavation stage, the maximum positive bending moment of the diaphragm wall is larger than the maximum negative bending moment. The maximum positive bending moment of the diaphragm wall is about 7/10~3/4 times of the final excavation depth of the foundation pit, and the maximum negative bending moment is about 4/5~49/50 times of the final excavation depth of the foundation pit.

FIGURE 10: The bending moment contour plot of suspended diaphragm wall under five excavation step conditions. (a) The first excavation step. (b) The third excavation step. (c) The fifth excavation step. (d) The seventh excavation step. (e) The tenth excavation step.
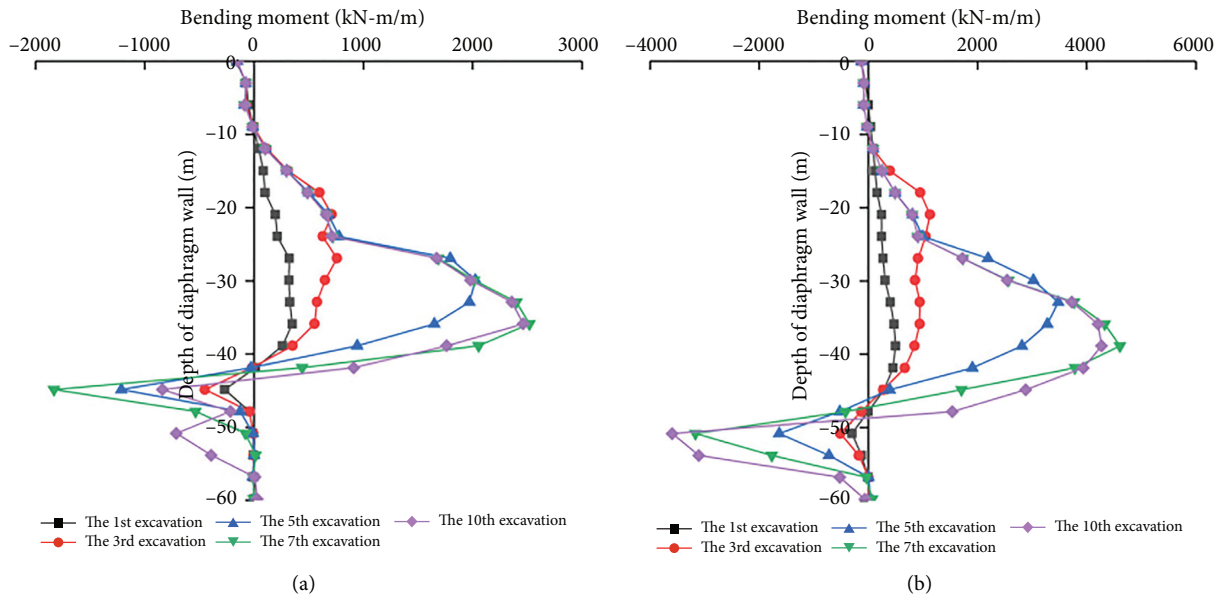
FIGURE 11: The bending moment curve of the diaphragm wall. (a) West wall. (b) East wall.

4.1.4. Analysis of Ground Settlement Simulation Results of Diaphragm Wall with the Same Length. The contour plot of soil surface settlement and deformation under five excavation conditions is shown in Figure 12.

By sorting and analyzing the simulated data of soil surface settlement under five excavation conditions, the surface settlement distance curve from the foundation pit can be obtained, as shown in Figure 13, and the data of the

TABLE 5: Summary of maximum bending moment corresponding to the depth of the ground wall.

Working procedure	Diaphragm wall (west)		Diaphragm wall (east)	
	Maximum bending moment (kN·m/m)	The depth of the diaphragm wall (m)	Maximum bending moment (kN·m/m)	The depth of the diaphragm wall (m)
The first excavation step (−2.000 m)	349.896/−269.976	−35.88/−44.85	497.000/−300.185	−38.87/−50.83
The third excavation step (−13.400 m)	757.587/−449.852	−26.91/−44.85	1127.313/−511.097	−20.93/−50.83
The fifth excavation step (−24.550 m)	2024.333/−1214.235	−29.90/−44.85	3480.993/−1632.490	−32.89/−50.83
The seventh excavation step (−34.145 m)	2518.406/−1831.024	−35.88/−44.85	4609.055/−3168.472	−38.87/−50.83
The tenth excavation step (−51.630 m)	2462.475/−838.087	−35.88/−44.85	4271.144/−3594.525	−38.87/−50.83
Remarks	Among the maximum bending moments in the table, the maximum positive bending moment value is before "/," and the maximum negative bending moment value is after "/," respectively, corresponding to the depth of the diaphragm wall			

(a)

(b)

(c)

(d)
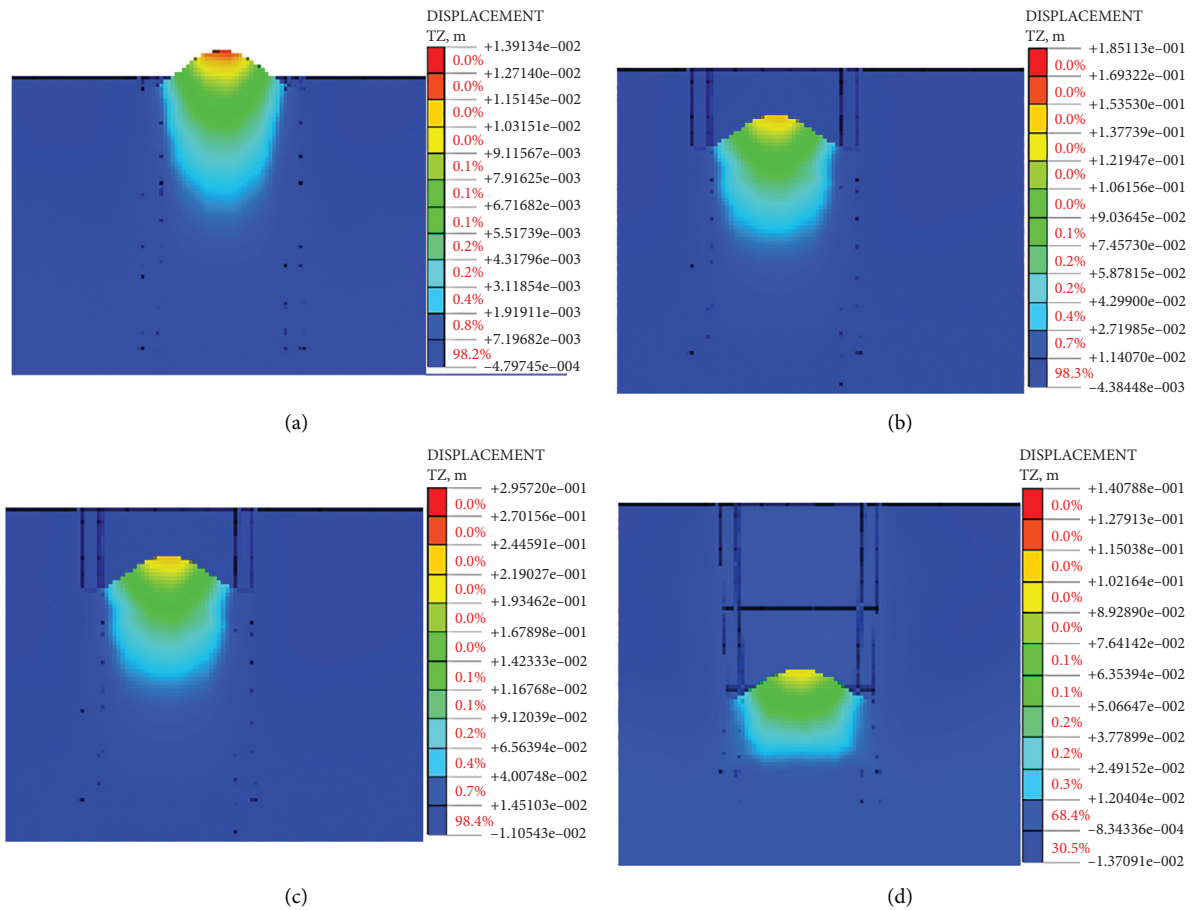
FIGURE 12: Continued.
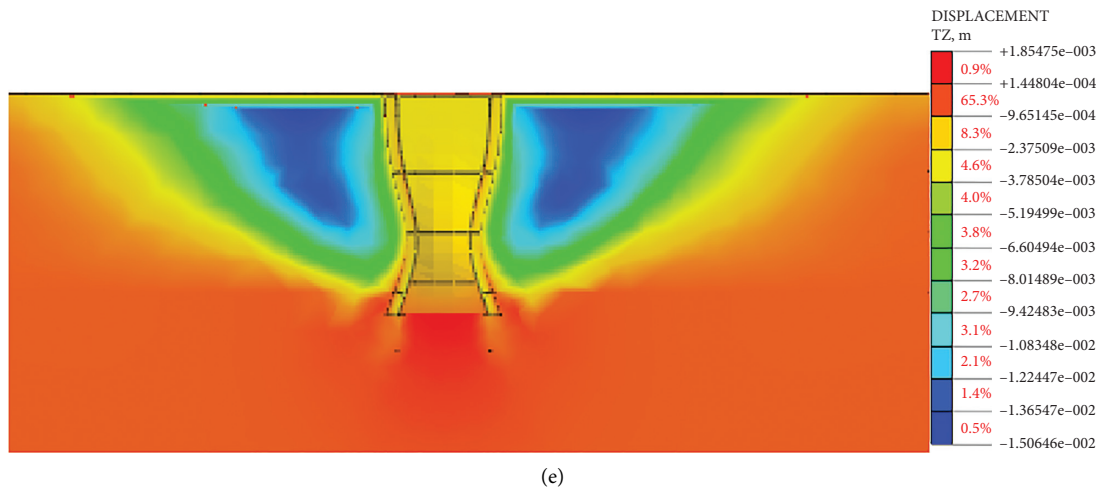
(e)

FIGURE 12: The contour plot of surface settlement and deformation under five excavation conditions. (a) The first excavation step. (b) The third excavation step. (c) The fifth excavation step. (d) The seventh excavation step. (e) The tenth excavation step.

location of the maximum surface settlement can be summarized into a table, as shown in Table 6.

Through comprehensive analysis of Figures 12 and 13 and Table 6, the following conclusions can be obtained:

(1) During the first excavation, the surface settlement of the soil is very small. The maximum surface settlement of the soil on the east and west sides is about 0.5 mm. The maximum settlement is located 10 m away from the edge of the foundation pit, and the settlement beyond 20 m is almost zero.

(2) During the third excavation, the soil surface settlement increased, and the maximum settlement was about 4.0~4.5 mm. The soil surface settlement position changed, all located 15 m away from the edge of the foundation pit, and the soil surface settlement outside 60 m was small.

(3) During the fifth excavation, the surface settlement of the soil continued to increase, and the maximum surface settlement was about 11.0 mm, an increase of about twice that of the third excavation, which was consistent with the sudden increase of the horizontal displacement and a bending moment of the diaphragm wall during the fifth excavation. Due to the deformation law of the diaphragm wall, the surface also had a large settlement. The maximum surface settlement position of the soil in the west remained unchanged, and it was still 15 m away from the foundation pit division. The maximum ground settlement position of the soil on the east side changes, which is 20 m away from the pit edge of the foundation pit, and the ground settlement of the soil outside 80 m is about 0.8 mm.

(4) During the seventh excavation, the surface settlement of soil continued to increase with a small increase. The maximum surface settlement of soil was about 13.0~14.0 mm, the maximum surface settlement position remained unchanged (15 m in the west and 20 m in the east), and the surface settlement outside 85 m was about 0.9 mm.

(5) During the tenth excavation, the soil surface settlement continued to increase with a smaller increase. The maximum soil surface settlement was about 15.0 mm, and the maximum surface settlement position remained unchanged (the west side is 15 m and the east side is 20 m). The maximum surface settlement is about 0.029% of the excavation depth of the foundation pit of 51.630 m, about 67% of the maximum horizontal displacement of the diaphragm wall. The maximum surface settlement is located 20 m away from the edge of the foundation pit, about 0.4 times the excavation depth of the foundation pit of 51.630 m.

(6) The maximum surface settlement of the soil in the east is slightly greater than that in the west (except for the third excavation step). The surface settlement curve of the soil in each construction stage first increases and then decreases with the distance from the edge of the foundation pit and finally tends to be stable, showing a "groove shape." According to the curve, the law of surface settlement and deformation on the east and west sides is basically the same. With the increase of foundation pit excavation depth, the maximum surface settlement increases continuously. The maximum settlement position of the west surface does not change with the change of excavation conditions (except the first excavation step). The maximum surface settlement is about 0.029% of the final excavation depth of the foundation pit and about 67% of the maximum horizontal displacement of the diaphragm wall. The maximum surface settlement is located 20 m away from the edge of the
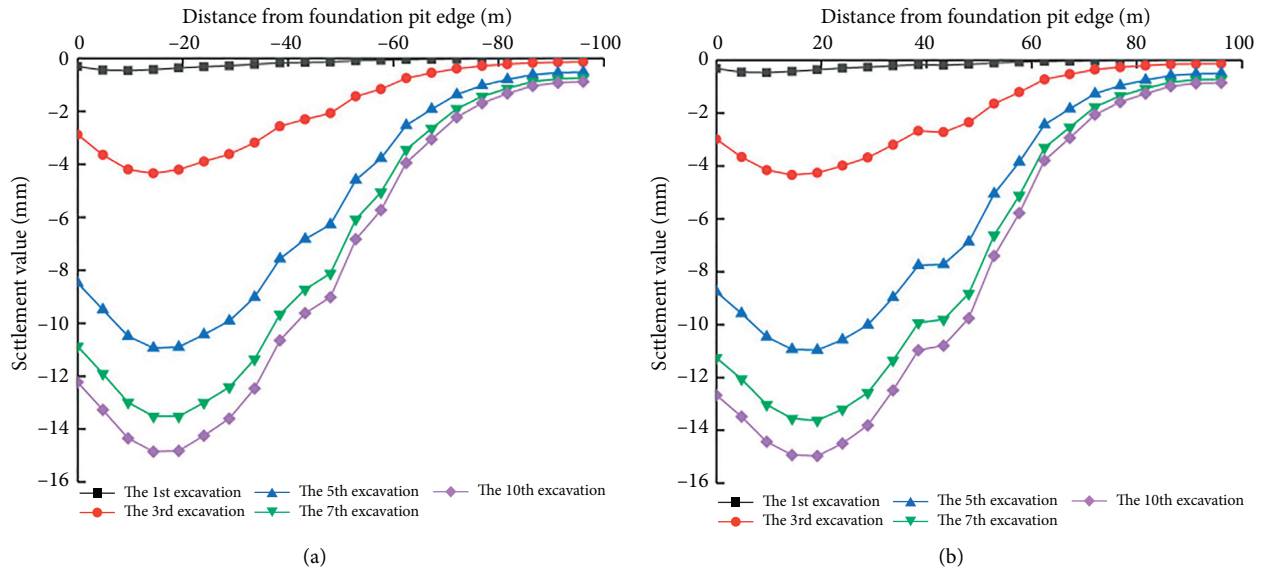
FIGURE 13: The curve of surface subsidence. (a) West wall. (b) East wall.

TABLE 6: Summary of the corresponding position of the maximum subsidence of the surface.

Working procedure	External surface of foundation pit (west)		External surface of foundation pit (east)	
	Maximum settlement (mm)	Distance from foundation pit edge (m)	Maximum settlement (mm)	Distance from foundation pit edge (m)
The first excavation step (−2.000 m)	−0.460	10.00	−0.470	10.00
The third excavation step (−13.400 m)	−4.340	15.00	−4.339	15.00
The fifth excavation step (−24.550 m)	−10.938	15.00	−10.968	20.00
The seventh excavation step (−34.145 m)	−13.515	15.00	−13.626	20.00
The tenth excavation step (−51.630 m)	−14.851	15.00	−14.967	20.00

foundation pit, about 0.4 times the final excavation depth of the foundation pit, and the main influence area is about 1.5 times the final excavation depth of the foundation pit.

4.2. Numerical Simulation Study on Construction Effect of Top-Down Construction Method for Foundation Pit with Suspended Foot Diaphragm Wall

4.2.1. Research Background of Optimization of Suspended Diaphragm Wall. In the original design scheme of the Jiangbei working shaft foundation pit, the height of the diaphragm wall is 59.8 m, the thickness is 1.5 m, and the bottom of the diaphragm wall is at the same elevation. However, in the construction process, due to the high strength of moderately weathered rock, the construction speed of existing wall forming equipment is too slow to meet the requirements of the construction period, and the cost is too high. Through the discussion of experts, it is proposed to change the insertion mode of in situ diaphragm wall into the design scheme of a suspended foot diaphragm wall with two

meters into the rock. The length of the left wall (west wall) of the suspended foot diaphragm wall is 45.82 m, and the length of the right wall (east wall) is 51.98 m, as shown in Figure 14. Other conditions are completely consistent with the same length diaphragm wall in Section 4.1.

Therefore, the purpose of numerical simulation under this condition is to study the deformation law of the suspended diaphragm wall foundation pit during top-down construction. Through the theoretical analysis of the data obtained from the numerical simulation, the purpose of optimizing the diaphragm wall can be achieved. The data and analysis results can be used as reference materials for related projects.

4.2.2. Analysis of Simulation Results of Horizontal Displacement of Suspended Diaphragm Wall (The Depth into Rock is 2 m). Here, it should be emphasized that since the horizontal displacement, bending moment, and surface settlement contour plot obtained by the simulation of the construction effect of the suspended diaphragm wall are similar to those of the diaphragm wall with the same length,
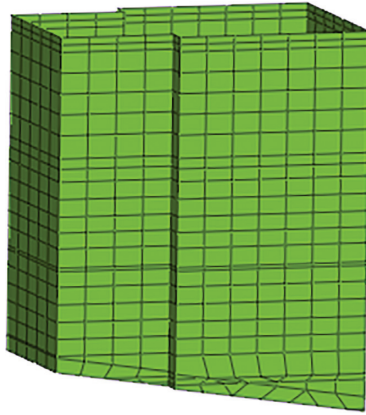
FIGURE 14: Schematic diagram of the ground connection wall (the depth into the rock is 2 m).

the simulation contour plot corresponding to the above three construction effect indexes is no longer displayed here.

The data of the horizontal displacement of the diaphragm wall under five simulated excavation conditions are sorted out and analyzed, and the depth-displacement curve of the diaphragm wall is obtained, as shown in Figure 15, and the maximum horizontal displacement and depth data of the diaphragm wall are summarized into a table, as shown in Table 7.

It can be seen from the above that the horizontal displacement of the foot diaphragm wall is small in the first excavation step. With the excavation of the foundation pit, the pouring of the middle plate structure, and the support of the ring frame beam, the horizontal displacement curve of the foot diaphragm wall is in the shape of "small at both ends, large in the middle." When the diaphragm wall is a suspended footing and the underlying strata are less embedded, the displacement and deformation of the end and bottom of the suspended footing diaphragm wall are larger. The maximum horizontal displacement of the east wall is greater than that of the west wall, which is due to the existence of the inclined rock surface. The displacement and deformation of the east and west walls are asymmetric. The maximum horizontal displacement of the diaphragm wall gradually moves down with the increase of the excavation depth and finally above the excavation surface. The maximum horizontal displacement is about 7/10 ~3/4 times the final excavation depth of the foundation pit.

4.2.3. Analysis of Bending Moment Simulation Results of Suspended Diaphragm Wall (The Depth into Rock Is 2 m).
By sorting and analyzing the data in the bending moment cloud part of the suspended footed diaphragm wall under five simulated excavation step conditions, the relationship curve between depth and bending moment of the suspended footed diaphragm wall can be obtained, as shown in Figure 16, and the maximum bending moment and depth data of the suspended footed diaphragm wall can be summarized into a table, as shown in Table 8.

It can be seen from the above that the bending moment of the diaphragm wall is small in the first excavation step,

and there is a reverse bending point. With the progress of excavation, the bending moment of the diaphragm wall increases gradually and then decreases slightly in the final excavation stage. The maximum positive moment is larger than the maximum negative moment at each excavation stage. The position of the maximum positive bending moment of the east and west walls first moves down and then rises and then remains unchanged after the original position. The position of the maximum negative bending moment does not change with the change of the excavation stage (except for the tenth excavation of the east wall). Due to the existence of inclined strata, the maximum bending moment of the east wall is larger than that of the west wall in each excavation stage (except for the negative bending moment of the tenth excavation step), and the deformation law of the east wall and the west wall is basically the same, but asymmetric. In each excavation stage, the maximum positive bending moment of the diaphragm wall is larger than the maximum negative bending moment. The maximum positive bending moment of the diaphragm wall is about 7/10~3/4 times the final excavation depth of the foundation pit, and the maximum negative bending moment is about 4/5~19/20 times the final excavation depth of the foundation pit.
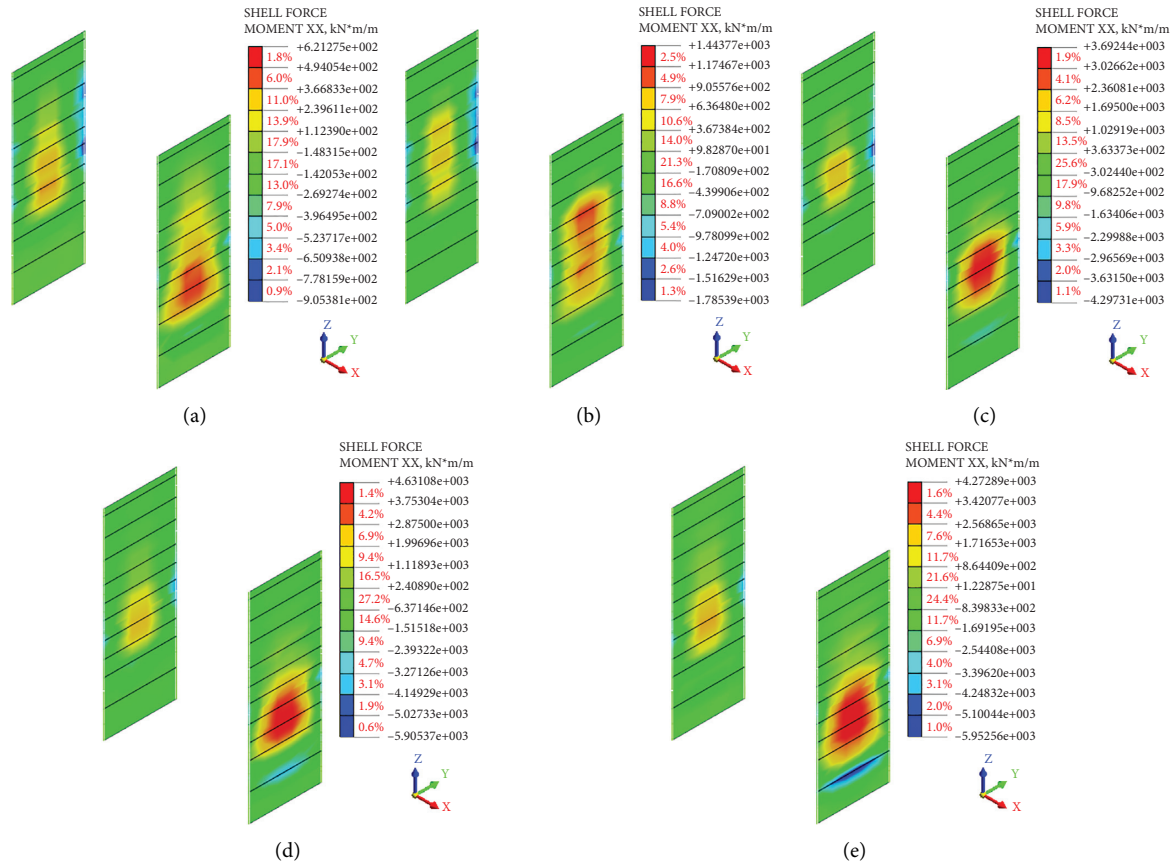
4.2.4. Analysis of Simulation Results of Ground Settlement of Suspended Diaphragm Wall (The Depth into Rock Is 2 m).
By sorting and analyzing the simulated data of soil surface settlement under five excavation step conditions, the surface settlement distance curve from the foundation pit can be obtained, as shown in Figure 17, and the data of the location of the maximum surface settlement can be summarized into a table, as shown in Table 9.

It can be seen from the above that the settlement of soil surface is small at the first excavation step and increases gradually with the increase of excavation depth. In each construction stage, the surface settlement curve of soil increases first, then decreases, and finally tends to be stable with the distance from the foundation pit edge, showing a "groove" curve, and the surface settlement deformation law of the east and west sides is basically the same. The maximum settlement of the east and west sides of the ground is the same, and the final settlement is 0.3 times the final excavation depth of the foundation pit. The maximum surface settlement is about 0.036% of the final excavation depth of the foundation pit, about 78% of the maximum horizontal displacement of the foot diaphragm wall. The maximum surface settlement is located at a distance of 15 m from the edge of the foundation pit, about 0.3 times the final excavation depth of the foundation pit, and the main impact area is about 1.5 times the final excavation depth of the foundation pit.

4.3. Comparative Analysis of Simulation Results under Two Conditions

4.3.1. Comparative Analysis of Horizontal Displacement of the Diaphragm Wall. After sorting and analyzing the data in
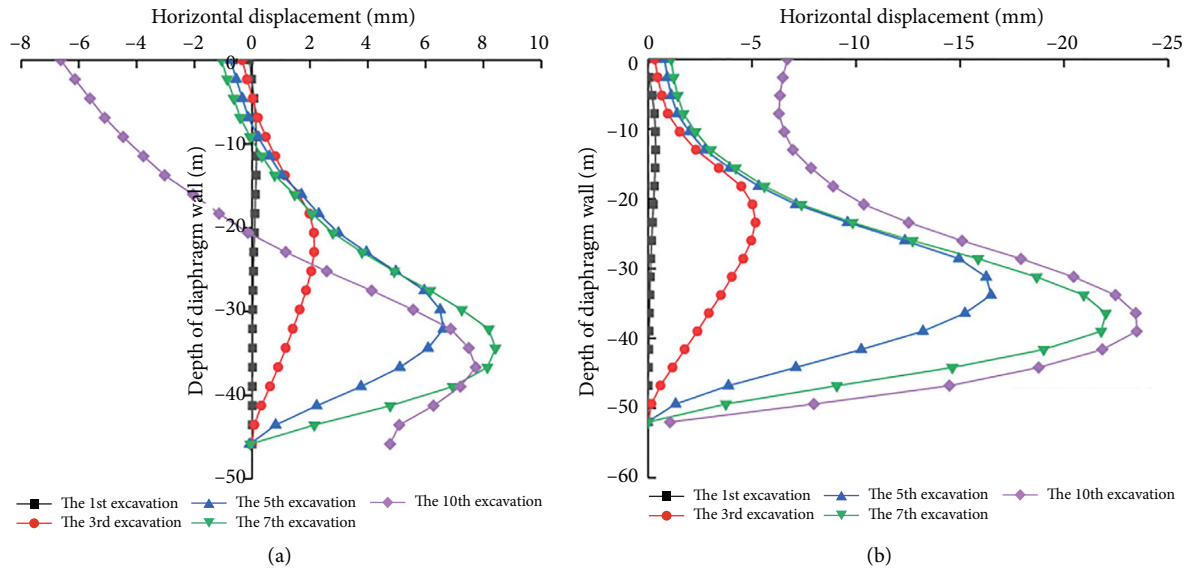
FIGURE 15: The horizontal displacement curve of the suspended foot diaphragm wall. (a) West wall. (b) East wall.

TABLE 7: Summary table of the corresponding depth of the maximum horizontal displacement of the suspended foot diaphragm wall.

Working procedure	Suspended foot diaphragm wall (west, the length is 45.82 m)		Suspended foot diaphragm wall (east, the length is 51.98 m)	
	Maximum horizontal displacement (mm)	The depth of the diaphragm wall (m)	Maximum horizontal displacement (mm)	The depth of the diaphragm wall (m)
The first excavation step (−2.000 m)	0.141	−11.46	−0.371	−13.00
The third excavation step (−13.400 m)	2.146	−22.91	−5.170	−23.39
The fifth excavation step (−24.550 m)	6.613	−32.07	−16.490	−33.79
The seventh excavation step (−34.145 m)	8.418	−34.37	−22.006	−36.39
The first excavation step (−2.000 m)	7.738	−36.66	−23.497	−38.99
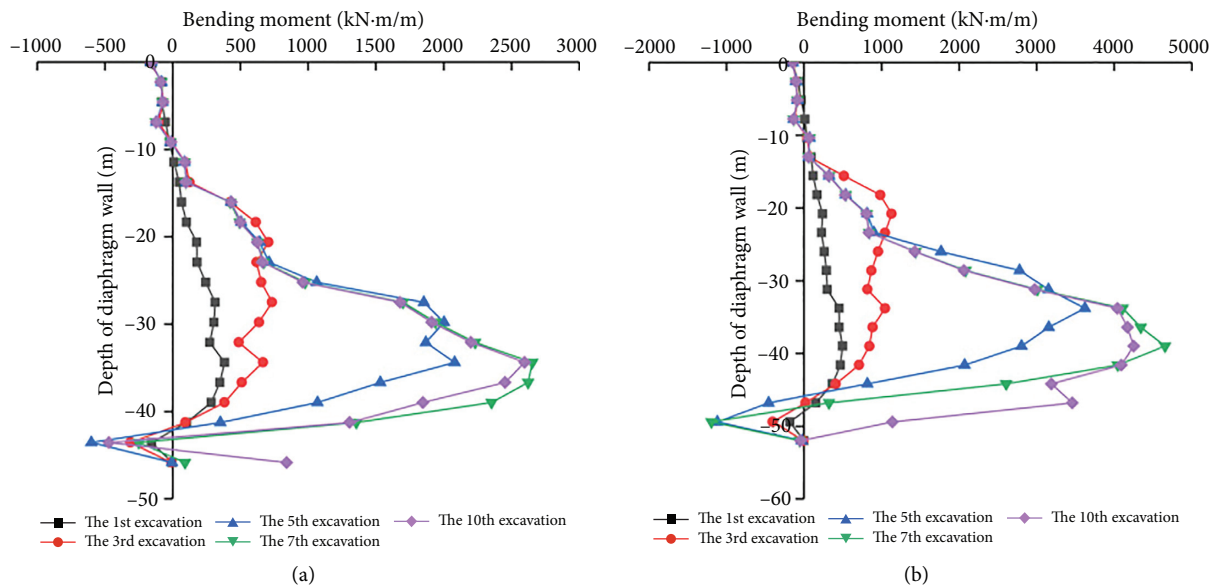
FIGURE 16: The bending moment curve of the suspended foot diaphragm wall. (a) West wall. (b) East wall.

TABLE 8: Summary of the corresponding depth of the maximum bending moment of the suspended foot connecting wall.

Working procedure	Suspended foot diaphragm wall (west, the length is 45.82 m)		Suspended foot diaphragm wall (east, the length is 51.98 m)	
	Maximum bending moment (kN·m/m)	The depth of the diaphragm wall (m)	Maximum bending moment (kN·m/m)	The depth of the diaphragm wall (m)
The first excavation step (−2.000 m)	383.553/−154.641	−34.37/−43.53	495.496/−183.378	−38.99/−49.38
The third excavation step (−13.400 m)	732.862/−311.066	−27.49/−43.53	1127.781/−404.225	−20.79/−49.38
The fifth excavation step (−24.550 m)	2080.852/−600.905	−34.37/−43.53	3621.628/−1118.857	−33.79/−49.38
The seventh excavation step (−34.145 m)	2654.072/−250.395	−34.37/−43.53	4654.927/−1193.643	−38.99/−49.38
The first excavation step (−2.000 m)	2596.608/−469.726	−34.37/−43.53	4251.651/−42.949	−38.99/−51.98
Remarks	Among the maximum bending moments in the table, the maximum positive bending moment value is before "/," and the maximum negative bending moment value is after "/," respectively, corresponding to the depth of the diaphragm wall			

FIGURE 17: The curve of the surface settlement of the suspended foot diaphragm wall. (a) West wall. (b) East wall.

TABLE 9: Summary of the corresponding position of the maximum subsidence of the surface.

Working procedure	External surface of foundation pit (west)		External surface of foundation pit (east)	
	Maximum settlement (mm)	Distance from foundation pit edge (m)	Maximum settlement (mm)	Distance from foundation pit edge (m)
The first excavation step (−2.000 m)	−0.459	10.00	−0.476	10.00
The third excavation step (−13.400 m)	−4.385	15.00	−4.393	15.00
The fifth excavation step (−24.550 m)	−11.511	20.00	−11.511	20.00
The seventh excavation step (−34.145 m)	−14.621	20.00	−14.526	20.00
The tenth excavation step (−51.630 m)	−18.419	15.00	−17.778	15.00

the contour plot of horizontal displacement of diaphragm wall during the 10th excavation step (that is, the foundation pit is excavated to the bottom) under two working conditions, the depth-displacement curve of the diaphragm wall under two working conditions can be obtained, as shown in Figure 18, and the maximum horizontal displacement and depth data of diaphragm wall under two working conditions can be summarized into a table, as shown in Table 10.

The following can be seen from Figure 18 and Table 10:

(1) In the tenth excavation step, it entered the moderately weathered rock with high strength. In case 1, the maximum horizontal displacement of the west wall is 8.256 mm, which is at the depth of −32.89 m. The maximum horizontal displacement of the east wall is −22.341 mm, which is located at the depth of −38.87 m. In case 2, the maximum horizontal displacement of the west wall is 7.738 mm at the depth of −36.66 m. The maximum horizontal displacement of the east wall is −23.497 mm, which is located at the depth of −38.99 m.

(2) From the comparison of the two working conditions, it can be seen that the maximum horizontal displacement of the west wall is reduced by 0.518 mm, the maximum horizontal displacement of the east wall is increased by 1.156 mm, the horizontal displacement of the end and bottom of the diaphragm wall is increased suddenly, and the stability of the diaphragm wall is poor, which is due to the large horizontal displacement and deformation due to the lack of rock embedment in working condition 2. Therefore, the horizontal displacement of condition 2 is larger than that of condition 1, and the maximum horizontal displacement of condition 2 moves down.

4.3.2. Bending Moment Analysis of Diaphragm.

By sorting and analyzing the data in the bending moment cloud part of the diaphragm wall during the 10th excavation step (i.e., the foundation pit is excavated to the bottom) under two working conditions, the depth-bending moment curve of the diaphragm wall under two working conditions can be obtained, as shown in Figure 19, and the maximum bending moment and depth data of diaphragm wall under two working conditions can be summarized into a table, as shown in Table 11.

The following can be seen from Figure 19 and Table 11:

(1) In the tenth excavation step, it enters the moderately weathered rock stratum with high strength on the left and low strength on the right. In case 1, the maximum positive bending moment of the west wall is 2462.475 kN·m/m, which is located at the depth of −35.88 m. The maximum positive bending moment of the east wall is 4271.144 kN·m/m, which is located at the depth of −38.87 m. The maximum negative bending moment of the west wall is −838.087 kN·m/m, which is located at the depth of −44.85 m. The maximum negative bending moment of the east wall is −3594.525 kN·m/m, which is located at the depth of −50.83 m. In case 2, the maximum positive bending moment of the west wall is 2596.608 kN·m/m, which is located at the depth of −34.37 m. The maximum positive bending moment of the east wall is 4251.651 kN·m/m, which is located at the depth of −38.99 m. The maximum negative bending moment of the west wall is −469.726 kN·m/m, which is located at the depth of −43.53 m. The maximum negative bending moment of the east wall is −42.949 kN·m/m, which is located at the depth of −51.98 m.

(2) From the comparison of the two working conditions, it can be seen that the maximum positive bending moment of the east wall and the west wall increases, and the maximum negative bending moment decreases sharply in case 2 compared with case 1. There is a large positive bending moment at the bottom of the west wall and a small negative bending moment at the bottom of the east wall. This is because when the foot diaphragm wall is excavated to the bottom of the foundation pit, the west wall has no embedded restraint effect of the rock layer, and the east wall is embedded in the rock layer very shallow. In case 2, the maximum positive (negative) bending moment of the west wall moves up slightly, the maximum positive (negative) bending moment of the east wall moves down slightly, and the maximum negative bending moment of the east wall is located at the bottom of the diaphragm wall. In both cases, the maximum positive bending moment of the east and west walls appears above the excavation face, which indicates that the rock embedment in the diaphragm wall has a great constraint on the bending moment deformation of the diaphragm wall. The maximum positive moment of the two walls is larger than the maximum negative moment. Because of the existence of inclined rock, the maximum bending moment of the east wall is larger than that of the west wall.

4.3.3. Comparative Analysis of Ground Settlement of Diaphragm Wall.

By sorting and analyzing the data in the contour plot of ground settlement of diaphragm wall soil mass during the 10th excavation step (i.e., excavation to the bottom) under two working conditions, the curve of ground settlement distance from the edge of the foundation pit under two working conditions can be obtained, as shown in Figure 20, and the data of maximum ground settlement position under two working conditions can be summarized into a table, as shown in Table 12.

The following can be seen from Figure 20 and Table 12:

(1) The tenth excavation step, into the moderately weathered rock. In case 1, the maximum settlement of the soil surface on the west side of the foundation pit is −14.851 mm, which is 15 m away from the side of the foundation pit. The maximum surface settlement of the east side soil is −14.967 mm, which is
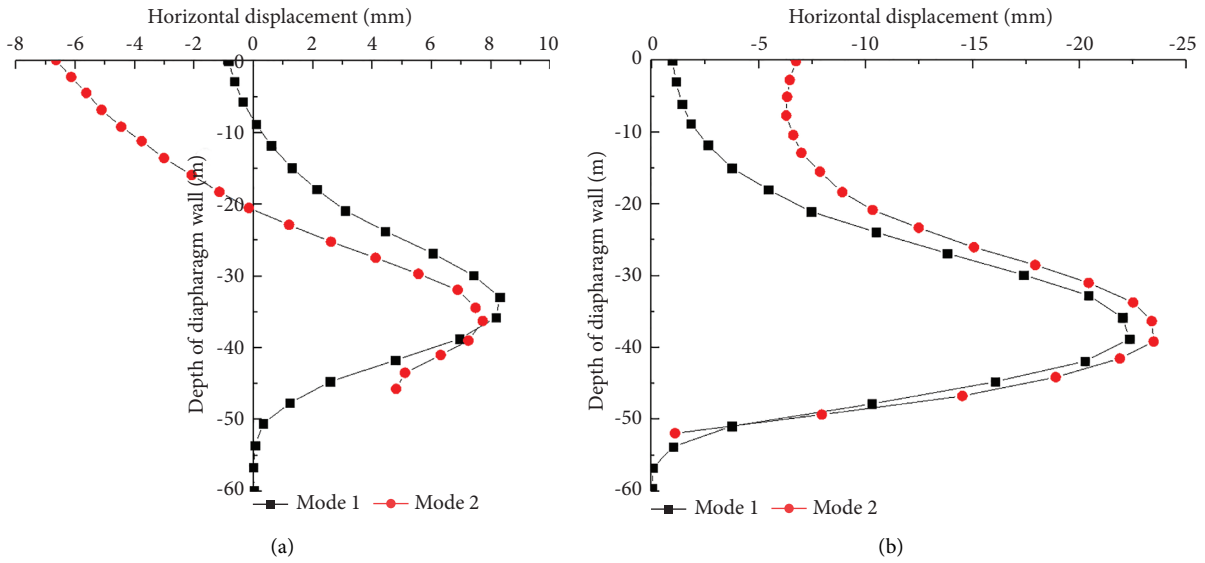
FIGURE 18: The horizontal displacement curve of the diaphragm wall. (a) West wall. (b) East wall.

TABLE 10: The corresponding depth of maximum horizontal displacement of diaphragm wall during the 10th excavation step under two working conditions.

Working procedure	Diaphragm wall (west)		Diaphragm wall (east)	
	Maximum horizontal displacement (mm)	The depth of the diaphragm wall (m)	Maximum horizontal displacement (mm)	The depth of the diaphragm wall (m)
Diaphragm wall of the same length (working condition 1)	8.256	−32.89	−22.341	−38.87
Suspended foot diaphragm wall (working condition 2)	7.738	−36.66	−23.497	−38.99
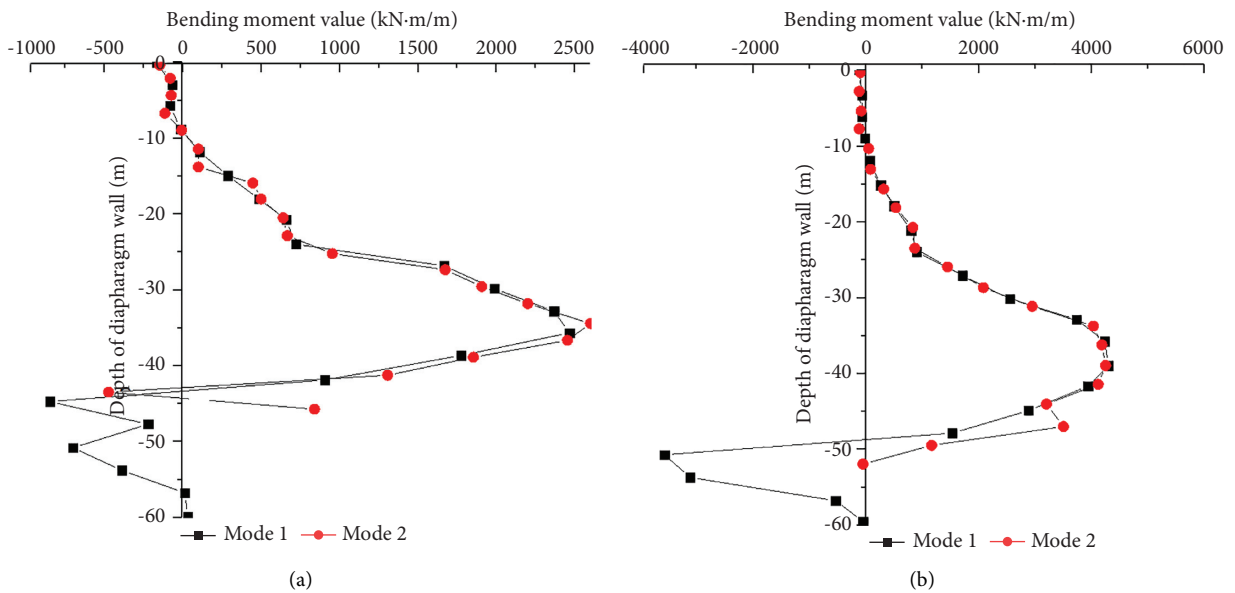
FIGURE 19: Bending moment diagram of the diaphragm wall. (a) West wall. (b) East wall.

TABLE 11: The corresponding depth of maximum bending moment of diaphragm wall in the 10th excavation step under two working conditions.

Working procedure	Diaphragm wall (west)		Diaphragm wall (east)	
	Maximum bending moment (kN·m/m)	The depth of the diaphragm wall (m)	Maximum bending moment (kN·m/m)	The depth of the diaphragm wall (m)
Diaphragm wall of the same length (working condition 1)	2462.475/−838.087	−35.88/−44.85	4271.144/−3594.525	−38.87/−50.83
Suspended foot diaphragm wall (working condition 2)	2596.608/−469.726	−34.37/−43.53	4251.651/−42.949	−38.99/−51.98
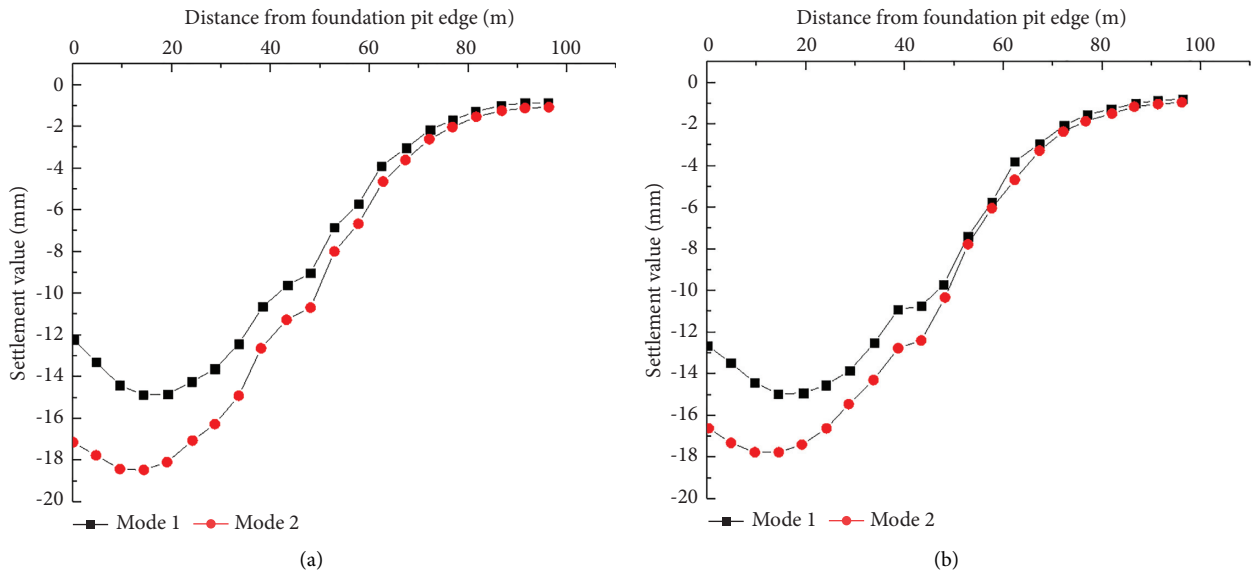
FIGURE 20: The curve of surface subsidence. (a) West wall. (b) East wall.

TABLE 12: Summary of corresponding positions of maximum ground settlement during the 10th excavation step under two working conditions.

Working procedure	External surface of foundation pit (west)		External surface of foundation pit (east)	
	Maximum settlement (mm)	Distance from foundation pit edge (m)	Maximum settlement (mm)	Distance from foundation pit edge (m)
Diaphragm wall of the same length (working condition 1)	−14.851	15.00	−14.967	20.00
Suspended foot diaphragm wall (working condition 2)	−18.419	15.00	−17.778	15.00

20 m away from the side of the foundation pit. In case 2, the maximum settlement of the soil surface on the west side of the foundation pit is −18.419 mm, which is 15 m away from the side of the foundation pit. The maximum surface settlement of the east side soil is −17.778 mm, which is 15 m away from the side of the foundation pit.

(2) From the comparison of the two conditions, it can be seen that compared with condition 1, the maximum settlement of soil surface in condition 2 increases by 2.5~3.5 mm, which is because the rock has a little constraint on the foot diaphragm wall. The maximum settlement position of the soil surface on the west side remains unchanged, and the maximum

settlement position of the soil surface on the east side moves to 15 m away from the edge of the foundation pit. With the distance from the foundation pit edge, the surface settlement curve of soil under the two conditions first increases, then decreases, and finally tends to be stable, showing a "groove" curve, and the surface settlement deformation law of the east and west sides is basically the same.

5. Field Measurement Verification

The top-down construction method of hanging footed diaphragm wall foundation pit is adopted. The surface settlement of the diaphragm wall, deep horizontal displacement
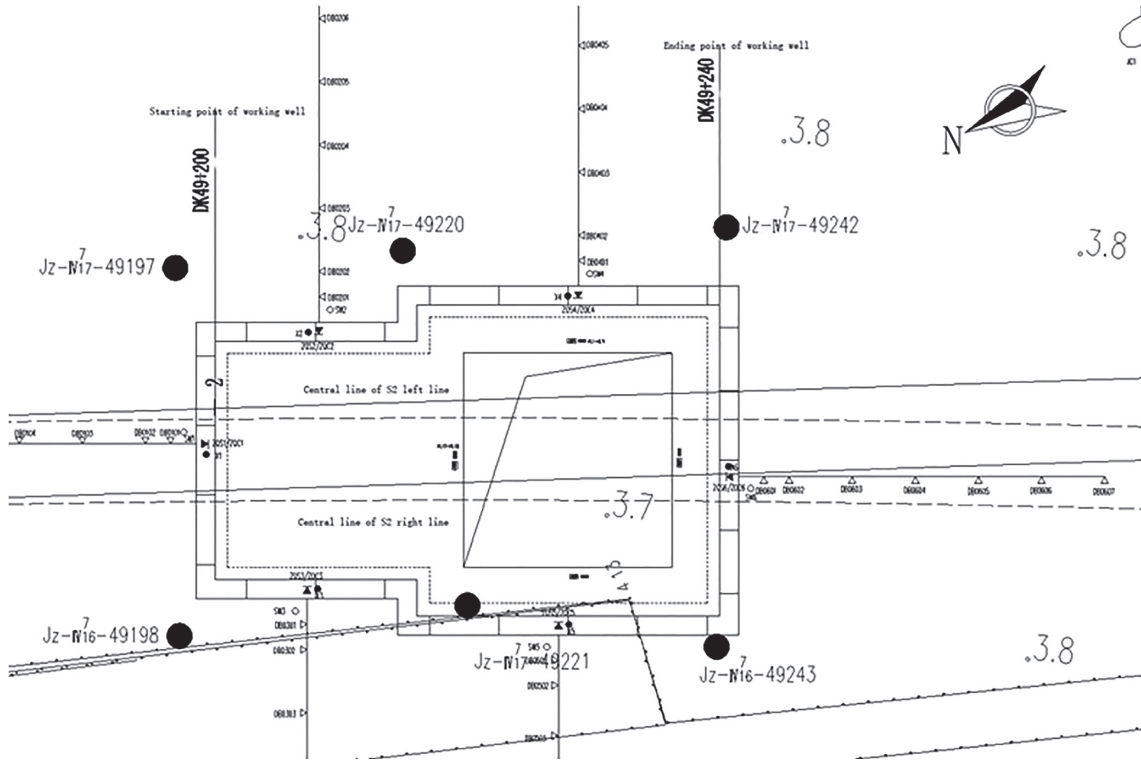
FIGURE 21: Layout of monitoring points.

TABLE 13: Measuring point information.

Monitoring content	Measuring point ID	Number of measuring points
Ground settlement of diaphragm wall	DBC-1-1~DBC-1-4 DBC-2-1~DBC-2-6 DBC-3-1~DBC-3-4 DBC-4-1~DBC-4-5 DBC-5-1~DBC-5-4 DBC-6-1~DBC-6-7	30
Deep horizontal displacement of diaphragm wall	CXQ1~CXQ6	6
Axial force of concrete support	ZCL1-1~ZCL1-4 ZCL2-1~ZCL2-4 ZCL3-1~ZCL3-4 ZCL4-1~ZCL4-4 ZCL5-1~ZCL5-4 ZCL6-1~ZCL6-4 ZCL7-1~ZCL7-4 ZCL8-1~ZCL8-4	32

of wall, and axial force of concrete support are monitored at the construction site. The layout of monitoring points is shown in Figure 21, and the label information of measuring points is shown in Table 13.

The cumulative deformation curve of surface settlement is shown in Figure 22, the variation curve of concrete support axial force is shown in Figure 23, and the variation curve of deep horizontal displacement of diaphragm wall is shown in Figure 24.

Through the analysis of the variation curve of the field measured data from Figures 22 to Figure 24 and the comparison with the above numerical simulation results, although there are differences in values, they are all within the acceptable range, which verifies the correctness of the
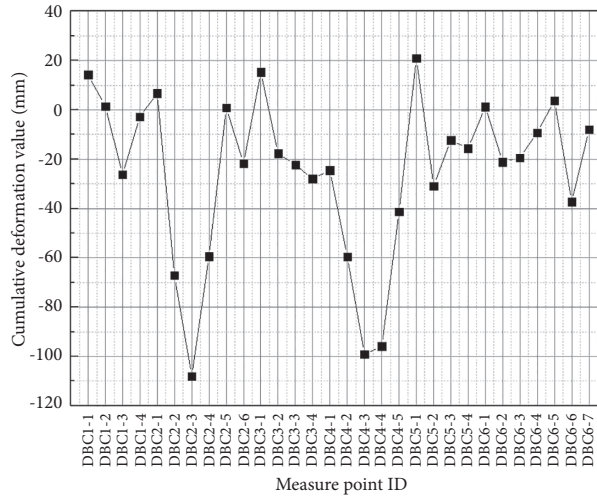
FIGURE 22: Cumulative deformation of surface settlement.
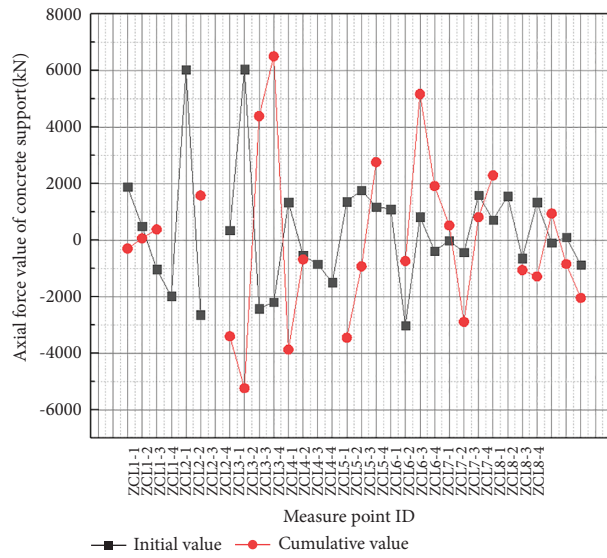
FIGURE 23: Variation curve of axial force of concrete support.

(a)

(b)
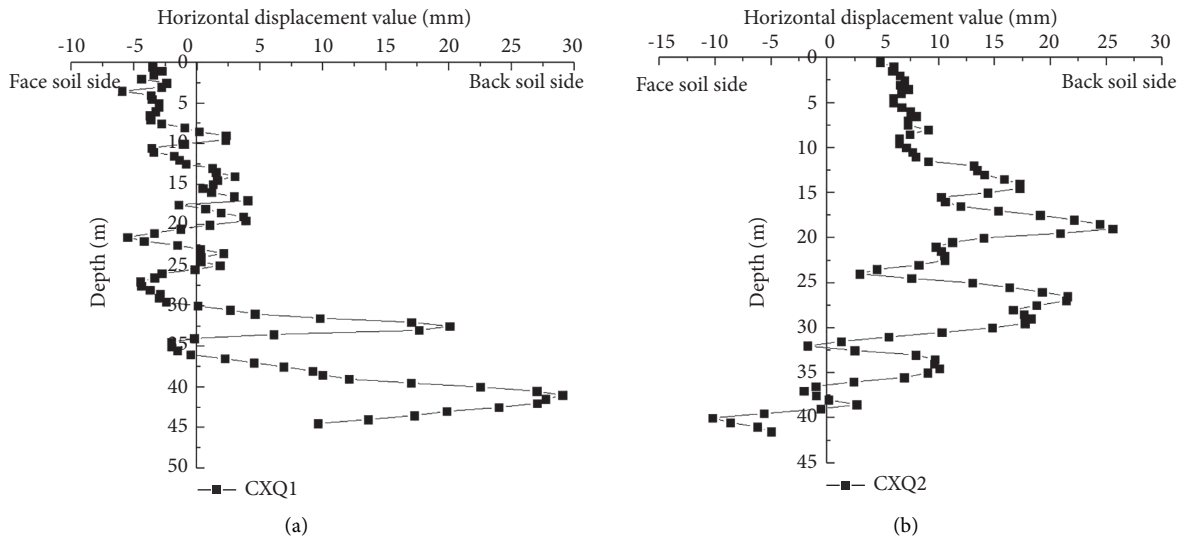
FIGURE 24: Continued.
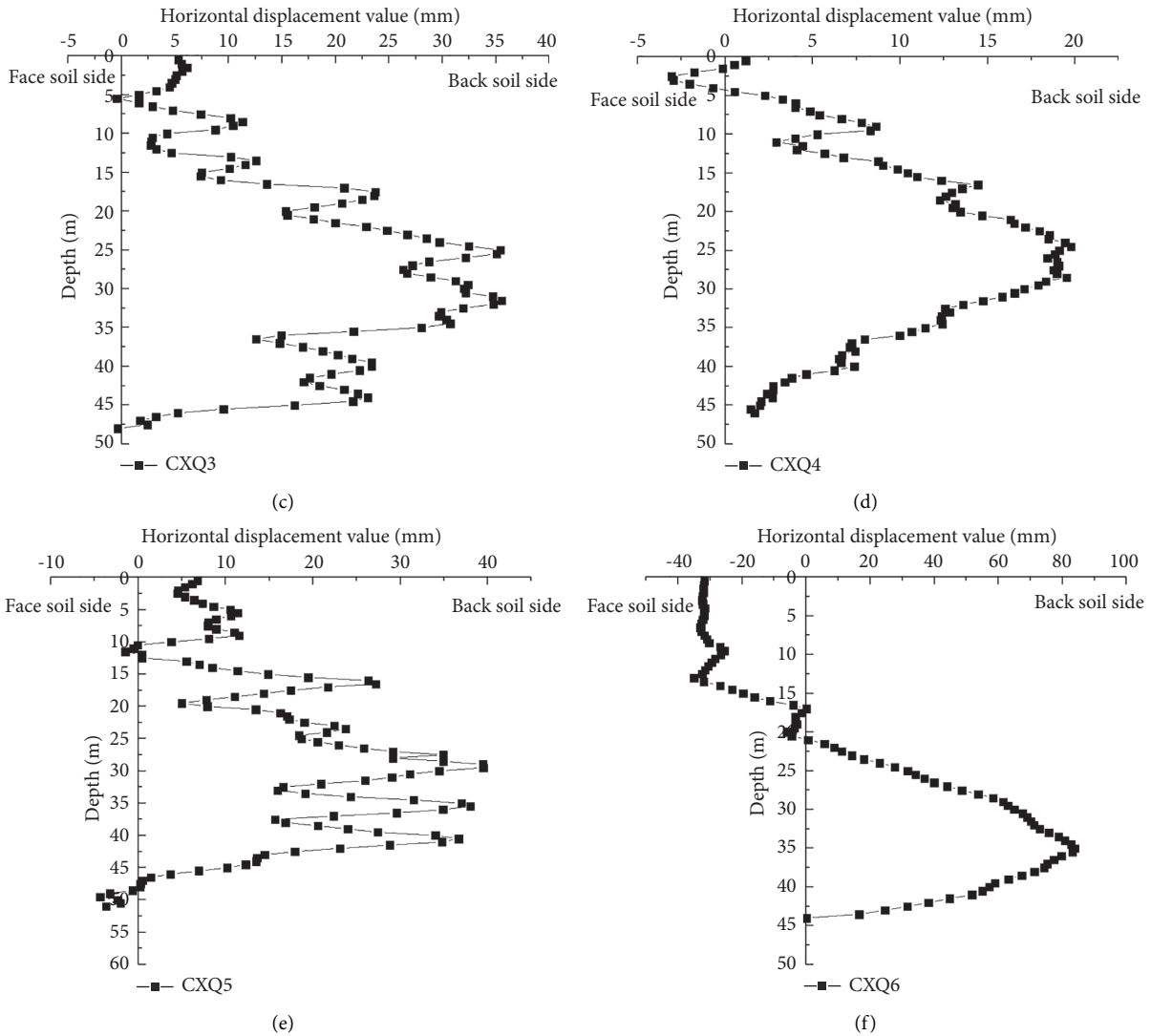
Figure 24: Variation curve of deep horizontal displacement of the diaphragm wall.

numerical simulation results and the reliability of the top-down construction of the foundation pit with suspended feet and ground walls.

6. Conclusion

In this paper, the construction effect of the top-down construction method for the diaphragm wall of foundation pit under two working conditions of diaphragm wall with the same length and suspended foot is simulated, and the horizontal displacement, bending moment, and surface settlement deformation law of diaphragm wall of foundation pit are analyzed.

(1) When the foundation pit with the same length is excavated by the top-down construction method, the horizontal displacement of the diaphragm wall is small at the first excavation. With the excavation of the foundation pit, the deformation law of "small at both ends and large in the middle" is formed as a whole of the horizontal displacement curve of the diaphragm wall. The position of the maximum horizontal displacement of the diaphragm wall gradually moves down with the increase of the excavation depth, which is 3/5~3/4 times the final excavation depth of the foundation pit, while the position of the maximum positive and negative bending moments of the diaphragm wall is close to the bottom of the foundation pit. The surface settlement of soil is very small during the first excavation step, and it is in "groove shape" with the gradual increase of excavation. The maximum surface settlement is smaller than the excavation depth and the maximum horizontal displacement of the diaphragm wall. This value occurs at a distance of 20 m from the edge of the foundation pit, and the main influence area is about 1.5 times the final excavation depth of the foundation pit.

(2) When the foundation pit of the hanging foot ground connecting wall is excavated by reverse method, The horizontal displacement curve of the hanging foot ground connecting wall is in the shape of "small at both ends and large in the middle." The maximum horizontal displacement position of the diaphragm wall gradually moves down with the increase of excavation depth, which is about 7/10~3/4 of the final excavation depth. In each excavation stage, the maximum positive bending moment of the diaphragm wall is greater than the maximum negative bending moment. The maximum positive and negative bending moments of the diaphragm wall are close to the bottom of the foundation pit. The maximum surface settlement is about 0.036% of the final excavation depth of the foundation pit, about 78% of the maximum horizontal displacement of the hanging foot ground connecting wall, which is 15 m away from the edge of the foundation pit, and the main influence area is about 1.5 times of the final excavation depth. The horizontal displacement, bending moment, and surface settlement of the suspended foot diaphragm wall decrease with the increase of the depth of the suspended foot diaphragm wall into the rock. However, the greater the depth into the rock, the better it becomes. When the depth of the rock increases to a certain extent, the role of continuously increasing the depth of the rock is no longer obvious. Therefore, in the actual project, the appropriate depth into the rock is selected on the premise of ensuring the safety of the foundation pit and reducing the cost.

Therefore, through the comparative analysis of the simulation results, it can be seen that compared with the top-down construction method of the same length diaphragm wall, the simulation results of the top-down construction method of the suspended foot diaphragm wall foundation pit are relatively better. At the same time, combined with the general situation of relying on the project and the suggestions given by experts, it is more suitable to use the suspended foot diaphragm wall for the construction of the foundation pit diaphragm wall.

(3) Through the comparative analysis of the field monitoring data and the simulation results, the correctness of the numerical simulation results is verified, and the reliability of the reverse construction method of the hanging foot ground wall foundation pit is also verified.

Data Availability

The data used to support the findings of this study are available from the corresponding author upon request.

Conflicts of Interest

The authors declare that they have no conflicts of interest.

References

[1] N. Benmebarek, S. Benmebarek, R. Kastner, and A.-H. Soubra, "Passive and active earth pressures in the presence of groundwater flow," *Géotechnique*, vol. 56, no. 3, pp. 149–158, 2006.

[2] G. Zheng and Y. Jiao, *Design Theory and Engineering Application of Deep Foundation Pit*, China Construction Industry Press, China, Chinese, 2010.

[3] X. Yang, "Application and development of new technology for deep foundation pit support in soft soil foundation along the coast of Zhejiang," *Journal of Geotechnical Engineering*, vol. 2012, no. S1, p. 7, 2012, in Chinese.

[4] X. Wang, "Analysis of deformation of retaining wall of deep foundation pit works in podium of Shanghai Center Tower," *Chinese Journal of Rock Mechanics and Engineering*, vol. 2, pp. 421–431, 2012, in Chinese.

[5] I. H. Wong, T. Y. Poh, and H. L. Chuah, "Performance of excavations for depressed expressway in Singapore," *Journal of Geotechnical and Geoenvironmental Engineering*, vol. 123, no. 7, pp. 617–625, 1997.

[6] K. Mccue and D. Clark, "Australian paleoseismology: towards a better basis for seismic hazard estimation," *Annals of Geophysics*, vol. 46, no. 5, 2003.

[7] Y. D. Wu, J. Liu, and C. W. W. Ng, "Effects of pile extraction and refilling with cement slurry on ground settlements," *Canadian Geotechnical Journal*, vol. 50, no. 3, pp. 343–349, 2013.

[8] J. W. Hong, H. E. Wei, and Y. I. Li-Yun, "Hand-dug hole pile foundation reinforcement by high-pressure grouting sodium silitcae cement slurry," *Technology & Economy in Areas of Communications*, 2015.

[9] H. B. Zhang, J. J. Chen, X. S. Zhao, J.-H. Wang, and H. Hu, "Displacement performance and simple prediction for deep excavations supported by contiguous bored pile walls in soft clay," *Journal of Aerospace Engineering*, vol. 28, no. 6, pp. A4014008.1–A4014008.10, 2015.

[10] P.-G. Hsieh and C.-Y. Ou, "Simplified approach to estimate the maximum wall deflection for deep excavations with cross walls in clay under the undrained condition," *Acta Geotechnica: An International Journal for Geoengineering*, vol. 11, no. 1, pp. 177–189, 2016.

[11] P.-G. Hsieh and C.-Y. Ou, "Shape of ground surface settlement profiles caused by excavation," *Canadian Geotechnical Journal*, vol. 35, no. 6, pp. 1004–1017, 1998.

[12] C. Yoo and D. Lee, "Deep excavation-induced ground surface movement characteristics—a numerical investigation," *Computers and Geotechnics*, vol. 35, no. 2, pp. 231–252, 2008.

[13] S. K. Bose and N. N. Som, "Parametric study of a braced cut by finite element method," *Computers and Geotechnics*, vol. 22, no. 2, pp. 91–107, 1998.

[14] C. W. Ng, B. Simpson, M. L. Lings, and D. Nash, "Numerical analysis of a multipropped excavation in stiff clay," *Canadian Geotechnical Journal*, vol. 35, no. 1, pp. 115–130, 1998.

[15] R. J. Finno, D. K. Atmatzidis, and S. B. Perkins, "Observed performance of a deep excavation in clay," *Journal of Geotechnical Engineering*, vol. 115, no. 8, pp. 1045–1064, 2016.

[16] H. G. Poulos, "Analysis of the settlement of pile groups," *Géotechnique*, vol. 18, no. 4, pp. 449–471, 1968.

[17] M. D. Bolton and W. Powrie, "Behaviour of diaphragm walls in clay prior to collapse," *Géotechnique*, vol. 38, no. 2, pp. 167–189, 1988.

[18] C.-Y. Ou, J.-T. Liao, and H.-D. Lin, "Performance of diaphragm wall constructed using top-down method," *Journal of Geotechnical and Geoenvironmental Engineering*, vol. 124, no. 9, pp. 798–808, 1998.

[19] J. Graham, "The 2003 R.M. Hardy Lecture: soil parameters for numerical analysis in clay," *Canadian Geotechnical Journal*, vol. 43, no. 2, pp. 187–209, 2006.

[20] J. Wang, Z. Xu, and J. Chen, "Etc Analysis on deformation characteristics of diaphragm wall of deep foundation pit in soft soil area of Shanghai," *Journal of Underground Space and Engineering*, vol. 1, no. 4, pp. 485–489, 2005, in Chinese.

[21] Z Xu, J Wang, and W Wang, "Deformation behavior of diaphragm wall in deep foundation pit engineering in Shanghai," *Journal of Civil Engineering*, vol. 41, no. 8, pp. 81–86, 2008, in Chinese.

[22] J. Qiu, A. Shi, and Y. Xia, "Etc Three dimensional finite element analysis of spatial deformation of double row lattice diaphragm wall," *Water Resources and Hydropower Technology*, vol. 45, no. 8, pp. 78–82, 2014, in Chinese.

[23] S He, G Wu, and Z Zhu, "Finite element analysis of influencing factors of deep foundation pit support design," *Journal of Rock Mechanics and Engineering*, vol. S22005, in Chinese.

Research Article

Predicting Compressive Strength of Concrete Containing Industrial Waste Materials: Novel and Hybrid Machine Learning Model

Mohammed Majeed Hameed [1], **Mustafa Abbas Abed,**[1] **Nadhir Al-Ansari** [2], **and Mohamed Khalid Alomar** [1]

[1]*Department of Civil Engineering, Al-Maarif University College, Ramadi, Iraq*
[2]*Civil Engineering Department, Environmental and Natural Resources Engineering, Lulea University of Technology, Lulea 97187, Sweden*

Correspondence should be addressed to Mohammed Majeed Hameed; mohmmag1@gmail.com
and Nadhir Al-Ansari; nadhir.alansari@ltu.se

In the construction and cement manufacturing sectors, the development of artificial intelligence models has received remarkable progress and attention. This paper investigates the capacity of hybrid models conducted for predicting the compressive strength (CS) of concrete where the cement was partially replaced with ground granulated blast-furnace slag (FS) and fly ash (FA) materials. Accurate estimation of CS can reduce the cost and laboratory tests. Since the traditional method of calculation CS is complicated and requires lots of effort, this article presents new predictive models called SVR – PSO and SVR – GA, that are a hybridization of support vector regression (SVR) with improved particle swarm algorithm (PSO) and genetic algorithm (GA). Furthermore, the hybrid models (i.e., SVR – PSO and SVR – GA) were used for the first time to predict CS of concrete where the cement component is partially replaced. The improved PSO and GA are given essential roles in tuning the hyperparameters of the SVR model, which have a significant influence on model accuracy. The suggested models are evaluated against extreme learning machine (ELM) via quantitative and visual evaluations. The models are evaluated using eight statistical parameters, and then the SVR-PSO has provided the highest accuracy than comparative models. For instance, the SVR – PSO during the testing phase provided fewer root mean square error (RMSE) with 1.386 MPa, a higher Nash–Sutcliffe model efficiency coefficient (NE) of 0.972, and lower uncertainty at 95% (U_{95}) with 28.776%. On the other hand, the SVR – GA and ELM models provide lower accuracy with RMSE of 2.826 MPa and 2.180, NE with 0.883 and 0.930, and U_{95} with 518.686 183.182, respectively. Sensitivity analysis is carried out to select the influential parameters that significantly affect CS. Overall, the proposed model showed a good prediction of CS of concrete where cement is partially replaced and outperformed 14 models developed in the previous studies.

1. Introduction

1.1. Background. As an essential in most civil engineering projects and activities, concrete is a standard man-made mixture consisting of specific components such as cement, water, and some additional materials. Since concrete manufacturing, many engineering projects have been carried out successfully using this profitable and imperative material. Traditional concrete is widely used in several construction areas, containing four classical materials: Portland cement, water, coarse aggregate, and fine aggregate. There is also a second type of concrete called high-strength concrete, which has unique properties due to the usage of additional materials that may not be used in ordinary concrete mixes. However, the estimation of hardened concrete properties is a critical obstacle for concrete technology due to several predicted and unpredicted parameters that may significantly influence the concrete properties [1, 2].

The compressive strength (CS) is one of the significant properties of concrete as it has a crucial role in designing engineering structures. Furthermore, other important properties of concrete, like water tightness and elastic modulus, have direct and significant relations with the CS of concrete. In current practice, to assess the CS of the concrete, many cylindrical or cubic samples are produced and tested at various sample ages. However, the conducted tests are time-consuming and expensive [3, 4]. Besides, the changes in the concrete mixes may lead to producing concrete with undesired characteristics. Hence, the tests should be repeated until the required properties of concrete are achieved by changing the magnitudes of the used ingredients [5]. Thus, this problem can be better encountered when pozzolan powders partially replace the cement content.

1.2. Using Ground Granulated Blast-Furnace Slag and Fly Ash Materials in the Concrete Mixture.

As a type of pozzolan powders, ground granulated blast-furnace slag (FS) and fly ash (FA) are generally used as a partial replacement material of concrete because they are easy to reach and economic [6, 7]. In general, FA is a fine powder of spherical particles (diameter of $1\,\mu m$ to $150\,\mu m$) obtained as a residual from the burning of pulverized coal in thermal power plant furnaces. As a result of its good performance and economic benefits, fly ash is used as a replacement for cement in 98% of American ready-mix companies [8]. As fly ash is an essential material in concrete mixture and thus it significantly affects the CS of concrete, several factors affect the characteristics of fly ash, such as the source of coal, heating and cooling mechanism, and combustion temperature [9]. The combustion process has a significant influence on the mechanical properties of FA. For instance, wet processing produces a FA with a high separated aggregate. On the other hand, dry processing can grow homogenous FA in particle size [10]. The utilization of FA material as partial replacement of cement in concrete mixture decreases the values of some concrete parameters like slump and CS. Still, it enhances the integrity and workability of the concrete [11]. Some studies recommend that in standard engineering and construction projects, the percentage of FA in concrete as a partial substitute for cement ranges from 20% to 50% of the total volume of cementitious aggregate [12]. However, concrete with fly ash increases the setting time; therefore, the CS of concrete varies by time and temperature of curing. Furthermore, fly ash concrete indicates an early development in concrete strength, particularly at elevated temperatures, which increases the CS in later stages compared to ordinary concrete [13].

Furnace slag (FS) is also considered a popular material used as partial cement replacement material. FS is a by-product of the manufacture of iron and steel in blast furnaces, the chemical composition of which is based on the raw materials from which it is produced [14]. Cooling status has great importance on the characteristics of the FS. For instance, if the molten slag is quickly cooled, it will be converted to noncrystalline components with hydraulic properties [15]. Additionally, concrete with higher CS and durability results in partial cement replacement with FS. However, a higher FS dosage can cause cracks and thermos-hygral (TH) damages, thereby negatively affecting the mechanical strength of concrete [16, 17].

The use of mentioned materials such as FS and fly ash in concrete as a partial replacement of cement is not only an effective waste disposal means but can be helpful as an alternative material for cement. Recent studies illustrated that the production of cement from different industries around the world case too much pressure on the environment by increasing the amount of carbon dioxide (CO_2) emissions in the atmosphere and, subsequently, global warming [18–20]. However, in the traditional concrete mixture, the relationship between the predictors (water, cement, fine and coarse aggregate) and CS property is nonlinear and challenging to capture. Furthermore, when the additives and other materials are used in concrete, such as FS and FA, CS and its parameters will become more complex. According to what mentioned before, there are no clear guidelines to select the optimum amount of FA and FS in concrete to ensure getting a desirable value of CS; therefore, a better understanding of that relation between CS and its variables using advanced approaches can help eliminate the carrying on the experiments and thus, reducing cost and time. Besides, it provides engineers with a simplified method to predict experimental outcomes.

Nevertheless, accurately predicting the CS of concrete where the cement martial is partially replaced has become a challenging issue in the concrete technology sector due to the complex and nonlinear relationship between CS property and the other materials used in manufacturing the concrete. Over the last decades, several scholars have developed models to estimate concrete CS. Moreover, scholars' attempts can be roughly divided into categories: (1) conventional artificial intelligence approaches such as soft computing models; (2) hybrid artificial intelligence models.

1.3. Soft Computing Models.

Soft Computing (SC), as an efficient approach, can estimate the magnitude of the CS of concrete. One of the significant SC advantages is providing solutions for linear and nonlinear problems where the mathematical models cannot easily derive the under relation among the involved parameters in a particular situation [21]. Furthermore, SC methods utilize human-based knowledge, understanding, recognition, and learning in computing. Recently, many researchers have used artificial intelligence (AI) approaches and machine learning (ML) techniques as a sub-branch of SC methods to predict different concrete properties. Keshavarz and Torkian [22] developed two SC systems called artificial neural networks (ANN) Adaptive Neuro-Fuzzy Inference (ANFIS) to estimate the CS of concrete based on several concrete mixed parameters. The study showed that both systems were predicting CS very well. However, the ANFIS model provides slightly better estimates than the ANN model. Another study by [23] presents the ability of both data-driven models, ANN and multiple linear regression (MLR) approaches to predict concrete CS. The study shows that the MLR model has less

prediction accuracy than the ANN model. Moreover, a comparison study has been published between ANN and ANFIS systems to estimate the CS of cement-based mortal materials [24]. The study concluded that the ANFIS faced an overfitting problem and produced undesirable predictions compared to the ANN model. Additionally, Ni and Wang [25] investigate the ability of artificial neural networks (ANN) to predict the CS of concrete. The study revealed that the proposed model provided higher prediction accuracy and could capture the complex relationships between CS and concrete variables.

Another study was conducted by Lee et al. [26] to investigate the potential of using different AI models such as support vector regression (SVR) and ANN models to predict CS of concrete at the age of 28 days. The results showed that SVR predicted CS more accurately than the ANN technique and was less time-consuming. Akande et al.[27] developed two predictive models called ANN and SVR to predict the CS of concrete and concluded that the SVR model was more stable and gave slightly higher prediction accuracy than ANN. Additionally, Ling et al. [28] presented a study to estimate the CS of concrete using a combined model called SVR-CV(SVR is coupled with a cross-validation approach). The proposed model provided a higher accuracy level than other AI models such as ANN and decision tree (DT). Furthermore, satisfactory performance of the ANN model has been noticed throughout the prediction of the CS of high-performance concrete (HPC) and self-compacting concrete (SCC) [29]. Moreover, the feasibility of using the SVR technique and multivariable nonlinear regression (MNR) has been investigated by [30] in terms of the prediction of CS of concrete of lightweight foamed concrete at an earlier age (7-day). The study concluded that the SVR model gives higher estimation accuracy and efficiently captures the non-linear relation between the input variables.

1.4. Hybrid Models. To overcome the issues related to standard models, several scholars have used hybrid AI-based metaheuristic algorithms to enhance the performances of these systems [31, 32]. In literature, several metaheuristic algorithms are employed to optimize AI models such as ANN, SVR, and ANFIS to enhance their performances and obtain much better predictions [10, 33–36]. There is an investigation for accurately predicting the CS of concrete was carried out by Madandoust et al. [37] using adaptive neuro-fuzzy inference systems (ANFIS) and Group method of data handling (GMDH) as a sort of ANN. The GMDH model is enhanced using a genetic algorithm (GA) and singular value decomposition method. The study also conducted sensitivity analyses to illustrate which variables have more effect on CS. The results showed that both adopted approaches could accurately estimate CS at different ages. Besides, another study also conducted a hybrid model carried out by the hybridization ANN with GA to predict CS of concrete in the presence of FA and FS materials [38]. The outcome of the proposed model is validated against the traditional ANN, which is trained by a backpropagation algorithm, and the assessment criteria showed that the

hybrid model (ANN-GA) yielded a minor error forecasted than the traditional ANN model. Han et al. [39] presented a hybrid model by combining ANN with particle swarm algorithm (PSO) to constitute the ANN-PSO model to estimate the CS of ground granulated blast furnace slag (GGBFS) concrete. For validation assessment, the performance of the hybrid model (ANN-PSO) is compared with the standard ANN model. The study showed a noticeable improvement in the estimations due to the presence of the PSO algorithm.

1.5. Research Motivation. There is evidence that energy savings, high cement costs, and pressure from environmental organizations and researchers have all led to an increase in the use of industrial waste materials such as fly ash and ground granulated blast-furnace slag in concrete mixing [40]. The use of such materials in concrete makes it more economical and enhances the strength, abrasion, heat evolution, workability, and shrinkage properties of concrete in both fresh and hardened states [41]. Partially replacing cement in concrete mixes is essential because it reduces carbon dioxide emissions into the atmosphere while at the same time lowering the overall cost of producing concrete mixes.

Many researchers proved that it is difficult to provide a consistent method for additive materials (such as fly ash and other cement replacement materials) in the design of concrete mixtures because of the complexity and uncertainty of the design parameters, which significantly influence the compressive strength of concrete. Due to these limitations, engineers in practical use a traditional method called the trial-and-error process to find the right concrete design. However, this approach requires time to accomplish the tests of compressive strength. Thus, applying a fast and efficient method that can predict the compressive strength of concrete immediately or provide the optimal mix design would be very useful. This paper uses artificial intelligence (AI) models to provide an efficient mix-design tool that overcomes these difficulties.

1.6. Research Significance. To the best of the authors' knowledge, no published work in the literature has employed hybrid SVR with GA or improved PSO algorithms to optimize the hyperparameters of SVR for the prediction of CS of concrete with partial cement replacement. The primary advantage of this research is to predict the compressive strength of concrete where the cement was partially replaced with furnace slag and fly ash. Furthermore, the presence of these materials in the concrete mixture makes the relationship between the compressive strength of concrete and other concrete components very complex. Therefore, the traditional modes in such cases could not provide accurate solutions; therefore, thinking of alternative methods having a satisfactory level of flexibility and predictability is vital. Furthermore, in construction and martial fields, accurate prediction of the CS can effectively minimize the costs by reducing the laboratory work and saving time and effort. Accordingly, this study provides an alternative approach to

efficiently estimate one of the most significant features of concrete (CS) in the presence of industrial waste materials. Establishing a systematic approach that can accurately predict the CS of concrete in earlier stages is significant in concrete development and manufacturing because this approach can generate the needed design data faster[42]. Thus, in this study, support vector regression (SVR) combined with two metaheuristic algorithms known as genetic optimizer (GA) and improved particle swarm optimization (PSO) to constitute SVR-PSO and SVR – GA predictive models. The mentioned algorithms optimize the hyper-parameters of SVR and kernel parameters and significantly improve the prediction accuracy. Next, the capacities of these models are examined in the case of compressive strength prediction. Accordingly, a powerful AI model called extreme learning machine (ELM) is also prepared and developed for verification purposes. Besides, the performance of the best model is also validated against 14 models developed in previous studies as a crucial step to examine the validity and reliability of the proposed model. Finally, sensitivity analyses are used to identify the most significant parameters that influence concrete CS.

2. Materials and Methods

2.1. Data Collection and Statistical Description. The experimental data used in this current study include seven variables called (Portland cement "ASTM type I"), furnace slag, fly ash (which is produced from the power plant), water, superplasticizer (**C**494[29] **type G**), coarse aggregate (maximum size of 1 cm), fine aggregate (fineness modulus size of 3), and one response variable represent the compressive strength at 28-day age. It is necessary to identify the primary ingredients to understand concrete behavior better. Several considerations should be taken into account through designing the concrete mixes. For instance, More cement content increases the cohesiveness of the mixture, resulting in stickier concrete, and thus cracks may occur. Nevertheless, reducing the cement content considering constant water content results in a mixture with poor cohesion. Therefore, cement content should be optimally assigned to ensure a more reliable concrete mix. On the other hand, the other contents, such as water-cement ratio and fine and coarse aggregate, significantly impact the concrete strength. A very fine aggregate requires more water content to produce a mixture with reasonable consistency. The consequences of increasing the water-cement ratio are significant in reducing the compressive strength of concrete. Therefore, increasing water content usually provides concrete with poor properties. Thus, several researchers have addressed this issue by using chemical additives such as superplasticizers. The primary purpose of conducting these experimental samples is to seek the capability of partially replacing the cement with furnace slag and fly ash. Table 1 presents the statistical description of all data used in this current study. Where Min, Max, Std, and CC symbols in Table 1 refer to the minimum, maximum standardization, and correlation coefficient with the Compressive strength, respectively. The statistical parameters are listed in the table

showing a nonlinear relationship between the target and input variables. Moreover, there is a positive relation between cement and fly ash and compressive strength. The cement has the highest correlation with compressive strength with a correlation coefficient (CC) of 0.446, followed by fly ash with a CC of 0.444. The other variables have a negative relationship with CS, and the range of CC is between -0.038 and -0.254.

For better assessing the quality of input parameters mentioned before, their variabilities are statistically compared. As the obtained data have different ranges, the normalization approach is beneficial for enhancing a better perspective. Consequently, all the input parameters and their target are separately normalized between one and zero as follow:

$$x_i' = \frac{x_i - x_{\min}}{x_{\min} - x_{\max}}, \tag{1}$$

where x_i' is the ith normalized value of a variable x.

Figure 1 compares the input variables' variability; therefore, the interquartile ranges (IQR) are calculated using respected quintiles ($Q_{75\%} - Q_{25\%}$). The IQR values of each normalized input variable are given in Figure 1 in the range of 0.274 to 0.650. Superplasticizer with IQR of 0.274) and cement with IQR of 0.641 have the lowest and highest variability compared to other input variables. Lastly, it is essential to mention that the data used in this study is collected from two different sources in the literature and includes 103 data samples [43, 44].

2.2. Genetic Algorithm. Genetic algorithm (GA) is one of the most popular algorithms introduced by John [45] for solving engineering and science optimization problems. This algorithm is inspired by the natural selection theory and then expanded by Goldenberg [46]. GA can find solutions for complex and nonlinear issues, and this aspect is considered one of the main advantages of this algorithm. Different optimization purposes can be addressed by GA, such as continuous or discontinuous or containing a random noise, linear or nonlinear, and static and dynamic. Thus, GA has succeeded in solving optimization problems in various areas. However, it is also characterized as a complicated algorithm because of its limitations, like determining several algorithm parameters (size of population and genetic operator rate) and creating the proper function. Better assigning these parameters is critical for getting highly accurate solutions and having a noticeable influence on the algorithm's convergence; consequently, the designer should be careful [47, 48]. Chromosomes in GA have a fixed length that encodes linear binary strings between 0 and 1. These Chromosomes are significant factors because it is responsible for producing the generations. The chromosome is selected as a random characteristic [49], and the Chromosomes are evaluated according to these characteristics. They are then selected via genetic operators of the remaining Chromosomes and begin producing new generations. Besides, in a range of 0 to 1, crossover selects between parents and mutation work.

Table 1: The statistical description of the used variables in this study.

Variable	Unite	Min	Max	Average	Std	CC
Cement	kg/m^3	137.000	374.000	229.894	78.877	0.446
Slag	kg/m^3	0.000	193.000	77.974	60.461	−0.332
Fly ash	kg/m^3	0.000	260.000	149.015	85.418	0.444
Water	kg/m^3	160.000	240.000	197.168	20.208	−0.254
Superplasticizer	kg/m^3	4.400	19.000	8.540	2.808	−0.038
Coarse aggregate	kg/m^3	708.000	1049.900	883.979	88.391	−0.161
Fine aggregate	kg/m^3	640.600	902.000	739.605	63.342	−0.154
Compressive strength	MPa	17.190	58.530	36.039	7.838	1.000

(a)

(b)
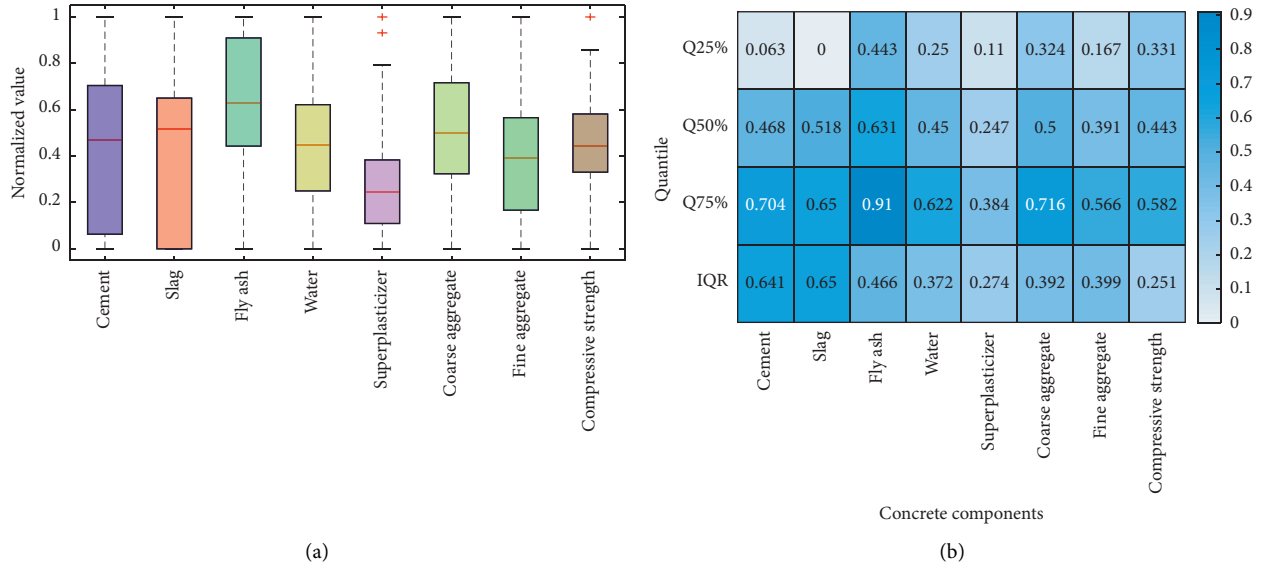
Figure 1: (a) Boxplot of normalized input and target variables and (b) Quantile percent of the concrete components.

This process is repeated several times until creating the best generations assessed according to their performance [50, 51].

2.3. Particle Swarm Optimization (PSO).

The second optimization algorithm used in this study is the PSO algorithm, an approach employed in optimization issues for solution purposes. The PSO algorithm was introduced to the scientific sectors for the first time by Kennedy and Eberhart in 1995 [52], inspired by the accumulative behavior of particles. Less memory required and high learning speed is considered the most compelling characteristic of the PSO compared to GA. The solution of optimization problems in a model based on the PSO algorithm appears like a particle that flies like a bird in the solution space. The framework algorithm of (PSO) is described as follows [53].

Given $x_j^{(i)}$ present the location and $v_j^{(i)}$ is the particle j speed at iteration i, so the following formulas have been utilized to determine the solution for j position and velocity at the following iteration:

$$v_j^{(i+1)} = wv_j^{(i)} + \left(c_1 * r_1 * \left(pbest_j - x_j^{(i)}\right)\right)$$
$$+ \left(c_2 * r_2 * \left(gbest_j - x_j^{(i)}\right)\right), \quad v_{\min} \le v_j^{(i)} \le v_{\max} \dots , \tag{2}$$

$$x_j^{(i+1)} = x_j^{(i)} + v_j^{(i+1)} = 1, 2, \dots, n. \tag{3}$$

In the above formula, i represents the number of iterations while w is the coefficient of inertial weight. The rest of the variables are explained as follows:

$pbest_j$: the ideal position for the particles throughout the PSO performance approach.

$gbest_j$: the perfect condition for the particle throughout the PSO performance approach.

r_1, r_2: the arbitrary value in the interval [0,1]. The algorithm of PSO is described as follows:

(i) Set the magnitude of iteration $i = 0$, and for starters, consider an arbitrary location and speed

for the generated particles. Secondly, the structure for every particle has to calculate the value of fitness adjustment.

 (ii) Then checking process takes place to compare fitness magnitude with pbest. If the result is improved, the system changes the value of pbest with the new one, leading to an updated magnitude of gbest.

 (iii) The PSO approach will calculate the speed value for every particle using equation (2), so the position of every particle will be updated as well using equation (3). Finally, iteration continues by increasing the value of i with $i + 1$ and repeating the process till verification of terminated criteria.

2.4. Support Vector Regression (SVR). In 1995 Cortes and Vapnik [54] developed a technique called Support Vector Machine (SVM) as a form of Artificial intelligence (AI) to deal with classification problems by combining SRM (Structural Risk Minimization) and SLT (Statistical Learning Theory). Consequently, various sectors have commonly employed this technique for regression and prediction problem-solving. The concept of support regression machine (SRM) is the framework of SVM depiction. It presents an effective implementation with high accuracy compared to classical Empirical Risk minimization (ERM), which depends on a conventional learning algorithm, such as neural network techniques. The objective of the SRM is to increase the precision of predicting by minimizing upper and lower limits while reducing training dataset total error is ERM responsibility. Therefore, SVM is considered a practical approach to solving several issues and producing more accurate and reliable predictions [55]. Lately, due to being a more efficient and reliable tool, researchers have been applying SVM in a tremendous section of the prognostication fields conducting various functions related to machine learning [56–60]. Let D denote dataset points $D = \{(x_i, y_i)\} \in R^d * R, i = 1: n$. The primary concept here is to obtain a function f that contains a connection between x variable and grandeur for determining model y where y is the function of x which is acquired from data D.

$$f(x) = (wx) + b, \quad b \in R, \tag{4}$$

$$f(x) = (w\varnothing(x)) + b. \tag{5}$$

These equations represent linear (4) and nonlinear (5) functions related to regression problems. This approach has involved two stages in obtaining the optimum value for the weight (w) and bias (b). These stages showed applying the Euclidean norm method in the first stage while the second stage presented decreasing produced error magnitude by utilizing empirical risk function. To sum up, minimizing risk function $R_{reg}(f)$ by

$$R_{reg}(f) = R_{emp}(f) + \frac{1}{2}\|w^2\|. \tag{6}$$

And exhibiting theoretical value empirical error by

$$R_{emp}(f) = C\frac{1}{N}\sum_{1}^{N} L(x_i, y_i, f(x_i, W)), \tag{7}$$

where $L(x_i, y_i, f(x_i, W))$ is the cost function and is derived as one of the two main cost functions used. ε–insensitive loss is the first function, while the second function has been connected with the least square support vector machine (LS-SVM) known as the quadratic loss [61].

Moreover, the equilibrium between empirical risk and the denominated regularization is implied by a regularization constant "C". The following equations present a primer formula for issues of optimization:

$$\min \frac{1}{2}\|w^2\| + C\sum_{i=1}^{n}(\xi_i + \xi_i^*), \tag{8}$$

$$\text{under the constraints} \begin{cases} y_i - w\varnothing(x) - b \leq \varepsilon + \xi_i, \\ y_i - w\varnothing(x) - b \geq -\varepsilon - \xi_i^* \forall_i \in \{1, \dots n\}, \\ \xi_i, \xi_i^* \geq 0. \end{cases} \tag{9}$$

So, it is more reasonable to consider certain error limits to increase problem solution competence. Therefore, the function accuracy will be approximated where ε indicated a tube size and the slack parameters characterized by ξ_i and ξ_i^*.

The quadratic initiative has been utilized to obtain superior minimized value for regularized risk related to estimating best weight magnitude according to the principle of Lagrange multipliers by implementing optimality constraints [62]. Calculating these multipliers, by using the formula below to the minimum value:

$$\min L(\alpha_i, \alpha_i^*) = -\sum_{i=1}^{n} y_i(\alpha_i - \alpha_i^*) + \varepsilon \sum_{i=1}^{n} y_i(\alpha_i + \alpha_i^*)$$

$$+ \frac{1}{2}\sum_{i=1}^{n}\sum_{j=1}^{n}(\alpha_i - \alpha_i^*)(\alpha_j - \alpha_j^*)K(X_i, X_j), \tag{10}$$

as α_i and α_i^* indicate the Lagrange multipliers where $i = 1$ to n at certain limits

$$0 \leq \alpha_i, \alpha_i^* \leq C, \quad i = 1, \dots n,$$
$$\sum_{i=1}^{n}(\alpha_i - \alpha_i^*) = 0. \tag{11}$$

Finally, a numerical expression for the regression function is described by:

$$f\left(x, \widehat{\alpha}_i, \widehat{\alpha}_j^*\right) = \sum_{i=1}^{n}\left(\widehat{\alpha}_i - \widehat{\alpha}_j^*\right)K(X, X_i) + b^*. \tag{12}$$

The kernel function can be characterized by $K(x_i, x_j) = \varnothing(x_i) * \varnothing(x_i)$ which would have a value depicted by the result of scalar for x_i and x_j vectors in $\varnothing(x_i)$ and $\varnothing(x_j)$ feature space.

One of the main steps to enhance the performance accuracy of the SVR approach is to select the kernel function

properly. The selection process depends mainly on the Mercer conditions [63]. Accordingly, the kernel function type that meets this criterion can be implemented. In this study, the Radial Basis Kernel function (RBF), as expressed below, is used to map the nonlinear relationship between CS of concrete and its dependent variables.

$$K(x_i, x_j) = \exp\left(-\frac{\|x_i, x_j\|^2}{2\sigma^2}\right), \quad (13)$$

where σ is the bandwidth of the RBF kernel.

2.5. Extreme Learning Machine.

Extreme learning machine (ELM) is an efficient and relatively modern-learning algorithm introduced in 2006 for training feedforward neural network (FFNN) instead of the conventional algorithm (i.e., backpropagation algorithm). The ELM model is the same as the structure of a single layer of FFNN, including three critical layers (input, hidden, and output). ELM has many advantages that surpass its counterpart FFNN, including speed and well generalization abilities [63, 64]. Moreover, the traditional FFNN has many defects and shortcomings, including low convergence, local minima problems, overfitting, and poorer generalization. Furthermore, classical FFNN is usually trained using a backpropagation algorithm, and hence, it becomes more likely to be stuck into local minima.

The structure of the ELM model consists of three successive layers called input, hidden, and output layers, respectively. The input layer receives the predictor vectors, while the hidden layer contains several hidden nodes to process the data to the output layer. It is important to say that data transmission from layer to next layer through neurons. Lastly, the output layer is responsible for producing the calculated outcomes of the model. The hidden layer is essential because it contains the majority of the information of the data.

The core concept of ELM is the weights and bias values used to link the transmission data from the input layer to the hidden layer. These values are assigned randomly and do not need to be corrected. Therefore, this algorithm is very fast. Then, the activation function is usually nonlinear applied to extract the most significant features from data which will be passed to the next layer. It is essential to mention that the output layer weights are calculated based on Moore–Penrose approach [65].

The steps below show the process of establishing the ELM model.

(i) Inputting the predictors and their corresponding targets (output values).

(ii) Defining the number of hidden nodes in the hidden layer using the trial-and-error procedure.

(iii) Assigning the weight and bias values of the hidden layer randomly.

(iv) Data normalization.

(v) Selecting transfer function.

(vi) Processing the data in hidden nodes using equation (14) to prepare it for the next layer (calculating the output of hidden layer H).

(vii) Determining the output layer weights using the Singular Value Decomposition (SVD) approach as shown in equations (15) and (16).

(viii) Computing the predicted targets (CS).

(ix) Denormalizing predicted targets (CS).

$$H(x, \alpha, \beta) = \begin{bmatrix} g(x_1) \\ . \\ . \\ . \\ g(x_N) \end{bmatrix} = \begin{bmatrix} g(a_1.x_1 + \beta_1) \cdots g(a_L.x_1 + \beta_L) \\ . \\ . \\ . \\ g(a_1.x_N + \beta_1) \cdots g(a_L.x_N + \beta_L) \end{bmatrix}, \quad (14)$$

where g is the activation function, x, β, a respectively are the input vectors, bias, and weight values.

$$HB = Y. \quad (15)$$

Then, calculate the output weights from equation (16)

$$\widehat{B} = H^\dagger Y, \quad (16)$$

where $H^\dagger$ denotes the Moore-Penrose generalized inverse of Hussain matrix, Y is the actual targets, and B is the vector that contains output weights calculated by the SVD method. It is essential to mention that the sigmoid transfer function is used as an activation function in the hidden layer.

2.6. Hybrid Models: Model Development.

The SVR algorithm usually uses a specific kernel function to calculate the hyperplane to fit the data well. The majority of engineering issues are very complex. Therefore, it is beneficial to use the nonlinear kernel function, and hence there will be three most efficient hyperparameters (C, ε, and ɣ) of the SVR approach that greatly influence the SVR performance. The gamma parameter (ɣ) increases the algorithm's capability to match the training data ideally with their corresponding target(s), while the cost parameter (C) is a penalty metric for promoting the process of predicting the data instances more correctly. Decreasing the value of ɣ ($1/2\sigma^2$) would negatively affect SVR performance and thus, underfitting the data; however, increasing too much gamma results in overfitting the dataset. Consequently, the optimal values of these hyperparameters (C, ε, and ɣ) significantly impact the SVR performance, thereby getting more accurate predictions.

In the literature, there are several attempts to select these hyperparameters of SVR. One of these strategies, using trial and error methods. However, this approach may not provide the optimal solutions as it is also limited in a specific range of assumptions. Moreover, this approach is time-consuming and requires a higher computational cost. The other procedure to compute the hyperparameters of SVR is called grid-search approach. This strategy also has several disadvantages, such as required computational efforts and time. In

addition, this strategy requires a limited range of assumptions of each parameter; it sometimes gives some of the hyperparameters less attention than others. Thus, in this study, these hyperparameters are efficiently optimized using two different optimizations, namely, genetic and particle swarm algorithms. Figure 2 and Figure 3 show the incorporation of SVR with these algorithms [66, 67]. The root mean square error formula is used as a fitness function of both algorithms.

The main steps regarding the hybridization of SVR (calibration processes) are stated below:

(i) Dividing data into sets, training (75%; 77 samples), and testing set (25%; 26-sample).

(ii) The training set data is used to develop SVR-GA and SVR-PSO models.

(iii) Selecting the root mean square error as an objective function.

(iv) Initializing the parameters for each algorithm (GA and PSO).

(v) Defining the range of each hyperparameter. In this study, the algorithms first search these parameters from 0 to 1.

(vi) As some hyperparameters such as C have a wide range of data (from 0 to infinity), we reconstruct this obtained value from the previous step as $C = 1/c$, where C is obtained from the previous step.

(vii) The algorithm starts finding the optimal parameters that reduce the objective function (in this study, RMSE is used as an objective function).

(viii) The applied algorithm has been given a significant task to increase the accuracy during the calibration process by minimizing the cost function.

(ix) In this study, the cost function is described as root mean square error (RMSE = $\sqrt{(1/N) \sum_{i=1}^{N} (CS_{obs_i} - CS_{pred_i})^2}$).

(x) The algorithm then starts using random numbers to assign the hyperparameters and updates these values until optimal accuracy or maximum iteration is achieved.

(xi) Inserting the reconstructed hyperparameters to the SVR algorithm.

(xii) Calculating the other SVR parameters like beta and alpha using minimal sequential optimization (SMO) is considered a more efficient algorithm [68].

(xiii) Calculate the cost function (RMSE).

(xiv) If the RMSE is very small or the algorithm reaches the maximum iterations, the algorithm stops the calibration process. Otherwise, the applied algorithm continues the updating of hyperparameters.

It is essential to mention that all predictive models used in this study are developed using MATLAB 2018b.
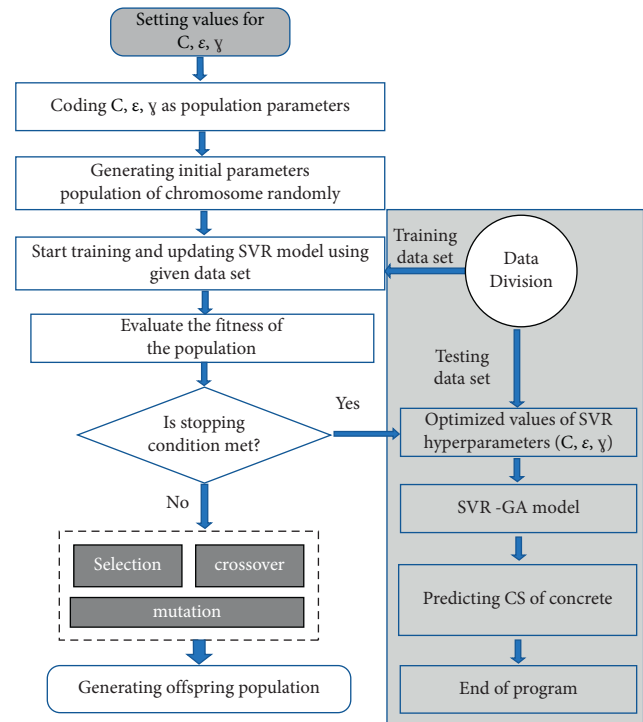
FIGURE 2: Incorporation of SVR with genetic algorithm.
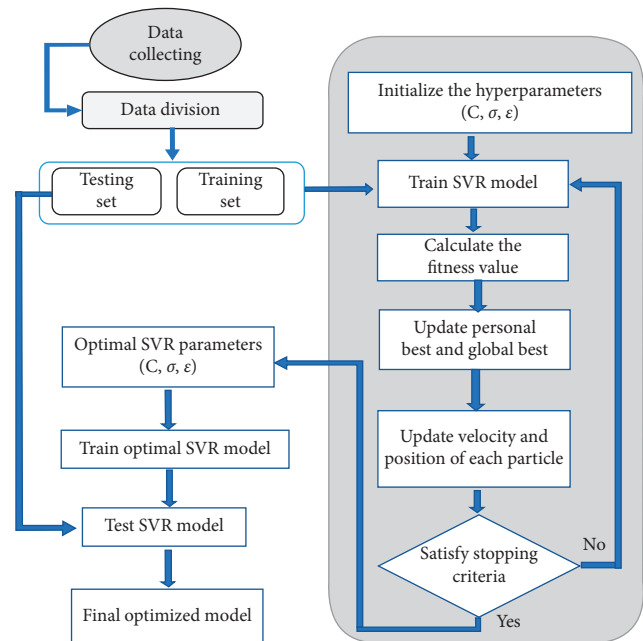
FIGURE 3: Incorporation of SVR with the genetic particle swarm algorithm.

Concerning PSO, it is used based on the algorithm described in Kennedy and Eberhart [52], with some modifications and improvements suggested by Pedersen [69] and Mezura-Montes and Coello Coello [70].

2.7. Statistical Matrices. In this paper, nine parameters accounting for the error between measured and predicted CS of concrete is used, namely; mean absolute relative error (MARE), root mean square error (RMSE), mean absolute error (MAE), maximum absolute percentage relative error (erMax), uncertainty at 95% (U95), correlation of coefficient (CC), correlation of determination (R^2), Nash–Sutcliffe model efficiency coefficient (NE), Index of Agreement or Willmott (WI), and relative error (RE). Some of the stated parameters like R^2, CC, NE, and WI measure the strength of the relation between predicted and actual vectors, usually having values in the range of 0 to 1. On the other hand, the error metrics like RMSE, MARE, MAE, erMax, U95 measures are used to compute the forecaster error. The best model should provide fewer values of error measures (as lower as possible) and the highest value of correlation measures (near to one). In this study, the U95 parameter is used to efficiently select the best model accuracy when some of the proposed models would give close estimates of CS of concreter, and hence it would be challenging to choose the best predictive model. Some earlier studies showed that the U95 could help in the detection of the statistical differences between outcomes of comparable models and the actual values much better than other statistical parameters such as RMSE, MAE, R^2, and so on [63]. Furthermore, the a-20 index as a new engineering metric is used to further assess the applied models' performances. It is essential to mention that the perfect and ideal model has a-20 index of 1. The a-20 index has an essential advantage in the engineering field because this factor quantifies the number of experimental samples that satisfy the predicted magnitudes with a deviation of ±20%, compared to the corresponding (experimental) values [71].

The mathematical expressions of these statistical parameters are derived from equations (17) to (26) [72, 73].

$$\text{MARE} = \frac{1}{N} \sum_{i=1}^{N} \left| CS_{obs_i} - CS_{pred_i} \right|, \tag{17}$$

$$\text{RMSE} = \sqrt{\frac{1}{N} \sum_{i=1}^{N} \left(CS_{obs_i} - CS_{pred_i} \right)^2}, \tag{18}$$

$$\text{MAE} = \frac{1}{n} \sum_{t=1}^{n} \left| CS_{obs_i} - CS_{pred_i} \right|, \tag{19}$$

$$CC = \frac{\sum_{t=1}^{n} \left[\left(CS_{obs_i} - \overline{CS_{obs_i}} \right) \left(CS_{pred_i} - \overline{CS_{pred_i}} \right) \right]}{\sqrt{\sum_{t=1}^{n} \left(CS_{obs_i} - \overline{CS_{obs_i}} \right)^2 \sum_{i=1}^{n} \left(CS_{pred_i} - \overline{CS_{pred_i}} \right)^2}}, \tag{20}$$

$$\text{erMAX} = \max\left(\left| \frac{CS_{obs_i} - CS_{pred_i}}{CS_{obs_i}} \right| \right), \tag{21}$$

$$U_{95} = 1.96 \left(SD^2 + RMSE^2 \right)^{1/2}, \tag{22}$$

$$R^2 = 1 - \frac{\sum_{i=1}^{n} \left(CS_{obs_i} - CS_{pred_i} \right)^2}{\sum_{i=1}^{n} \left(CS_{pred_i} - \overline{CS_{pre\,d}} \right)^2}, \tag{23}$$

$$\text{WI} = 1 - \frac{\sum_{i=1}^{n} \left(CS_{obs_i} - CS_{pred_i} \right)^2}{\sum_{i=1}^{n} \left(\left| CS_{pred_i} - \overline{CS_{obs}} \right| + \left| CS_{obs_i} - \overline{CS_{obs}} \right| \right)^2}, \tag{24}$$

$$NS = 1 - \frac{\sum_{i=1}^{n} \left| CS_{obs_i} - CS_{pred_i} \right|}{\sum_{i=1}^{n} \left| CS_{obs} - \overline{CS_{obs}} \right|}, \tag{25}$$

$$RE\% = \frac{CS_{obs_i} - CS_{pred_i}}{CS_{obs_i}} * 100, \tag{26}$$

$$a20\,\text{index} = \frac{m20}{n}, \tag{27}$$

where CS_{obs_i} and CS_{pred_i} are respectively observed and predicted value of i-th sample; CS_{obs}, and CS_{pred_i} are the average of observed and predicted values separately. While n refers to the total number of samples, and $m20$ refers to the number of samples with an experimental rate value/predicted value between 0.80 and 1.20. Lastly, SD is the standard deviation of the forecasted errors.

3. Results and Discussion

Compressive strength (CS) of ordinary and high-strength concrete is a significant property during manufacturing the cement. Many factors affect CS, and the relationship between them and CS of concrete is highly nonlinear for classical and high strength concrete. This part of the study discusses the calculated results obtained by three different models, ELM, SVR-GA, and SVR-PSO.

Table 2 provides more information regarding the performance of each predictive model during the training phase. At first glance, the hybrid model (SVR-GA and SVR-PSO) provided much more accurate predictions than the ELM model. Moreover, the ELM could not recognize very well the complex relation between CS and its' factors thereby decreasing the accuracy and increasing the forecasting errors (MAE = 1.890, RMSE = 2.614, MAPE = 0.054, CC = 0.939, U_{95} = 370.638, NE = 0.883, WI = 0.968, $a20$-index = 0.974 and erMax = 0.212). However, the other both models (SVR-GA and SVR-PSO) gave high accurate forecasting in addition to a slight preference in favor of SVR-GA model (MAE = 0.673, RMSE = 1.011, MAPE = 0.021, CC = 0.993, U_{95} = 6.882, NE = 0.982, WI = 0.995, and erMax = 0.102).

The quantitative assessment is in Table 2 illustrates that the SVR-PSO model can predict CS of concrete at a good

TABLE 2: Assessing the performance of each suggested model: training set.

Model/statistical measures	SVR-PSO	SVR-GA	ELM
MAE (MPa)	0.978	**0.673**	1.890
RMSE (MPa)	1.163	**1.011**	2.614
MAPE (MPa)	0.028	**0.021**	0.054
CC	**0.997**	0.993	0.939
U_{95}%	**6.107**	6.882	370.638
NE	0.977	**0.982**	0.883
WI	0.994	0.995	**0.968**
erMax	**0.065**	0.102	0.212
a20-index	**1**	**1**	0.974

Bold values represent the higher accuracy value.
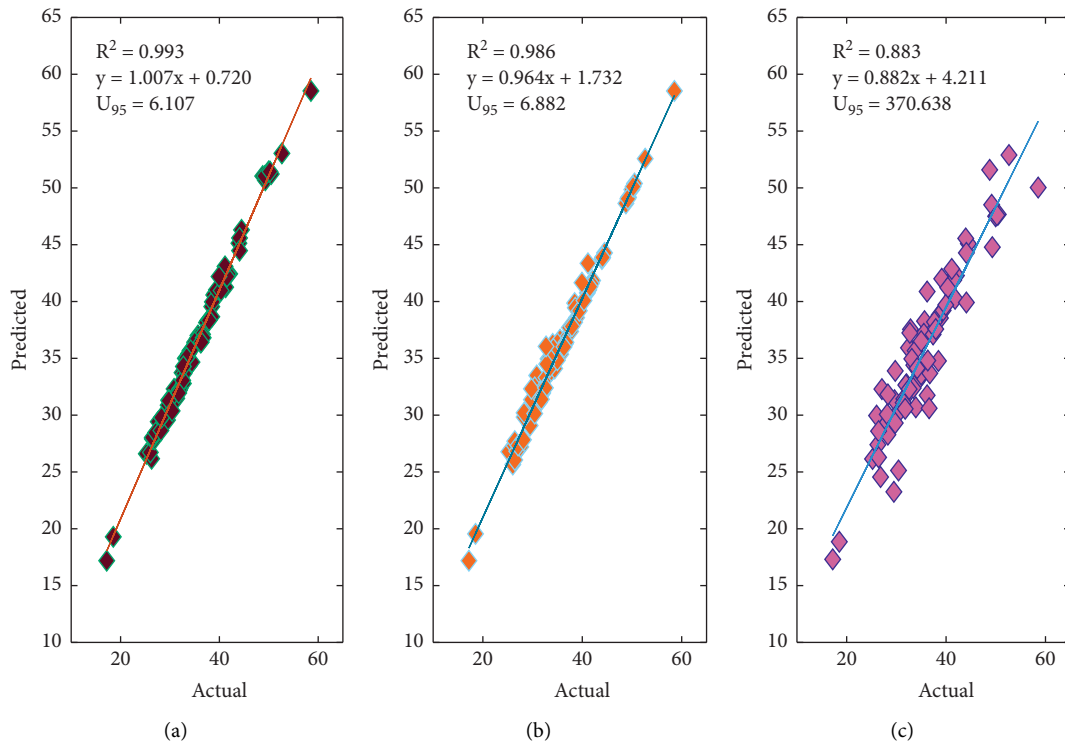
FIGURE 4: Comparing between actual and predictive values: correlation of determination, a, b, and c are respectively referring to SVR-PSO, SVR-GA, and ELM.

level of accuracy with MAE of 0.978, RMSE of 1.163, MAPE of 0.028, CC of 0.997, U_{95} of 6.107, NE of 0.977, WI of 0.994, and erMax of 0.065. Finally, the most important note that can be drawn based on the given outcomes is that the differences between the performances of the applied three modes under statistical measures, in general, are minimal except the given assessments obtained from the U_{95} parameter.

As shown in Figure 4, scatter plots prove helpful information on the performance of each adopted model by explaining the diversion of every predicted point to the actual value. According to the figure, it can be shown that the SVR-PSO model is considered the best model in the prediction of CS of concrete and provides the highest R^2 (0.993), followed respectively by the SVR-GA with R^2 of 0.986 and

ELM with R^2 of 0.883. Moreover, the predicted values obtained by the SVR-PSO model are found to have less dispersion and sticker to the fitted line than other comparable models (i.e., ELM and SVR-PSO).

Although the SVR-GA and SVR-PSO provided the highest prediction accuracies compared to the ELM model, very few statistical differences were found between their performances, and the training set could not give a robust assessment as the models were trained based on known targets. Therefore, the testing phase is crucial in assigning the best predictive models for CS of standard and high strength of concrete. At the testing phase, the model would assess under unknown targets. Thus, the generalization capabilities of each adopted model can be revealed [74]. Several

TABLE 3: Assessing the performance of each suggested model: testing set.

Model/statistical measures	SVR-PSO	SVR-GA	ELM
MAE (MPa)	1.101	2.008	1.657
RMSE (MPa)	1.386	2.826	2.180
MAPE (MPa)	0.034	0.067	0.047
CC	0.989	0.956	0.965
U_{95}%	28.776	518.686	183.182
NE	0.972	0.883	0.930
WI	0.992	0.962	0.981
erMax	0.151	0.417	0.175
a20-index	**1**	**0.923**	**1**

Bold values represent the higher accuracy values.

statistical metrics are tabulated in Table 3 to evaluate the proficiency of the proposed models. Following statistical metrics, the SVR-PSO is found to have the highest accuracy of prediction with the fewest metrics errors (MAE = 1.101, RMSE = 1.386, MAPE = 0.034, CC = 0.989, U_{95} = 28.776, NE = 0.972, WI = 0.992, and erMax = 0.151). Based on the same table, the forecasted error increased in related to applying SVR – GA of estimation CS during tidying set (MAE = 2.008, RMSE = 2.826, MAPE = 0.067, CC = 0.956, U_{95} = 518.686, NE = 0.883, WI = 0.962, and erMax = 0.417). The presented results explain the ELM model's performance gives much better predictions than the SVR-GA model with MAE of 1.657, RMSE of 2.614, MAPE of 0.047, CC of 0.956, U_{95} of 183.182, NE = 0.930, WI of 0.981, and erMax of 0.175.

The presented statistical parameters indicate that all used models except SVR-PSO gave relatively higher errors in the testing phase than their training performance. As a result, the SVR-GA and ELM models have faced overfitting issues. The other most significant observation extracted from the statistical description shown in Table 3 is that the statistical metric (U_{95}%) is the most efficient parameter in determining the best accuracy model. The importance of that parameter appears in selecting the highest quality model among several modeling techniques when the values of other statistical indicators are much closer to each other and no significant differences are noticed. Thus, the SVR-PSO model performs superior to all comparable models.

As the testing part is very significant, visualization assessments are excessively used to identify the best model's capacity and verify whether the SVR – PSO still outperforms other used techniques according to visual assessments. As illustrated in Figure 5, the scatter plots clearly showed that the SVR – PSO model is closer to the actual CS of concrete than other used models. The given results indicated a higher accuracy prediction of CS than other models. Moreover, the SVR-PSO model recorded the highest value of R^2 of 0.978 followed by SVR – GA (R^2 = 0.931), and ELM (R^2 = 0.914). Despite the SVR-GA provider higher value of R^2 than the ELM model, it produces very high uncertainty compared to the ELM technique. In order to obtain adequate and informative graphical evaluation error forecasting, relative error, as shown in Figures 6(a)–6(c), is established for exhibiting the relative error (RE %) for every sample over the testing set. The figure can also give a better understanding of

the model's efficiency in predicting CS for every single sample. It can be observed that the proposed SVR – PSO generates the fewest RE% values compared to the other modeling approaches. The average absolute relative error for the SVR – PSO model was recorded significantly fewer (3.40%) compared to other models ELM (4.74%) and SVR-GA (6.71%), respectively.

Moreover, the distribution of RE% for each suggested model is plotted in Figure 6(d). The boxplot presentations are created to evaluate the suggested models' performances and illustrate the visualized information regarding the efficiency of the models in predicting the CS of standard and high strength concrete. The comparable models (SVR-GA and ELM) generated undesirable outlier values with a relatively higher interquartile range (IQR). However, the SVR-PSO model performance is excellent. The estimates were noticed to have the fewest extreme values compared to adopted models. Moreover, the predicted median of RE% obtained by the SVR-PSO model was nearest to zero. Concerning interquartile range (IRQ), the proposed model (SVR-PSO) predicts a more desirable value of IRQ (5.235) compared to SVR-GA (6.662) and SVR-PSO (7.439).

Furthermore, Table 4 is created based on the predicted compressive strength of concrete values using the applied models during the testing phase. It shows that the SVR – GA model sometimes provides estimates with higher errors than the other models. For instance, the difference between the experimental value and predicted value in sample 19 was noticed to be very high (8.08 MPa). Furthermore, the other vital observation that can be concluded from that table is that the applied model (PSO – SVR) generates very accurate predictions for CS of high and normal strength of concrete. It can be said that (PSO – SVR) models are more efficient for predicting the cs in the presence of waste industrial material in the concrete than the SVR – GA and ELM. Moreover, Figure 7 provides more information about the efficiency of the predicted models during the testing phase. Based on that figure, the estimated values by the SVR-PSO model are very accurate and closer to their corresponding observations.

In order to evaluate the performances of all suggested models more efficiently, the Taylor diagram, as shown in Figure 8, is created based on the outcomes of each predictive model developed in this study during the testing phase. In this figure, both axes (vertical and horizontal) are connected via a circular line, representing the standard deviation. The value of the coefficient of correlation as a performance indicator is indicated by the black radial lines drawn from the center of the coordinates, and the circular walnut lines indicate the value of root mean square error (RMSE) and another significant performance indicator. In this figure, the actual dataset is placed in the base of the Taylor diagram and assumes that the data have the highest correlation of coefficient (i.e., CC = 1), RMSE of zero, and a calculated standard deviation (SD) value. Then, the performances of each model in terms of the three statistical parameters (RMSE, CC, and SD) are compared with those evaluated from the actual dataset. Thus, the efficiency of the predictive modeling approach can be easily identified via assessing its

(a)   (b)   (c)
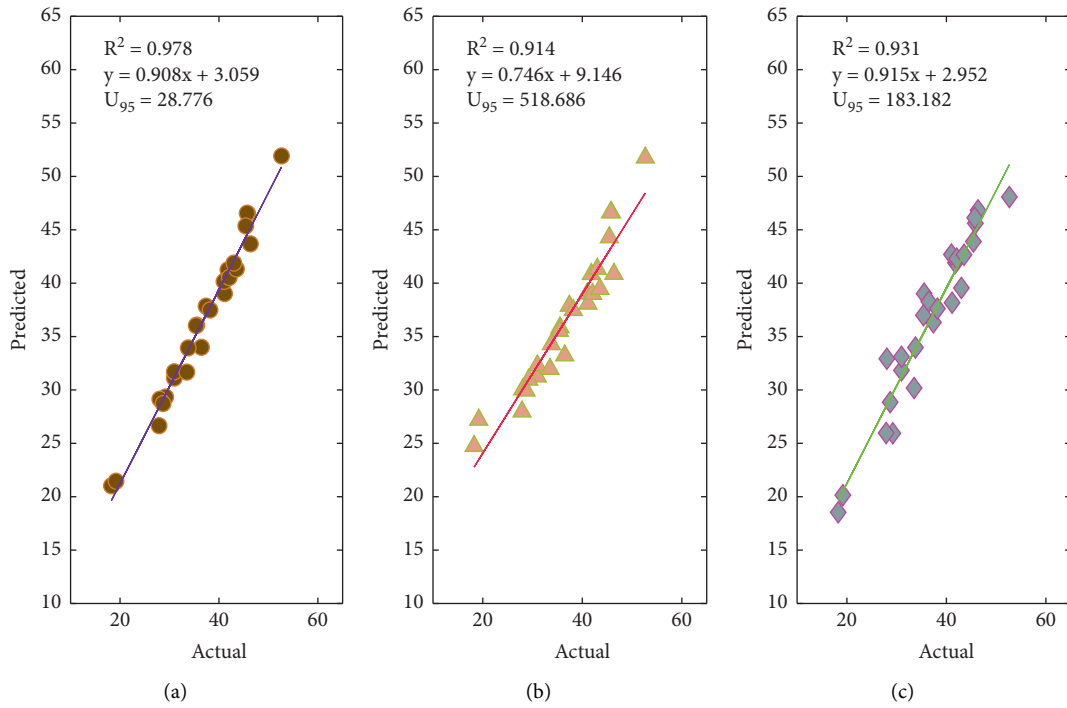
FIGURE 5: Comparing between actual and predictive values: correlation of determination, (a, b, and c) respectively belong to SVR-PSO, ELM, and SVR-GA.

(a)   (b)

(c)   (d)
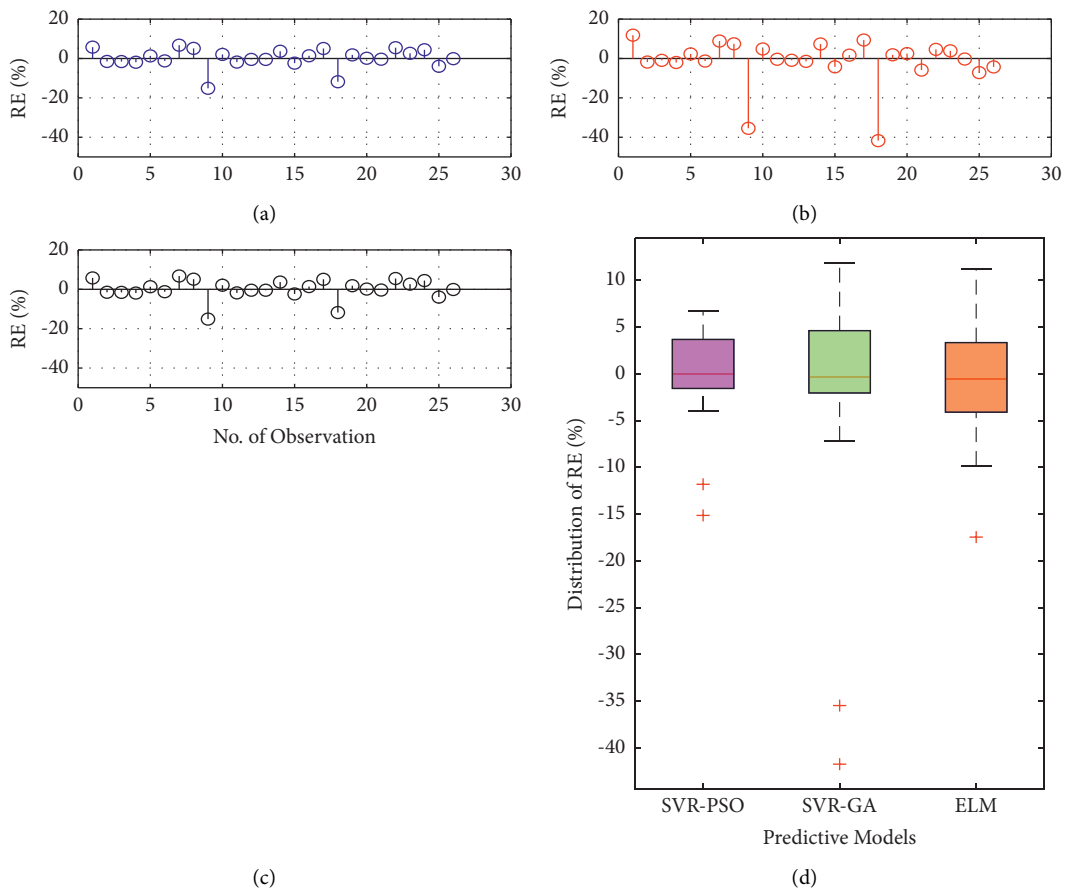
FIGURE 6: Comparison of the performances of three adopted models: (a, b, and c respectively belong to SVR-PSO, SVR-GA, and ELM, while d shows the boxplot presentation for illustrating the distribution of relative error for all adopted models in a single plot.

TABLE 4: The predicted compressive strength values using applied models versus the experimental values during the testing phase.

No. Sample	SVR-PSO (MPa)	SVR-GA (MPa)	ELM (MPa)	Experimental (MPa)
1	28.73	29.93	28.85	28.70
2	36.07	35.85	39.02	35.52
3	46.56	46.62	46.12	45.69
4	41.26	40.84	41.91	41.81
5	37.85	37.87	36.34	37.39
6	34.00	33.23	38.27	36.46
7	39.03	38.07	38.17	41.14
8	21.02	24.74	18.54	18.26
9	40.16	39.03	42.69	41.01
10	36.03	35.53	37.00	35.39
11	31.11	31.25	31.83	30.97
12	43.68	40.87	46.82	46.36
13	33.94	34.27	33.97	33.78
14	40.53	38.98	42.30	42.08
15	31.70	32.28	33.11	30.97
16	46.51	46.64	45.61	45.82
17	51.92	51.76	48.07	52.65
18	41.33	39.46	42.66	43.54
19	21.46	27.20	20.15	19.19
20	37.49	37.47	37.62	38.19
21	45.36	44.29	43.90	45.42
22	29.34	30.95	25.94	29.23
23	31.67	31.96	30.18	33.51
24	41.88	41.33	39.55	43.01
25	26.65	27.97	25.97	27.89
26	29.14	30.04	32.92	28.03
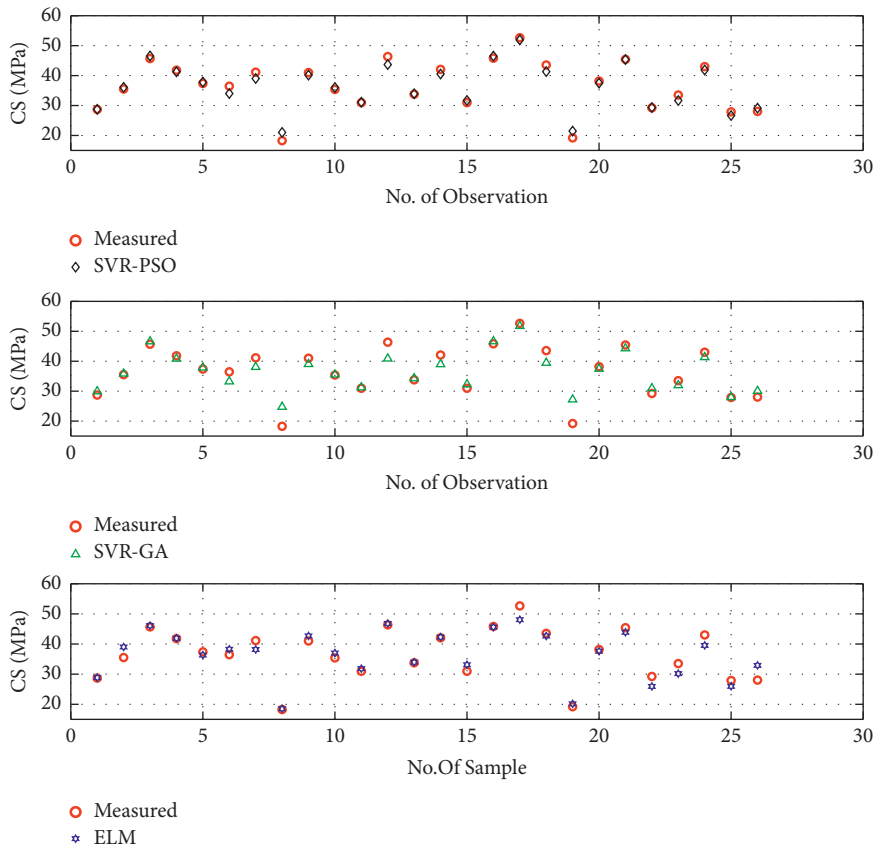
FIGURE 7: Comparison between the measured compressive strength of concrete and the predicted values.
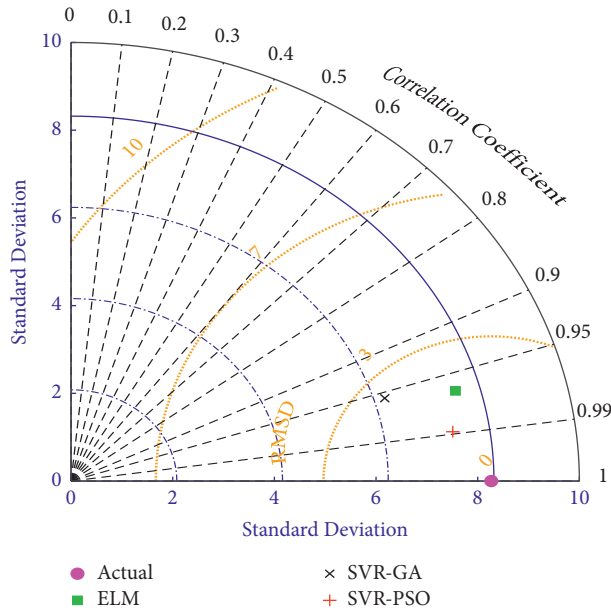
Figure 8: Taylor diagram for comparing the performances of the proposed models: testing set.

Table 5: The optimized hyper-parameters of SVR by PSO and GA.

Parameter	GA	PSO
C	1.160329	8.511694
γ	$8.007E-03$	0.015044
ε	0.990097	0.048581

similarity with the based model of the actual dataset. It can be seen from this figure that the SVR-PSO model takes the closest position to the actual data, which indicates the excellent performance of this model. However, the other models (SVR-GA and ELM) show a lower similarity with the actual data than the SVR-PSO model during the testing phase.

Finally, both quantitative and visualized assessments referred to the adopted predictive model (SVR-PSO) have performed very well in training and testing phases to predict the compressive strength of standard and high-performance concrete. Although the CS has had a complex relationship with the existing parameters, the proposed modeling approach was very stable and gave the highest accuracy results compared to other comparable models. For ensuring the reliability of the proposed model (SVR-PSO), the outcome of this model during the testing set will be compared with other predictive models conducted in previous studies in terms of coefficient of determination (R^2). This indicator is very efficient when comparing a specific model's outcomes to others developed in other studies with a different dataset. The most important thing is that this parameter is not affected by normalization and the scale of the dataset. The models are developed based on a given dataset from different ranges and distributions. However, most other statistical criteria such as RMSE, NSE, and other criteria are mainly influenced by the scale of the used data set. When comparing different predictive models established from several datasets, these parameters may be misleading. Finally, the hyperparameters of SVR, which PSO and GA have optimized, are presented in Table 5.

3.1. Comparing the Proposed Model with Others Developed in Previous Studies. Shariati et al. [10] presented a novel model by incorporating the extreme learning machine and grey wolf optimizer to predict the concrete CS. For

compression purposes, the authors used standard extreme learning machine (ELM), support vector regression (SVR) with different kernel functions, artificial neural network, and adaptive neuro-fuzzy inference system (ANFIS). The assessment results revealed that the proposed modeling approach outperformed other modeling approaches with desirable accuracy ($R^2 = 0.9381$). Another study [75] investigated using the data mining approach as a computer aid to predict CS of high-strength concrete. The authors used a cross-validation (CV) approach with a multiple additive regression tree (Mars). The proposed model is evaluated with other approaches like ANN and SVR, statistical model, and bagging regression trees. The results discovered that the comparable models gave undesirable performances while the proposed model achieved the highest accuracy with R^2 of 0.943. The study conducted that the other modeling approaches gave lower accuracy and suffered overfitting problems. Chou et al. [27] applied two approaches to estimate concrete CS, called ANN and SVR. In order to achieve better performances, the authors developed both models using the same dataset. However, the performance of the ANN model was slightly lower than the SVR model. The study concluded that the SVR is more stable and hence gives the higher prediction accuracy with R^2 of 0.9551. Moreover, Pham et al. [76] investigated the hybridization of least square support vector regression with a firefly algorithm to establish a hybrid model called (LS-SVR-FFA) for predicting CS of high-performance concrete. For verification of the performance of the hybrid model, authors used other benchmark models called SVR and ANN. the results found that the LS-SVR-FFA model was very accurate compared to SVR and ANN models in the prediction of CS of concrete with R^2 of 0.89. Bui et al. [77] hybridized the novel whale optimization algorithm with the ANN approach to enhance the model's performance in predicting concrete CS. The authors also incorporated the neural network with several algorithms (ant colony optimization and dragonfly algorithm). The outcomes of the study showed that the proposed model (WOA-NN) gains the fewest error forecasting and best performance ($R^2 = 0.898$). Another study was conducted by Hameed and AlOmar [4] to predict CS of concrete using the ANN-CV model. The study used the multiple linear regression (MLR) model for comparison and validation of the performance of the proposed model. The study concluded that the MLR approach could not provide desirable results as ANN models though using CV techniques with both models. However, the superiority of the ANN model is obvious in terms of accuracy performance ($R^2 = 0.931$). Table 6 provides more reverent studies which developed different prediction models for the prediction of CS of concrete. Based on the outcome of the reviewed models collected

TABLE 6: Validating the SVR – PSO against predictive models collected from the literature.

Reference	Model	R^2
[10]	ELM-GWO	0.9381
[75]	MART-CV	0.943
[27]	SVR	0.9551
[76]	LS-SVR-FA	0.89
[77]	WOA-ANN	0.898
[4]	ANN-CV	0.931
[78]	MARS-GBM	0.956
[79]	ANN	0.922
[80]	Neural-expert system(NEX)	0.76
[81]	Fuzzy polynomial neural networks (FPNN)	0.821
[82]	ANN	0.934
[83]	EFSIM	0.927
[84]	RELM- CV	0.884
[85]	XGBoost with feature selection	0.9339
Proposed model (SVR-PSO)		**0.978**

from the literature, the suggested model (SVR-PSO) outperformed all comparable models developed and used in previous studies.

3.2. Sensitivity Analysis. After assessing the reliability of the proposed model (SVR-PSO) and validating its performance against different models developed in previous studies to predict CS of concrete, it is vital to conduct sensitivity analyses to identify the most significant parameters that have an important influence on CS of concrete. Moreover, the selection of the most influential parameters has great importance in minimizing time and cost as well as this step is vital in structural and material engineering [86]. The cosine amplitude method is applied in this current paper [47, 87]. The mathematical expression of the amplitude method can be seen according to the following equation:

$$R_{ij} = \frac{\sum_{k=1}^{n} \left(X_{ik} * X_{jk} \right)}{\sqrt{\sum_{k=1}^{n} X_{ik}^2 \sum_{k=1}^{n} X_{jk}^2}}, \tag{28}$$

where R_{ij} is the correlation degree between each input variable and target (CS of concrete). This factor ranges between 0 and 1. If there is a high correlation between a parameter with CS of concrete, the value of R_{ij} is becoming close to one. On the other hand, if there is no relation between a variable and CS of concrete, the value R_{ij} equals zero. Moreover, in the stated equation, n is the number of samples during the crucial step of this study (i.e., testing set), and the parameters X_i and X_j, respectively are the input and output values (CS of concrete). Figure 9 shows the influence of each used parameter on the CS of concrete. It found that the fine aggregate, coarse aggregate, water, and cement variables have the highest impact on CS. However, the other input parameters (i.e., SP, fly ash, and slag) have a lower impact on the CS of concrete.

3.3. Limitation of the Proposed Method and Possible Future Research. The obtained results have proved the capability of SVR-PSO in the prediction of CS of concrete where the cement was partially replaced with other materials. The
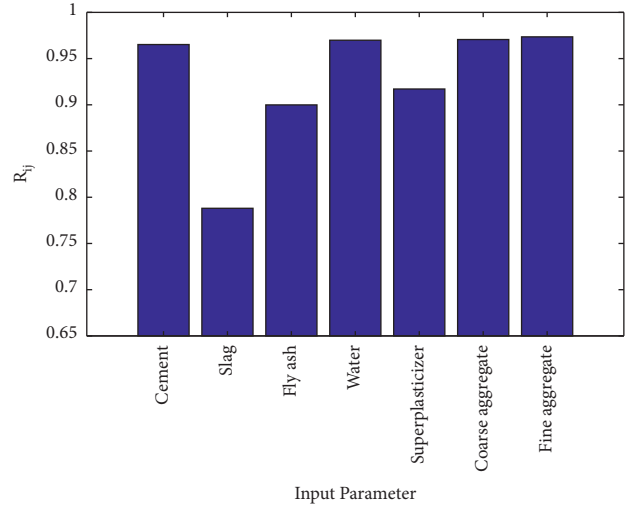
FIGURE 9: Sensitivity analysis results.

proposed model showed an important improvement in prediction capacity compared to other comparable models such as ELM and SVR-GA. Besides, the input predictors of this study, including seven different materials, are introduced to the models to predict the CS property. However, the prediction accuracy of the proposed model may improve if the advanced data preprocessing technique is applied. Moreover, the input vectors may have uncertainties and are correlated, which eventually hider the model's performance. Therefore, this study recommends applying the principal component analyses (PCA) approach before training the model. Applying the PCA approach has a significant advantage in eliminating the redundant information and correlation between input data, thereby enhancing the predicting accuracy of the applied model.

4. Conclusions

The significant contribution of this research was to develop a hybrid AI model for the prediction of compressive strength of concrete with 28-day age where the cement was partially replaced with the pozzolan powders such as furnace slag and fly ash. The traditional approaches such as the trial-and-error method applied to find the optimal concrete design have some limitations since the process is time-consuming and needs several experimentals. Furthermore, the process of partially replacing cement in concrete manufacturing makes the relationships between CS and concrete components very complex. Accordingly, the classical method does not provide the most optimal solutions. Thus, this research has introduced a novel approach as an efficient and cost-effective method to early estimate the CS. For this regard, SVR is hybridized with two different nature-inspired optimizations like modified PSO and GA, constituting SVR-PSO and SVR-GA models, respectively. These algorithms are given a significant task in optimizing the hyperparameters of SVR. Furthermore, the ELM model is also developed for validating the performances of both SVR-PSO and SMR-GA. There were eight statistical matrices used for assessing

the performance of each model separately. The results showed that all proposed models (ELM, SVR-GA, and SVR-PSO) provided good estimates. However, there were significant differences reported throughout the testing set. Additionally, the reported results uncovered that the SVR-GA suffered overfitting problems. Although the ELM model has been found to provide highly accurate estimates compared to the SVR-GA model, the SVR-PSO model was superior in predicting the compressive strength of concrete. Among all eight statistical parameters that are used in this study, the uncertainty at 95% (U95) is noticed as a more efficient parameter in evaluating the prediction capacity of used models. The proficiency of U_{95} is remarkably noticed to efficiently identify the most efficient predictive modeling approach when other statistical parameters such as coefficient of determination (R^2), mean absolute error (MAE), and Index of Agreement or Willmott (WI) gave almost very close assessments for all comparable models. Furthermore, visualization assessments such as boxplots, scatter plots, and Taylor diagrams have been carried out and pointed out that the SVR-PSO models were the best predictive models in the prediction of CS. Besides, further assessment has been carried out by comparing the performance of the proposed model (SVR-PSO) with 14 models that had been developed in the literature. It is found that the proposed model of this study gave more excellent estimates than the comparable models. Sensitivity analysis using the cosine amplitude method also has been done in this study to select the most influential input parameters on the outputs. It was found that the fine aggregate, coarse aggregate, water, and cement variables have the highest impact on CS, respectively. Finally, the hybridization of SVR with modified PSO provided more accurate CS predictions and thus can help to enhance the understanding of the underlying relations between concrete mix components and CS property.

Using Seven input variables may hinder the performance of the applied models because these variables may have redundant information. Besides, these parameters may be correlated to each other or have uncertainties that reduce the efficiency of the predicted model. For future studies, this study recommends using the PCA approach before training the models to remove the redundant information from input vectors and eliminate the correlation between inputs data.

Abbreviations

AI: Artificial intelligence
ANFIS: Adaptive neuro-fuzzy inference
ANN: Artificial neural networks
CC: Correlation of coefficient
CO_2:   Carbon dioxide
CS: Compressive strength
CV: Cross-validation
DT: Decision tree
EFSIMT: Evolutionary fuzzy support vector machine inference model
ELM: Extreme learning machine
ELM-GWO: Extreme learning machine integrated with grey wolf optimizer
erMAX: Maximum absolute percentage relative error
FA: Fly ash
FFNN: Feedforward neural network
FPNN: Fuzzy polynomial neural network
FS: Furnace slag
GA: Genetic algorithm
GGBFS: Ground granulated blast furnace slag
GMDH: Group method of data handling
HPC: High-performance concrete
IQR: Interquartile range
LS-SVR-FA: Least square support vector regression coupled with firefly algorithm
MAE: Mean absolute error
MARE: Mean absolute relative error
MARS: Multivariate adaptive regression spline
MAX: Maximum value
Min: Minimum value
MLR: Multiple linear regression
NE: Nash–Sutcliffe model efficiency coefficient
NEX: Neural-expert system
PSO: Particle swarm algorithm
RE: Relative error
R^2:   Correlation of determination
RELM: Regularized extreme learning machine
SC: Soft Computing
SCC: Self-compacting concrete
Std: Standard deviation
SVR: Support vector regression
U_{95}:   Uncertainty at 95
WI: Index of Agreement or Willmott
WOA-ANN: Incorporation of the whale optimization algorithm with artificial neural network
XGBoost: Extreme gradient boosting.

Data Availability

The data are available from the corresponding author upon request.

Conflicts of Interest

The authors declare that there are no conflicts of interest.

Acknowledgments

References

[1] İ. B. Topçu and M. Sarıdemir, "Prediction of compressive strength of concrete containing fly ash using artificial neural networks and fuzzy logic," *Computational Materials Science*, vol. 41, no. 3, pp. 305–311, 2008.

[2] M. Shariati, S. Rafie, Y. Zandi et al., "Experimental investigation on the effect of cementitious materials on fresh and mechanical properties of self-consolidating concrete," *Advances in concrete construction*, vol. 8, no. 3, pp. 225–237, 2019.

[3] P. Chopra, R. K. Sharma, and M. Kumar, "Prediction of compressive strength of concrete using artificial neural network and genetic programming," *Advances in Materials Science and Engineering*, vol. 2016, pp. 1–10, 2016.

[4] M. M. Hameed and M. K. AlOmar, "Prediction of compressive strength of high-performance concrete: hybrid artificial intelligence technique," in *Applied Computing to Support Industry: Innovation and Technology*, pp. 323–335, Springer International Publishing, Cham, 2020.

[5] H. Naderpour, A. H. Rafiean, and P. Fakharian, "Compressive strength prediction of environmentally friendly concrete using artificial neural networks," *Journal of Building Engineering*, vol. 16, pp. 213–219, 2018.

[6] C. Duran Atiş, "Strength properties of high-volume fly ash roller compacted and workable concrete, and influence of curing condition," *Cement and Concrete Research*, vol. 35, no. 6, pp. 1112–1121, 2005.

[7] S. K. Antiohos, V. G. Papadakis, E. Chaniotakis, and S. Tsimas, "Improving the performance of ternary blended cements by mixing different types of fly ashes," *Cement and Concrete Research*, vol. 37, no. 6, pp. 877–885, 2007.

[8] T. Kim, J. M. Davis, M. T. Ley, S. Kang, and P. Amrollahi, "Fly ash particle characterization for predicting concrete compressive strength," *Construction and Building Materials*, vol. 165, pp. 560–571, 2018.

[9] S. Kang, Z. Lloyd, T. Kim, and M. T. Ley, "Predicting the compressive strength of fly ash concrete with the Particle Model," *Cement and Concrete Research*, vol. 137, Article ID 106218, 2020.

[10] M. Shariati, M. S. Mafipour, B. Ghahremani et al., "A novel hybrid extreme learning machine-grey wolf optimizer (ELM-GWO) model to predict compressive strength of concrete with partial replacements for cement," *Engineering with Computers*, vol. 38, no. 1, pp. 757–779, 2020.

[11] G. Li and X. Zhao, "Properties of concrete incorporating fly ash and ground granulated blast-furnace slag," *Cement and Concrete Composites*, vol. 25, no. 3, pp. 293–299, 2003.

[12] L. Lam, Y. L. Wong, and C. S. Poon, "Effect of fly ash and silica fume on compressive and fracture behaviors of concrete," *Cement and Concrete Research*, vol. 28, no. 2, pp. 271–283, 1998.

[13] Y. Poojari and V. Kampilla, "Strength behavior analysis of fiber reinforced fly ash concrete," *Materials Today Proceedings*, vol. 43, pp. 1659–1665, 2021.

[14] D. Suresh and K. Nagaraju, "Ground granulated blast slag (GGBS) in concrete–a review," *IOSR Journal of Mechanical and Civil Engineering*, vol. 12, no. 4, pp. 76–82, 2015.

[15] M. A. Abd-El.Aziz, S. Abd.El.Aleem, and M. Heikal, "Physico-chemical and mechanical characteristics of pozzolanic cement pastes and mortars hydrated at different curing temperatures," *Construction and Building Materials*, vol. 26, no. 1, pp. 310–316, 2012.

[16] E. Özbay, M. Erdemir, and H. İ. Durmuş, "Utilization and efficiency of ground granulated blast furnace slag on concrete properties – a review," *Construction and Building Materials*, vol. 105, pp. 423–434, 2016.

[17] H. Bınıci, M. Y. Durgun, T. Rızaoğlu, and M. Koluçolak, "Investigation of durability properties of concrete pipes incorporating blast furnace slag and ground basaltic pumice as fine aggregates," *Scientia Iranica*, vol. 19, no. 3, pp. 366–372, 2012.

[18] Y. Geng, Z. Wang, L. Shen, and J. Zhao, "Calculating of CO2 emission factors for Chinese cement production based on inorganic carbon and organic carbon," *Journal of Cleaner Production*, vol. 217, pp. 503–509, 2019.

[19] J. Wei and K. Cen, "Empirical assessing cement CO2 emissions based on China's economic and social development during 2001-2030," *The Science of the Total Environment*, vol. 653, pp. 200–211, 2019.

[20] J. An, R. S. Middleton, and Y. Li, "Environmental performance analysis of cement production with CO2 capture and storage technology in a life-cycle perspective," *Sustainability*, vol. 11, no. 9, p. 2626, 2019.

[21] M. Hameed, S. S. Sharqi, Z. M. Yaseen, H. A. Afan, A. Hussain, and A. Elshafie, "Application of artificial intelligence (AI) techniques in water quality index prediction: a case study in tropical region, Malaysia," *Neural Computing & Applications*, vol. 28, no. S1, pp. 893–905, 2017.

[22] Z. Keshavarz and H. Torkian, "Application of ANN and ANFIS models in determining compressive strength of concrete," *Journal of Soft Computing in Civil Engineering*, vol. 2, no. 1, pp. 62–70, 2018.

[23] F. Khademi and K. Behfarnia, "Evaluation OF concrete compressive strength using artificial neural network and multiple linear regression models," *INTERNATIONAL JOURNAL OF OPTIMIZATION IN CIVIL ENGINEERING*, vol. 6, no. 3, 2016, [Online]. Available: https://www.sid.ir/en/journal/ViewPaper.aspx?id=500731.

[24] D. J. Armaghani and P. G. Asteris, "A comparative study of ANN and ANFIS models for the prediction of cement-based mortar materials compressive strength," *Neural Computing & Applications*, vol. 33, no. 9, pp. 4501–4532, 2021.

[25] H.-G. Ni and J.-Z. Wang, "Prediction of compressive strength of concrete by neural networks," *Cement and Concrete Research*, vol. 30, no. 8, pp. 1245–1250, 2000.

[26] J.-J. Lee, D.-K. Kim, S.-K. Chang, and J.-H. Lee, "Application of support vector regression for the prediction of concrete strength," *Computers and Concrete*, vol. 4, no. 4, pp. 299–316, 2007.

[27] K. O. Akande, T. O. Owolabi, T. O. Owolabi, S. Twaha, and S. O. Olatunji, "Performance comparison of SVM and ANN in predicting compressive strength of concrete," *IOSR Journal of Computer Engineering*, vol. 16, no. 5, pp. 88–94, 2014.

[28] H. Ling, C. Qian, W. Kang, C. Liang, and H. Chen, "Combination of Support Vector Machine and K-Fold cross validation to predict compressive strength of concrete in marine environment," *Construction and Building Materials*, vol. 206, pp. 355–363, 2019.

[29] B. K. R. Prasad, H. Eskandari, and B. V. V. Reddy, "Prediction of compressive strength of SCC and HPC with high volume fly ash using ANN," *Construction and Building Materials*, vol. 23, no. 1, pp. 117–128, 2009.

[30] A. M. Abd and S. M. Abd, "Modelling the strength of lightweight foamed concrete using support vector machine (SVM)," *Case Studies in Construction Materials*, vol. 6, pp. 8–15, 2017.

[31] X. Xue, "Evaluation of concrete compressive strength based on an improved PSO-LSSVM model," *Computers and Concrete*, vol. 21, no. 5, pp. 505–511, 2018.

[32] L. Sun, M. Koopialipoor, D. Jahed Armaghani, R. Tarinejad, and M. M. Tahir, "Applying a meta-heuristic algorithm to predict and optimize compressive strength of concrete samples," *Engineering with Computers*, vol. 37, no. 2, pp. 1133–1145, 2021.

[33] D. Zhang, W. Xiang, Q. Cao, and S. Chen, "Application of incremental support vector regression based on optimal training subset and improved particle swarm optimization algorithm in real-time sensor fault diagnosis," *Applied Intelligence*, vol. 51, no. 6, pp. 3323–3338, 2021.

[34] H. Jahangir and D. Rezazadeh Eidgahee, "A new and robust hybrid artificial bee colony algorithm - ANN model for FRP-concrete bond strength evaluation," *Composite Structures*, vol. 257, p. 113160, 2021.

[35] Z. Yuan, L.-N. Wang, and X. Ji, "Prediction of concrete compressive strength: research on hybrid models genetic based algorithms and ANFIS," *Advances in Engineering Software*, vol. 67, pp. 156–163, 2014.

[36] E. Li, J. Zhou, X. Shi et al., "Developing a hybrid model of salp swarm algorithm-based support vector machine to predict the strength of fiber-reinforced cemented paste backfill," *Engineering with Computers*, vol. 37, no. 4, pp. 3519–3540, 2021.

[37] R. Madandoust, J. H. Bungey, and R. Ghavidel, "Prediction of the concrete compressive strength by means of core testing using GMDH-type neural network and ANFIS models," *Computational Materials Science*, vol. 51, no. 1, pp. 261–272, 2012.

[38] M. Shariati, M. S. Mafipour, P. Mehrabi, K. Wakil, N. T. Trung, and A. Toghroli, "Prediction of concrete strength in presence of furnace slag and fly ash using Hybrid ANN-GA (Artificial Neural Network-Genetic Algorithm)," *Smart Structures and Systems*, vol. 25, no. 2, pp. 183–195, 2020.

[39] I.-J. Han, T.-F. Yuan, J.-Y. Lee, Y.-S. Yoon, and J.-H. Kim, "Learned prediction of compressive strength of GGBFS concrete using hybrid artificial neural network models," *Materials*, vol. 12, no. 22, p. 3708, 2019.

[40] F. Özcan, C. D. Atiş, O. Karahan, E. Uncuoğlu, and H. Tanyildizi, "Comparison of artificial neural network and fuzzy logic models for prediction of long-term compressive strength of silica fume concrete," *Advances in Engineering Software*, vol. 40, no. 9, pp. 856–863, 2009.

[41] C. D. Atiş, "High-volume fly ash concrete with high strength and low drying shrinkage," *Journal of Materials in Civil Engineering*, vol. 15, no. 2, pp. 153–156, 2003.

[42] A. Behnood, V. Behnood, M. Modiri Gharehveran, and K. E. Alyamac, "Prediction of the compressive strength of normal and high-performance concretes using M5P model tree algorithm," *Construction and Building Materials*, vol. 142, pp. 199–207, 2017.

[43] I.-C. Yeh, "Modeling slump flow of concrete using second-order regressions and artificial neural networks," *Cement and Concrete Composites*, vol. 29, no. 6, pp. 474–480, 2007.

[44] I.-C. Yeh, "Simulation of concrete slump using neural networks," *Proceedings of the Institution of Civil Engineers - Construction Materials*, vol. 162, no. 1, pp. 11–18, 2009.

[45] H. H. John, "Index," in *Adaptation in Natural and Artificial Systems: An Introductory Analysis with Applications to Biology, Control, and Artificial Intelligence*, pp. 207–211, MIT Press, Cambridge, Massachusetts, United States, 1992.

[46] D. E. Goldenberg, *Genetic Algorithms in Search, Optimization and Machine Learning*, Addison-Wesley, Reading: MA, 1989.

[47] E. Momeni, R. Nazir, D. Jahed Armaghani, and H. Maizir, "Prediction of pile bearing capacity using a hybrid genetic algorithm-based ANN," *Measurement*, vol. 57, pp. 122–131, 2014.

[48] M. Khandelwal and D. J. Armaghani, "Prediction of drillability of rocks with strength properties using a hybrid GA-ANN technique," *Geotechnical & Geological Engineering*, vol. 34, no. 2, pp. 605–620, 2016.

[49] M. Koopialipoor, A. Fallah, D. J. Armaghani, A. Azizi, and E. T. Mohamad, "Three hybrid intelligent models in estimating flyrock distance resulting from blasting," *Engineering with Computers*, vol. 35, no. 1, pp. 243–256, 2019.

[50] M. Beiki, A. Majdi, and A. D. Givshad, "Application of genetic programming to predict the uniaxial compressive strength and elastic modulus of carbonate rocks," *International Journal of Rock Mechanics and Mining Sciences*, vol. 63, pp. 159–169, 2013.

[51] E. T. Mohamad, R. S. Faradonbeh, D. J. Armaghani, M. Monjezi, and M. Z. A. Majid, "An optimized ANN model based on genetic algorithm for predicting ripping production," *Neural Computing & Applications*, vol. 28, no. S1, pp. 393–406, 2017.

[52] J. Kennedy and R. Eberhart, "Particle swarm optimization,"vol. 4, pp. 1942–1948, in *Proceedings of the ICNN'95-International Conference on Neural Networks*, vol. 4, pp. 1942–1948, IEEE, Perth, WA, Australia, 1995.

[53] B. Gordan, D. Jahed Armaghani, M. Hajihassani, and M. Monjezi, "Prediction of seismic slope stability through combination of particle swarm optimization and neural network," *Engineering with Computers*, vol. 32, no. 1, pp. 85–97, 2016.

[54] C. Cortes and V. Vapnik, "Support-vector networks," *Machine Learning*, vol. 20, no. 3, pp. 273–297, 1995.

[55] A. A. Farag and R. M. Mohamed, "Classification of multispectral data using support vector machines approach for density estimation," in *Proceedings of the International conference on intelligent engineering system*, pp. 6–8, Citeseer, 2003.

[56] J. Fan, L. Wu, F. Zhang et al., "Evaluating the effect of air pollution on global and diffuse solar radiation prediction using support vector machine modeling based on sunshine duration and air temperature," *Renewable and Sustainable Energy Reviews*, vol. 94, pp. 732–747, 2018.

[57] X. Ji, X. Shang, R. A. Dahlgren, and M. Zhang, "Prediction of dissolved oxygen concentration in hypoxic river systems using support vector machine: a case study of Wen-Rui Tang River, China," *Environmental Science and Pollution Research*, vol. 24, no. 19, pp. 16062–16076, 2017.

[58] K. Mohammadi, S. Shamshirband, M. H. Anisi, K. A. Alam, and D. Petković, "Support vector regression based prediction of global solar radiation on a horizontal surface," *Energy Conversion and Management*, vol. 91, pp. 433–441, 2015.

[59] K. Roushangar, M. T. Alami, J. Shiri, and M. M. Asl, "Determining discharge coefficient of labyrinth and arced labyrinth weirs using support vector machine," *Hydrology Research*, vol. 49, no. 3, pp. 924–938, 2018.

[60] A. S. Abobakr Yahya, A. N. Ahmed, F. Binti Othman et al., "Water quality prediction model based support vector machine model for Ungauged River catchment under dual scenarios," *Water*, vol. 11, no. 6, p. 1231, 2019.

[61] N. Sapankevych and R. Sankar, "Time series prediction using support vector machines: a survey," *IEEE Computational Intelligence Magazine*, vol. 4, no. 2, pp. 24–38, 2009.

[62] V. Vapnik, *The Nature of Statistical Learning theory*, p. 27, Springer science & business media, Berlin, Germany, 2013.

[63] M. K. AlOmar, M. M. Hameed, N. Al-Ansari, and M. A. AlSaadi, "Data-driven model for the prediction of total dissolved gas: robust artificial intelligence approach," *Advances in Civil Engineering*, vol. 2020, pp. 1–20, 2020.

[64] R. C. Deo, N. Downs, A. V. Parisi, J. F. Adamowski, and J. M. Quilty, "Very short-term reactive forecasting of the solar ultraviolet index using an extreme learning machine integrated with the solar zenith angle," *Environmental Research*, vol. 155, pp. 141–166, 2017.

[65] G.-B. Huang, Q.-Y. Zhu, and C.-K. Siew, "Extreme learning machine: theory and applications," *Neurocomputing*, vol. 70, no. 1-3, pp. 489–501, 2006.

[66] H.-H. Liu, L.-C. Chang, C.-W. Li, and C.-H. Yang, "Particle swarm optimization-based support vector regression for tourist arrivals forecasting," *Computational Intelligence and Neuroscience*, vol. 2018, pp. 1–13, 2018.

[67] I. O. Alade, M. A. Abd Rahman, and T. A. Saleh, "Modeling and prediction of the specific heat capacity of Al2 O3/water nanofluids using hybrid genetic algorithm/support vector regression model," *Nano-Structures & Nano-Objects*, vol. 17, pp. 103–111, 2019.

[68] M. Sornalakshmi, S. Balamurali, M. Venkatesulu et al., "Hybrid method for mining rules based on enhanced Apriori algorithm with sequential minimal optimization in healthcare industry," *Neural Computing & Applications*, 2020.

[69] M. E. H. Pedersen, "Good parameters for particle swarm optimization," Technical Report HL1001, pp. 1551–3203, Hvass Lab, Copenhagen, Denmark, 2010.

[70] E. Mezura-Montes and C. A. Coello Coello, "Constraint-handling in nature-inspired numerical optimization: past, present and future," *Swarm and Evolutionary Computation*, vol. 1, no. 4, pp. 173–194, 2011.

[71] P. G. Asteris, I. Argyropoulos, L. Cavaleri et al., "Masonry compressive strength prediction using artificial neural networks," in *Transdisciplinary Multispectral Modeling and Cooperation for the Preservation of Cultural Heritage*, pp. 200–224, Springer International Publishing, Cham, 2019.

[72] M. K. AlOmar, M. M. Hameed, and M. A. AlSaadi, "Multi hours ahead prediction of surface ozone gas concentration: robust artificial intelligence approach," *Atmospheric Pollution Research*, vol. 11, no. 9, pp. 1572–1587, 2020.

[73] H. Tao, A. A. Ewees, A. O. Al-Sulttani et al., "Global solar radiation prediction over North Dakota using air temperature: development of novel hybrid intelligence model," *Energy Reports*, vol. 7, pp. 136–157, 2021.

[74] G. Zhang, Z. H. Ali, M. S. Aldlemy et al., "Reinforced concrete deep beam shear strength capacity modelling using an integrative bio-inspired algorithm with an artificial intelligence model," *Engineering with Computers*, 2020.

[75] J.-S. Chou, C.-K. Chiu, M. Farfoura, and I. Al-Taharwa, "Optimizing the prediction accuracy of concrete compressive strength based on a comparison of data-mining techniques," *Journal of Computing in Civil Engineering*, vol. 25, no. 3, pp. 242–253, 2011.

[76] A.-D. Pham, N.-D. Hoang, and Q.-T. Nguyen, "Predicting compressive strength of high-performance concrete using metaheuristic-optimized least squares support vector regression," *Journal of Computing in Civil Engineering*, vol. 30, no. 3, p. 06015002, 2016.

[77] D. T. Bui, M. a. M. Abdullahi, S. Ghareh, H. Moayedi, and H. Nguyen, "Fine-tuning of neural computing using whale optimization algorithm for predicting compressive strength of concrete," *Engineering with Computers*, vol. 37, no. 1, pp. 701–712, 2019.

[78] M. R. Kaloop, D. Kumar, P. Samui, J. W. Hu, and D. Kim, "Compressive strength prediction of high-performance concrete using gradient tree boosting machine," *Construction and Building Materials*, vol. 264, p. 120198, 2020.

[79] I.-C. Yeh, "Modeling of strength of high-performance concrete using artificial neural networks," *Cement and Concrete Research*, vol. 28, no. 12, pp. 1797–1808, 1998.

[80] R. Gupta, M. A. Kewalramani, and A. Goel, "Prediction of concrete strength using neural-expert system," *Journal of Materials in Civil Engineering*, vol. 18, no. 3, pp. 462–466, 2006.

[81] M. H. Fazel Zarandi, I. B. Türksen, J. Sobhani, and A. A. Ramezanianpour, "Fuzzy polynomial neural networks for approximation of the compressive strength of concrete," *Applied Soft Computing*, vol. 8, no. 1, pp. 488–498, 2008.

[82] I.-C. Yeh and L.-C. Lien, "Knowledge discovery of concrete material using Genetic Operation Trees," *Expert Systems with Applications*, vol. 36, no. 3, pp. 5807–5812, 2009.

[83] M.-Y. Cheng, J.-S. Chou, A. F. V. Roy, and Y.-W. Wu, "High-performance concrete compressive strength prediction using time-weighted evolutionary fuzzy support vector machines inference model," *Automation in Construction*, vol. 28, pp. 106–115, 2012.

[84] A. K. Al-Shamiri, T.-F. Yuan, and J. H. Kim, "Non-tuned machine learning approach for predicting the compressive strength of high-performance concrete," *Materials*, vol. 13, no. 5, p. 1023, 2020.

[85] Z. Wan, Y. Xu, and B. Šavija, "On the use of machine learning models for prediction of compressive strength of concrete: influence of dimensionality reduction on the model performance," *Materials*, vol. 14, no. 4, p. 713, 2021.

[86] M. M. Hameed, M. K. AlOmar, W. J. Baniya, and M. A. AlSaadi, "Prediction of high-strength concrete: high-order response surface methodology modeling approach," *Engineering with Computers*, 2021.

[87] X. Ji and S. Y. Liang, "Model-based sensitivity analysis of machining-induced residual stress under minimum quantity lubrication," *Proceedings of the Institution of Mechanical Engineers - Part B: Journal of Engineering Manufacture*, vol. 231, no. 9, pp. 1528–1541, 2017.

Research Article

Numerical Simulation Study on Construction Effect of Top-Down Construction Method of Suspended Diaphragm Wall for Deep and Large Foundation Pit in Complex Stratum

Yunhui Zhu,[1] Fuxue Sun [iD],[2] Mingqing Liu,[1] Qifeng Liu,[3] Xiaochun Li,[4] and Gang Ge[4]

[1]*Wenzhou University of Technology, Wenzhou 325035, China*
[2]*Wenzhou University, Wenzhou 325035, China*
[3]*Wenzhou Railway and Rail Transit Investment Co., Ltd, Wenzhou 325035, China*
[4]*Shanghai Tunnel Engineering Co., Ltd, Shanghai 200000, China*

Correspondence should be addressed to Fuxue Sun; sunfuxue@163.com

In order to study the deformation of a diaphragm wall and the settlement of surrounding soil under the complicated conditions of the deep and soft soil layer, which is underlying inclined rock and top-down construction method, the construction scheme of suspended diaphragm wall based on the engineering practice of Oujiang North Estuary deep and large foundation pit of Wenzhou S2 railway is proposed, and the research method of numerical simulation is adopted in this article. By using Midas GTS finite element software, a three-dimensional model of deep and large foundation pit excavation with top-down construction method is established, and the internal force, deformation, and surface settlement of surrounding soil of suspended diaphragm wall with different depths into rock (1 m, 2 m, and 4 m) are analyzed. Furthermore, the optimization simulation research on the anchor locking scheme is carried out for the determined footed diaphragm wall. Similarly, the anchor locking scheme at a depth of 1 m into the interface between soil and rock is selected as the supporting scheme of the footed diaphragm wall through the simulation results. The research results of this article can guarantee the safety of diaphragm wall construction of deep and large foundation pit in complex stratum.

1. Introduction

At present, deep foundation pit engineering is more and more widely applied, and the depth of foundation pit is also becoming deeper and deeper. Most of the deep foundation pits must be supported during the construction period. The purpose of foundation pit support is to ensure the safety of the surrounding environment of the foundation pit and the construction process of the underground structure [1]. The temporary enclosure, support, or reinforcement measures taken around the working face of the basement create favorable conditions for the construction of the underground structure and ensure a good working environment for the underground construction.

In the 1920s–1930s, Germany, France, and Italy obtained the initial patent of diaphragm wall through practical certification and adopted the "pile wall integration" technology to reduce the thickness of the basement exterior wall and the area of the foundation pit. The design comprehensively considers the load transfer structure of waterproof [2] and diaphragm wall and checks the strength and durability under different loads through different stages of foundation pit construction and external factors [3], such as earthquakes [4]. In 1950, Italy built the first pile row diaphragm wall reservoir dam, and later in Milan metro project, the subway retaining wall has been built in pebble foundation [5], which shows the good advantages of diaphragm wall technology and further promotes the development of diaphragm wall and "pile wall integration" technology. Since then, Germany, France, Japan, the United States, and other countries have introduced diaphragm wall and "pile wall integration" technology [6] and continuously improved and

developed. At present, the technology of diaphragm wall in Japan is at the leading level in the world. The diaphragm wall with the deepest depth of 140 m and thickness of 2.8 m has been built, and the deep well with an inner diameter of 144 m and a depth of 110.1 m has been built.

At present, the foundation pit engineering is developing in the direction of large scale, large depth, tight construction period, and short distance [7]. The foundation pit support methods are diversified. Various support forms can be seen in the same foundation pit. Soil nailing wall support and pile row support are combined, and slope excavation is combined with the diaphragm wall. Because the urban land is more and more expensive and the urban traffic pressure and the population are increasing, the top-down construction method for foundation pit design has become the first choice for the foundation pit excavation adjacent to the urban underground pipeline and subway. The top-down construction method for foundation pit design is suitable for large-area and deep foundation pits. It can simultaneously construct the superstructure, effectively shorten the construction period, save the cost, and control the deformation of the foundation pit and soil outside the pit. With the further improvement of the construction accuracy of column piles in underground structures, more and more civil engineers favor the reverse method design for constructing basement foundation pits of high-rise buildings, and many typical projects have emerged [8, 9]. At the same time, many scholars have conducted in-depth research on reverse practice and achieved some important results.

Ou et al. [10] conducted field measurement on the foundation pit excavated by the top-down construction method, analyzed the data, and concluded that the horizontal displacement of soil close to the diaphragm wall is similar to that of the wall. Long [11] conducted a large number of field measurements by studying the relationship between foundation pit deformation and excavation depth with different soft soil thicknesses between the bottom-up construction method and the top-down construction method. It is concluded that the top-down construction method can reduce the deformation of the foundation pit. Gong et al. [12] proposed that the top-down construction method avoids repeated labor such as dismantling and replacing supports, saves resources and construction cost, and requires a small site during construction, which brings many conveniences to the construction. Kung [13] collected and summarized the actual construction cases of 26 foundation pits in the Taipei silty clay area. The analysis results show that the horizontal displacement of diaphragm wall in bottom-up construction method foundation pit is 1.28 times that in top-down construction method foundation pit under similar engineering conditions. Regardless of the thermal shrinkage effect of concrete floor, the average horizontal displacement of diaphragm wall in bottom-up construction method foundation pit is 1.1 times that in the top-down construction method. Aye et al. [14] used the finite element software PLAXIS to analyze the influence of the underground passage constructed by the top-down construction method in Bangkok on the upper existing overpass, obtained the stratum calculation parameters through the inversion

analysis, calculated and analyzed the deformation of the underground diaphragm wall of the passage, and compared it with the field measured data. The results show that the maximum horizontal displacement of the underground diaphragm wall is only 0.29% times of the excavation depth. The bending moment and axial force of the bored cast-in-place pile near the existing overpass are increased. Liu et al. [15] analyzed the field monitoring data of a 38 m deep foundation pit constructed by a top-down construction method in Shanghai, including the horizontal displacement of the diaphragm wall and the variation of differential settlement of intermediate piles with the progress of construction. The results showed that the maximum horizontal displacement of the diaphragm wall was within the range of 0.2%~0.3% times the excavation depth, and the maximum differential settlement of intermediate piles was less than 1/500 of the column spacing, all of that meet the deformation control requirements.

With the rapid development of urban rail transit construction, deep foundation pit engineering, to a certain extent, meets the needs of urban construction and development. Still, the surrounding environment of the foundation pit is more complex, the geological conditions are worse, and the research on the construction of foundation pits in underlying strata is less; these factors bring great challenges to the safety of foundation pit construction. In this context, based on the deep foundation pit engineering of Jiangbei working shaft of S2 line of Wenzhou City railway, using the three-dimensional finite element numerical simulation method, aiming at the underground continuous wall support, the soft soil layer of underlying inclined rock surface, and the top-down construction technology, this article makes a comprehensive study on the internal force and deformation effect of deep foundation pit suspended foot diaphragm wall construction. Through the comparative analysis of the numerical simulation results and the field measured data, the construction and support scheme of the diaphragm wall suitable for relying on the project is determined to provide a guarantee for the safety of construction.

2. Project Overview

The project on which this article relies is the foundation pit project of the exit shaft of the S2 shield tunnel of Wenzhou City railway in Zhejiang Province, China. The length of the foundation pit is 43 m, the width is 21.9 m or 27.6 m, and the excavation depth is 51.63 m. The foundation pit is located in the deep muddy soil layer in the Oujiang shoal area. The upper part is about 46 m of muddy soil and clay layer. There is a deep riprap layer in the middle and a weakly weathered tuff layer in the lower part. The rock surface is horizontally extraverted, and the geological conditions are complex (as shown in Figure 1).

The foundation pit is protected by a diaphragm wall, the thickness of the diaphragm wall is 1.5 m, the width of the standard section is generally 5.5 m, the length of the local special-shaped diaphragm wall is adjusted properly, and the reinforced concrete ring frame beam and each floor plate are
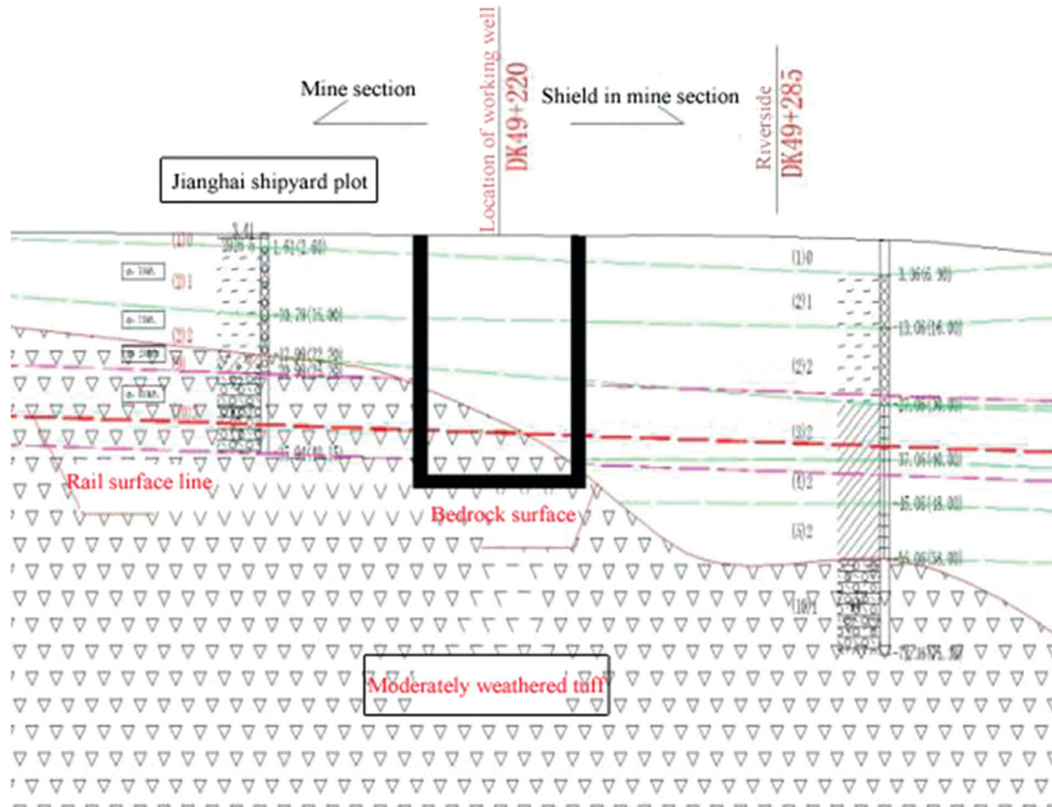
FIGURE 1: Geological profile of Jiangbei working well.

used as the support (as shown in Figure 2). Due to the complex geological conditions, the reverse construction method is adopted in the foundation pit construction. Therefore, how to carry out diaphragm wall construction and foundation pit excavation and support under complex geological conditions and effectively control foundation pit deformation to ensure construction safety is a construction difficulty of the project and also the research focus of this article.

According to the field investigation data, the existing construction equipment and the results of expert discussion, it is proposed to use the suspended foot diaphragm wall for the construction of the foundation pit diaphragm wall, but the specific depth into the rock remains to be determined. In this article, the numerical simulation method will be used to simulate the construction of the suspended footed diaphragm wall so as to determine the depth of the suspended footed diaphragm wall into the rock (1 m, 2 m, and 4 m) and the locking reinforcement scheme of the suspended footed diaphragm wall so as to provide a reference for the smooth progress of the project.

3. Simulation Scheme Design

Midas GTS NX is selected as the numerical simulation software in this article because its simulation results are very similar to the measured data (this is because Midas GTS NX can truly simulate the actual construction process according to the setting process of the on-site retaining structure and

soil excavation), the constitutive model is rich, and the simulation results have high accuracy in the simulation of foundation pit, slope, tunnel, and other practical projects.

3.1. Establishment of Numerical Model

3.1.1. Model Size. According to the actual size of the foundation pit, the calculation model diagram is established (as shown in Figure 3): the length of the foundation pit relying on the project is 43 m, the left width is 21.9 m, the right width is 27.6 m, and the excavation depth is 51.63 m. According to the previous modeling experience, the size of the foundation pit model can generally be 3–5 times the excavation depth of the foundation pit [10]. Finally, the overall size of the foundation pit model is determined as 287 m long, 227.6 m wide, and 100 m high.

3.1.2. Formation Treatment Method. According to the detailed investigation report of the Oujiang North portal tunnel, the soil layer is fine. Through sorting and merging the soil materials with similar properties, the soil materials are divided into five different layers, and the modified Mohr–Coulomb constitutive model is adopted. The material parameters of each layer are shown in Table 1. (Note: the parameters that cannot be provided in the geological survey report are calculated by the empirical method. The other two stiffness properties can be selected according to the compression modulus of a certain ratio. Generally, the secant
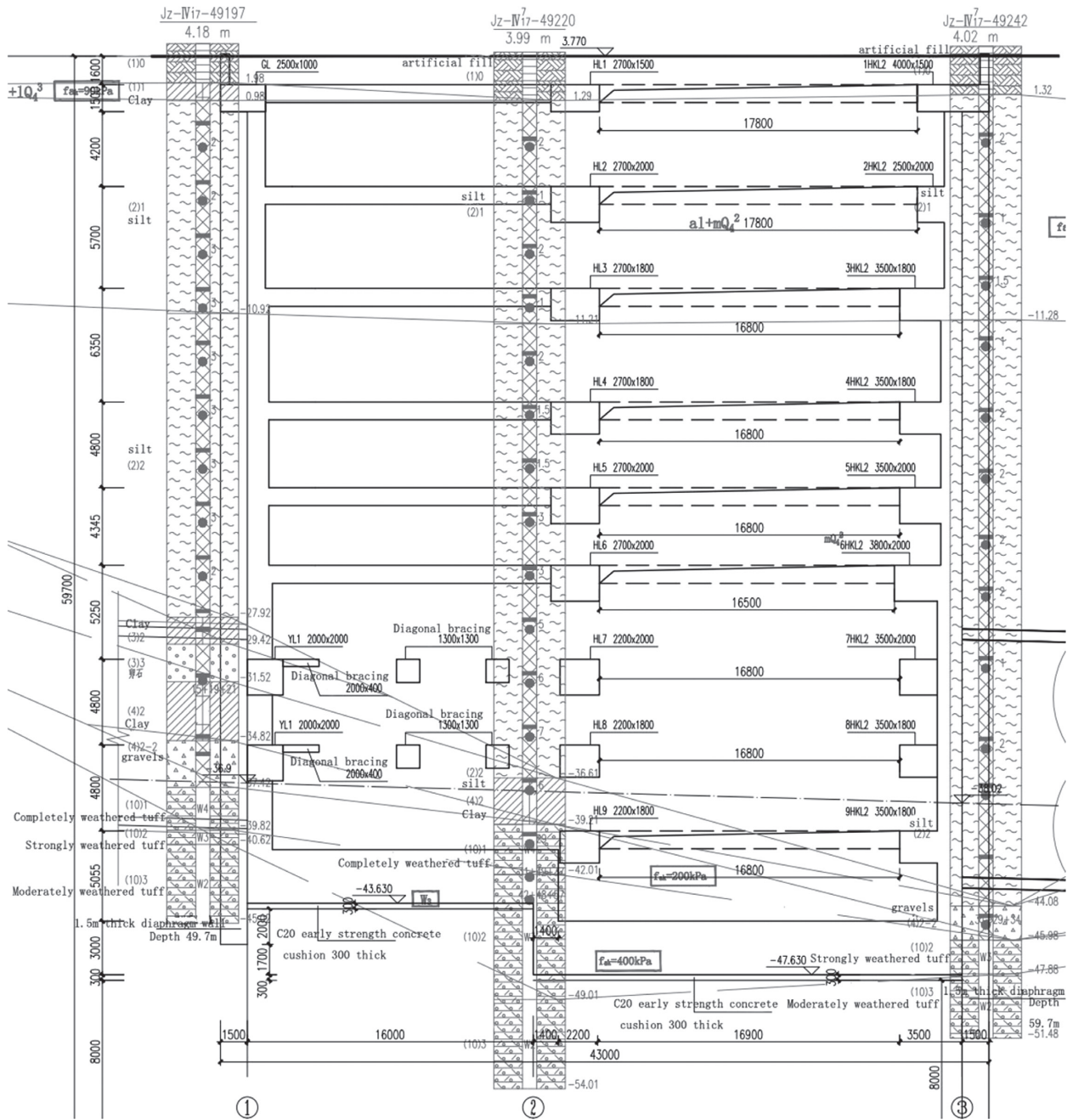
Figure 2: Section diagram of foundation pit supporting structure.

modulus is equal to the tangent modulus and three times the compression modulus.)

3.1.3. Treatment Method of Inclined Strata.

According to the geological survey data, the inclined rock surface is diagonally inclined, and the slope of the rock surface is not uniform. It is difficult to model and simulate according to the actual trend, and there are too many irregular grid cells, leading to poor grid quality. When running on a low configuration computer, the calculation process is very slow. In order to meet the needs of simulation calculation, according to the rock surface depth around the foundation pit determined by

the investigation, after determining the depth of moderately weathered rock at the interface between the rock surface and the foundation pit, the rock surface trend inside the foundation pit is determined by the slope average method, and the rock surface trend outside the foundation pit is extended according to the slope inside the foundation pit to form the internal rock surface trend of the model. The size of the completed model is shown in Figure 1.

3.2. Selection of Structural Elements and Material Parameters.

The supporting structure of the deep foundation pit of the Beikou well is mainly the diaphragm wall, supporting plate,
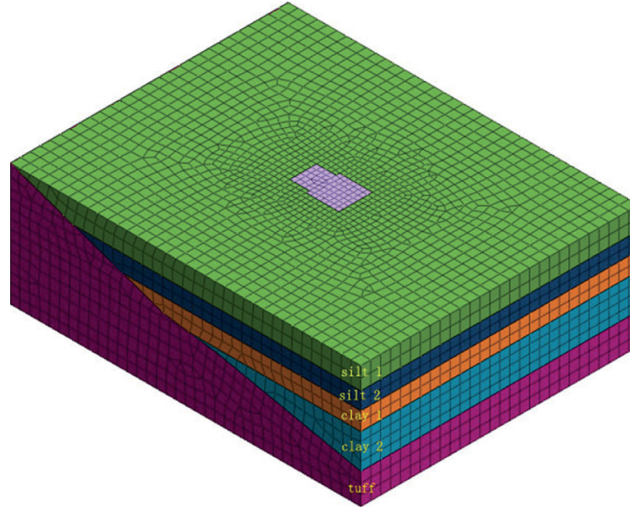
FIGURE 3: Overall calculation model of foundation pit.

TABLE 1: Material parameters of soil layer.

Number	Layer	Layer thickness (m)	Compression modulus (MPa)	Poisson's ratio	Unit weight (kN/m^3)	Cohesion (kPa)	Internal friction angle (°)
①	Silt 1	18	1.97	0.30	18	6.05	2.93
②	Silt 2	14	2.09	0.30	15	6.38	3.11
③	Clay 1	14.8	2.98	0.40	20	10.23	3.10
④	Clay 2	3.18	3.80	0.35	18	12.45	7.58
⑤	Tuff	1.65	500.00	0.30	23	20.00	33.00

and reinforced concrete ring frame beam (as shown in Figure 2). The elastic constitutive model is selected for all supporting structures, in which the diaphragm wall and each floor structure adopt a two-dimensional plate element, which is extracted from the three-dimensional solid element. The reinforced concrete ring frame beam is mainly flexural, and its length is larger than the cross-sectional area, so a one-dimensional beam element is adopted, which is extracted from the three-dimensional solid element. The material parameters of the supporting structure are shown in Table 2.

3.3. Boundary Conditions and Mesh Generation.

In the length direction (x-direction) of the model, the displacement of the X-axis is limited, that is, $u = 0$, $V \neq 0$, $w \neq 0$. In the width direction (Y-direction), the displacement of the Y-axis is limited, that is, $u \neq 0$, $v = 0$, $w \neq 0$. In the height direction (z-direction), the upper boundary of the model is free, i.e., unrestricted, and the lower boundary of the model is fully constrained, i.e., $u = 0$, $v = 0$, $w = 0$ (U is displacement in X-direction, V is displacement in Y-direction, and W is displacement in Z-direction).

Midas GTS provides two types of mesh generation: tetrahedral mesh and hybrid mesh. In this model, the hybrid grid is used. The mixed mesh is mainly hexahedron, with pentahedron and tetrahedron as the transition mesh. Compared with tetrahedral mesh, the hybrid mesh has better stability and higher accuracy. In addition, the number of meshes generated by hybrid mesh is far less than that generated by tetrahedron under the same cell size, which

greatly improves the calculation speed. Therefore, when the size of a large engineering model is larger, the hybrid mesh is usually used.

3.4. Determination of Simulated Construction Process.

The deep foundation pit is constructed by the top-down method. According to the design and construction technology of the foundation pit, the foundation pit excavation is simulated according to the actual technology. The foundation pit excavation is divided into 12 steps, and the specific construction process is shown in Table 3.

3.5. Determination of Simulation Conditions.

According to the needs of the project, the following two working conditions are determined for the study: ① suspended foot diaphragm wall; ② suspended foot to connect the wall, adding anchor lock foot. The construction process of condition ① is shown in Table 3 above. The first 11 steps of condition ② are the same as those of condition ①. The 12th step is the tenth excavation to −51.630 m, and the anchor rod and bottom plate are activated. According to the needs of simulation, the horizontal displacement, bending moment deformation, and surrounding ground settlement of the diaphragm wall are selected as the construction effect indexes.

3.6. Simulation Assumptions.

In this article, the outlet well foundation pit is selected, and the calculation model is established considering the surrounding soil. According to

TABLE 2: Material parameters of supporting structure.

Structure name	Element type	Constitutive model	Modulus of elasticity (kN/m^2)	Poisson's ratio	Unit weight (kN/ m^3)	Thickness/diameter (m)
Diaphragm wall	Plate	Elastic	32500000	0.2	24.5	1.5
Ring frame beam	Beam	Elastic	32500000	0.2	24.5	3.5 × 1.8
Top plate/middle plate	Plate	Elastic	32500000	0.2	24.5	0.4
Floor	Plate	Elastic	32500000	0.2	24.5	3

TABLE 3: Details of construction procedures.

Process number	Process node
1	The original stratum is established, and the initial stress is analyzed by applying boundary constraint and self-weight load
2	Activate diaphragm wall and clear displacement
3	The first excavation to −2.000 m, the first ring frame beam and roof was activated
4	The second excavation was to −7.700 m, and the second ring frame beam and the middle slab of the negative first floor were activated
5	After the third excavation to −13.400 m, the third ring frame beam and the middle slab of the second floor were activated
6	The fourth excavation to −19.750 m, the fourth ring frame beam and the negative third-floor slab were activated
7	The fifth excavation to −24.550 m, the fifth ring frame beam and the negative fourth-floor slab were activated
8	The sixth excavation was to −28.895 m, and the sixth ring frame beam and the middle slab of the fifth floor were activated
9	The seventh excavation was carried out to −34.145 m, and the seventh ring frame beam and the middle slab of the sixth floor were activated
10	The eighth excavation to −38.945 m, the eighth ring frame beam and the negative seventh-floor middle plate were activated
11	The ninth excavation was carried out to −43.575 m, and the ninth ring frame beam and the middle slab of the eighth floor were activated
12	The tenth excavation to −51.630 m, the floor was activated

the actual stratum situation and the calculation needs of the model, the following assumptions are made: ① the soil is isotropic and evenly distributed; ② the influence of the surrounding environment induced by diaphragm wall construction is not considered; ③ the influence of soil drainage consolidation and groundwater seepage is not considered.

4. Simulation Study on Construction Effect of Top-Down Construction Method for Foundation Pit with Suspended Foot Diaphragm Wall

In the original design scheme of Jiangbei working shaft foundation pit, the height of the diaphragm wall is 59.8 m, the thickness is 1.5 m, and the bottom of the diaphragm wall is at the same elevation. However, in the construction process, due to the high strength of moderately weathered rock, the construction speed of existing wall forming equipment is too slow to meet the requirements of the construction period, and the cost is too high. Through the discussion of experts, it is proposed to change the insertion mode of the in situ diaphragm wall into the design scheme of the suspended foot diaphragm wall, which is 2 m into the rock. The left wall (West wall) of the suspended foot diaphragm wall is 45.82 m long, and the right wall (east wall) is 51.98 m long (as shown in Figure 4). It can be seen from Table 3 that there are many excavation conditions, so the 1st,
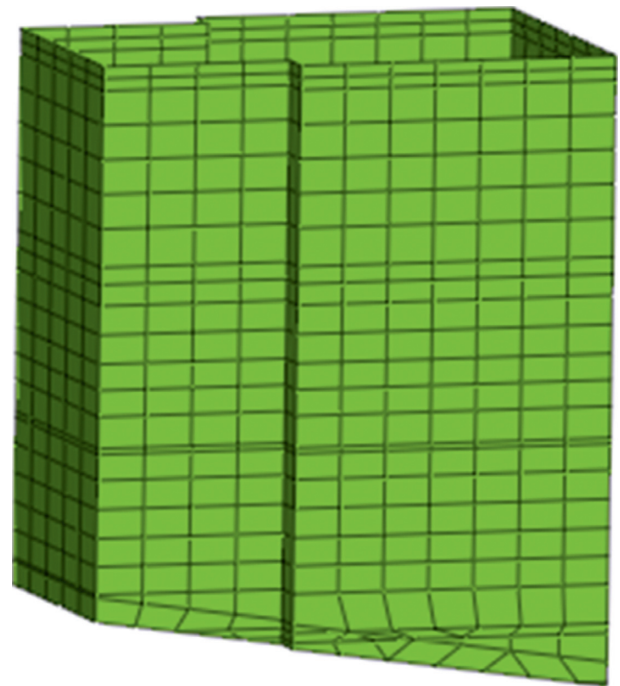
FIGURE 4: Schematic diagram of the ground connection wall the depth into rock is 2 m.

3rd, 5th, 7th, and 10th excavations (corresponding to process No. 3rd, 7th, 9th, and 12th in Table 3) are selected to study and analyze the foundation pit construction effect.

4.1. The Horizontal Displacement Analysis. The horizontal displacement contour plot of the diaphragm wall under five excavation conditions is shown in Figure 5. In the contour plot, the one on the left is the west wall, and the one on the right is the east wall (the same below).

After sorting and analyzing the data in Figure 5, we can get the relationship curve between the depth and displacement of the footed diaphragm wall (as shown in Figure 6) and combine the maximum horizontal displacement and depth data of the footed diaphragm wall into a table (as shown in Table 4).

It can be seen from Figure 6 and Table 4 that the horizontal displacement of the foot diaphragm wall is small in the first excavation. With the excavation of the foundation pit, the pouring of the middle plate structure, the support of the ring frame beam, and the horizontal displacement curve of the foot diaphragm wall are in the shape of "small at both ends, large in the middle." The maximum horizontal displacement of the diaphragm wall gradually moves down with the increase of excavation depth and finally locates above the excavation surface. The maximum horizontal displacement is about 7/10~3/4 times the final excavation depth of the foundation pit.

In addition, when the diaphragm wall is a suspender and the underlying strata are less embedded, the displacement and deformation of the end and bottom of the suspender diaphragm wall are larger. The maximum horizontal displacement of the east wall is larger than that of the west wall, which is due to the existence of inclined rock surface. The displacement and deformation law of the east and west walls is asymmetric, and the maximum horizontal displacement position gradually moves down with the excavation condition.

4.2. Bending Moment Analysis. The bending moment contour plot of the diaphragm wall under five excavation conditions is shown in Figure 7.

By sorting and analyzing the data in Figure 7, the relationship curve between depth and bending moment of the hanging foot ground connecting wall can be obtained, as shown in Figure 8, and the maximum bending moment and depth data of the hanging foot ground connecting wall can be summarized into a table, as shown in Table 5.

It can be seen from Figure 7 and Table 5 that the bending moment of the diaphragm wall is small in the first excavation, and there is a reverse bending point. With the progress of excavation, the bending moment of the diaphragm wall increases gradually and then decreases slightly in the final excavation stage. In each excavation stage, the maximum positive bending moment of the diaphragm wall is larger than the maximum negative bending moment. The maximum positive bending moment of the diaphragm wall is about 7/10~3/4 times the final excavation depth of the foundation pit, and the maximum negative bending moment is about 4/5~19/20 times the final excavation depth of the foundation pit.

In addition, the maximum positive bending moment is larger than the maximum negative bending moment in each excavation stage. The position of the maximum positive bending moment of the east and west walls first moves down and then rises and then remains unchanged after the original position. The position of the maximum negative bending moment does not change with the change of the excavation stage (except for the tenth excavation of the east wall). Due to the existence of inclined strata, the maximum bending moment of the east wall is larger than that of the west wall in each excavation stage (except for the negative bending moment of the tenth excavation), and the deformation law of the east wall and the west wall is basically the same but asymmetric.

4.3. Analysis of Surface Subsidence. The contour plot of soil surface settlement under five excavation conditions is shown in Figure 9.

By sorting and analyzing the data in Figure 9, the relationship curve between surface settlement and distance from foundation pit can be obtained, as shown in Figure 10, and the data of maximum surface settlement position can be summarized into a table, as shown in Table 6.

Through comprehensive analysis of Figures 9 and 10 and Table 6, the following conclusions can be obtained:

(1) During the first excavation, the surface settlement of the soil is very small. The maximum surface settlement of the soil on the east and west sides is about 0.5 mm. The maximum settlement is located 10 m away from the edge of the foundation pit, and the settlement beyond 20 m is almost zero.

(2) During the third excavation, the soil surface settlement increased, and the maximum settlement was about 4.0~4.5 mm. The soil surface settlement position changed, all located 15 m away from the edge of the foundation pit, and the soil surface settlement outside 60 m was small.

(3) During the fifth excavation, the surface settlement of the soil continued to increase, and the maximum surface settlement was about 11.5 mm, an increase of about 1.8 times that of the third excavation, which was consistent with the sudden increase of the horizontal displacement and a bending moment of the diaphragm wall during the fifth excavation. Due to the deformation law of the diaphragm wall, the surface also had a large settlement. The maximum surface settlement positions of the soil on the east and west sides changed and were located away from the foundation at 20 m around the pit; the surface settlement of soil mass beyond 80 m is about 0.8~0.9 mm.

(4) During the seventh excavation, the soil surface settlement continues to increase with a small increase. The maximum surface settlement of the soil is about 14.0~15.0 mm, the maximum surface settlement position remains unchanged (20 m in the west and 20 m in the east), and the surface settlement outside 85 m is about 0.8~0.9 mm.
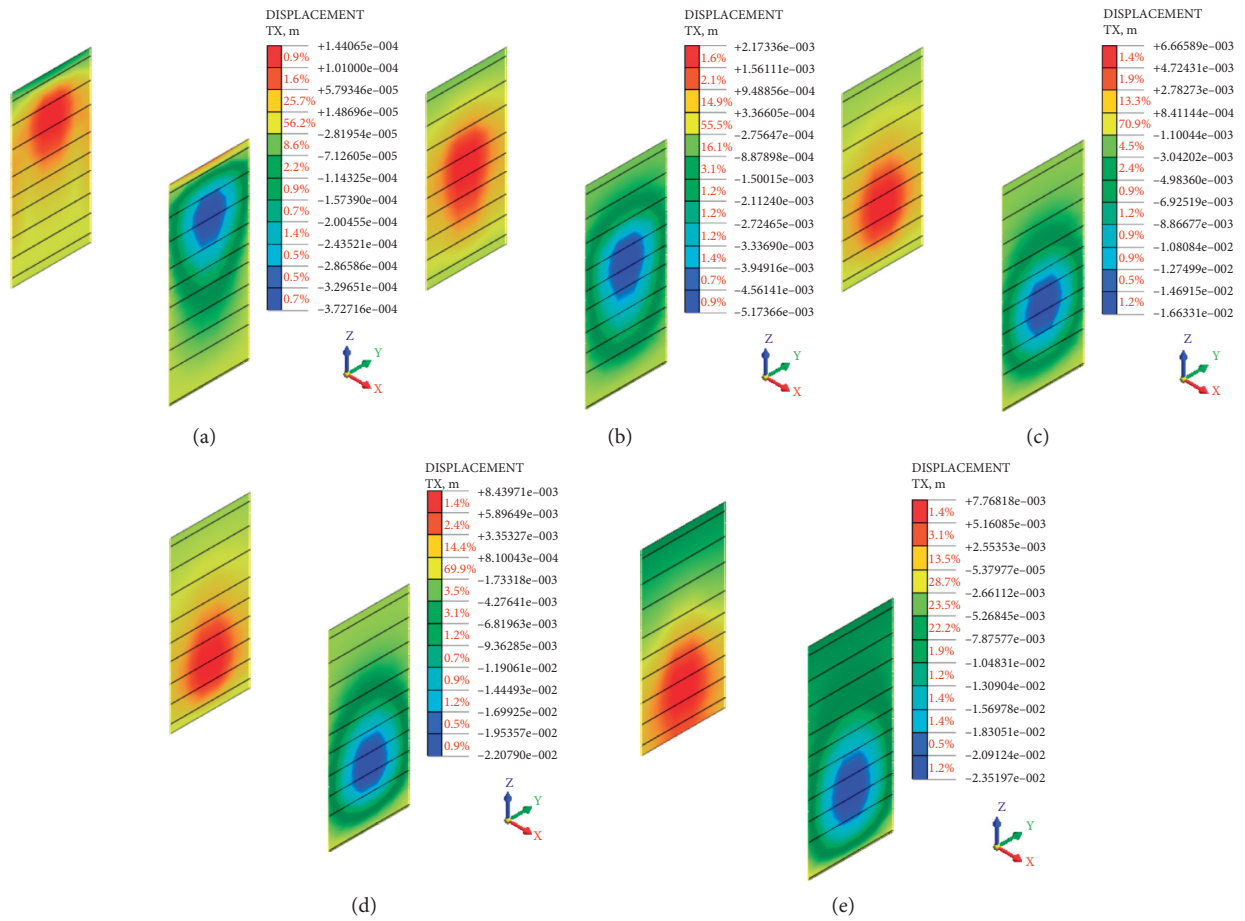
FIGURE 5: Horizontal displacement contour plot of suspended diaphragm wall under five excavation conditions. (a) First excavation, (b) third excavation, (c) the fifth excavation, (d) the seventh excavation, and (e) the tenth excavation.
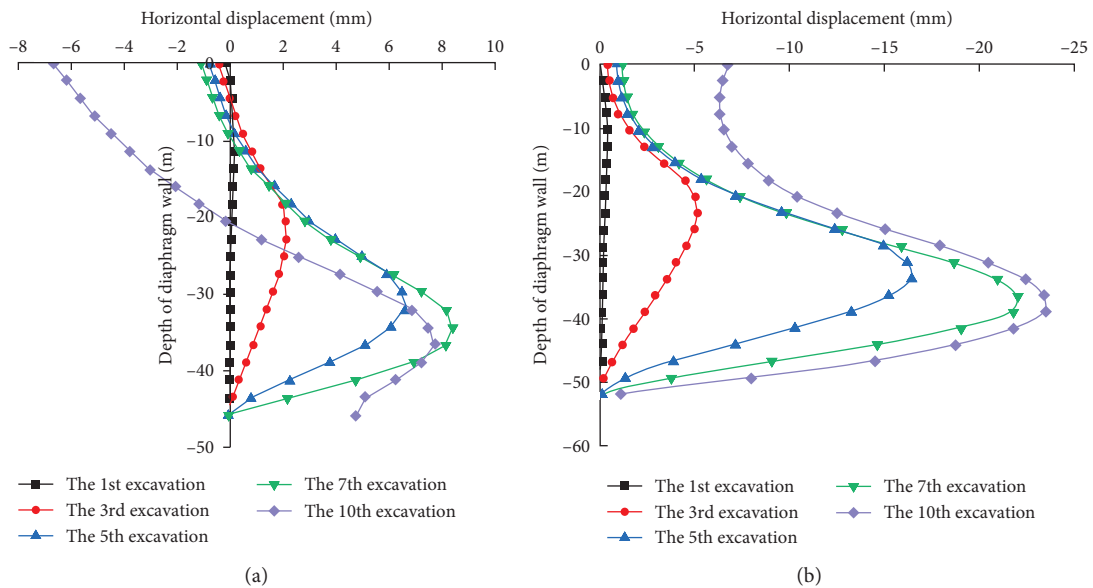
FIGURE 6: The relation curve of depth horizontal displacement of the foot diaphragm wall. (a) The west wall and (b) the east wall.

TABLE 4: Summary of the corresponding depth of the maximum horizontal displacement of the suspended foot connected wall.

Working procedure	Suspended foot diaphragm wall (west, the length is 45.82 m)		Suspended foot diaphragm wall (east, the length is 51.98 m)	
	Maximum horizontal displacement (mm)	The depth of the diaphragm wall (m)	Maximum horizontal displacement (mm)	The depth of the diaphragm wall (m)
The first excavation (−2.000 m)	0.141	−11.46	−0.371	−13.00
The third excavation (−13.400 m)	2.146	−22.91	−5.170	−23.39
The fifth excavation (−24.550 m)	6.613	−32.07	−16.490	−33.79
The seventh excavation (−34.145 m)	8.418	−34.37	−22.006	−36.39
The tenth excavation (−51.630 m)	7.738	−36.66	−23.497	−38.99
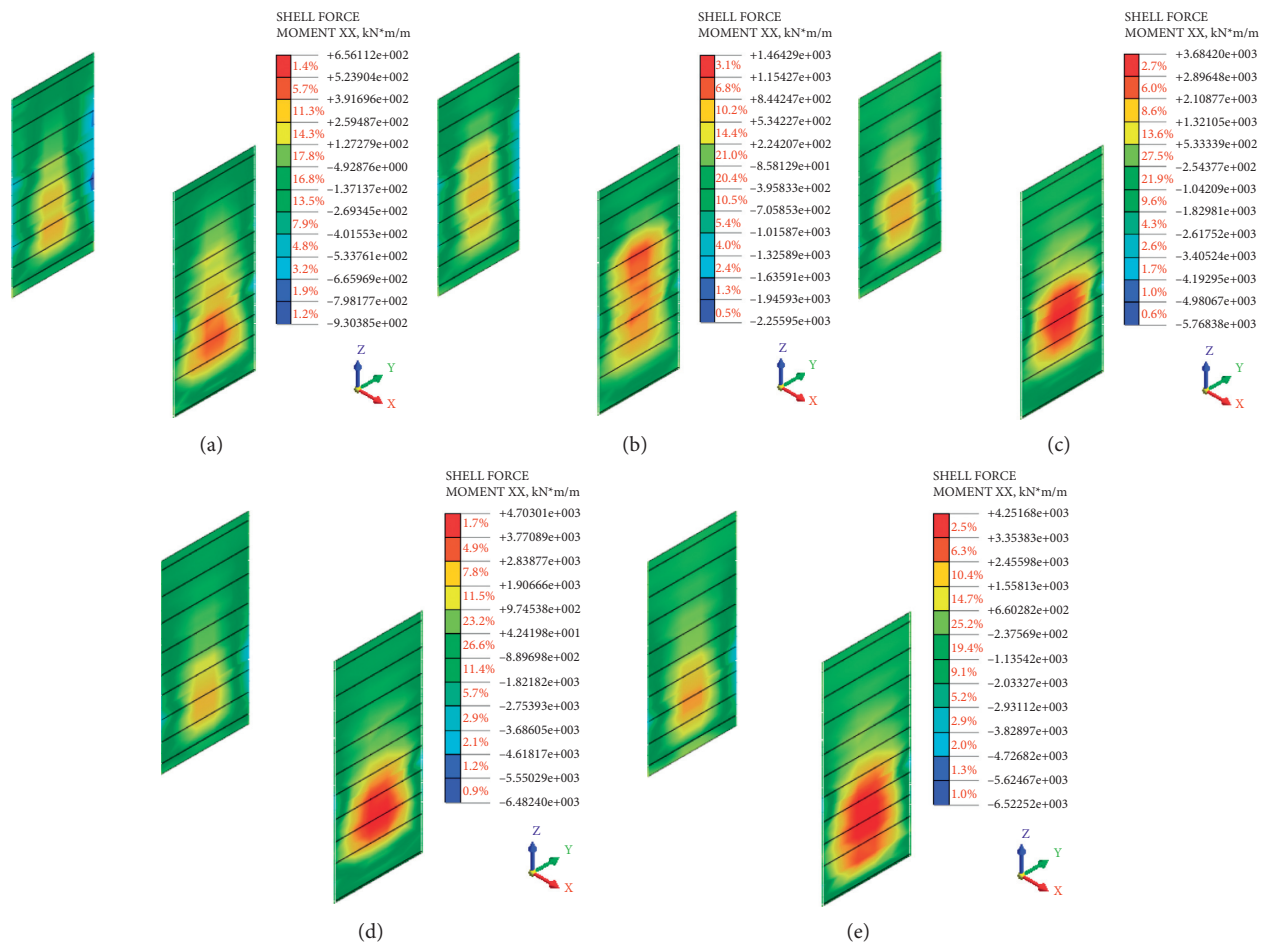
FIGURE 7: The bending moment contour plot of suspended diaphragm wall under five excavation step conditions. (a) The first excavation step, (b) the third excavation step, (c) the fifth excavation step, (d) the seventh excavation step, and (e) the tenth excavation step.

(5) After the tenth excavation, the surface settlement of soil continued to increase, the maximum surface settlement of soil was about 18.4 mm, and the location of the maximum surface settlement changed (the west side is 15 m and the east side is 15 m). The maximum surface settlement is about 0.036% of the excavation depth of the foundation pit of 51.630 m, about 78% of the maximum horizontal displacement of the hanging foot ground connecting wall. The maximum surface settlement is located 15 m away from the edge of the foundation pit, about 0.3 times the excavation depth of the foundation pit of 51.630 m.
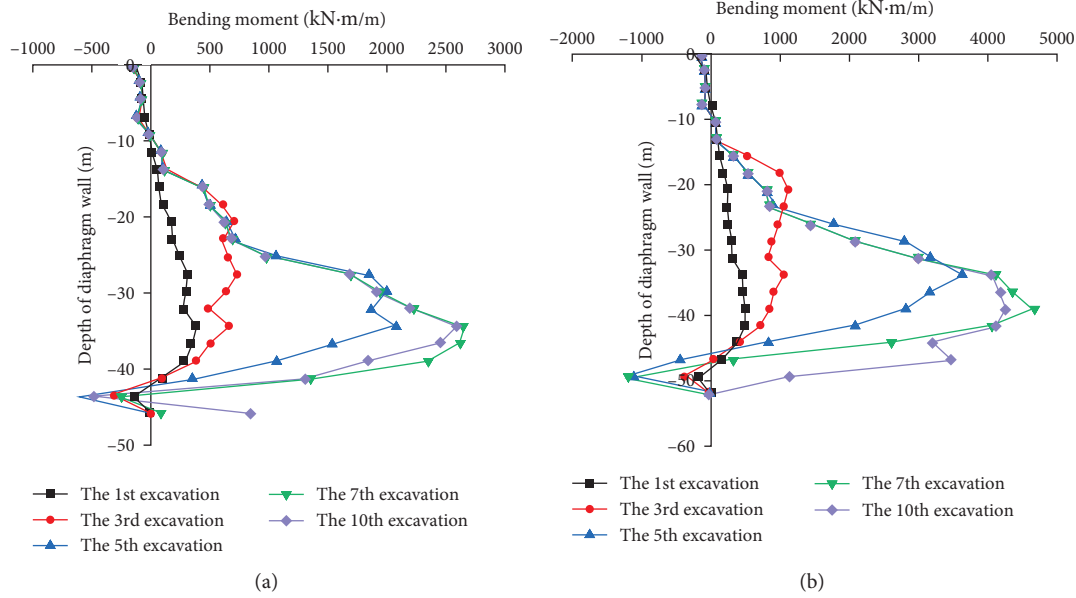
FIGURE 8: The relation curve between depth and horizontal displacement of the foot diaphragm wall. (a) The west wall and (b) the east wall.

TABLE 5: Summary of the corresponding depth of the maximum bending moment of the suspended foot connecting wall.

Working procedure	Suspended foot diaphragm wall (west, the length is 45.82 m)		Suspended foot diaphragm wall (east, the length is 51.98 m)	
	Maximum bending moment (kN•m/m)	The depth of the diaphragm wall (m)	Maximum bending moment (kN•m/m)	The depth of the diaphragm wall (m)
The first excavation (−2.000 m)	383.553/−154.641	−34.37/−43.53	495.496/−183.378	−38.99/−49.38
The third excavation (−13.400 m)	732.862/−311.066	−27.49/−43.53	1127.781/−404.225	−20.79/−49.38
The fifth excavation (−24.550 m)	2080.852/−600.905	−34.37/−43.53	3621.628/−1118.857	−33.79/−49.38
The seventh excavation (−34.145 m)	2654.072/−250.395	−34.37/−43.53	4654.927/−1193.643	−38.99/−49.38
The tenth excavation (−51.630 m)	2596.608/−469.726	−34.37/−43.53	4251.651/−42.949	−38.99/−51.98
Remarks	Among the maximum bending moments in the table, the maximum positive bending moment value is before "/" and the maximum negative bending moment value is after "/," respectively, corresponding to the depth of the diaphragm wall.			

(6) It can be seen from the above construction stages that the soil surface settlement curve in each construction stage first increases and then decreases with the distance from the edge of the foundation pit and finally tends to be stable, showing a "groove shape." According to the curve, the law of surface settlement and deformation on the east and west sides is basically the same. The maximum settlement position of the surface on the east and west sides is the same, which is finally located at 0.3 times the final excavation depth of the foundation pit, and the main influence area is about 1.5 times the final excavation depth of the foundation pit.

4.4. Simulation Study on the Influence of Embedded Depth of Foot Diaphragm Wall on Foundation Pit. In order to further

determine the relationship between the foot and the depth of rock in the foot diaphragm wall, the numerical simulation models of the foot diaphragm wall with the depth of 1 m and 4 m are established, respectively. The other setting conditions are completely consistent with the depth of 2 m. The maximum horizontal displacement, maximum bending moment, and maximum surface settlement of the foot diaphragm wall with different depths of rock are obtained and summarized into a table (as shown in Table 7).

The following can be seen from Table 7:

(1) The results show that the horizontal displacement, bending moment, and surface settlement of the diaphragm wall decrease with the increase of the depth of the diaphragm wall.

(2) When the depth of the suspended footed diaphragm wall increases from 1 m to 2 m, the horizontal

FIGURE 9: The contour plot of surface settlement under five excavation step conditions. (a) The first excavation step, (b) the third excavation step, (c) the fifth excavation step, (d) the seventh excavation step, and (e) the tenth excavation step.

displacement of the suspended footed diaphragm wall decreases by 0.916 mm and 0.975 mm for every 1 m increase. When the rock depth increases from 2 m to 4 m, the horizontal displacement and surface settlement decrease by 0.470 mm and 0.578 mm for each 1 m increase. When the rock depth increases from 1 m to 4 m, the bending moment of the diaphragm wall decreases gradually.
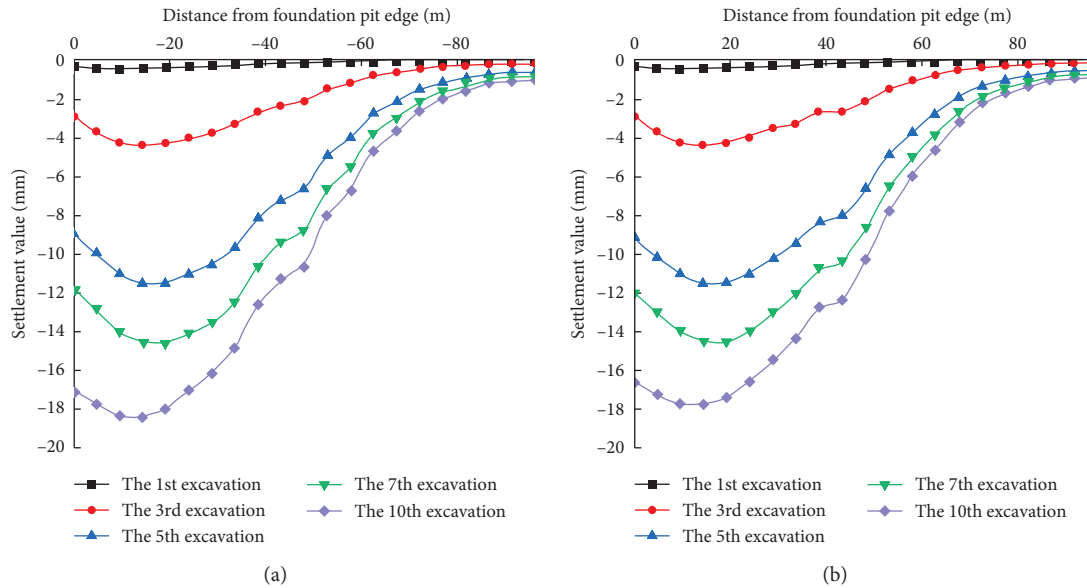
FIGURE 10: The curve of surface subsidence. (a) The west wall and (b) the east wall.

TABLE 6: Summary of the corresponding position of the maximum subsidence of the surface.

Working procedure	External surface of foundation pit (west)		External surface of foundation pit (east)	
	Maximum settlement (mm)	Distance from foundation pit edge (m)	Maximum settlement (mm)	Distance from foundation pit edge (m)
The first excavation (−2.000 m)	−0.459	10.00	−0.476	10.00
The third excavation (−13.400 m)	−4.385	15.00	-4.393	15.00
The fifth excavation (−24.550 m)	−11.511	20.00	−11.511	20.00
The seventh excavation (−34.145 m)	−14.621	20.00	−14.526	20.00
The tenth excavation (−51.630 m)	−18.419	15.00	−17.778	15.00

(3) Through the analysis of the data, it can be seen that the increase of the depth of the foot diaphragm wall into the rock can effectively reduce the deformation of the foundation pit. However, when the depth of the rock increases to a certain extent, the effect of continuing to increase the depth of the rock is no longer obvious, so on the premise of the safety and stability of the foundation pit and reducing the cost, this article selects the foot diaphragm wall foundation pit with the depth of 2 m into the rock to continue to optimize.

5. Simulation Study on Locking Reinforcement Scheme of Suspended Diaphragm Wall

In practical engineering, when the footwall is excavated below the footwall, the footwall may be separated from the rock, resulting in large displacement, affecting the stability of the foundation pit, so it is necessary to lock the footwall. According to the engineering experience, the reinforcement measures of the locking anchor are often adopted. Therefore, this article optimizes the reinforcement based on the depth (2 m) of the suspended foot diaphragm wall into the rock.

5.1. Design Parameters of Foot Bolt. According to the bolt design specification, the horizontal spacing of bolts should be greater than 1.5 m, and the mesh size of the foundation pit in the model is 4, which is greater than 1.5. The angle of the inclined anchor should be from 15 to 25, so the angle of the anchor should be 20, and the thickness of the overlying soil should be more than 4 m. The project is covered with soft clay about 46 m, and the bolt is a full grouting bolt with a length of 10 m. The anchor rod is arranged 1 m below the soil rock interface. The elastic constitutive model is selected for the bolt. Because the bolt ignores the bending deformation and mainly bears the axial force, the one-dimensional embedded truss element is used to directly divide the one-dimensional element, and the material parameters of the bolt are shown in Table 8. Other conditions are completely

TABLE 7: Summary of maximum deformation of foundation pit with different rock entry depths.

Rock penetration depth of foot diaphragm wall (m)	1	2	4
Horizontal displacement of foot diaphragm wall (mm)	−24.413	−23.497	−22.557
Bending moment of foot diaphragm wall (kN•m/m)	4697.035	4654.927	4285.135
Surface settlement (mm)	−19.394	−18.419	−17.263

TABLE 8: Anchor material parameters.

Structure name	Element type	Constitutive model	Modulus of elasticity (kN/m^2)	Poisson's ratio	Unit weight (kN/m^3)	Thickness/diameter (m)
Anchor	Embedded truss	Elastic	200000000	0.3	76.98	0.025

consistent with those of the suspended diaphragm wall (the model is shown in Figure 11).

5.2. Simulation Study on Construction Effect of Bolt Foot Locking and Foot Suspended Diaphragm Wall.

It can be seen from Table 3 that due to many excavation conditions, the 1st, 3rd, 5th, 7th, and 10th excavations (corresponding to the 3rd, 7th, 9th, and 12th processes in Table 3) are selected to study and analyze the construction effect of anchor bolt foot locking and foot suspended diaphragm wall foundation pit.

Here, it should be emphasized that since the horizontal displacement, bending moment, and surface settlement cloud pictures obtained by the simulation of the construction effect of the anchor bolt locking foot and the suspended foot diaphragm wall are similar to those of the suspended foot diaphragm wall, the simulation cloud pictures corresponding to the above three construction effect indexes are no longer displayed here.

5.2.1. Horizontal Displacement Analysis.

By sorting and analyzing the data in the horizontal displacement cloud diagram obtained from the simulation, the relationship curve between the depth and horizontal displacement of the anchor bolt foot hanger diaphragm wall can be obtained, as shown in Figure 12, and the maximum horizontal displacement and depth data of the anchor bolt foot hanger diaphragm wall can be summarized into a table, as shown in Table 9.

It can be seen from Figure 12 and Table 9 that the horizontal displacement of the anchor bolt locking foot suspended diaphragm wall is small in the first excavation. With the excavation of the foundation pit, the horizontal displacement curve of the suspended foot diaphragm wall is in the shape of "small at both ends and large in the middle." When the footed diaphragm wall is excavated to the bottom and separated from the rock stratum, adding bolt locking feet can effectively restrain the displacement and deformation of the end and bottom of the footed diaphragm wall, so as to reduce the overall horizontal displacement and deformation of the footed diaphragm wall. The maximum horizontal displacement of the east
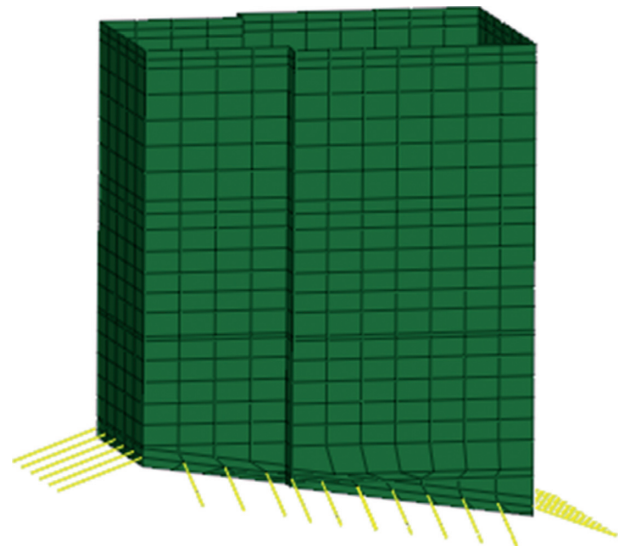
FIGURE 11: Schematic diagram of anchor lock foot suspended foot connecting wall model.

wall is larger than that of the west wall, which is due to the existence of inclined rock surface. The displacement and deformation law of the east and west walls is asymmetric, and the maximum horizontal displacement position gradually moves down with the excavation condition. The maximum horizontal displacement of the east wall is larger than that of the west wall, which is due to the existence of inclined rock surface. The displacement and deformation law of the east and west walls is asymmetric, and the maximum horizontal displacement position gradually moves down with the excavation condition. The maximum horizontal displacement of diaphragm wall moves downward with the increase of excavation depth, and finally above the excavation surface. The maximum horizontal displacement is about 7/10~3/4 times of the final excavation depth of foundation pit. Compared with the cantilever diaphragm wall, the increase of displacement is more stable. The bolt can effectively restrain the increase of displacement at the end and bottom of the diaphragm wall, and the restraint effect of the end displacement is more obvious.
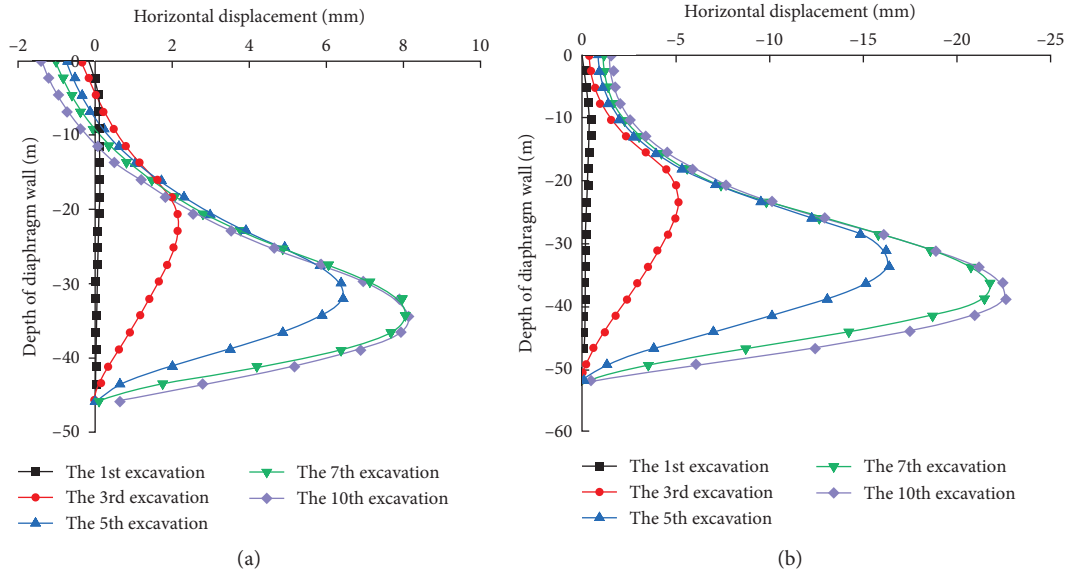
FIGURE 12: The horizontal displacement curve of anchor bolt locking foot suspended foot diaphragm wall. (a) The west wall and (b) the east wall.

TABLE 9: Summary of the corresponding depth of the maximum horizontal displacement of the anchor lock foot connecting wall.

Working procedure	Suspended foot diaphragm wall (west, the length is 45.82 m)		Suspended foot diaphragm wall (east, the length is 51.98 m)	
	Maximum horizontal displacement(mm)	The depth of the diaphragm wall(m)	Maximum horizontal displacement(mm)	The depth of the diaphragm wall(m)
The first excavation (−2.000 m)	0.142	−11.46	−0.371	−13.00
The third excavation (−13.400 m)	2.151	−22.91	−5.158	−23.39
The fifth excavation (−24.550 m)	6.463	−32.07	−16.400	−33.79
The seventh excavation (−34.145 m)	8.099	−34.37	−21.823	−36.39

5.2.2. The Bending Moment Analysis. By sorting and analyzing the data in the bending moment cloud diagram obtained from the simulation, the relationship curve between the depth and bending moment of the anchor bolt foot hanger diaphragm wall can be obtained, as shown in Figure 13, and the maximum bending moment and depth data of the anchor bolt foot hanger diaphragm wall can be summarized into a table, as shown in Table 10.

It can be seen from Figure 13 and Table 10 that the bending moment of the first excavation of the diaphragm wall with bolt locking and foot suspended is small, and there is a reverse bending point. With the progress of excavation, the bending moment of the diaphragm wall gradually increases, and then slightly decreases compared with the previous excavation stage. In each excavation stage, the maximum positive bending moment of the diaphragm wall is larger than the maximum negative bending moment. The maximum positive moment is larger than the maximum negative moment at each excavation stage. The location of the maximum negative moment of the east and west walls

does not change with the excavation stage. Due to the existence of inclined strata, the maximum positive bending moment of the east wall is larger than that of the west wall in each excavation stage, and the deformation law of the east wall and the west wall is basically the same, but asymmetric. The maximum positive bending moment of diaphragm wall is about 7/10~3/4 times of the final excavation depth of foundation pit, and the maximum negative bending moment is about 4/5~19/20 times of the final excavation depth of foundation pit. Compared with the suspended diaphragm wall, the anchor can effectively control the bending moment deformation of diaphragm wall, especially the bottom bending moment deformation of diaphragm wall.

5.2.3. Analysis of Surface Subsidence. By sorting and analyzing the data in the simulated surface settlement cloud map, the curve of surface settlement distance from the foundation pit edge can be obtained, as shown in Figure 14, and the data of the location of the maximum surface
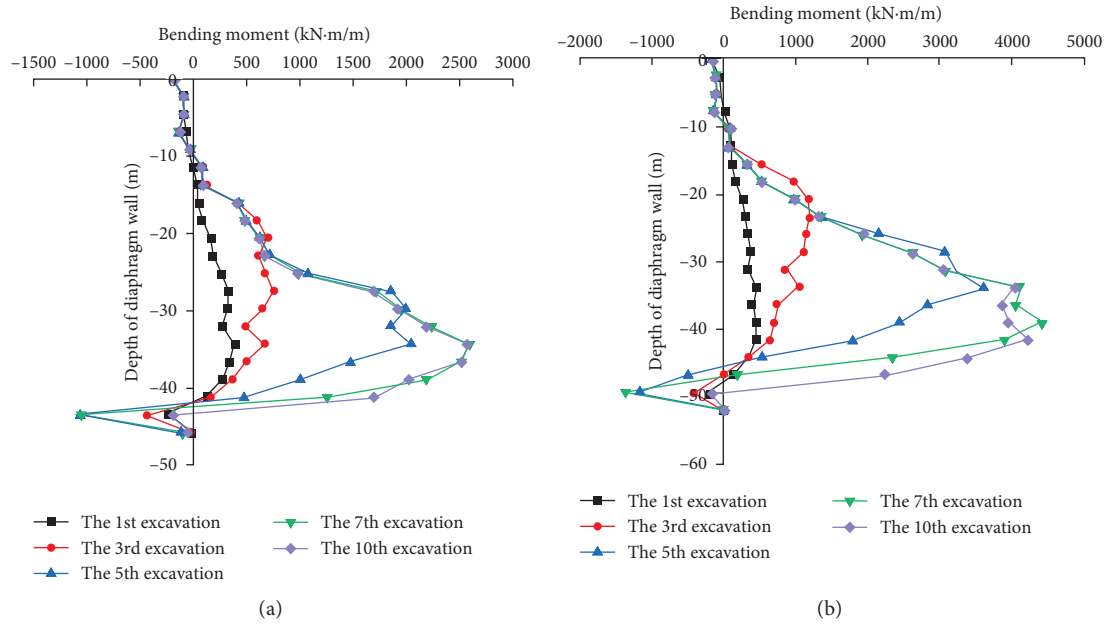
FIGURE 13: The bending moment curve of anchor bolt locking foot suspended foot diaphragm wall. (a) West wall, (b) east wall.

TABLE 10: Summary of the corresponding depth of the maximum bending moment of the anchor lock foot suspended foot connecting wall.

Working procedure	Suspended foot diaphragm wall (west, the length is 45.82 m)		Suspended foot diaphragm wall (east, the length is 51.98 m)	
	Maximum bending moment(kN•m/m)	The depth of diaphragm wall(m)	Maximum bending moment(kN•m/m)	The depth of diaphragm wall(m)
The first excavation(−2.000 m)	333.942/−230.579	−27.49/−43.53	460.319/−184.544	−33.79/−49.38
The third excavation(−13.400 m)	751.792/−436.294	−27.49/−43.53	1198.865/−414.313	−23.39/−49.38
The fifth excavation(−24.550 m)	2042.740/−1060.720	−34.37/−43.53	3626.023/−1160.760	−33.79/−49.38
The seventh excavation(−34.145 m)	2596.272/−1049.140	−34.37/−43.53	4425.413/−1356.545	−38.99/−49.38
The first excavation(−2.000 m)	2576.597/−191.356	−34.37/−43.53	4239.727/−168.822	−41.58/−49.38
Remarks	Among the maximum bending moments in the table, the maximum positive bending moment value is before "/", and the maximum negative bending moment value is after "/", respectively corresponding to the depth of diaphragm wall.			

settlement can be summarized into a table, as shown in Table 11.

It can be seen from Figure 14 and Table 11 that the settlement of soil surface is small at the first excavation, but it increases gradually with the excavation. In each construction stage, the surface settlement curve of soil increases first, then decreases, and finally tends to be stable with the distance from the foundation pit edge, showing a "groove" curve, and the surface settlement deformation law of the east and west sides is basically the same. The maximum surface settlement is about 0.03% of the final excavation depth of the foundation pit, about 70% of the maximum horizontal displacement of the suspended foot diaphragm wall. The maximum surface settlement is located at a distance of 15 m from the edge of the foundation pit, about 0.3 times of the final excavation depth of the foundation pit, and the main

impact area is about 1.5 times of the final excavation depth of the foundation pit. Compared with the suspended foot diaphragm wall, the anchor rod controls the surface settlement to a certain extent.

5.3. Simulation Study on the Influence of Different Anchor Positions of Lock Foot on Foundation Pit. In order to further determine the relationship between the reinforcement effect of anchor foot and anchor position, the model of anchor position at the soil rock interface is established. Other setting conditions are consistent with the standard model. The maximum horizontal displacement, maximum bending moment and maximum surface settlement of foundation pit at different anchor positions are obtained and summarized into a table, as shown in Table 12.
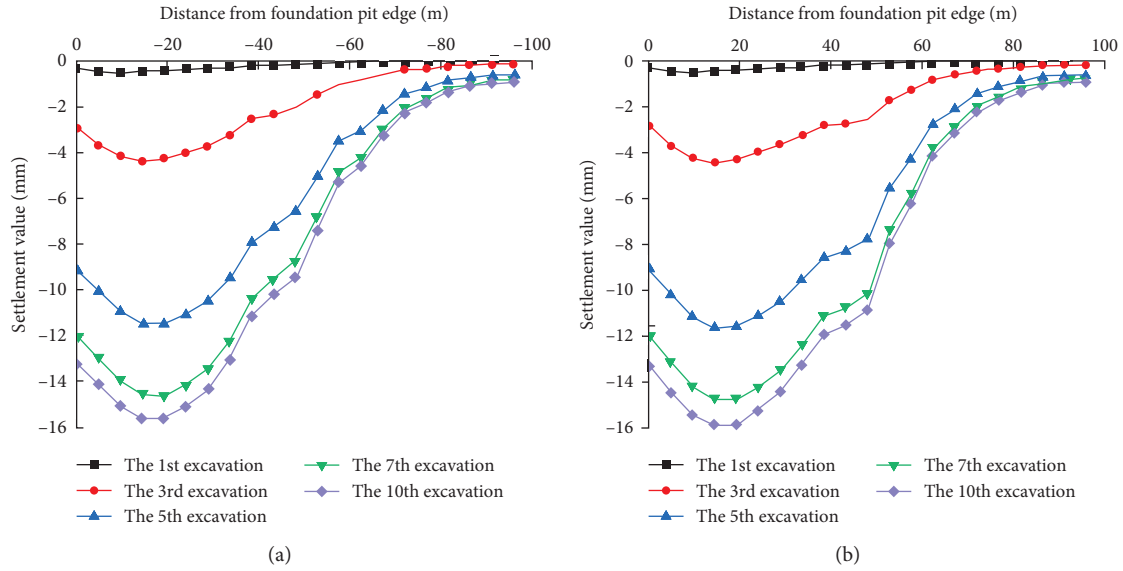
FIGURE 14: The curve of surface subsidence. (a) West wall, (b) east wall.

TABLE 11: Summary of the corresponding position of the maximum subsidence of the surface.

Working procedure	External surface of foundation pit (west)		External surface of foundation pit (east)	
	Maximum settlement (mm)	Distance from foundation pit edge (m)	Maximum settlement (mm)	Distance from foundation pit edge (m)
The first excavation(−2.000 m)	−0.467	10.00	−0.482	10.00
The third excavation(−13.400 m)	−4.380	15.00	−4.369	15.00
The fifth excavation(−24.550 m)	−11.468	20.00	−11.594	15.00
The seventh excavation(−34.145 m)	−14.601	20.00	−14.741	15.00
The first excavation(−2.000 m)	−15.600	20.00	−15.913	15.00

TABLE 12: Summary of maximum deformation of foundation pit with different anchoring positions.

Anchor position of lock foot	The interface between soil and rock	1 m below the interface between soil and rock
Horizontal displacement of diaphragm wall (mm)	−23.494	−22.665
Bending moment value of diaphragm wall(kN•m/m)	4668.444	4425.413
Surface settlement (mm)	−18.224	−15.913

It can be seen from Table 12 that as followings:

(1) The horizontal displacement, bending moment and ground settlement of the diaphragm wall decrease with the downward movement of the anchor position.

(2) Through the analysis of the data, it can be seen that the anchor can effectively reduce the deformation of the foundation pit, but if the anchor position is not set reasonably, it will not only not achieve the goal of effectively reducing the deformation, but also increase the cost. Therefore, on the premise of ensuring the safety and stability of the foundation pit, the anchor position should be selected properly. Therefore, based

on the analysis of the simulation results and the reality, this paper selects 1 m below the interface between soil and rock as the anchorage position.

6. Comparative Analysis of Simulation Results of Diaphragm Wall Construction Effect under Different Working Conditions

6.1. Comparative Analysis of Horizontal Displacement of Diaphragm Wall. After sorting and analyzing the data in the horizontal displacement contour plot of diaphragm wall during the 10th excavation (i.e. the foundation pit is excavated to the bottom) under two working conditions, the

depth-displacement curve of diaphragm wall under two working conditions can be obtained, as shown in Figure 14, and the maximum horizontal displacement and depth data of diaphragm wall under two working conditions can be summarized into a table, as shown in Table 13.

It can be seen from Figure 15 and Table 13 that the 10th excavation entered into moderately weathered rock stratum with high strength. In case 1, the maximum horizontal displacement of the west wall is 8.256 mm, which is at the depth of −32.89 m. The maximum horizontal displacement of the east wall is −22.341 mm, which is located at the depth of −38.87 M. In case 2, the maximum horizontal displacement of the west wall is 7.738 mm at the depth of −36.66 m. The maximum horizontal displacement of the east wall is −23.497 mm, which is located at the depth of −38.99 m.

From the comparison of the two working conditions, it can be seen that the maximum horizontal displacement of the west wall is reduced by 0.518 mm, the maximum horizontal displacement of the east wall is increased by 1.156 mm, the horizontal displacement of the end and bottom of the diaphragm wall is increased suddenly, and the stability of the diaphragm wall is poor, which is due to the large horizontal displacement and deformation due to the lack of rock embedment in working condition 2, Therefore, the horizontal displacement of condition 2 is larger than that of condition 1, and the maximum horizontal displacement of condition 2 moves down.

6.2. The Bending Moment Analysis of Diaphragm Wall. By sorting and analyzing the data in the bending moment contour plot of diaphragm wall during the 10th excavation (i.e. the foundation pit is excavated to the bottom) under two working conditions, the depth bending moment curve of diaphragm wall under two working conditions can be obtained, as shown in Figure 16, and the maximum bending moment and depth data of diaphragm wall under two working conditions can be summarized into a table, as shown in Table 14.

It can be seen from Figure 16 and Table 14 that the tenth excavation entered the moderately weathered rock stratum with high strength on the left and low strength on the right. In case 1, the maximum positive bending moment of the west wall is 2596.608 kN•m/m, which is located at the depth of −34.37 m. The maximum positive bending moment of the east wall is 4251.651 kN•m/m, which is located at the depth of −38.99 m. The maximum negative bending moment of the west wall is −469.726 kN•m/m, which is located at the depth of −43.53 m. The maximum negative bending moment of the east wall is −42.949 kN•m/m which is located at the depth of −51.98 m. In case 2, the maximum positive bending moment of the west wall is 2576.597 kN•m/m, which is located at the depth of −34.37 m; The maximum positive bending moment of the east wall is 4239.727 kN•m/m, which is located at the depth of −41.58 m. The maximum negative bending moment of the west wall is −191.356 kN•m/m, which is located at the depth of −43.53 m; The maximum negative bending moment of the east wall is −168.822 kN•m/m, which is located at the depth of −49.38 m.

From the comparison of the two working conditions, it can be seen that the maximum positive bending moment of the east wall and the west wall is reduced, the maximum negative bending moment of the west wall is reduced, and the maximum negative bending moment of the east wall is increased. There is a small negative bending moment at the bottom of the west wall, and the bending moment at the bottom of the east wall is almost zero. This is due to the important constraint of the anchor, which effectively reduces the maximum positive bending moment of the diaphragm wall and the bending moment at the bottom of the diaphragm wall, In case 2, the location of the maximum positive (negative) bending moment of the west wall remains unchanged, the location of the maximum positive bending moment of the east wall moves down, and the location of the maximum negative bending moment of the east wall moves up. In both cases, the maximum positive bending moment of the east and west walls appears above the excavation face, which indicates that the rock embedment in the diaphragm wall has a great constraint on the bending moment deformation of the diaphragm wall. The maximum positive moment of the two walls is larger than the maximum negative moment. Because of the existence of inclined rock, the maximum bending moment of the east wall is larger than that of the west wall.

6.3. Comparative Analysis of Ground Settlement of Diaphragm Wall. By sorting and analyzing the data in the contour plot of ground settlement of diaphragm wall soil mass during the 10th excavation (i.e. excavation to the bottom) under two working conditions, the curve of ground settlement distance from the edge of foundation pit under two working conditions can be obtained, as shown in Figure 17, and the data of maximum ground settlement position under two working conditions can be summarized into a table, as shown in Table 15.

It can be seen from Figure 17 and Table 15 that the tenth excavation entered the moderately weathered rock stratum. In case 1, the maximum settlement of the soil surface on the west side of the foundation pit is −18.419 mm, which is 15 m away from the side of the foundation pit; The maximum surface settlement of the east side soil is −17.778 mm, which is 15 m away from the side of the foundation pit. In case 2, the maximum settlement of the soil surface on the west side of the foundation pit is −15.600 mm, which is 20 m away from the side of the foundation pit; The maximum settlement of the east soil surface is −15.913 mm, which is 15 m away from the foundation pit. The maximum settlement of soil surface is about 15.0 mm. The maximum settlement of soil surface remains unchanged (15 m in the West and 20 m in the East). The maximum settlement of soil surface is about 0.029% of the excavation depth of 51.630 m and 67% of the maximum horizontal displacement of diaphragm wall. The maximum settlement of soil surface is 20 m away from the edge of foundation pit, It is about 0.4 times of the excavation depth of 51.630 m.

From the comparison of the two conditions, it can be seen that compared with condition 1, the maximum

TABLE 13: The corresponding depth of maximum horizontal displacement of diaphragm wall during the 10th excavation under two working conditions.

Working conditions	Diaphragm wall (west)		Diaphragm wall (east)	
	Maximum horizontal displacement (mm)	The depth of diaphragm wall(m)	Maximum horizontal displacement (mm)	The depth of diaphragm wall(m)
Suspended foot diaphragm wall (working condition 1)	7.738	−36.66	−23.497	−38.99
Suspended foot diaphragm wall (reinforcement) (Working condition 2)	8.143	−34.37	−22.665	−38.99
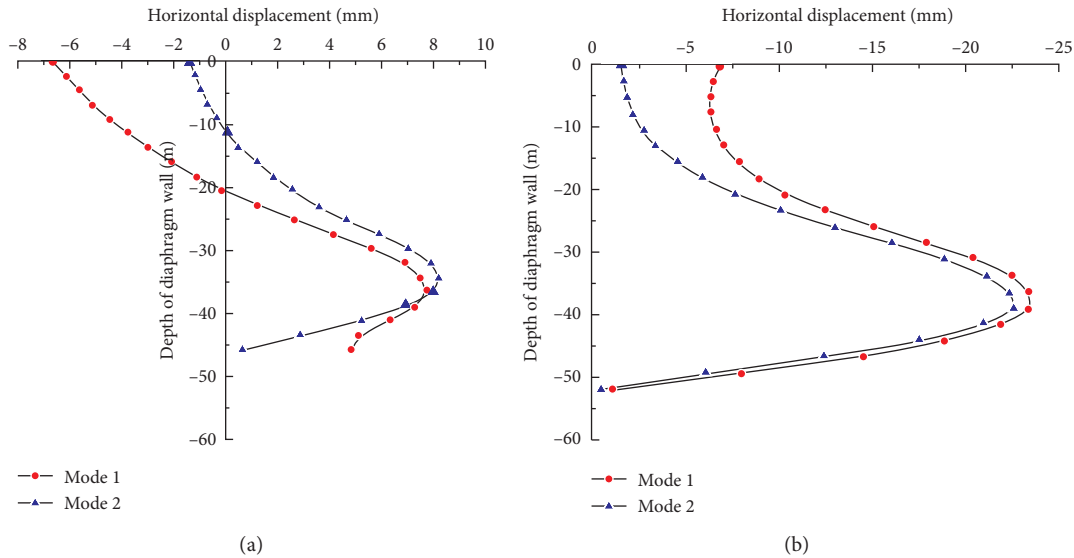
(a)

(b)

FIGURE 15: The horizontal displacement curve of diaphragm wall. (a) West wall, (b) east wall.

(a)

(b)
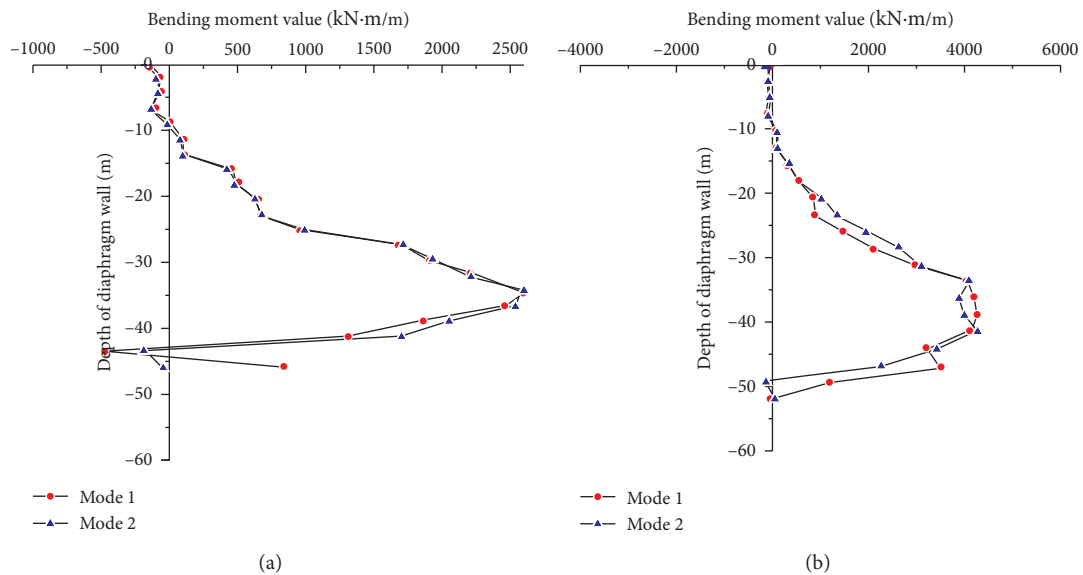
FIGURE 16: The bending moment diagram of diaphragm wall. (a) West wall, (b) east wall.

settlement of soil surface on both sides of the East and the West decreases by 1.5 ~ 3.0 mm in condition 2, which is due to the effective restraint effect of the anchor rod. The maximum settlement position of soil surface on the west side moves to 20 m away from the edge of the foundation pit, while the maximum settlement position of soil surface on the

TABLE 14: The corresponding depth of maximum bending moment of diaphragm wall during the 10th excavation under two working conditions.

Working conditions	Diaphragm wall (west)		Diaphragm wall (east)	
	Maximum bending moment(kN•m/m)	The depth of diaphragm wall(m)	Maximum bending moment(kN•m/m)	The depth of diaphragm wall(m)
Suspended foot diaphragm wall (working condition 1)	2596.608/−469.726	−34.37/−43.53	4251.651/−42.949	−38.99/−51.98
Suspended foot diaphragm wall (reinforcement) (Working condition 2)	2576.597/−191.356	−34.37/−43.53	4239.727/−168.822	−41.58/−49.38
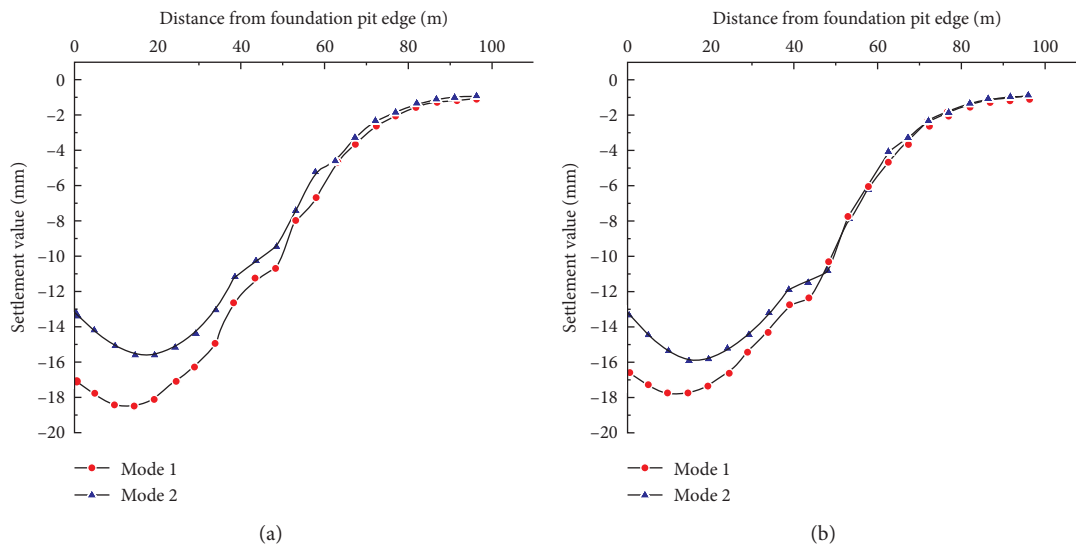
FIGURE 17: The curve of surface subsidence. (a) West wall, (b) east wall.

TABLE 15: Summary of corresponding positions of maximum ground settlement during the 10th excavation under two working conditions.

Working conditions	Diaphragm wall (west)		Diaphragm wall (east)	
	Maximum settlement (mm)	Distance from foundation pit edge (m)	Maximum settlement (mm)	Distance from foundation pit edge (m)
Suspended foot diaphragm wall (working condition 1)	−18.419	15.00	−17.778	15.00
Suspended foot diaphragm wall (reinforcement) (working condition 2)	−15.600	20.00	−15.913	15.00

east side remains unchanged. The results show that the settlement curves of soil surface under two conditions increase first, then decrease, and finally tend to be stable with the distance from the foundation pit edge, showing a "groove" curve, and the surface settlement deformation laws of the east and west sides are basically the same.

7. Conclusion

In this paper, numerical simulation method is used to study the construction effect of top-down construction method for deep and large foundation pit with underlying inclined rock surface. The horizontal displacement of diaphragm wall,

bending moment of diaphragm wall and ground settlement deformation of foundation pit with suspended foot diaphragm wall and anchor bolt locking foot diaphragm wall are analyzed respectively.

(1) When the foundation pit of hanging foot ground connecting wall is excavated by top-down construction method, the horizontal displacement curve of hanging foot ground connecting wall is in the shape of "small at both ends and large in the middle." With the excavation of the foundation pit, the position of the maximum horizontal displacement of the diaphragm wall gradually moves downward, and the maximum positive moment of the diaphragm

wall is greater than the maximum negative moment. The maximum surface settlement is located 15 m away from the edge of the foundation pit, which is about 0.3 times the final excavation depth of the foundation pit. The horizontal displacement, bending moment and surface settlement of the hanging foot diaphragm wall decrease with the increase of the rock depth. When the rock depth increases to a certain extent, the effect of continuously increasing the rock depth is no longer obvious. Therefore, in the actual project, the appropriate rock depth is selected on the premise of ensuring the safety of the foundation pit and reducing the cost.

(2) When the foundation pit is excavated by the top-down construction method, the horizontal displacement curve of the ground wall is in the shape of "small at both ends and large in the middle." Compared with the hanging foot ground wall, the displacement, bending moment deformation and surface settlement of the hanging foot ground wall are effectively controlled under the action of the anchor bolt. The horizontal displacement, bending moment value and surface settlement of the hanging foot diaphragm wall decrease with the downward movement of the anchor bolt anchorage position. The addition of anchor bolts can effectively reduce the deformation of the foundation pit, but the anchor position needs to be set reasonably, otherwise, it will not achieve the purpose of effectively reducing the deformation, but also increase the cost. Therefore, the anchor position should be properly selected on the premise of ensuring the safety and stability of the foundation pit.

Data Availability

The data used to support the findings of this study are available from the corresponding author upon request.

Conflicts of Interest

The authors declare that they have no conflicts of interest.

Acknowledgments

References

[1] Chinese Academy of Building Sciences, *Technical Specification for Building Foundation Pit Support: JGJ120-2012*, Chinese Academy of Building Sciences, Beijing, China, 2012, in Chinese.

[2] Y. Huang, W. Guo, H. Xiong, and Y. Xiao, "Waterproofing construction technology for underground engineering of large complex," *China Building Waterproofing*, no. 13, pp. 37–41, 2016, in Chinese.

[3] R. N. Hwang, B. S. Chen, T. E. Wu, and S. W. Duann, *Damage to a Metro Tunnel Due to Adjacent Excavation*, Springer, India, 2016.

[4] Y. Arai, O. Kusakabe, O. Murata, and S. Konishi, "A numerical study on ground displacement and stress during and after the installation of deep circular diaphragm walls and soil excavation," *Computers and Geotechnics*, vol. 35, no. 5, pp. 791–807, 2008.

[5] E. Pujades, J. Carrera, and E. Vázquez-SuÉ, "Hydraulic characterization of diaphragm walls for cut and cover tunnelling," *Engineering Geology*, vol. 125, pp. 1–10, 2012.

[6] W. Wang and J. Shen, "Design and analysis of "pile wall integration" of foundation pit retaining piles and basement external wall," *Journal of geotechnical engineering*, vol. 34, pp. 303–308, 2012, in Chinese.

[7] Y. Lou, "Retaining design and monitoring analysis of deep foundation pit on soft soil foundation," *Journal of Zhejiang water conservancy Shuitun college*, vol. 13, no. 3, pp. 7-8, 2001, in Chinese.

[8] M. S. Caspe, "Surface settlement adjacent to braced open cuts," *Journal of the Soil Mechanics and Foundations Division*, vol. 92, no. 4, pp. 51–59, 1966.

[9] C.-Y. Ou, B.-Y. Shiau, and I.-W. Wang, "Three-dimensional deformation behavior of the Taipei National Enterprise Center (TNEC) excavation case history," *Canadian Geotechnical Journal*, vol. 37, no. 2, pp. 438–448, 2000.

[10] C. Y. Ou, J. T. Liao, and H. D. Lin, "Performance of diaphragm wall constructed using top-down method," *Journal of Geotechnical and Geoenvironmental Engineering, ASCE*, vol. 124, no. 9, pp. 798–808, 1998.

[11] M. Long, "Database for retaining wall and ground movements due to deep excavation," *Journal of Geotechnical and Geoenvironmental Engineering, ASCE*, vol. 127, no. 33, pp. 203–224, 2001.

[12] X. Gong, E. song, and H. Guo, *Etc Example of Foundation Pit Engineering*, pp. 15–23, China Construction Industry Press, Beijing, China, 2006, in Chinese.

[13] T. C. Kung, "Comparison of excavation-induced wall deflection using top-down and bottom-up construction methods in Taipei silty clay-ScienceDirect," *Computers and Geotechnics*, vol. 36, no. 3, pp. 373–385, 2009.

[14] Z. Z. Aye, T. Boonyarak, N. Thasnanipan, and S. Chea, "Effects of cut-and-cover tunnel construction on adjacent piles of an overpass in Bangkok soft clay," in *Proceedings of the Fourth Geo-China International Conference*, Shandong, China, 25 July 2016.

[15] G. B. Liu, R. J. Jiang, C. Ng, and Y. Hong, "Deformation characteristics of a 38m deep excavation in soft clay," *Canadian Geotechnical Journal*, vol. 48, no. 12, pp. 1817–1828, 2011.

Research Article

Safety Risk Evaluation of Large and Complex Bridges during Construction Based on the Delphi-Improved FAHP-Factor Analysis Method

Teng Ji,[1] **Ji-Wei Liu,**[1] **and Qing-Fu Li** [2]

[1]*Powerchina Roadbridge Group Co., Ltd., Beijing 100048, China*
[2]*School of Water Conservancy Engineering Zhengzhou University, Zhengzhou 450001, China*

Correspondence should be addressed to Qing-Fu Li; lqflch@zzu.edu.cn

With the increase in construction scale and difficulty of large and complex bridges in China, it has become increasingly difficult to assess the safety risks of bridges during the construction period. Therefore, how to reasonably assess the safety risk of large, complex bridges during construction has become particularly important. Existing assessment methods are subjective in assigning weights, and it is difficult to select representative important factors to focus on for the prevention and control of numerous risk sources; they do not comprehensively consider the correlation of various risk sources during the construction period. To address the above shortcomings, a safety risk assessment of large and complex bridges during the construction period based on the Delphi-improved fuzzy analytic hierarchy process (FAHP) factor analysis method is proposed in this paper. First, the Delphi method was used to conduct a general survey of safety risk factors during the bridge construction period, and then the work breakdown structure-risk substructure (WBS-RBS) was used to establish the evaluation index system. Second, the improved FAHP was combined with it to calculate the weight of each risk factor. Finally, the factor analysis method was used to determine the correlation degree of each risk factor, and representative factors were selected to express the risk degree of the object to be evaluated to screen out major risk factors in the construction process. Finally, the feasibility and practicality of the method are verified by combining an actual engineering case with AHP (analytic hierarchy process) to perform a comparative study, which provides a reference basis for subsequent bridge construction risk prevention.

1. Introduction

In recent years, as China's demand for transport infrastructure has increased, the construction of bridges in China has accelerated accordingly, and construction locations have gradually shifted from mountainous to coastal areas. The construction of large and complex bridges in coastal areas is characterized by high construction difficulty, long construction times, and many uncontrollable factors. Because it involves marine operations, the building of these bridges leads to innovation in construction methods; coupled with the complex and changing environment of coastal areas, the construction conditions are harsher than in other environments, leading to greater difficulty in the construction of complex bridges. Therefore, the dangers of the constructing

complex bridges in coastal areas are greatly increased. Some scholars have pointed out that the risks faced by structures such as bridges during the construction period are much higher than those during the operational period [1, 2]. In addition, due to the influence of factors such as geology, hydrology, and construction complexity, bridge construction safety accidents occur frequently in China, resulting in very large numbers of casualties and a very large amount of property losses, as well as adverse effects on society. For example, according to the analysis of 84 collapse accidents of various engineering structures in the United States from 1977 to 1981, 21 of them occurred during the construction period, accounting for 25% of the total. Further, more than two-thirds of bridge collapse accidents that occurred in China from 1984 to 1988 occurred during the construction

period. This shows that there is a high risk during the construction of bridges, which must be given sufficient attention. Therefore, to ensure the quality of bridge construction and the safety of the construction process, it is necessary to analyze and study the safety risks during the bridge construction period and to correct and prevent the construction process and management steps with potential safety hazards to ensure the construction quality and safety. For example, adverse factors such as ship collisions, sea breezes, surge tide pressure, and deep marine accumulation of soft ground foundations exist.

Today, the domestic and international research on the construction period safety risk assessment of complex bridges in coastal areas is still in its infancy, and both theoretical research and practical application still need to be expanded. There are many risk factors in the construction period of complex bridges in coastal areas; for example, given adverse factors such as ship collisions, sea breeze, surge tide pressure, and deep marine accumulation of soft ground foundations, each factor is interrelated and dependent on each other, and the threat of hidden risk factors to the construction period is no less than that of explicit risk factors. The scientific identification method and evaluation analysis method are the basis of controlling the safety risk during the construction period. The main methods commonly used for risk evaluation are Monte Carlo simulation analysis [3], analytic hierarchy process (AHP) [4], Technique for Order Preference by Similarity to an Ideal Solution (TOPSIS) method [5], machine learning method [6, 7], triangular fuzzy number (TFN) and the AHP [8]. The idea of risk analysis originated in France and was first used in the insurance industry; in the 1950s, risk management was established as a separate discipline in the face of the threat of the nuclear industry. Risk analysis encompasses the risk assessment of things, and conducting safety risk assessment is beneficial in understanding the risk state of the structure and identifying specific risk source factors. A number of scholars have conducted studies on the safety risk assessment of large and complex bridges during the construction period. Peng [9] applied the integrated hierarchical analysis method and cloud model to propose a cluster decision-making method of cloud clustering to determine the main risk factors and risk losses by means of expert scoring and applied the cloud generator to calculate the numerical features of expert scoring to quantitatively assess bridge safety risks. Gong [10] summarized the risk factors for the bridge construction period, which are divided into internal factors, external factors, and human factors. Internal factors mainly include internal action, material properties, and geometric parameters, external factors include external temporary supports, natural climate, and external loads, and human factors mainly include management, design, construction, modeling, and statistics. Different factors will have different consequences according to their degree of influence, and when several risk factors cross each other, the probability of risk is greatly increased. Lai et al. [11] used the likelihood, exposure, criticality (LEC) method to select the potential risk, risk conditions, and triggers of the bridge structure construction period as risk indicators to calculate

the weights, used gray correlation theory to evaluate the risk in terms of risk occurrence probability and loss, and ranked the risk sources according to their indicators in order of merit to determine significant risk sources. The levels of risks at all levels were clarified, and the empirical study showed that the method effectively improved the evaluation accuracy of the evaluation model. Liu [12] applied a fuzzy comprehensive evaluation model to evaluate bridge construction safety risks based on the study of advanced risk management at home and abroad. Liu [13] combined the ant colony algorithm and BP neural network to optimize the model of the BP neural network for bridge construction period risk by using the ant colony algorithm. Yang et al. [14] established an assessment model based on extended belief rule base (EBRB) joint optimization for bridge risk assessment. The work first proposed the generation method and the approximate reduction method of the extended belief rule by introducing parameter optimization and data envelopment analysis, respectively; then, the joint optimization method of EBRB was proposed based on iterative optimization by linking these two methods together to ensure that the constructed EBRB has the optimal parameter values and number of parameters. Finally, the validity of the proposed model was tested by introducing a recognized dataset commonly used in the field of bridge risk assessment. The results showed that the proposed model can significantly improve the accuracy of bridge risk assessment. Khan et al. [15] proposed a framework for assessing bridge fire risk. Within this framework, each criterion, subcriterion, and alternative that may affect bridge fire risk is assigned a weight value based on its importance. Using AHP to determine the weights of different factors and validating the analysis with examples, the method can estimate the fire risk of a specific bridge in a region or the entire bridge network, which can help in the prevention and control of bridge risks. Regarding risk assessment models, Stewart [16] assessed the reliability of bridges based on risk levels and environmental analysis, which provides a better assessment model for the structural inspection of bridges. Yang et al. [17] developed a new disjunctive belief rule-based (DBRB) expert system for bridge risk assessment that takes BRB into account as a type of belief rule-based (BRB) system, thus overcoming the most common conjunctive belief rules (CBR) consisting of a BRB expert system with a combinatorial explosion problem. With the proposed dynamic parameter optimization model and improved differential evolution (IDE) algorithm, the DBRB expert system is complete and can obtain globally optimal parameter values for modeling bridge risks compared to the existing CBR and DBR-related parameter optimization models. Andric and Lu [18] combined fuzzy hierarchical analysis with fuzzy logic to propose a basic framework for bridge risk assessment and showed that both models can be effective in achieving bridge risk assessment.

Scientific assessment methods are an important part of safety risk evaluation and measure the accuracy of risk analysis. Although many scholars have conducted many theoretical and applied studies on bridge risk assessment, there are few studies on safety risk assessment during the construction period, which is much riskier than other

periods. In addition, existing studies have not considered the identification of dynamic risk sources as the most fundamental part of risk assessment, which is not conducive to reflecting the potential risk factors for bridge projects, and the assessment methods used are more subjective in assigning weights. It is difficult to select representative and important factors to focus on prevention and control for many risk sources without considering the correlation among risk sources during the construction period. The premise of risk assessment is identifying risk sources; however, there are many dynamic risk sources in the construction process that are gradually generated during the construction process. Some evaluation indices in the bridge construction process are fuzzy, and when using hierarchical analysis to determine the weight of the indices, the relative importance of each index cannot be determined at all. Factor analysis explains the meaning of each factor by using the idea of dimensionality reduction to study the interrelationships among many variables, find the truly correlated variables, and divide the variables with high correlation into one category, each of which represents a common factor. Its main function is to simplify the data, explain the relationship between the original variables, and emphasize the correlation between the variables. It is suitable for selecting representative factors from many risk factor indicators to express the degree of risk of the object to be evaluated. For large and complex bridge construction projects in coastal areas, it is difficult to conduct an accurate analysis using the existing risk assessment methods. Through an in-depth study of the special environment of coastal areas and the construction characteristics of large and complex bridges, this paper establishes a comprehensive analysis method based on the existing evaluation and analysis, including the Delphi method, improved FAHP, and factor analysis, and applies it to the analysis of safety risks during the construction period of large and complex bridges in coastal areas, taking the premise of risk source identification combined with the Delphi method for initial screening of risk sources and using improved FAHP for weight calculation of risk factors to reduce the influence of human subjective factors on weight values. Finally, the correlation between risk factors was analyzed using the factor analysis method, and construction projects with higher risk coefficients were determined, which improved the comprehensiveness and accuracy of the evaluation process.

The main contributions of this paper are as follows:

(i) The Delphi method and improved FAHP were used to identify and calculate the weight of risk sources during the construction period of large and complex bridges. By establishing a census list of risk sources and combining the Delphi method, the risk sources are scored, and the risk sources generated during the whole construction process can be considered.

(ii) The factor analysis method was proposed to assess the safety risks during the bridge construction period, and the factors with higher comparative risk levels were screened out, taking the correlation between the risk factors into full consideration.

(iii) The rationality and feasibility of the Delphi-improved FAHP factor analysis method were applied and studied on actual engineering cases, and a comparative study with AHP was performed to verify the applicability of the method, which provides a reference for the safety risk assessment of similar large and complex bridges during the construction period.

The rest of this paper is summarized as follows. Section 2 describes the methods used for safety risk evaluation during bridge construction and their risk identification process. Section 3 presents an applied study of the methods used in this paper with practical cases. Conclusions are given and discussed in Section 4. Figure 1 is a flowchart of the method used in this paper.

2. Identification Process and Methods

2.1. Identification of Risk Sources during Bridge Construction. There are many risk sources in the construction period of large and complex bridges, which are closely related to each other. The application of reasonable methods for screening can ensure the accuracy, scientific design, and effectiveness of construction safety risk assessment. These risk factors include the complex and not clear geological and hydrological environment in which the bridge is located, and foundation of the construction plan often has to change and replace the construction equipment due to sudden changes in geology and hydrology. The bridge foundation structure not only needs to bear the effect of large vertical loads, but also needs to directly bear the effect of large horizontal loads such as wind and waves, water currents, and ice pressure and faces greater risks in construction of bridges in coastal areas, as the construction conditions are more complicated. On the one hand, due to the large scope of the project itself, material supply, operating sites, and other factors and a wide range of construction vessels, it is easy to experience difficulties in the organization of the construction site. On the other hand, offshore construction is more affected by cold currents, waves, high winds, and other hydrological and meteorological influences, and risk events such as concrete pouring of bearing platforms and superstructure construction are increased. The main methods of risk identification mainly include expert scoring methods and checklist methods. However, due to the lengthy construction period and complex process of bridge construction, the potential risk sources are not static as the construction process gradually completes the bridge superstructure, substructure, bearings, and other structures. There will be dynamic risk sources, and so the above method for identification is more difficult, and it is difficult to exhaustively identify the risk sources. The Delphi method can concentrate the rich engineering experience of experts and thus effectively identify risks [19]. WBS-RBS was originally proposed by David Hilson, a leader in the field of PMI in the U.S. The basic principle is to decompose the risk source into two parts: the work breakdown structure (WBS) and the risk breakdown structure (RBS). When using the WBS-RBS system, it is
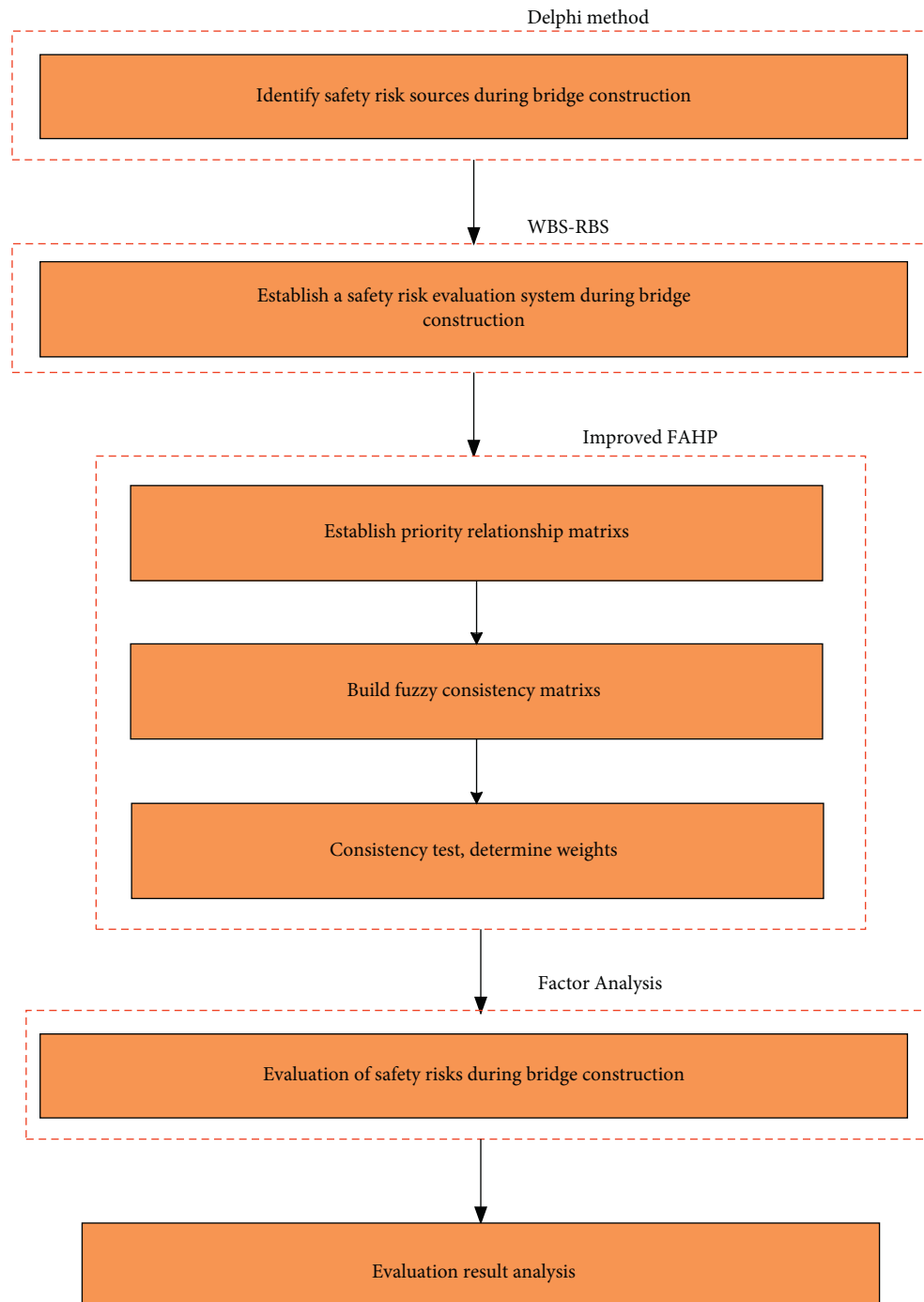
FIGURE 1: Flow chart of the method used in this paper.

possible to analyze any of the risk factors present in the construction process. In the lower part of the system, the work is further divided into more independent parts, called work units, which are theoretically more conducive to the analysis of subprojects. WBS-RBS is an engineering risk identification method that can be used to discern the overall picture of an engineering project but can also go into the specific details of engineering construction [20]. Based on these factors, this paper uses the Delphi method to identify risk sources and determines the main risk sources through expert assignment. Then, using WBS-RBS, each process is

decomposed and analyzed to identify the risk sources level by level to achieve the purpose of risk source identification.

2.1.1. Decomposition Structure of Bridge Construction Technology. The construction technology decomposition of large and complex bridges in coastal areas should consider not only the construction sequence, but also the formation mechanism of risk sources. Bridge engineering is a bottom-up structural system that includes the structural characteristics and construction sequences of bridges. Bridge

construction technology can be divided into foundation engineering, temporary engineering, tower column engineering, and beam slab engineering. The construction procedures for large and complex bridges are shown in Figure 2.

The risks of subprojects should be considered for specific project capacity and enter into the next level of project division, as shown by Table 1. When users decompose the construction process for other types of bridges, the analysis should be carried out in conjunction with the construction process of the bridge itself. For example, simply supported beam bridges can be divided into lower engineering, upper engineering, and auxiliary engineering.

2.1.2. Decomposition Structure of Bridge Construction Technology.

Different scholars use different risk classifications according to the characteristics of risk formation. Combined with the environmental characteristics of coastal areas, the division of safety risk factors for large and complex bridge construction should follow the principle of easy risk identification. Combined with the theory of system safety engineering and bridge construction engineering, the Delphi method was used to invite 15 experts from different fields, and after the experts' opinions about the classification of bridge construction risk factors were obtained, they were collated, summarized, counted, and anonymously fed back to each expert, and opinions were again sought, concentrated, and fed back, until a unanimous opinion was obtained. The expert questionnaire is shown in Table 2. When users conduct a survey of safety risk sources during the construction period of other types of bridges, the survey should be carried out in conjunction with the specific construction processes of the bridge; for example, the possible risk sources for the lower engineering of simply supported beam bridges are pile foundation construction, reinforcement cage tying, and welding.

Finally, the bridge construction risk factors can be divided into four types of risk sources: human, machine, material, and environment, thus dividing the bridge construction risk source system into four subsystems, human, machine, material, and environment, and establishing a WBS decomposition tree, where WBS refers to the identification of bridge construction risk sources as a general objective and is then decomposed into multiple independent units. The decomposition diagram is shown in Figure 3. Users can directly refer to the WBS decomposition tree based on the four categories of risk sources: human, machine, material, and environment.

Human factor risk refers to a source of risk from human error. The construction of the whole bridge project is a process that is dominated by people, mainly performing surveys, measurements, designs, construction, management, detection, and maintenance. Therefore, human error has the greatest impact on the entire bridge project.

Machine factor risk refers to the source of risk caused by mechanical failure. Mechanical failures include mechanical loss, mechanical aging, mechanical failure, mechanical mismatch, and insufficient mechanical production capacity.

For large bridge construction, human power is limited, and machinery is required to assist the construction. The quality of machinery directly determines the occurrence rate of safety incidents.

Material factor risk refers to the risk source formed by material factors. The materials here do not only refer to the reinforcement, cement, sand and gravel, asphalt, etc., required for the construction of bridges, but also include the temporary materials used, such as hanging baskets, grouting machines, supports, welds, cutting devices, and various kinds of spammers and other application tools. Materials are the pillars of the project, which directly affects the quality of the project. With the continuous innovation of the bridge structure situation and span, new materials and new technologies are always emerging for engineering applications. Therefore, the influence of the quality of materials in the construction process is becoming increasingly obvious.

Environmental factor risk refers to the risk source formed by environmental factors. Environmental risk sources include the natural environment and construction environment. The natural environment refers to the wind, rain, lightning, temperature, humidity, earthquakes, volcanoes, tsunamis, etc., at the project location. The construction environment refers to the convenience conditions that can be provided for construction based on existing technical conditions and capital level. All kinds of environmental factors in construction can affect the safety risk.

There are many risk factors in the construction period of large and complex bridges in coastal areas, and their influence degrees are different. The reasonable division of risk sources is an important part of safety risk assessment. Therefore, continuing to use the Delphi method, inviting experts from construction units, supervision units, design units, etc., and considering the four aspects of human, machine, material, and environment can determine the risk events that each risk source subsystem has. The results of the are expressed using RBS, where RBS refers to the decomposition of the four main factors of bridge construction safety risk into individual basic events. At this time, WBS is combined to obtain the factors affecting the risk sources of the bridge construction period, and the final results are shown in Table 3. The specific risk [11] sources of various risk factors are shown in Table 2. Users can create an RBS based on the division of risk events in the four areas of people, machines, materials, and environment that different types of bridges have during construction.

2.1.3. Identification of Risk Sources during Bridge Construction.

Combined with the construction process breakdown structure table and the risk sources of various risk factors, the project is reviewed item by item. First, the risk checklist, as shown in Table 4, is sent to the relevant technical personnel, including the main project leader, project construction personnel, project supervision personnel, experts, and scholars related to the project and public officials, for scoring and assignment. If more than 93% of the requested data are collected, the data source is considered
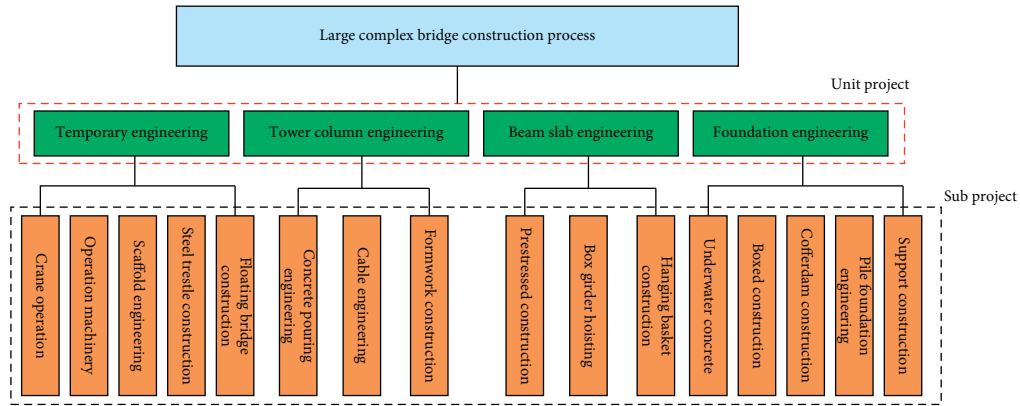
FIGURE 2: Organizational chart of construction procedures for large and complex bridges.

TABLE 1: Decomposition of the large complex bridge construction process.

Unit project	Subproject
Foundation engineering a_1	Support construction a_{11}, pile foundation engineering a_{12}, cofferdam construction a_{13}, boxed construction a_{14}, underwater concrete a_{15}
Temporary engineering a_2	Floating bridge construction a_{21}, steel trestle construction a_{22}, scaffold engineering a_{23}, operation machinery a_{24}, crane operation a_{25}
Tower column engineering a_3	Formwork construction a_{31}, cable engineering a_{32}, concrete pouring engineering a_{33}
Beam slab engineering a_4	Hanging basket construction a_{41}, box girder hoisting a_{42}, prestressed construction a_{43}

TABLE 2: Questionnaire on safety risk sources during bridge construction.

Project	Risk sources				Harmful consequences	Level of risk (please compare and quantify two by two)	Remarks
	Human factor	Machine factor	Material factor	Environmental factor			
...	...	...	...	...	...	...	...
...	...	...	...	...	...	...	...
...	...	...	...	...	...	...	...
Filler:			Proofreader:			Date of filling out the form:	
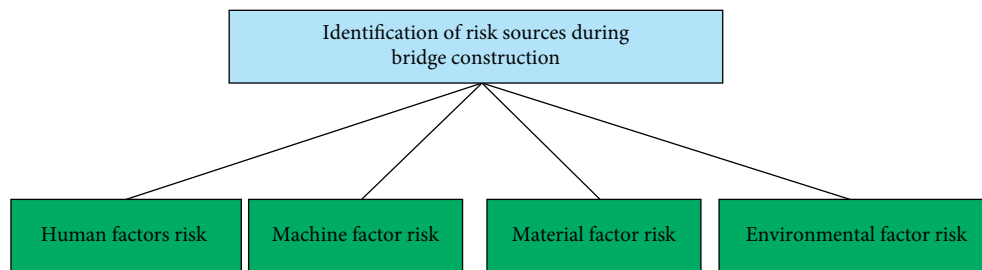
FIGURE 3: WBS decomposition of risk sources during bridge construction.

TABLE 3: Construction risk factor decomposition.

Risk factor	Subproject
Human risk b_1	Personnel operation error b_{11}, human design error b_{12}, inexperience of personnel b_{13}
Machine risk b_2	Device not running b_{21}, equipment mismatch b_{22}
Material risk b_3	Insufficient material strength b_{31}, defective materials b_{32}, materials expired b_{33}
Environmental risk b_4	Tsunami disaster b_{41}, typhoon b_{42}, heavy rain b_{43}, earthquake disaster b_{44}

reliable, and the construction safety risk source data are sorted out, which require further analysis. After performing the previous task, when determining the unique construction technology of other types of bridges and the safety risk sources during the construction period, users should develop a general survey table for the safety risk

TABLE 4: Survey on safety risk sources of bridge construction.

Project	Risk sources	b_1				b_2	
		b_{11}	b_{12}	b_{13}	$\ldots$	b_{21}	$\ldots$
	a_{11}	✓	✗	✗	$\ldots$	✓	$\ldots$
	a_{12}						
a_1	a_{13}						
	$\ldots$						
a_2	a_{21}						
$\ldots$	$\ldots$						

sources of the bridge during the construction period and lay the foundation for the subsequent weight assignment.

2.2. Risk Source Weight Assignment. The improved FAHP is adapted from AHP. By introducing the theory of fuzzy mathematics, the consistency test problem in AHP is solved. The fuzzy judgment matrix in this method conforms to people's thinking and logic, and the form is simple and accurate. AHP is a combined qualitative and quantitative method proposed by Professor Saaty in the US in the 1970s. The method is a decision-making tool for complex systems, which mainly involves constructing a judgment matrix, comparing the relative importance in each level, calculating the relative weight of each item in that level, and finally combining the relative weights of each level [21]. AHP does not require a large amount of data and can quantify some qualitative issues through the scoring of experts. The method does not take into account the dynamics of decision-makers in a dynamic environment, so it is difficult to express objectivity in the evaluation results; therefore, some scholars have combined fuzzy mathematics and hierarchical analysis methods to form a new decision-making method, FAHP [22]. FAHP is a new method of risk assessment formed by combining fuzzy analysis with hierarchical analysis. When using AHP, it is difficult to maintain consistency in ways of thinking when there are many indicators at different levels, and fuzzy hierarchical analysis can solve this problem by introducing the "affiliation degree" in fuzzy mathematics [23] and using the affiliation function for the indicators with a fuzzy nature (see Table 5).

In general, the improved FAHP method has the following advantages over AHP:

(1) Simple in theory. The FAHP method is simple to calculate during the process of determining weights and only needs to build a comparison matrix between two and two, without a complicated calculation process, which is convenient for decision-makers to operate.

(2) Strong engineering applicability. FAHP can be analyzed from both qualitative and quantitative aspects. As a huge decision system, engineering needs a combination of qualitative understanding and quantitative description to fully interpret all its information, and the method is widely used in engineering practice.

(3) Good overall performance. When using FAHP for analysis, the whole problem is first regarded as a system, and the purpose of decision-making as a whole is achieved by analyzing each part of the system, which can be applied to the decision-making problems of complex systems.

2.3. Improved FAHP. After the risk sources are identified, they need to be categorized and analyzed, such as what risk sources are involved in the foundation project and what are the risk events; we rely on the WBS-RBS to gradually expand these risks by level, which involves the allocation problem. At this time, we need to listen to expert opinions regarding the bridge construction of each structure in the human, machine, and material ring, which may provide the risk sources according to the Delphi method to enumerate and combine with the actual construction of the project. The division is carried out according to the Delphi method, taking into account the actual construction characteristics of the project and listening to the experts' opinions. Then, values are assigned to the identified risk sources. The method of assignment is based on the possibility of risk sources, the controllable degree of risk sources, the maturity of construction technology, and the frequency of risk sources through the Delphi method. Combined with the judgment ideas of AHP [24], it is more flexible and convenient to assign the weight of risk sources.

The improved FAHP mainly establishes the comparison matrix of assessment indices by comparing the relative importance of risk source factors, constructs the fuzzy consistency judgment matrix of assessment indices, calculates the weight vector of assessment indices, and then conducts risk evaluation and analysis of bridges. The user needs to compare the risk sources of other types of bridges during the construction period and determine the relative importance of the risk source factors to establish a comparison matrix of evaluation indicators. The subsequent weight calculation can be calculated according to the following calculation formula, and the parameters involved in each step formula are explained.

2.3.1. Fuzzy Evaluation. The traditional fuzzy analytic hierarchy process (FAHP) evaluation concept is rough, as follows:

$$\begin{cases} b_i > b_j, & b_{ij} = 1, \\ b_i = b_j, & b_{ij} = 0.5, \\ b_i < b_j, & b_{ij} = 0. \end{cases} \quad (1)$$

Scaling	Definition	Explanation
0.5	Equally important	Element i has the same importance compared to element j
0.6	Slightly more important	Element i is slightly more important than element j
0.7	Obviously important	Element i is significantly more important than element j
0.8	More important	Element i is much more important than element j
0.9	Extremely important	Element i is extremely more important than element j
0.1, 0.2, 0.3, 0.4	Inverse comparison	The result of comparing the importance of element i over element j is b_{ij}; then element j is more important by 1- b_{ij} than i.

The evaluation steps of the improved FAHP are similar to those of the fuzzy chromatography analysis method. First, according to the scoring situation of experts, the data are sorted out and processed to improve the rationality of the evaluation standard [25]. Compared with the traditional evaluation concept, it is humanized and conforms to the logical thinking mode of human beings. The traditional expert scoring comparison method uses the 1–9 scale method [26], while Table 1 shows that the distribution of the affiliation function is 0 to 1 to ensure that the overall affiliation interval is 0 to 1. Therefore, the refinement process of the severity level and the possibility level is realized by linear interpolation, which refines these two levels from 1 scale to the 0 to 1 scale, and this shift can effectively improve the calculation accuracy and unify the interval variables for special bridge construction. The stability and reliability of the risk level estimation results are guaranteed [27]. The expert scoring processing is shown in

$$b_j = \frac{\sum_{i=1}^{n} V_{ij}}{n \cdot 100}, \quad j = 1, 2, \ldots m, \tag{2}$$

where b_j is the j-th risk source scoring value after data processing, and V_{ij} is the actual scoring value of the i-th expert for the j-th risk source. In addition, 100 is the percentage scalar.

2.3.2. Establish a Priority Relation Matrix.
The priority relation matrix compares the risk sources of the same type, judges the risk degree of each risk source, and determines the overall weight coefficient according to the lower-level risk matrix. The length of the b_{ij} interval is 2, and the median value is 0. According to the mapping principle, b_{ij} is converted into the value of the 0-1 interval, and 0.5 is taken as the median value of the interval. The changed form is as follows:

$$b_{ij} = b_i - b_j, \tag{3}$$

$$b_{ij}^* = \frac{b_{ij}}{2} + 0.5, \tag{4}$$

where b_{ij} is the difference between Row i and Column j, and b_{ij}^* is the comparison value after the change.

2.3.3. Establishing Fuzzy Consistent Matrix R and Relative Weight.
According to equations (2)–(4), the fuzzy consistent matrix R is established.

$$R_{ij} = \frac{k_i - k_j}{2n} + 0.5, \tag{5}$$

$$k_i = \sum_{j=1}^{n} b_{ij}, \quad i = 1, 2, \ldots, n. \tag{6}$$

The elements in the fuzzy consistent judgment matrix R are added in rows to obtain vector c, and the vector c is normalized to obtain the relative weight w [28].

$$c_i = \sum_{j=1}^{n} R_{ij}, \quad i = 1, 2, \ldots, n, \tag{7}$$

$$w_i = \frac{c_i}{\sum_{k=1}^{n} c_k}, \quad i = 1, 2, \ldots, n. \tag{8}$$

2.4. Factor Analysis Method.
The bridge construction process is a dynamic system. Through construction process decomposition and project risk factor decomposition, the risk source identification method shows that the same risk source does not exist solely in a fixed project process, but that risk sources may be related and influenced by each other. If only the identified risk sources are controlled, the management method will be too mechanical and will play an ineffective role in risk control. Therefore, the factor analysis method is used to conduct microanalysis on the obtained risk sources. By combining the occurrence mechanism of risk sources and internal complex internal relations, the correlation degree of various risk sources was evaluated to determine the major risk sources [29]. The user can perform the corresponding calculations by the following calculation steps and formulas to obtain the evaluation results, where the parameters involved in each step are explained.

(1) Principle of factor analysis

First, the variables are standardized, so that the mean value of each variable is 0, and the standard deviation is 1. Then, the original variable is represented by a linear combination of k ($k < p$) factors f_k[30], namely,

$$\begin{cases} x_1 = a_{11}f_1 + a_{12}f_2 + \ldots + a_{1k}f_k + \varepsilon_1, \\ x_2 = a_{21}f_1 + a_{22}f_2 + \ldots + a_{2k}f_k + \varepsilon_2, \\ \quad \ldots, \\ x_p = a_{p1}f_1 + a_{p2}f_2 + \ldots + a_{pk}f_k + \varepsilon_p, \end{cases}$$

$$x = af + \varepsilon, \tag{9}$$

$$h_i^2 = \sum_{j=1}^{k} a_{ij}^2,$$

$$s_i = \sum_{j=1}^{p} a_{ij}^2.$$

(2) BM SPSS statistics V21.0 software was used to solve and process the data, and the feasibility of the method was determined by means of factor extraction, consistency analysis, and construction validity analysis [31]. Finally, the factor score is calculated according to equation (13), and the safety risk of large and complex bridges in coastal areas during the construction period is quantitatively evaluated.

$$F = a_1 f_1 + a_2 f_2 + \ldots + a_n f_n, \tag{10}$$

$$f = \sum_{i=1}^{v} vq. \tag{11}$$

(3) In particular, a is the factor contribution rate, f is the factor score coefficient, n is the number of factors, the maximum eigenvalue method is selected for the number of factors, the factor has an eigenvalue greater than 1, v is the number of original factors, and q is the factor weight in the factor score matrix.

3. Engineering Application

3.1. Engineering Background. The Zhongkai expressway is an east-west expressway planned by Zhongshan City, Jiangmen City, Guangdong Province connecting Hong Kong and Macao, Shenzhen, Zhongshan, Jiangmen main city, Kaiping City and Taishan City, of which Yinzhou Lake Bridge is a control node project of Zhongshan Kaiping expressway, whose geographical location is Sanjiang Town, Jiangmen City, Guangdong Province, spanning Shazai Island, Tanjiang River, and connecting with Shuangshui Town. Its main channel bridge includes a double tower and double cable plane hybrid composite beam cable-stayed bridge with a semifloating system. The span combination is $56.8 + 64.8 + 66.4 + 530 + 66.4 + 64.8 + 56.8$ m, and the total length of the main bridge is 903 m, the total width of the

main beam top is 36 m, the mid-span is a PK box composite beam, and the side span is a concrete beam. The cable tower is an A-type bridge tower, and the auxiliary pier and transition pier are box-type piers.

The lower part of the bridge structure has a box-type thin-walled pier and column foundation pier with a bored pile foundation. The main pier is arranged with 36 Φ2.8 m bored piles, 53 m long on the east side, and 67 m long on the west side; 13 Φ2.2 m bored piles, 54 m and 55 m long on the east auxiliary pier; 2×6 Φ2.2 m bored piles, 70 m and 58 m long on the west auxiliary pier; 13 Φ2.2 m bored piles, 62 m long on the east transition pier; and 13 Φ2.2 m bored piles, 49 m long on the west transition pier. The tower bearing platform is 60.1 m in the cross-bridge direction and 22.4 m in the along-bridge direction, with a thickness of 7 m and a tower height of 2.5 m; the bearing platform of the east side transition pier, auxiliary pier, and west side transition pier adopts an integral-type bearing platform, and the left and right side bearing platforms are connected with cross-ties, such that each bearing platform has a plan size of 13.6 m × 9 m and a thickness of 3.5 m; the bearing platform of the west side auxiliary pier adopts a separation-type bearing platform. The west side auxiliary pier bearing adopts a separated bearing, with a plane size of 13.6 m × 9 m and a thickness of 3.5 m.

3.2. Risk Source Identification. The WBS-RBS method was used to establish a specific risk source index system, and then the Delphi method was used to score the participating experts to identify the safety risk sources of the construction of the lower part of the Yinzhou Lake Bridge. The risk source identification table established by the WBS-RBS method is shown in Table 6. The scoring data of 15 experts are processed by equation (2). The final construction safety risk identification of the lower part of the Yinzhou Lake Bridge is shown in Table 7.

3.2.1. Establish a Priority Relation Matrix. Taking D_{12}, fire prevention on-site, as an example, the priority relationship matrix between D_{12}-E is established by applying the improved fuzzy analytic hierarchy process (FAHP) theory, combined with the site construction situation and expert scoring value, as shown in Table 8.

According to equations (2)–(8), the fuzzy consistent matrix and relative weight of D_{12}-E are calculated. The results are shown in Table 9.

3.2.2. Total Weight of the Fuzzy Hierarchy. The above methods were applied to solve the priority relationship matrix and to calculate the relative weights for A_{11}–D_{12}, which will not be repeated herein. Finally, the fuzzy hierarchical relative weight matrix w was established for the construction risks of the lower part of the Yinzhou Lake Bridge to determine the importance of each risk factor to the construction process.

TABLE 6: Risk source identification table established using the WBS-RBS method.

		Risk sources			
	Project	Human risk E_1	Machine material risk E_2	Environmental risk E_3	Construction technology impact E_4
Foundation pit engineering (A)	Foundation pit excavation A_{11}	...	...	...	...
	Foundation pit support A_{12}	...	...	...	...
Pile foundation construction (B)	Equipment transportation and installation B_{11}	...	...	...	...
	Embedded casing B_{12}	...	...	...	...
	Drilling with drilling machine B_{13}	...	...	...	...
	Hole cleaning B_{14}	...	...	...	...
	Hoisting reinforcement cage B_{15}	...	...	...	...
	Underwater concrete pouring B_{16}	...	...	...	...
Pile cap construction (C)	Boxed cofferdam C_{11}	...	...	...	...
	Cofferdam hoisting C_{12}	...	...	...	...
	Pile cap construction C_{13}	...	...	...	...
	Formwork engineering C_{14}	...	...	...	...
Other(D)	Construction electricity D_{11}	...	...	...	...
	Fire prevention on-site D_{12}	...	...	...	...

TABLE 7: Risk source score table for the lower part of the Yinzhou lake bridge.

Project		Risk sources			
		E_1	E_2	E_3	E_4
A	A_{11}	0.791	0.701	0.705	0.734
	A_{12}	0.789	0.776	0.746	0.697
B	B_{11}	0.703	0.832	0.607	0.612
	B_{12}	0.817	0.822	0.714	0.734
	B_{13}	0.748	0.737	0.694	0.735
	B_{14}	0.797	0.767	0.714	0.742
	B_{15}	0.784	0.801	0.718	0.780
	B_{16}	0.894	0.815	0.698	0.795
C	C_{11}	0.795	0.795	0.707	0.749
	C_{12}	0.800	0.749	0.701	0.735
	C_{13}	0.797	0.782	0.732	0.793
	C_{14}	0.816	0.816	0.750	0.841
D	D_{11}	0.807	0.831	0.790	0.840
	D_{12}	0.755	0.809	0.689	0.801

TABLE 8: D_{12}-E priority relationship matrix.

D_{12}	E_1	E_2	E_3	E_4
E_1	0.500	0.546	0.602	0.541
E_2	0.454	0.500	0.556	0.495
E_3	0.398	0.444	0.500	0.439
E_4	0.459	0.505	0.561	0.500

TABLE 9: D_{12}-E fuzzy consistent matrix and relative weight.

D_{12}	E_1	E_2	E_3	E_4	W_1
E_1	0.500	0.523	0.551	0.521	0.262
E_2	0.477	0.500	0.528	0.498	0.250
E_3	0.449	0.472	0.500	0.470	0.236
E_4	0.480	0.503	0.531	0.500	0.252

$$W = \begin{bmatrix} 0.257 & 0.255 & 0.252 & 0.256 & 0.252 & 0.255 & 0.252 & 0.262 & 0.254 & 0.257 & 0.253 & 0.251 & 0.249 & 0.249 \\ 0.246 & 0.253 & 0.268 & 0.256 & 0.251 & 0.252 & 0.254 & 0.252 & 0.254 & 0.250 & 0.251 & 0.251 & 0.252 & 0.256 \\ 0.246 & 0.249 & 0.240 & 0.243 & 0.246 & 0.245 & 0.243 & 0.237 & 0.243 & 0.244 & 0.244 & 0.243 & 0.247 & 0.241 \\ 0.251 & 0.243 & 0.240 & 0.245 & 0.251 & 0.248 & 0.251 & 0.249 & 0.248 & 0.249 & 0.252 & 0.254 & 0.253 & 0.255 \end{bmatrix}^T. \quad (12)$$

3.3. Risk Assessment and Analysis.

The internal relationship between risk sources and engineering projects is determined with the factor analysis method, and the relative weight W calculated by the fuzzy hierarchy is imported into IBM SPSS for factor analysis and calculation.

3.3.1. Data Analysis.

The variance contribution rate of factors is calculated with software, as shown in Table 10. Among them, the first set of data describes the initial solution of the factor, the characteristic root of the first factor is 1.773, the explained total variance of the original four variables is 44.335%, and the cumulative variance contribution rate is 44.335%; the ending mode of the second and third factors is similar to that of the first factor; the third group of data describes the factor solution, with a total variance of 99.877%, which indicates that the three factors reflect 99.877% of the information of the original variable.

Figure 4 shows that the first factor has the highest eigenvalue and largest contribution rate to the variable interpretation, while the eigenvalue of the third factor is smaller, therefore contributing less to the explanatory variables, and they can be ignored.

3.3.2. Factor Score.

Table 11 is the factor score matrix, and the factor score function can be calculated according to the regression algorithm. According to equations (10)-(11), the final score of the factors is calculated and sorted. The data results are shown in Table 12.

3.3.3. Result Analysis.

According to the fuzzy comprehensive calculation method, the foundation excavation factor score is 0.83, ranking the first, and the risk coefficient is the largest; the score of the foundation pit support factor is 0.55, ranking the second, with the same risk; the score of the hole cleaning work factor after drilling is 0.33, which is slightly lower than the first two construction procedures, but there are also greater risks; the other construction processes are also high. The factor scores and the risk order of the project are shown in Table 13. During the construction progress of the project, according to the known risk coefficient, scientific management methods are applied to pay attention to the construction process with high risk and take reasonable construction measures to avoid risks in time and reduce economic losses.

The main purpose of bridge construction safety risk identification and analysis is to perform better risk management and control to ensure the safety of people and structures during bridge construction. This process requires reasonable risk response measures, scientific risk management measures that are the key to risk disposal,

consideration that different sizes of risk disposal programs are not the same, and the requirement of scientific consideration that is not arbitrary, which requires compliance with certain principles. The specific principles of risk response strategies are as follows.

(i) Availability and validity

Risk control should pay attention to the availability of control methods, and the methods should be combined with the practical factors of the situation to ensure that they are available in engineering practice. The risk decision should be made according to the characteristics of the risk occurrence. At the same time, the effectiveness of the control method should be ensured, and the proposed risk control method should be able to prevent and control the risk effectively.

(ii) Cost reasonableness

The bridge construction process has many kinds of risks and great difficulty in prevention, which causes the cost of the control process to also be larger. Therefore, in the process of risk control, the issue of cost should be considered, the size of the cost and benefit should be compared, and the funds should be reasonably controlled to ensure that the premise of solving the risk is to try to save costs and balance the gains and losses.

(iii) Comprehensiveness

Bridge construction projects are large and complex systems, and construction processes face numerous risks. Each risk control program has its own uniqueness and limitations. The control process should be considered cross-use to ensure that the control scope and control benefits are maximized.

(iv) Science

The selection of a risk control program should have a scientific basis and not be a blind decision. The risk identification and assessment of the entire bridge are rigorously scientifically proven, thus ensuring the accuracy of risk recognition.

3.4. Risk Assessment and Analysis.

The most commonly used method for risk assessment is the AHP method [32, 33], which we adopted as a comparative study. The main steps of the AHP method are establishing a hierarchical structure model, constructing all judgment matrices in each level, using the two-by-two comparison method to derive the weights of individual influencing factors, and ranking the weights of each influencing factor.

TABLE 10: Total variance explained.

Component	Initial eigenvalues			Extraction sums of squared loadings			Rotation sums of squared loadings		
	Total	% of variance	Cumulative %	Total	% of variance	Cumulative %	Total	% of variance	Cumulative %
1	1.773	44.335	44.335	1.773	44.335	44.335	1.759	43.980	43.980
2	1.243	31.081	75.416	1.243	31.081	75.416	1.257	31.437	75.416
3	0.978	24.461	99.877						
4	0.005	0.123	100.000						

Extraction method: principal component analysis.
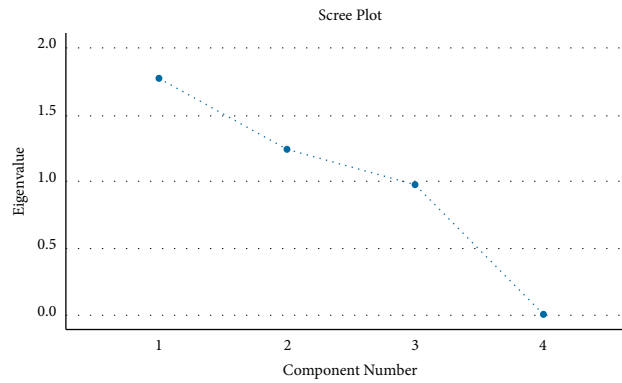
FIGURE 4: Factor eigenvalue distribution.

TABLE 11: Component score coefficient matrix.

	Component	
	1	2
Risk sources 1	−0.031	0.787
Risk sources 2	−0.539	−0.350
Risk sources 3	0.320	−0.147
Risk sources 4	0.420	−0.187

TABLE 12: Factor score table.

Project name	Factor score	Sequence
A_{11}	0.83	1
A_{12}	0.55	2
B_{11}	−1.12	13
B_{12}	0.16	4
B_{13}	−0.27	12
B_{14}	0.33	3
B_{15}	0.03	9
B_{16}	−0.2	11
C_{11}	0.12	5
C_{12}	0.07	7
C_{13}	0.05	8
C_{14}	−0.53	14
D_{11}	0.11	6
D_{12}	−0.12	10

TABLE 13: Scale of proportions.

The relative importance of the i-th risk event over the j-th risk event	Quantified values
Equally important	1
Slightly more important	3
Stronger and more important	5
Strongly important	7
Extremely important	9
Intermediate value of two adjacent judgments	2, 4, 6, 8

evaluation indicators. According to on-site research, literature review, and expert opinion, it was determined that the risk source engineering items of the lower part of the Yinzhou Lake Bridge are foundation pit engineering, pile foundation engineering, bearing platform construction, and others, and each risk source engineering item contains multiple risk factors. Finally, a three-layer hierarchical structure model containing the target layer, criterion layer, and indicator layer is established. As shown in Figure 5, A, B, C, D and A_{11}, A_{12}, ..., D_{12} refer to risk source engineering projects and risk source factors, respectively; the details are the same as those in Table 6 for risk events and risk source designations.

3.4.1. Building Hierarchical Structure Model. The hierarchical structure diagram is generally divided into 3 layers, the top layer, middle layer, and bottom layer, representing the target layer, criterion layer, and indicator layer, respectively. In actual case analysis, the structure can be divided according to the objectives to be evaluated, the factors to be considered and the interrelationship points among

3.4.2. Construction of Judgment Matrix at Each Layer. By inviting experts such as construction experts and supervision experts, the relative importance of the two factors is calibrated using a scale of proportionality, as shown in Table 13, and the judgment matrix of risk source factors at the criterion level relative to the target level is shown in Table 14.
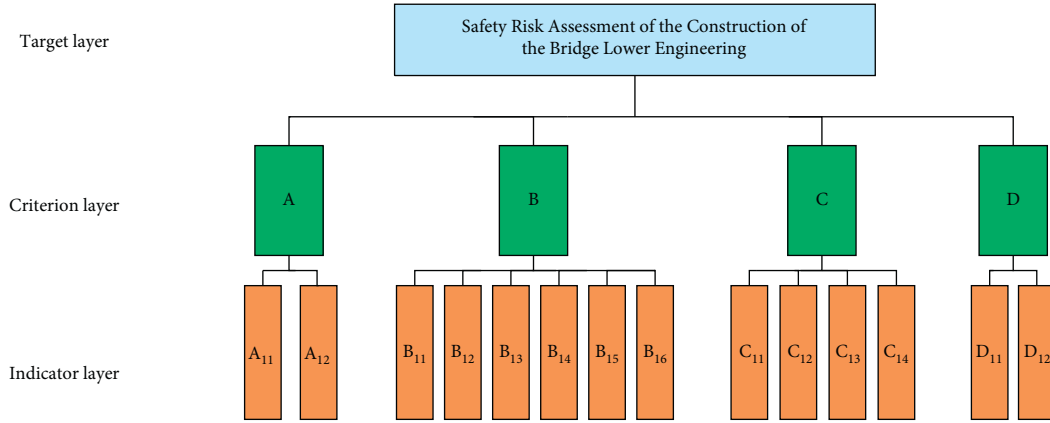
FIGURE 5: The hierarchical structure model of the safety risk assessment of the project under the pile of the Yinzhou lake bridge.

TABLE 14: Judgment matrix of the objective layer-criterion layer.

	A	B	C	D
A	1	3	5	7
B	1/3	1	5	3
C	1/5	1/5	1	1/3
D	1/7	1/3	3	1

To ensure that the results obtained with this method are reasonable and reliable, it is necessary to judge the consistency of the target layer-criterion layer judgment matrix. The consistency check is shown in

$$CR = \frac{CI}{RI} < 0.1, \tag{13}$$

where RI is the average random consistency index. The equation for CI is $CI = \lambda_{max} - n/n - 1$, n is the order of the judgment matrix, RI takes the values shown in Table 15, and λ_{max} is the maximum eigenvalue.

The square root method is adopted to find the solution of λ_{max} [34] as follows: Step one: multiply each element by row to obtain u_{ij}; see equation (13); Step 2: raise u_{ij} to the power of n to obtain u_i; see equation (15); Step 3: normalize u_i to obtain the weight vector ω_i; see equation (16); Step 4: calculate the maximum characteristic root λ_{max} of the judgment matrix; see equation (17).

$$u_{ij} = \prod_{j=1}^{n} b_{ij}, \tag{14}$$

$$u_i = \sqrt[n]{u_{ij}}, \tag{15}$$

$$\omega_i = \frac{u_i}{\sum_{i=1}^{n} u_i}, \tag{16}$$

$$\lambda_{max} = \sum_{i=1}^{n} \frac{(A\omega)_i}{n\omega_i}, \tag{17}$$

where b_{ij} is the relative importance value of the i-th evaluation index relative to the j-th evaluation index, which is the value in the judgment matrix; A is the judgment matrix; ω is the eigenvector; and n is the number of elements. In this

TABLE 15: Average random consistency index.

1	2	3	4	5	6	7	8	9
0.00	0.00	0.58	0.9	1.12	1.24	1.32	1.41	1.45

case, the maximum eigenvalue of CI is 4.235, RI is 0.078, and CR is 0.9. Therefore, since 0.087 < 0.1, the consistency requirement is satisfied. The weight vector occupied by $A–D$ is $w = (0.566, 0.265, 0.060, 0.109)$.

The following is the judgment matrix of each factor in the index layer relative to the criterion layer. The relative importance of each factor in the index layer to the criterion layer is calculated by two comparisons, and the results are shown in Tables 16–19.

According to the calculation method of the weight feature vector of each evaluation factor in the criterion layer relative to the target layer, the weight vector of the judgment matrix of A-A$_{1-2}$ is obtained, and it is calculated that $\lambda_{max} = 2$, $CI = 0$, $RI = 0$, and $CR = 0 < 0.1$, which meets the consistency requirement. The weight vector occupied by A-A$_{1-2}$ is $w = (0.750, 0.250)$.

The same calculation method is used to obtain the weight vector of the judgment matrix of B–B$_{1-6}$, and it is calculated that $\lambda_{max} = 6.563$, $CI = 0.113$, $RI = 1.24$, and $CR = 0.091 < 0.1$, which satisfies the consistency requirement. The weight vector occupied by B–B$_{1-6}$ is $w = (0.157, 0.398, 0.055, 0.240, 0.119, 0.031)$.

In the same way, the weight vector of the judgment matrix C–C$_{1-4}$ is obtained, and after calculation, $\lambda_{max} = 4.076$, $CI = 0.025$, $RI = 0.9$, and $CR = 0.028 < 0.1$, which meets the consistency requirements. The weight vector occupied by C–C$_{1-4}$ is $w = (0.543, 0.254, 0.085, 0.119)$.

The same calculation method is used to obtain the weight vector of the judgment matrix of D-D$_{1-2}$, and it is calculated that $\lambda_{max} = 2$, $CI = 0$, $RI = 0$, and $CR = 0 < 0.1$, which also meets the consistency requirements. The weight vector occupied by D-D$_{1-2} = (0.750, 0.250)$.

3.4.3. Calculation of Combination Weights and Total Hierarchical Ranking. The combined weight of each risk source is the product of the weight of each risk source in the

TABLE 16: A-$A_{1\text{-}2}$ judgment matrix.

A	A_1	A_2
A_1	1	3
A_2	1/3	1

TABLE 17: B–$B_{1\text{-}6}$ judgment matrix.

B	B_1	B_2	B_3	B_4	B_5	B_6
B_1	1	1/3	3	1/3	3	5
B_2	3	1	7	3	3	7
B_3	1/3	1/7	1	1/3	1/5	3
B_4	3	1/3	3	1	3	7
B_5	1/3	1/3	5	1/3	1	5
B_6	1/5	1/7	1/3	1/7	1/2	1

TABLE 18: C–$C_{1\text{-}4}$ judgment matrix.

C	C_{11}	C_{12}	C_{13}	C_{14}
C_{11}	1	3	3	7
C_{12}	1/3	1	3	3
C_{13}	1/3	1/3	1	1/3
C_{14}	1/7	1/3	3	1

TABLE 19: D-$D_{1\text{-}2}$ judgment matrix.

D	D_1	D_2
D_1	1	3
D_2	1/3	1

indicator layer and the feature vector of the weight of the indicator layer. Then, the calculated weight of each risk source index was sorted from large to small, and the results are shown in Table 20.

The total ranking results of all risk factors that are involved in bridge construction were obtained as follows: foundation pit excavation A_{11}, foundation pit support A_{12}, embedded casing B_{12}, construction electricity D_{11}, hole cleaning B_{14}, equipment transportation and installation B_{11}, boxed cofferdam C_{11}, hoisting reinforcement cage B_{15}, fire prevention on-site D_{12}, cofferdam hoisting C_{12}, drilling with drilling machine B_{13}, underwater concrete pouring B_{16}, formwork engineering C_{14}, and pile cap construction C_{13}.

Comparing the improved fuzzy hierarchical factor analysis method with the AHP method in the bridge construction safety risk evaluation study, we can see that both of them use the expert scoring method to determine the relative importance of the risk sources. However, for the initial identification of risk sources, this paper adopts the fuzzy hierarchical analysis method, which can solve the problem of fuzzy evaluation indices in the bridge construction process by introducing an "affiliation degree" in fuzzy mathematics and using the affiliation function to deal with the fuzzy indices. The method proposed in this paper considers the dynamic risk sources in the construction process and selects the representative risk sources for analysis and consideration.

TABLE 20: Hierarchical total sorting results.

Risk factors	Single weight				Weights	Sequence
	A 0.566	B 0.265	C 0.060	D 0.109		
A_{11}	0.750				0.4245	1
A_{12}	0.250				0.1415	2
B_{11}		0.157			0.0417	6
B_{12}		0.398			0.1056	3
B_{13}		0.055			0.0147	11
B_{14}		0.240			0.0636	5
B_{15}		0.119			0.0315	8
B_{16}		0.031			0.0081	12
C_{11}			0.543		0.0326	7
C_{12}			0.254		0.0152	10
C_{13}			0.085		0.0051	14
C_{14}			0.119		0.0071	13
D_{11}				0.750	0.0818	4
D_{12}				0.250	0.0273	9

4. Conclusions and Discussion

There are many risk factors present during the construction period of a large and complex bridge. In this paper, the Delphi method and WBS-RBS method are employed to identify potential dynamic risk sources, establish a safety risk evaluation index system for the construction period of a large and complex bridge, use improved fuzzy hierarchical analysis for weight calculation, and combine factor analysis to evaluate the safety risk of a large and complex bridge during the construction period. An empirical study was conducted to assess the practical application of the method, and the main conclusions are as follows.

(1) Through the construction process decomposition and construction safety factor decomposition method, a set of safety risk census systems applicable to the bridge construction period is established, which can more perfectly identify the dynamic risks in the construction process and identify them more comprehensively and accurately. Whether the results are obtained using the method proposed in this paper or the comparative study, it is concluded that foundation pit excavation and foundation pit support are relatively dangerous risk events, and so risk prevention should be strengthened in actual construction and similar projects to pay attention to these types of risk.

(2) Through the organic combination of the Delphi method, FAHP, and factor analysis method, the advantages of the above three methods are integrated to compensate for their defects. The safety risk situation of bridge construction periods is complex, and there are many uncertainties and fuzziness. This method can quantitatively analyze this kind of complex system and calculate the risk value accurately.

(3) The fuzzy comprehensive evaluation method is applied to quantitatively evaluate the safety risk of the lower part of the Yinzhou Lake Bridge during its

construction period, and reasonable disposal measures are presented according to the risk of the project to prevent the occurrence of safety risk events and provide guidance for the safety risk assessment of the bridge construction period in the future. A comparative study was also conducted, and the scientific and accurate nature of the proposed method was fully demonstrated.

This paper provides a new method that is applicable to the evaluation of safety risks during the construction period of large and complex bridges; however, the method also has some limitations, the main 2 of which are as follows: first, the method requires the user to have a certain level of mathematical calculation ability, and the formula has some calculation complexity; second, some risk source factors may exist in the operational period or design period, and since their risk hazard levels may also be high, these factors need to be integrated with the factors of other periods. In general, as a major infrastructure country, China's infrastructure construction is accelerating, and the construction of bridges has reached new heights in terms of span, construction difficulty, and construction technology, and so traditional evaluation methods need to be innovated. Our next study will focus on the acquisition and calculation of unidentified factors, taking into account the complexity of the actual construction environment, the numerous risk sources during bridge construction, the decision to deploy these risk events, and the identification of the more important risk sources to assess their degree of risk to the overall project. For the purpose of this paper, this involves intelligent calculations, which need to rely on language programming to edit the formulas involved in these methods and transform them into source code language programs, and in practice, the user only needs to input the relevant parameters to obtain the evaluation results. To promote the use of this method, we are also strengthening it to study the risk evaluation of other types of bridges during the construction period, and we will also carry out the safety risk evaluation of other types of bridges during the construction period.

Data Availability

The data used to support the findings of this study are included within the article.

Conflicts of Interest

The authors declare that there are no conflicts of interest regarding the publication of this paper.

References

[1] T. Zayed, R. E. Minchin, and A. J. Boyd, "Model for the physical risk assessment of bridges with unknown foundation," *Journal of Performance of Constructed Facilities*, vol. 21, pp. 44–52, 2007.

[2] Y. Q. Xiang, Q. .Q. Wu, and T. T. Zhang, "Research on risk assessment of bridge design based on AHP-FCE model," *China Civil Engineering Journal*, vol. 43, pp. 275–280, 2010, (in Chinese).

[3] H. Naderpour, A. Kheyroddin, and S. Mortazavi, "Risk assessment in bridge construction projects in Iran using Monte Carlo simulation technique," *Practice Periodical on Structural Design and Construction*, vol. 24, Article ID 04019026, 2019.

[4] J. X. Xu, B. You, S. L. Shi, H. Q. Liu, and Y. Q. Zhang, "Bridge construction risk identification and assessment analysis based on analytic hierarchy process," *Mining Engineering Research*, vol. 35, pp. 59–64, 2020, (in Chinese).

[5] H. Wu, S. Liu, J. Wang, and T. Yang, "Construction safety risk assessment of bridges in the marine environment based on CRITIC and TOPSIS models," *Journal of Coastal Research*, vol. 108, pp. 206–210, 2020.

[6] W. Fan, Y. Chen, J. Li, Y. Sun, J. Feng, and P. Sareh, "Machine learning applied to the design and inspection of reinforced concrete bridges: resilient methods and emerging applications," *Structures*, vol. 33, pp. 3954–3963, 2021.

[7] S. Lin, S. L. Shen, A. Zhou, and Y. Xu, "Risk assessment and management of excavation system based on fuzzy set theory and machine learning methods," *Automation in Construction*, vol. 122, Article ID 103490, 2021.

[8] Q. Zheng, H. M. Lyu, A. Zhou, and S. Shen, "Risk assessment of geohazards along Cheng-Kun railway using fuzzy AHP incorporated into GIS," *Geomatics, Natural Hazards and Risk*, vol. 12, pp. 1508–1531, 2021.

[9] K. Peng, "Risk evaluation for bridge engineering based on cloud-clustering group decision method," *Journal of Performance of Constructed Facilities*, vol. 33, Article ID 04018105, 2018.

[10] C. L. Gong, "Risk analysis and countermeasures for the construction of long-span cable-stayed bridges," Doctoral Dissertation, Tongji University, Shanghai, China, 2006.

[11] X. Lai, F. Wang, and Y. Tan, "Research on the construction of grey correlation risk assessment model based on bridge risk assessment," *Highway Engineer*, vol. 43, pp. 205–209, 2018, (in Chinese).

[12] Y. F. Liu, "Research on risk assessment methods of bridge construction," Master's thesis, Chang'an University, Xi'an, China, 2005.

[13] Q. C. Liu, "Research on safety risk assessment of bridge engineering construction," Master's thesis, Shandong University, Jinan, China, 2017.

[14] L. H. Yang, F. F. Ye, and Y. M. Wang, "Bridge risk assessment based on extended belief rule base with joint optimization," *Systems engineering-theory and practice*, vol. 40, pp. 1870–1881, 2020.

[15] M. A. Khan, A. A. Khan, G. A. Anwar, and A. Usmani, "Framework for fire risk assessment of bridges," *Structures*, vol. 33, pp. 523–532, 2021.

[16] M. G. Stewart, "Reliability-based assessment of ageing bridges using risk ranking and life cycle cost decision analyses," *Reliability Engineering & System Safety*, vol. 74, pp. 263–273, 2001.

[17] H. Yang, Y. M. Wang, L. L. Chang, and Y. Fu, "A disjunctive belief rule-based expert system for bridge risk assessment with dynamic parameter optimization model," *Computers & Industrial Engineering*, vol. 113, pp. 459–474, 2017.

[18] J. M. Andric and D. G. Lu, "Risk assessment of bridges under multiple hazards in operation period," *Safety Science*, vol. 83, pp. 80–92, 2016.

[19] A. S. Ribeiro, C. M. De, and X. Costoya, "A delphi method to classify wave energy resource for the 21st century: application

to the NW Iberian Peninsula," *Energy*, vol. 235, Article ID 121396, 2021.

[20] G. H. Chen, W. S. Wu, S. Y. Xu, and K. Liu, "HSE risk assessment of cross-sea bridge construction based on WBS-RBS and AHP," *China Safety Science Journal*, vol. 23, pp. 51–57, 2013.

[21] T. L. Saaty, *Group Decision Making and the AHP, the Analytic Hierarchy Process*, Springer Berlin Heidelberg, Berlin, Germany, 1989.

[22] F. P. Liu and J. T. Zhou, "Comprehensive evaluation of long-span bridges based on fuzzy extension analytic hierarchy process," *China and Foreign Highway*, vol. 35, pp. 93–99, 2015, (in Chinese).

[23] H. Qian, S. Yang, Q. Q. Peng, X.Q. Liu, and M. Chen, "Risk assessment of withstand voltage test system under high voltage based on fuzzy analytic hierarchy process," *Safety and Environmental Engineering*, vol. 26, pp. 111–116, 2019, (in Chinese).

[24] Y. W. Pan, J. L. Yu, and Q. Zhang, "Application of analytic hierarchy process in the selection of construction schemes for deep water caps," *Construction Technology*, vol. 43, pp. 72–75, 2014, (in Chinese).

[25] J. Zhang, "Research on risk analysis methods during construction of long-span bridges," Master's thesis, Tongji University, Shanghai, China, 2007.

[26] K. P. Wang, C. G. Lu, and Q. F. Li, "Study on identifying significant risk sources during bridge construction based on grey entropy correlation analysis method," *Mathematical Problems in Engineering*, vol. 2021, Article ID 6618039, 15 pages, 2021.

[27] W. L. Yang and Y. D. Xue, "Improved method of special risk grade estimation for highway and bridge construction," *Journal of Disaster Prevention and Mitigation Engineering*, vol. 35, pp. 624–629+673, 2015, (in Chinese).

[28] X. Chen, "Risk analysis of long-span suspension bridge construction," Master's thesis, Nanchang Hangkong University, Nanchang, China, 2017.

[29] Z. X. Li, "Research on risk assessment of long-span bridges in construction period," Master's thesis, Zhengzhou University, Zhengzhou, China, 2011.

[30] D. L. Feng, "Research on safety risk assessment and control of tunnel civil construction based on factor analysis-fuzzy analysis method," Master's thesis, Southwest Jiaotong University, Chengdu, China, 2013.

[31] C. B. Wang and Y. M. Song, "Research on risk factors of bridge construction based on factor analysis method," *Journal of Hunan University of Arts and Science (Natural Science Edition)*, vol. 30, pp. 45–50, 2018, (in Chinese).

[32] A. Ghosh and R. Maiti, "Development of new ecological susceptibility index (ESI) for monitoring ecological risk of river corridor using F-AHP and AHP and its application on the Mayurakshi river of Eastern India," *Ecological Informatics*, vol. 63, Article ID 101318, 2021.

[33] Y. Wang, J. Liu, and T. M. S. Elhag, "An integrated AHP–DEA methodology for bridge risk assessment," *Computers & Industrial Engineering*, vol. 54, pp. 513–525, 2008.

[34] Q. F. Li, H. D. Zhou, and H. Zhang, "Durability evaluation of highway tunnel lining structure based on matter element extension-simple correlation function method-cloud model: a case study," *Mathematical Biosciences and Engineering*, vol. 18, pp. 4027–4054, 2021.

Research Article

Concrete Spalling Severity Classification Using Image Texture Analysis and a Novel Jellyfish Search Optimized Machine Learning Approach

Nhat-Duc Hoang [1,2] **Thanh-Canh Huynh** [1,2] **and Van-Duc Tran** [2,3]

[1]*Institute of Research and Development, Duy Tan University, Da Nang 550000, Vietnam*
[2]*Faculty of Civil Engineering, Duy Tan University, Da Nang 550000, Vietnam*
[3]*International School, Duy Tan University, Da Nang 550000, Vietnam*

Correspondence should be addressed to Nhat-Duc Hoang; hoangnhatduc@duytan.edu.vn

During the phase of building survey, spalling and its severity should be detected as earlier as possible to provide timely information on structural heath to building maintenance agency. Correct detection of spall severity can significantly help decision makers develop effective maintenance schedule and prioritize their financial resources better. This study aims at developing a computer vision-based method for automatic classification of concrete spalling severity. Based on input image of concrete surface, the method is capable of distinguishing between a minor spalling in which the depth of the broken-off material is less than the concrete cover layer and a deep spalling in which the reinforcing steel bars have been revealed. To characterize concrete surface condition, image texture descriptors of statistical measurement of color channels, gray-level run length, and center-symmetric local binary pattern are used. Based on these texture-based features, the support vector machine classifier optimized by the jellyfish search metaheuristic is put forward to construct a decision boundary that partitions the input data into two classes of shallow spalling and deep spalling. A dataset consisting of 300 image samples has been collected to train and verify the proposed computer vision method. Experimental results supported by the Wilcoxon signed-rank test point out that the newly developed method is highly suitable for concrete spall severity classification with accuracy rate = 93.33%, $F1$ score = 0.93, and area under the receiver operating characteristic curve = 0.97.

1. Introduction

Spalling is a notable defect widely encountered in surface of reinforced concrete structures (refer to Figure 1). The appearance of spalling significantly deteriorates the integrity and durability of reinforced concrete elements. This defect can be caused by severe servicing environment and loads. More importantly, the appearance of spalls may indicate more serious damages in the internal structure of reinforced concrete elements, e.g., corrosion of steel reinforcement.

Spalling should be detected as earlier as possible due to several reasons. First, spall objects badly affect the aesthetics of building structures and therefore bring about discomfort for occupants. Second, if the layer of concrete cover is removed due to spalling, reinforcing steel bars are exposed to

the environment and this fact expedites the corrosion of the steel bars (as shown in Figure 1(b)). Subsequently, the area and the depth of spall objects increase over time. Third, spalling appeared in ceilings, cladding structures, or concrete beams is particularly hazardous for occupants. The materials broken off from spalled areas can cause significant injuries and even loss of human lives.

As a consequence, periodic visual inspection is necessary to detect and evaluate the severity of spalling defects. Most importantly, deep spalling in which the layer of concrete cover has completely broken off and steel reinforcement has been exposed should be detected timely and requires urgent remedy. In Vietnam as well as in other developing countries, visual inspection performed by human technicians and manual visual data processing are the main approaches for
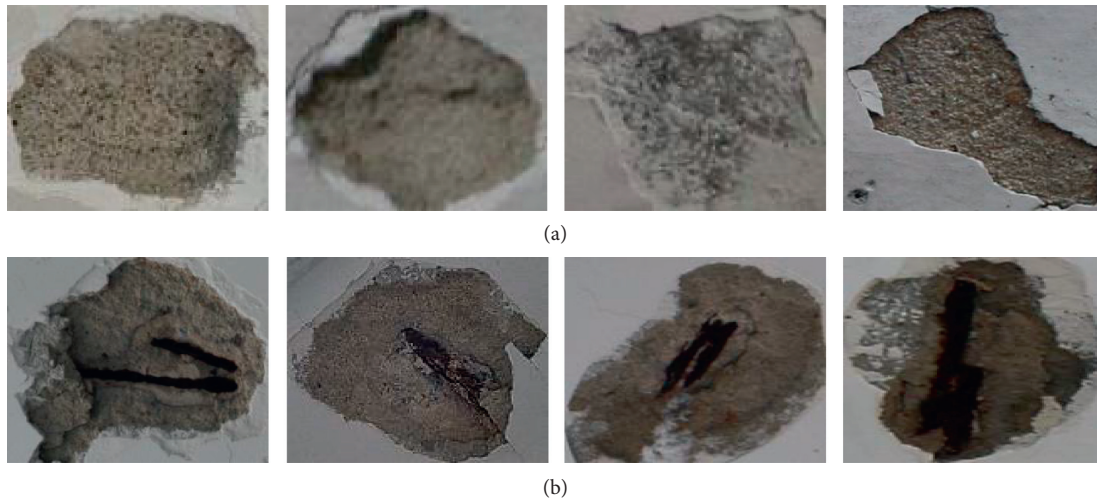
(a)

(b)

Figure 1: Appearances of spall in reinforced concrete surface: (a) shallow spall and (b) deep spall.

spall detection. Although these approaches can help to detect and evaluate the severity of this distress accurately, they are also notoriously known to be labor and time-consuming. With a large surface area of concrete structure, timely inspection and fast visual data processing are virtually impossible for a limited number of inspectors.

Therefore, maintaining good serviceability via periodic visual inspection and evaluation is crucial to keep building environment operational and protect occupants' health. In recent years, due to the availability of low-cost digital cameras as well as a rapid improvement of image processing techniques, computer vision-based structural health monitoring systems have been increasingly used to enhance the productivity of periodic building survey [1–3]. These systems have been demonstrated to be viable tools for building defect detections. They are capable of not only producing acceptable detection accuracy but also guaranteeing consistency in assessment outcomes. The computer vision-based methods yield objective evaluation results; they are not affected by subjective judgments in data processing performed by humans.

Due to the aforementioned advantages, various automated and data-driven methods used for concrete spalling detection have been constructed in the literature. German et al. [4] constructed an automated model for detecting spalled regions on the surfaces of concrete columns based on a local entropy-based thresholding algorithm, a global adaptive thresholding algorithm, and morphological operations; the model is tested with concrete columns during a postearthquake investigation. Dawood et al. [5] proposed a computer vision-based approach for spalling detection and quantification in subway networks; this study employs various image processing techniques including image thresholding, histogram equalization, and filtering in an attempt to detect the quantify the severity of spall objects. This computer vision-based method is validated with a set of 75 image samples and attains an accuracy rate of 89.3%.

Hoang [6] relied on a steerable filter used for feature extraction and machine learning-based data classification to recognize wall defects including concrete spalling. The method of roughness descriptor based on Hough transformation and similarity analysis is described in Wu et al. [7]; this approach is utilized for recognizing concrete spalling occurring in metro tunnel surface. A model that integrates image processing techniques of texture analysis and machine learning has been proposed in Hoang et al. [8]; a piecewise linear stochastic gradient descent logistic regression has been used to categorized images of concrete surface into two classes of "nonspall" and "spall."

Abdelkader et al. [9] harnessed the capability of particle swarm optimization metaheuristic coupled with the Tsallis entropy function and discrete wavelet transform to automate the detection of spalling area. Hoang [10] developed an image processing-based spall object detection method relying on Gabor filter for region of interest extraction, texture analysis methods for characterizing feature of concrete surface, and logistic regression models used for data classification; this integrated approach can effective locate the spall objects but is not capable of classifying spall severity.

Abdelkader et al. [11] developed an entropy-based automated approach for detection and assessment of spalling severities in reinforced concrete bridges; invasive weed optimization-based image segmentation, information theory-based formalism of images, and the Elman neural network are hybridized to formulate the proposed method. Zhao et al. [12] investigated various feature selection strategies used with machine learning models and texture descriptors to detect concrete surface voids.

Recently, deep learning methods have also been applied to tackle the problem of interest. The main advantage of the deep learning models is that the feature extraction phase can be performed automatically [13, 14]. Through various convolutional and pooling operations, useful features such as edges, shapes, texture, and so on can be revealed by the machine and used for the subsequent pattern recognition tasks in a fully connected layer [15]. Wei et al. [16] proposed deep learning-based recognition and quantification for concrete surface bughole; the employed artificial intelligent

method is convolutional neural network (CNN); the main research finding is that the CNN-based model can effectively replace the traditional detection methods carried out by manual inspection.

Another deep learning-based concrete surface void detection method has been put forward in [17]; this method is trained by small-sized image of 28×28 pixels, and its performance outperformed conventional image processing techniques of the Laplacian of Gaussian algorithm and the Otsu method. A CNN-based method used for detecting building defects has been developed in [18]; this method is capable of automatically detecting and localizing key building defects such as mould, deterioration, and stain.

Although CNN-based methods are generally capable tools for detecting spalling and other defects in concrete surface, the deep learning approaches typically demand a large volume of image datasets in order to construct reliable classifiers [13, 19]. This fact requires a great effort in visual data collection and a meticulous data labeling process. In addition, successful implementation of deep learning models also necessitates experience and the trial-and-error process to adjust a significant number of model tuning parameters.

In general, based on recent reviewing works performed by Koch et al. [20]; Feng and Feng [21]; Dong and Catbas [22]; and Yadhunath et al. [23], there is an increasing trend of applying image processing and machine learning for automatically detecting concrete surface distresses including spall. Therefore, investigations of other image processing tools and machine learning frameworks are helpful to provide a broader view on the possibility and capability of computer vision methods in dealing with the task at hand. It is also noted that although various models for spall object detection have been put forward and verified, few studies have constructed spall severity classification models based on two-dimensional digital images. Such models can be immensely helpful for the decision maker and building maintenance agencies to schedule their maintenance and prioritize their budgets spent on treatment of building elements effectively.

In addition, although machine learning methods have been extensively used in computer vision-based structural health monitoring [3, 12, 24–26], hybrid approaches that combine the strengths of machine learning and metaheuristic algorithms are rarely investigated in this field especially for concrete spall recognition. Metaheuristic algorithms can be used to optimize the learning phase of machine learning models and therefore help to achieve better predictive performances [27–33].

Accordingly, the current study aims at contributing to the body of knowledge by constructing a hybrid machine learning and metaheuristic approach used for computer vision-based concrete spall severity recognition. The employed machine learning method is support vector machine [34] because SVM has been proven to be a highly capable tool for pattern recognition especially for nonlinear and multivariate datasets [35–40]. To optimize the performance of SVM, a novel and recently proposed metaheuristic approach of jellyfish search is utilized.

The jellyfish search metaheuristic algorithm is employed to identify the most suitable tuning parameters of the SVM model that yields the desired predictive performance on reinforced concrete spall severity recognition. SVM is used in this study to recognize concrete surface subject to the defects of shallow spall and deep spall. Herein, the first class represents spall objects with its depth smaller than the concrete cover; the latter class contains spall objects having their embedded reinforcement exposed.

Moreover, since the areas of the aforementioned classes have different surfacing properties such as coarseness/fineness, image texture descriptors of statistical measurements of color channels [41], gray-level run length [42, 43], and center-symmetric local binary pattern [44] are used to characterize the surface properties of concrete used for spall severity classification. These texture descriptors have been selected by this study due to their ease of implementation, fast computation, and good discriminative capability [8, 45–50]. In addition, as demonstrated in previous studies [25, 51, 52], the combination of image's color properties and texture is able to bring about good image classification accuracy.

In summary, the main contribution of the current study to the body of knowledge can be stated as follows:

(i) This study proposes and verifies a computer vision-based method that is capable of categorizing concrete spall severity. This approach can significantly boost the productivity and effectiveness of the periodic survey on the structural health of concrete elements.

(ii) The proposed approach is a hybridization of JSO metaheuristic and SVM. The JSO algorithm is used to optimize the SVM training phase automatically.

(iii) The integration of various texture descriptors, which include statistical measurements of color channels, gray-level run length, and center-symmetric local binary pattern, aims at describing the surface feature of concrete surface effectively.

(iv) The computer vision-based method is trained and optimized automatically with minimum human intervention and effort on parameter fine-tuning.

The subsequent sections of the study are organized as follows. Section 2 reviews the research methodology. The next section describes the structure of the proposed computer vision-based approach employed for spall severity classification. Experimental results are reported in Section 4. Concluding remarks and main research findings are summarized in the last section of the article.

2. Research Methodology

This section of the article presents the research methodology of the current study. The research methodology includes four main sections: image acquisition, image texture computation, model optimization, and model construction. The overall research methodology is depicted in Figure 2. The subsequent parts of this section review the image texture descriptors used for feature extraction, the machine learning, and the metaheuristic algorithm employed for model optimization.
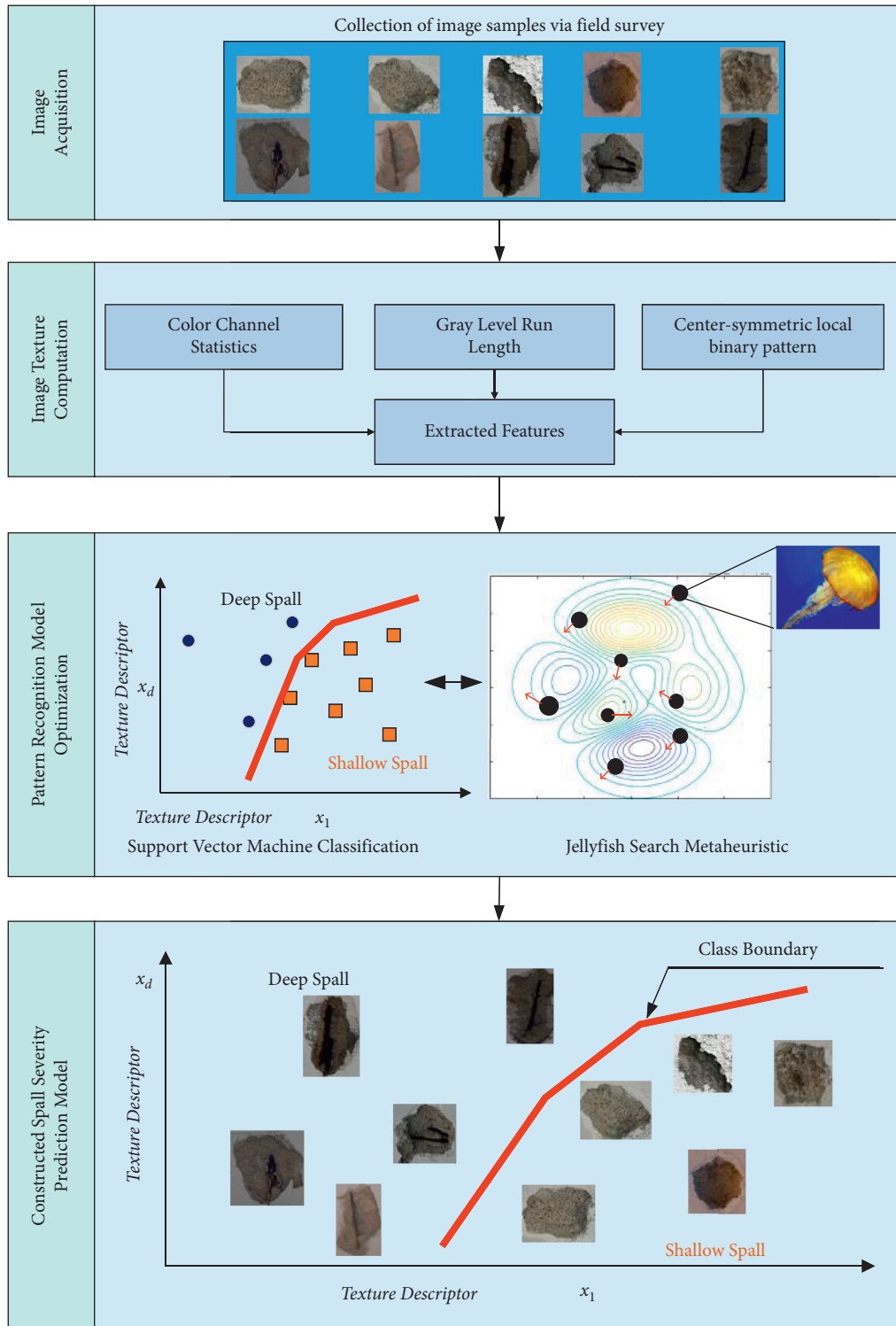
FIGURE 2: Research methodology overview.

2.1. The Employed Image Texture Descriptors. It is observable that surfacing properties of concrete with different categories of spalling severity can be used for pattern classification. Therefore, this study relies on the statistical measurement of image pixel intensity [41], the gray-level run length [42, 43], and the center-symmetric local binary pattern for concrete spall severity classification [44].

2.1.1. Statistical Measurement of Image Pixel Intensity. This study relies on 2-dimensional RGB image samples to recognize concrete spall severity. One image sample has three color channels of red (R), green (G), and blue (B) and is commonly represented by three separated matrices, each of which contains information of pixel intensity in one color channel. To extract the statistical

measurements of image pixel intensity of an image sample I, it is necessary to establish the first-order histogram $P(I)$ describing the statistical distribution of pixels' gray level. Using $P(I)$, the metrics of mean (μ_c), standard deviation (σ_c), skewness (δ_c), kurtosis (η_c), entropy (ρ_c), and range (Δ_c) are computed for a color channel $c = \{R, G, B\}$. Since each color channel yields six statistical measurements, the total number of features describing the pixel intensity distribution of one image sample with three color channels is $6 \times 3 = 18$.

The indices of mean (μ_c), standard deviation (σ_c), skewness (δ_c), kurtosis (η_c), entropy (ρ_c), and range (Δ_c) are obtained in the following equations [51]:

$$\mu_c = \sum_{i=0}^{NL-1} I_{i,c} \times P_c(I),$$

$$\sigma_c = \sqrt{\sum_{i=0}^{NL-1} \left(I_{i,c} - \mu_c \right)^2 \times P_c(I)},$$

$$\delta_c = \frac{\sum_{i=0}^{NL-1} \left(I_{i,c} - \mu_c \right)^3 \times P_c(I)}{\sigma_c^3},$$

$$\eta_c = \frac{\sum_{i=0}^{NL-1} \left(I_{i,c} - \mu_c \right)^4 \times P_c(I)}{\sigma_c^4},$$

$$\rho_c = - \sum_{i=0}^{NL-1} P_c(I) \times \log_2 \left(P_c(I) \right),$$

$$\Delta_c = \text{Max}\left(I_c\right) - \text{Min}\left(I_c\right),$$

where $NL = 256$ represents the number of discrete intensity values, c is the index of color channels (R, G, or B), and $P(I)$ denotes the first-order histogram of an image.

2.1.2. Gray-Level Run Length (GLRL). GLRL, proposed in [42], is a powerful method for extracting statistical properties of spatial distribution of gray levels. This method utilizes higher-order statistics that analyze the joint distribution of multiple pixels [48]. First, GLRL matrices are computed from a gray-scale image. Subsequently, the occurrence of runs of pixels in a given direction is inspected and statistically quantified. GLRL is useful for characterizing the coarseness or fineness of image region due to the observation that coarse textures are presented by a large number of neighboring pixels featuring the same gray intensity. On the contrary, a small number of neighboring pixels with similar gray-level intensity are observed in fine textures. Given an image of interest, the GLRL constructs a run-length matrix as the number of runs that stems from a location (i, j) of the image in a certain direction [47]. Commonly, for one image sample, four GLRL matrices are computed for the horizontal direction, vertical directions, and two diagonal directions [53].

Let $p(i, j)$ denote a run-length matrix, and the short run emphasis (SRE), long run emphasis (LRE), gray-level nonuniformity (GLN), run length nonuniformity (RLN), and run percentage (RP) are calculated as follows [19, 42]:

$$SRE = \frac{1}{N_r} \sum_{i=1}^{M} \sum_{j=1}^{N} \frac{p(i, j)}{j^2},$$

$$LRE = \frac{1}{N_r} \sum_{i=1}^{M} \sum_{j=1}^{N} p(i, j) \times j^2,$$

$$GLN = \frac{1}{N_r} \sum_{i=1}^{M} \left(\sum_{j=1}^{N} p(i, j) \right)^2, \qquad (2)$$

$$RLN = \frac{1}{N_r} \sum_{j=1}^{N} \left(\sum_{i=1}^{M} p(i, j) \right)^2,$$

$$RP = \frac{N_r}{N_p},$$

where M and N denote the number of gray levels and the maximum run length, N_r represents the total number of runs and N_p is the number of pixels, and i and j denote the coordinates of a pixel within an image sample.

In addition to the aforementioned indices, Chu et al. [54] proposed the low gray-level run emphasis (LGRE) and high gray-level run emphasis (HGRE) described as follows:

$$LGRE = \frac{1}{N_r} \sum_{j=1}^{N} \sum_{i=1}^{M} \frac{p(i, j)}{i^2},$$

$$\qquad (3)$$

$$HGRE = \frac{1}{N_r} \sum_{j=1}^{N} \sum_{i=1}^{M} p(i, j) \times i^2.$$

Dasarathy and Holder [55] put forward additional indices extracted from GLRL matrices. These indices are the short run low gray-level emphasis (SRLGE), short run high gray-level emphasis (SRHGE), long run low gray-level emphasis (LRLGE), and long run high gray-level emphasis (LRHGE); their equations are given by

$$SRLGE = \frac{1}{N_r} \sum_{j=1}^{N} \sum_{i=1}^{M} \frac{p(i, j)}{i^2 \times j^2},$$

$$SRHGE = \frac{1}{N_r} \sum_{j=1}^{N} \sum_{i=1}^{M} \frac{p(i, j) \times i^2}{j^2},$$

$$\qquad (4)$$

$$LRLGE = \frac{1}{N_r} \sum_{j=1}^{N} \sum_{i=1}^{M} \frac{p(i, j) \times j^2}{i^2},$$

$$LRHGE = \frac{1}{N_r} \sum_{j=1}^{N} \sum_{i=1}^{M} p(i, j) \times i^2 \times j^2.$$

2.1.3. Center-Symmetric Local Binary Pattern (CS-LBP).

CS-LBP, proposed in [44], is a modified version of the standard local binary pattern (LBP) [56, 57]. CS-LBP inherits the capability of LBP in describing the texture of an interest region via the distribution of its local structures as well as the intolerance against illumination changes. Both CS-LBP and LBP are widely recognized as simple yet effective texture descriptors [50, 58]. Nevertheless, one major drawback of the original LBP is that it yields a long histogram and therefore produces a large number (i.e., 256) of features to be learnt. A large number of data dimensions usually impose a significant challenge for machine learning model which relies on the data to construct classifiers of interest [59, 60]. Furthermore, the standard texture descriptor is not robust in describing flat image regions [44, 58].

To improve the performance of LBP, CS-LBP is devised by proposing a new scheme of pairwise pixel comparison as shown in Figure 3.Given a patch of $\times 3$ pixels, the CS-LBP compares center-symmetric pairs of pixels in the neighborhood to yield different binary patterns. The function Δ is employed for comparing pairs of pixels; its formula is given by

$$\Delta(x) = \begin{cases} 1, & \text{if } x > T, \\ 0, & \text{otherwise,} \end{cases} \tag{5}$$

where T denotes a thresholding value employed to inspect the significance of the gray intensity differences of 2 pixels.

The center-symmetric pairs of pixel are compared to characterize the local structure of image texture. Therefore, the total number of extracted features is only 16 instead of 256 as required by LBP. In addition, to meliorate the robustness on flat image region, a thresholding value T is used to determine the significance of the gray-level differences between two pixels of interest. The thresholding value T is commonly set to be 3 as suggested in [61]. Accordingly, the formula used to compute the CS-LBP descriptor is given by

$$F_{\text{CS–LBP}}(i, k) = \sum_{i=0}^{(N/2)-1} \Delta\left(p_i - p_{i+(N/2)}\right) \times 2^i, \tag{6}$$

where i and k denote the coordination of a pixel within an image sample and $N = 8$ which is the number of neighboring pixels.

2.2. Support Vector Machine Classification (SVC).

The pattern recognition method of SVC was first proposed in [34]. This method is a highly effective tool suitable for dealing with classification tasks in high-dimensional space. In this study, SVC is used to categorize the input image data into two class labels of deep and shallow concrete spalling. Let $D = \{(x, y)|x \in S \text{ and } y = f(x)\}$ denote a training dataset. Herein, the input feature refers to numerical data extracted by the aforementioned texture descriptors of the statistical measurement of color channels, GLRL, and CS-LBP. Using SVC, an approximated function $\hat{f}(x): X \longrightarrow \{-1, +1\}$ can be established with the label -1 which means "shallow spall" and the label $+1$ which corresponds to "deep spall."

To cope with nonlinear separable datasets, SVC relies on kernel functions to construct a mapping from the original input space to a high-dimensional feature space within
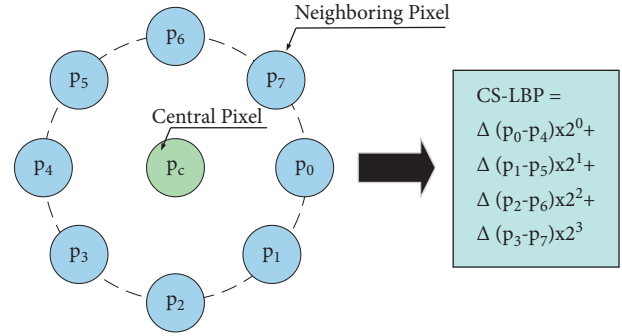
FIGURE 3: Demonstration of the CS-LBP texture descriptor.

which linear separation of datasets is feasible. The data mapping and the construction of a hyperplane used for data separation are demonstrated in Figure 4. To establish such hyperplane, the following nonlinear optimization problem must be solved:

$$\text{minimize } J_p(w, e) = \frac{1}{2}w^T w + C\frac{1}{2}\sum_{k=1}^{N} e_k^2$$

$$\text{subjected to} \quad y_k\left(w^T \varphi(x_k) + b\right) \geq 1 - e_k, \quad k = 1, \ldots, N, \ e_k \geq 0, \tag{7}$$

where $w \in R^n$ and $b \in R$ are the parameters of the hyperplane, e denotes the vector of slack variables, and C and $\varphi(x)$ represent the penalty coefficient and the nonlinear data mapping function, respectively.

In the formulation of a SVC model, the explicit form of the mapping function is not required. Instead of that, the dot product of $\varphi(x)$ denoting a kernel function $K(x_k, x_l)$ can be obtained. For nonlinear pattern recognition, the kernel function of choice is the radial basis kernel function (RBKF) [62]; its formula is given by

$$K(x_k, x_l) = \exp\left(-\frac{\|x_k - x_l\|^2}{2\sigma^2}\right), \tag{8}$$

where σ denotes a hyperparameter of the kernel function.

2.3. Jellyfish Search (JS) Metaheuristic.

As can be shown in the previous section, the establishment of a SVC model used for spall severity classification requires a suitable determination of the penalty coefficient C and the kernel function-based data mapping which is reflected in the tuning parameter σ of the RBKF. The penalty coefficient C indicates the amount of penalty suffered by misclassified data samples during the model training phase; the tuning parameter σ of the RBKF controls the locality of the kernel function which influences the generalization of a SVC model [63].

It is noted that the task of searching for those hyperparameters can be considered as a global optimization problem [28, 32, 64–71]. Moreover, since C and σ are searched in continuous space, the number of parameter combinations is infinitely large. This fact makes an exhaustive search for the best

FIGURE 4: Demonstration of the SVC-based spalling severity classification.

hyperparameters infeasible. Therefore, this study employs on the JS metaheuristic to tackle such optimization problem.

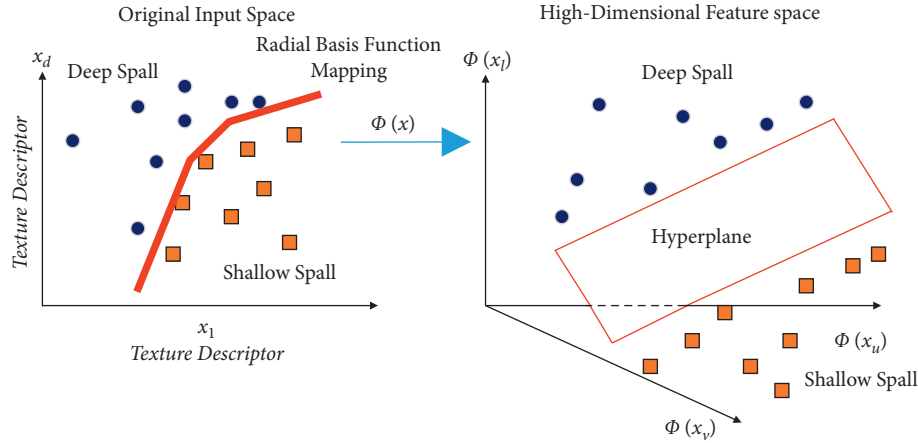The JS metaheuristic, proposed in [72], is a nature-inspired algorithm highly suitable for solving global optimization problems. This metaheuristic is motivated by the behaviors of jellyfish in the ocean. Herein, each searching agent is modeled as a jellyfish. The movements of searching agents in an artificial ocean which is the search space of interest mimic their actually movements in the real-world ocean which are governed by the ocean current, the motion within a swarm, and a time control mechanism for motion mode changing.

Chou and Truong [72] proposed three idealized rules to formulate the JS optimization algorithm. The first rule is that the jellyfish may either follow the ocean current or change their locations within a swarm and there is a time control function that governs their switching of motion type. The second rule is that the jellyfish alter their location in order to search for better food source. The third rule is that the fitness of a location (reflected in the value of the cost function) as well as the jellyfish at this location is proportionate to the amount of food.

After a swarm of jellyfish is randomly generated, the searching agents start to explore and exploit the artificial ocean to search for better food source. The first type of jellyfish movement is following the ocean current. Herein, the direction of the current is expressed as follows:

$$T = X_{\text{Best}} - \beta \times \text{rand} \times \frac{\sum_{i=1}^{\text{NJ}} X_i}{\text{NJ}}, \tag{9}$$

where T denotes the direction of the ocean current, X_{Best} is the location of the current best jellyfish, NJ is the number of jellyfish, $\beta = 3$ is the scaling factor, and rand denotes a uniform random number within $[0, 1]$.

Accordingly, the location of a jellyfish is updated via

$$\begin{aligned} X_i(t + 1) &= X_i(t) + \text{rand} \times T \\ &= X_i(t) + \text{rand} \times \left(X_{\text{Best}} - \beta \times \text{rand} \times \frac{\sum_{i=1}^{\text{NJ}} X_i}{\text{NJ}} \right). \end{aligned} \tag{10}$$

Inside a swarm, jellyfish demonstrate both passive and active motions [73, 74]. Initially, when a swarm has just been established, the jellyfish tend to exhibit passive motion. Subsequently, the jellyfish have the tendency to follow active motion. The passive motion is mathematically formulated as follows:

$$X_i(t + 1) = X_i(t) + \gamma \times \text{rand} \times (\text{UB} - \text{LB}), \tag{11}$$

where $\gamma = 0.1$ is a motion coefficient and LB and UB are the lower and upper boundaries of the search variables.

The active motion of jellyfish is determined by the quantity of food stored in a randomly selected location. Generally, jellyfish approach a better food source in a swarm. The location of an individual within a swarm is iteratively revised as follows:

$$X_i(t + 1) = X_i(t) + \text{rand} \times \text{DJ},$$

$$\text{DJ} = \begin{cases} X_j(t) - X_i(t), & \text{if } f(X_i) \geq f(X_j), \\ X_i(t) - X_j(t), & \text{if } f(X_i) < f(X_j), \end{cases} \tag{12}$$

where DJ denotes the direction of a jellyfish, X_i is the target jellyfish, X_j is a randomly selected jellyfish within the swarm, and f denotes the cost function of the problem of interest.

Furthermore, to govern the movement of jellyfish between following the ocean current and moving inside the swarm, the time control mechanism including a time control function $c(t)$ and a constant $C_0 = 0.5$ is employed. The time control function yields a random value ranging from 0 to 1. If the value of $c(t)$ surpasses C_0, the jellyfish attach to the ocean current. On the contrary, the jellyfish move within a swarm. The time control function is mathematically described as follows:

$$c(t) = \left| \left(1 - \frac{t}{T_{\text{Max}}} \right) \times (2 \times \text{rand} - 1) \right|, \tag{13}$$

where T_{Max} denotes the maximum number of searching iterations.

2.4. The Collected Image Samples.

The objective of this work is to process image samples of reinforced concrete surface for the task of spalling severity classification. To achieve such

objective, this study has carried out field surveys in Danang city (Vietnam) to collect image samples of reinforced concrete surface. This image set includes two categories of shallow spalling and deep spalling. The first category consists of spalling objects in which the depth of spalling is smaller than the concrete cover layer. The second category includes spalling objects in which reinforcing bars have been exposed to the outside environment.

The total number of collected image samples is 300; the number of data in each category is 150 to ensure a balanced classification problem. The collected image samples are illustrated in Figure 5. It is noted that the image samples have been captured by the 18-megapixel resolution Canon EOS M10 and the 16.2-megapixel resolution Nikon D5100. The labels of the image data have been assigned by human inspectors.

3. The Computer Vision-Based Jellyfish Search Optimized Support Vector Classification (JSO-SVC) for Concrete Spalling Severity Classification

This section of the article aims at describing the overall structure of the proposed computer vision-based approach used for automatic classification of concrete spalling severity. The overall structure of the newly developed approach consists of three modules: (i) image texture computation, (ii) JS-based model optimization, and (iii) SVC-based spalling severity categorization based on input image samples. Figure 6 demonstrates integrated modules of the proposed model named as JSO-SVC. The proposed method for automatic classification of concrete spalling severity is an incorporation of image texture descriptions, supervised machine learning-based pattern recognition, and stochastic search-based model optimization.

The image texture description methods of statistical measurements of pixel intensity, GLRL, and CS-LBP are used to extract texture-based features from the collected digital images. The SVC pattern recognizer assisted by the JS stochastic search is employed to establish a class boundary that divided the input feature space into two categories of "shallow spall" and "deep spall." The role of the JS stochastic search is to optimize the parameter setting of the SVC model. It is noted that the texture computation module has been developed by the authors in Microsoft Visual Studio with Visual C# .NET. Furthermore, the SVC model optimized by the JS algorithm is coded in MATLAB environment with the help of the Statistics and Machine Learning Toolbox [75] and the source code of JS which can be accessed at [76]. The optimized computer vision-based model which relies on the module of texture computation and the JS-SVC model has been coded and compiled in Visual C# .NET Framework 4.7.2 and the built-in functions provided by the Accord.NET Framework [77].

To characterize the properties of concrete surface, this study relies on texture description methods of statistical measurements of pixel intensity, GLRL, and CS-LBP. The first texture descriptor measures statistical indices of the three color channels (red, green, and blue). For each channel, six indices of mean, standard deviation, skewness, kurtosis, entropy, and range are computed. Therefore, the first descriptor produces $3 \times 6 = 18$ features. Moreover, since one objective of the study is to detect the appearance of reinforcing bars within an image sample, the occurrence of runs of pixels in a given direction can be useful. Thus, it is beneficial to employ the GLRL approach in the feature extraction phase. Four GLRL matrices with orientations of $0°$, $45°$, $90°$, and $135°$ are computed, each of which yields 11 statistical measurements. Accordingly, the GLRL descriptor produces $4 \times 11 = 44$ features. Finally, the CS-LBP texture description method is computed to characterize the local pattern of image regions. It is noted that to compute the CS-LBP, the number of neighboring pixels around a central pixel is 8. In other words, the radius of this texture descriptor is 1 pixel. As mentioned earlier, the CS-LBP yields 16 texture-based features. Accordingly, the total number of texture-based features used for spall severity classification is $18 + 44 + 16 = 78$. The texture computation processes for the two class labels of interest area are demonstrated in Figure 7.

To train and validate the proposed JSO-SVC model, the collected dataset has been randomly partitioned into a training set (90%) and a testing set (10%). The training set is used for model construction phase; the testing set is reserved for inspecting the model predictive capability when predicting unseen data sample. In addition, prior to the model training phase, the Z-score normalization is commonly employed preprocess the extracted features [78]. Accordingly, all of the extracted features are approximately centered at 0 and have a unit standard deviation. The Z-score equation is given by

$$X_Z = \frac{X_D - M_X}{\text{STD}_X}, \tag{14}$$

where X_Z and X_D denote the normalized and the original input data, respectively, and M_X and STD_X represent the mean value and the standard deviation of the original input data, respectively.

In addition, the jellyfish stochastic search with 20 jellyfish is used to assist the SVC training phase. It is noted that the number of optimization iterations of the JS metaheuristic is 100. The JS algorithm's parameters including the scaling factor (β), the motion coefficient (γ), and the parameter C_0 of the time control function are set to be 3, 0.1, and 0.5 according to the suggestions of Chou and Truong [72].

This stochastic search engine optimizes the model selection of the SVC model used for spall severity classification via an appropriate setting of the model hyperparameters. Through operations based on ocean current following and motions within a swarm, a population of jellyfish gradually explores and exploits an artificial ocean and identifies a good set of the penalty coefficient and the RBFK parameter. Herein, the lower and upper boundaries of the searched variables are [0.1, 0.01] and [1000, 1000], respectively. Furthermore, to effectively optimize the machine learning model, a 5-fold cross-validation-based objective function has been employed. This objective function of the JSO-SVC is given by [19]
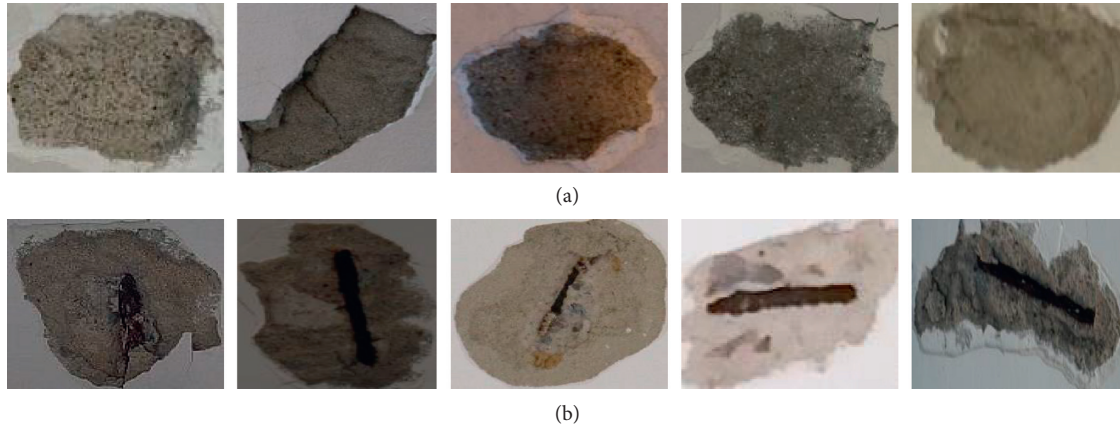
(a)

(b)

FIGURE 5: Demonstration of the collected image samples: (a) class label −1 (shallow spall) and (b) class label +1 (deep spall).

$$F_{\text{JSO–SVC}} = \frac{\sum_{k=1}^{5}\left(\text{FNR}_k + \text{FPR}_k\right)}{5}, \tag{15}$$

where FNR_k and FPR_k denote false negative rate (FNR) and false positive rate (FPR) computed in the kth data fold, respectively.

The FNR and FPR metrics are given by

$$\text{FNR} = \frac{\text{FN}}{\text{FN} + \text{TP}},$$
$$\text{FPR} = \frac{\text{FP}}{\text{FP} + \text{TN}}, \tag{16}$$

where FN, FP, TP, and TN refer to the false negative, false positive, true positive, and true negative data samples, respectively.

4. Experimental Results and Discussion

As mentioned earlier, the JS-SVC model has been coded and complied in Visual C# .NET Framework 4.7.2. Moreover, experiments with the compiled computer program have been performed on the ASUS FX705GE-EW165T (Core i7 8750H and 8 GB Ram) platform. The JS metaheuristic is used to fine-tune the SVC-based spall severity classification approach. After 100 iterations, the JS metaheuristic has located the best values of the search variables as follows: the penalty coefficient = 867.6788 and the RBKF parameter = 58.6156. The best-found cost function value is 1.0696. The optimization process of the jellyfish swarm is demonstrated in Figure 8.

As described in the previous section, the collected dataset which includes 300 data samples has been randomly separated into a training set (90%) and a testing set (10%). Moreover, to reliably evaluate the predictive performance of the proposed JSO-SVC, this study has repeated the model training and testing processes with 20 independent runs. The statistical measurements obtained from these 20 independent runs are employed to quantify the model predictive capability in the task of concrete spalling severity recognition. This repeated model evaluation aims at reducing the variation caused by the randomness in the data separation process.

In addition, to demonstrate the JSO-SVC predictive performance, the random forest classification (RFC) model [79] and convolutional neural network (CNN) models [80] have been employed as benchmark approaches. The RFC and CNN are selected for result comparison in this study because these two machine learning approaches have been successfully applied in various works related to computer vision-based or nondestructive testing-based structural health monitoring/diagnosis [14, 26, 81–88].

The RFC has been constructed with the MATLAB's Statistics and Machine Learning Toolbox [75]. Adaptive moment estimation (Adam) [89] and root mean square propagation (RMSprop) [90] are the two state-of-the-art approaches for training the deep neural network. The CNN models trained by Adam and RMSprop are denoted as CNN-Adam and CNN-RMSprop, respectively. These two models are constructed with the help of the MATLAB deep learning toolbox [91]. The model structures of the benchmark methods have been identified via several trial-and-error experiments with the collected dataset. The number of classification trees used in the random forest ensemble is 50. In addition, the two CNN models have been trained with 3000 epochs and the batch size of 8. The employed CNN models have been trained with the learning rate parameter = 0.001; moreover, L_2 regularization with the regularization coefficient of 0.0001 has been employed to mitigate model overfitting [91]. To implement the deep neural computing models, the size of the input images has been standardized to be 32×32 pixels. The model structure of the employed CNN models is shown in Table 1.

In addition, to appraise the prediction capability of the proposed JSO-SVC and the employed benchmark approaches, a set of performance measurement metrics is employed in this section. Since the problem of spall severity has been modeled as a two-class classification problem, the indices of classification accuracy rate (CAR), precision, recall, negative predictive value (NPV), $F1$ score, and area under the receiver operating characteristic curve (AUC) [92, 93] are employed to quantify the classification model
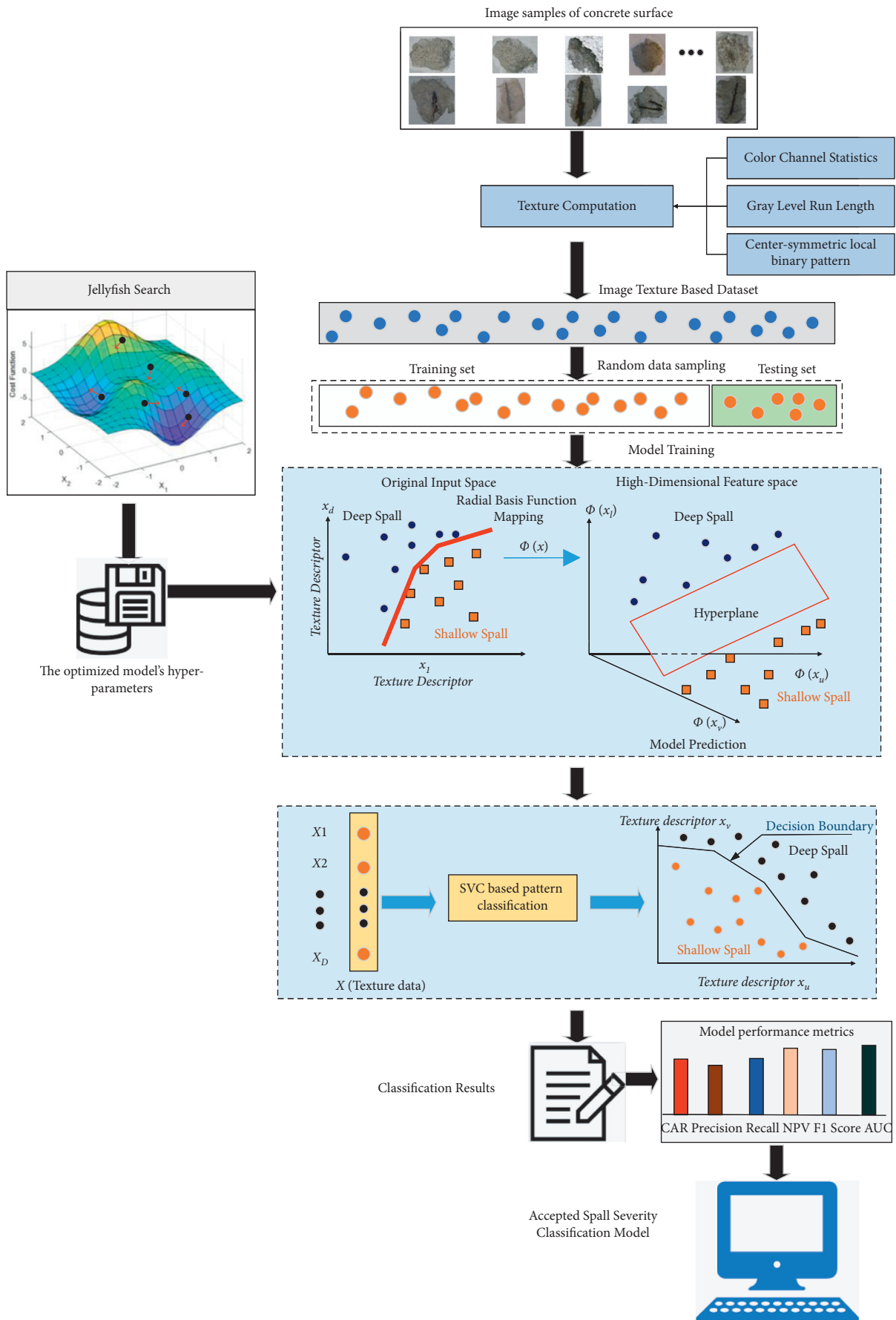
FIGURE 6: The proposed computer vision method for automatic concrete spall severity classification.

Image Sample

X1	X2	X3	X4	X5	…	X74	X75	X76	X77	X78
133.498	127.574	115.246	29.278	31.056	…	0.018	0.084	0.020	0.099	0.069

(a)

Image sample

X1	X2	X3	X4	X5	…	X74	X75	X76	X77	X78
148.035	137.513	123.466	31.532	34.691	…	0.007	0.083	0.005	0.048	0.017

(b)

FIGURE 7: Demonstration of the feature extraction process: (a) a sample of the "shallow spall" class and (b) a sample of the "deep spall" class.
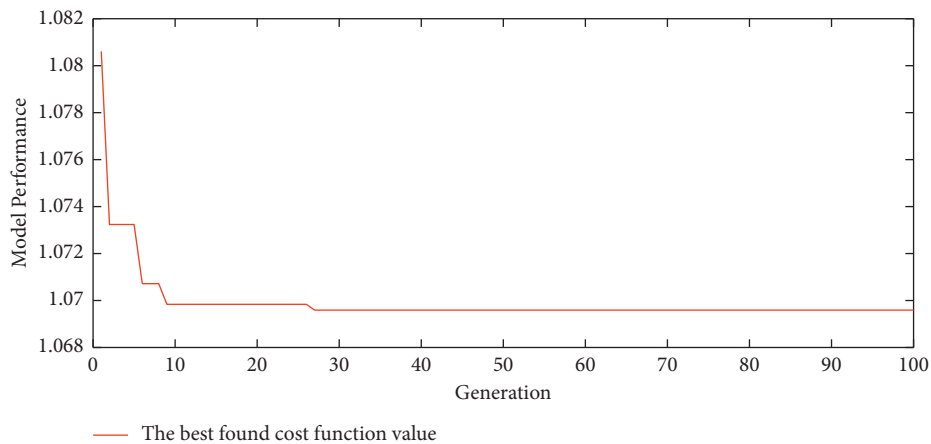
FIGURE 8: The JS-based model optimization progress.

TABLE 1: The structures of the employed CNN model.

| CNN layers | Convolutional layers | | Pooling layers |
	Number of filters	Filter size	Filter size
1	32	8	4
2	32	4	4
3	16	2	2

performance. For the plotting of the receiver operating characteristic curve and computation of the AUC, readers are guided to the previous work of van Erkel and Pattynama [94]. The detailed calculations of CAR, precision, recall, NPV, and $F1$ score are given by [92, 95]

$$\text{CAR} = \frac{N_C}{N_A} 100\%,$$

$$\text{precision} = \frac{\text{TP}}{\text{TP} + \text{FP}},$$

$$\text{recall} = \frac{\text{TP}}{\text{TP} + \text{FN}}, \qquad (17)$$

$$\text{NPV} = \frac{\text{TN}}{\text{TN} + \text{FN}},$$

$$F1 \text{ score} = \frac{2\text{TP}}{2\text{TP} + \text{FP} + \text{FN}},$$

where N_C and N_A denote the numbers of correctly predicted data and the total number of data, respectively. As mentioned earlier, FN, FP, TP, and TN represent the false negative, false positive, true positive, and true negative data samples, respectively.

The prediction performances of the proposed JSO-SVC and other benchmark methods are shown in Table 2 which reports the mean and standard deviation (Std) of the employed performance measurement metrics. Observable from this table, the proposed hybridization of JS and SVC has at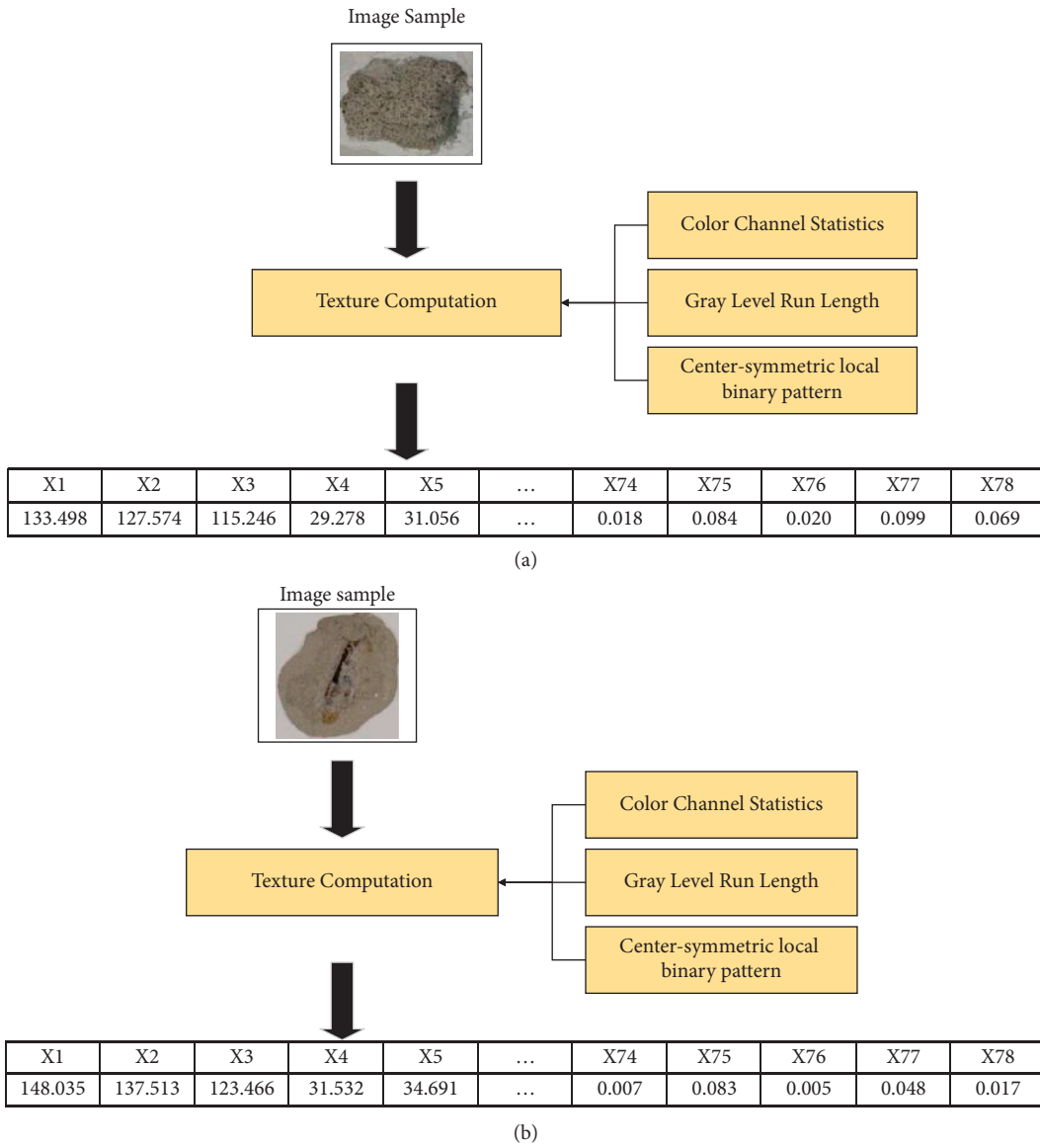tained the most accurate classification of concrete spalling severity with CAR = 93.333%, precision = 0.932, recall = 0.936, NPV = 0.963, and $F1$ score = 0.933. The model construction phase of the JSO-SVC requires a computational time of 1067.4 s. The computational time of the proposed approach is roughly 3.3 s.

The RFC is the second best method with CAR = 87.500%, precision = 0.871, recall = 0.890, NPV = 0.892, and $F1$ score = 0.877, followed by CNN-Adam (CAR = 81.500%, precision = 0.877, recall = 0.750, NPV = 0.788, and $F1$ score = 0.799) and CNN-RMSprop (CAR = 79.167%, precision = 0.809, recall = 0.777, NPV = 0.794, and $F1$ score = 0.785). With CAR > 90% and $F1$ score > 0.9, it can be seen that the predictive result of the JSO-SVC is highly accurate. The performance of the decision tree ensemble of RFC with CAR = 87.5% and $F1$ score = 0.877 is fairly accurate and acceptable. Meanwhile, with CAR values of around 80% and $F1$ score approaching 0.8, the performance of the CNN models is clearly inferior to the machine learning approaches of JSO-SVC and RFC. The boxplots demonstrating the statistical distributions of the models' performance in terms of CAR and $F1$ score

obtained from 20 independent runs are provided in Figures 9 and 10.

Besides the aforementioned metrics, ROC curves and AUC are also important indicators of classification performance. A ROC curve is a graph depicting the performance of a model when classification threshold varies. The horizontal axis of the graph is the false positive rate and the vertical axis of the graph is the true positive rate. The ROC curves of the proposed JSO-SVC and other benchmark models are provided in Figures 11–14. From those curves, the AUC values can be computed. AUC measures the two-dimensional area beneath the ROC curves. This indicator depicts an aggregate evaluation of the model performance with all possible values of the classification threshold. AUC varies between 0 and 1 with 0 indicating a useless classifier and 1 demonstrating a perfect classifier. Observed from the experimental outcomes, the JSO-SVC has also attained the highest AUC of 0.969, followed by RFC (AUC = 0.944), CNN-Adam (AUC = 0.896), and CNN-RMSprop (AUC = 0.855). The boxplot of the AUC results is illustrated in Figure 15.

In addition, to reliably assert the superiority of the newly developed JSO-SVC model used for concrete spalling severity classification, this study has employed the Wilcoxon signed-rank test [96] with the significant level (p value) = 0.05. The Wilcoxon signed-rank test is a widely employed nonparametric statistical hypothesis test used for model performance comparison [97]. One significant advantage of this statistical hypothesis test is that it does not require the assumption of normally distributed data [65]. Therefore, the Wilcoxon signed-rank test offers robust statistical power and is likely to yield statistical significant outcome.

The important performance measurement metrics of CAR, $F1$ score, and AUC are subject to this nonparametric hypothesis test. Herein, the null hypothesis is that the means of the prediction performances of two models are actually equal. The Wilcoxon signed-rank test outcomes are reported in Tables 3–5. Observably, with p values <0.05, the null hypothesis can be rejected and the superiority of the proposed hybrid method can be firmly stated.

The experimental results have shown the superiority of the JSO-SVC over deep neural computing approaches of CNN models. It can be seen that although the CNN models have been demonstrated to be powerful methods in various computer vision tasks, their performance largely depends on the size of the training samples [48]. The main advantages of CNN lie in its capability of automatic feature representation via convolutional operators and its hierarchical architecture for learning high-level features from raw data. However, both of these advantages can only be realized with a sufficiently large number of image samples with correct ground truth labeling. As stated in [98], when the number of training samples is insufficient, the performance of deep learning models can be inferior to those of hand-crafted features-based prediction approaches.

For the case in which there are a limited number of data samples, the CNN models have difficulties in properly fine-tuning their internal structures with a huge number of parameters needed to be specified in various hidden layers

TABLE 2: Experimental result comparison.

| Phase	Metrics	JSO-SVC		RFC		CNN-Adam		CNN-RMSprop	
		Mean	Std	Mean	Std	Mean	Std	Mean	Std
Training	CAR (%)	95.926	0.574	98.500	0.441	90.278	3.341	89.056	5.207
	Precision	0.950	0.008	0.978	0.005	0.932	0.052	0.915	0.062
	Recall	0.969	0.007	0.993	0.006	0.875	0.079	0.870	0.113
	NPV	0.969	0.007	0.993	0.006	0.887	0.060	0.886	0.076
	$F1$ score	0.960	0.006	0.985	0.004	0.899	0.039	0.885	0.068
	AUC	0.983	0.002	0.998	0.001	0.966	0.025	0.952	0.039
Testing	CAR (%)	93.333	3.801	87.500	4.941	81.500	5.669	79.167	8.298
	Precision	0.932	0.048	0.871	0.070	0.877	0.090	0.809	0.104
	Recall	0.936	0.062	0.890	0.069	0.750	0.118	0.777	0.136
	NPV	0.935	0.057	0.892	0.062	0.788	0.076	0.794	0.098
	$F1$ score	0.933	0.042	0.877	0.047	0.799	0.067	0.785	0.096
	AUC	0.969	0.020	0.944	0.046	0.896	0.060	0.855	0.080
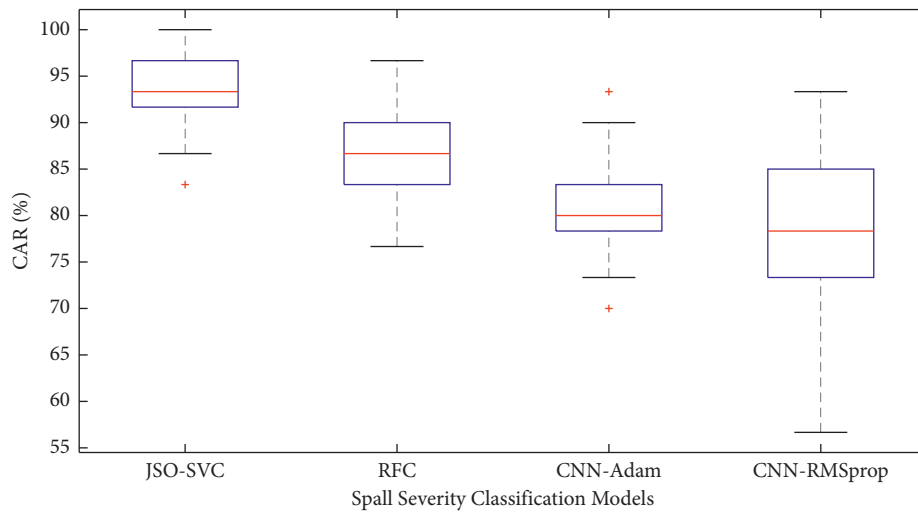
FIGURE 9: Boxplot of CAR values obtained from the employed machine learning models.
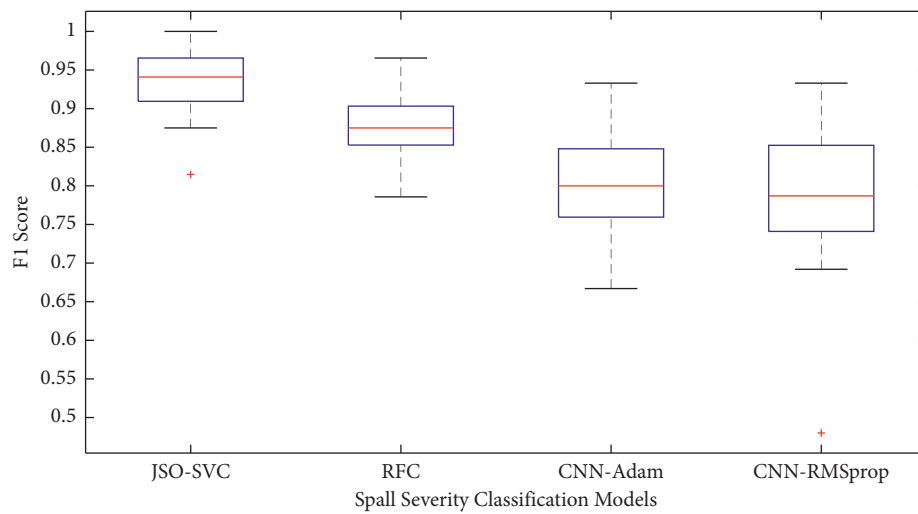
FIGURE 10: Boxplot of $F1$ score values obtained from the employed machine learning models.

(a)

(b)
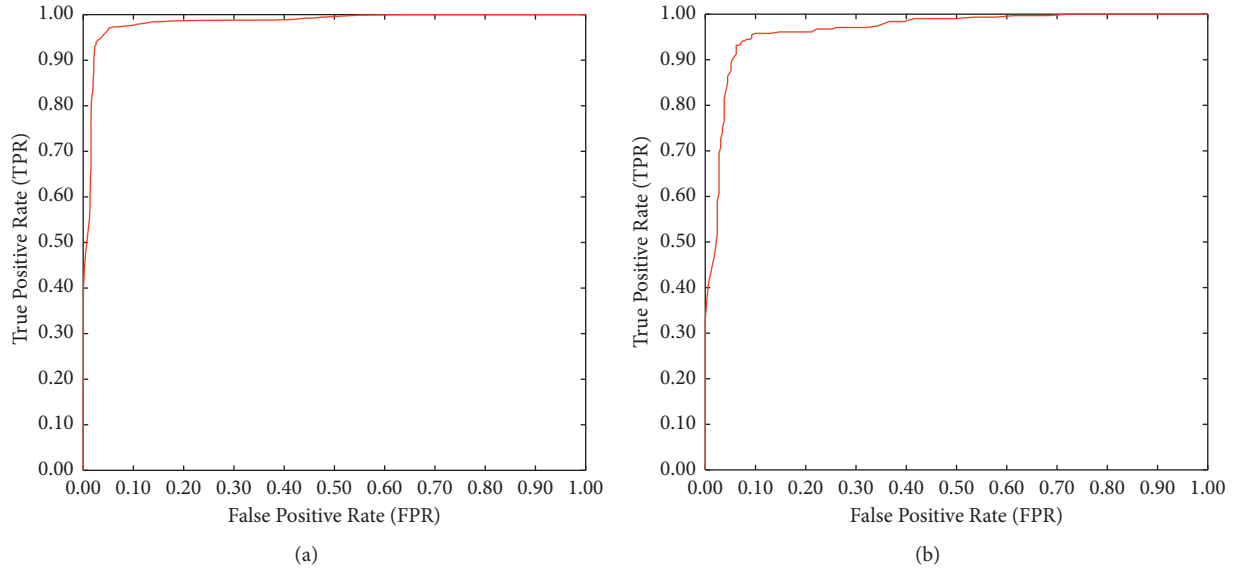
FIGURE 11: ROCs of JSO-SVC: (a) training phase and (b) testing phase.

(a)

(b)
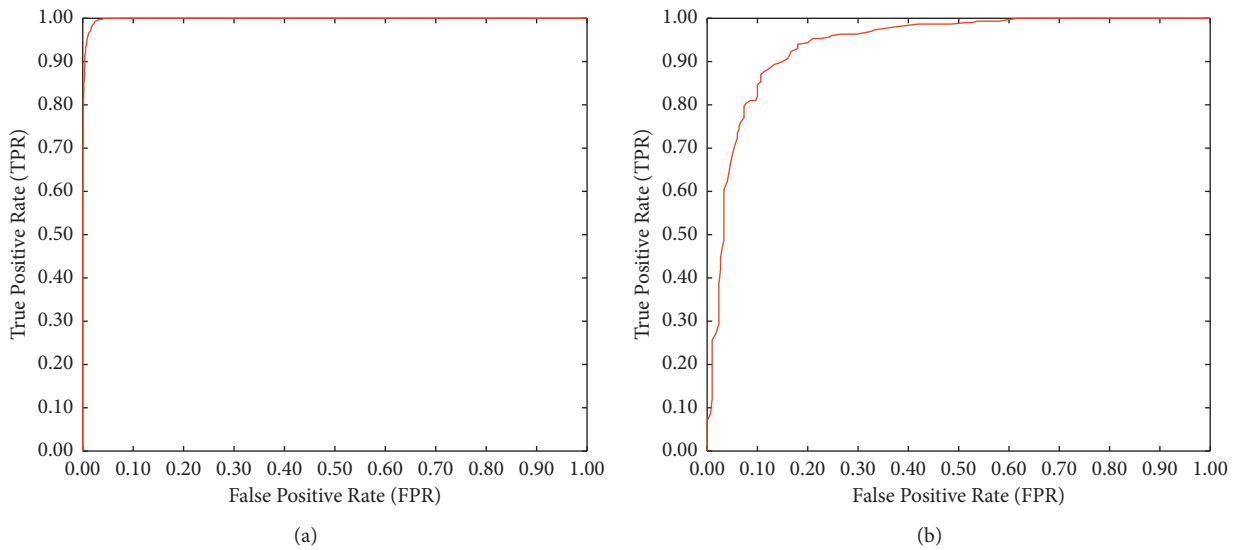
FIGURE 12: ROCs of RFC: (a) training phase and (b) testing phase.

[58, 99]. Therefore, with a dataset of 300 image samples, the hybrid machine learning method of JSO-SVC with texture-based feature extraction is capable of outperforming the CNN methods. The model optimization process via gradient descent algorithms employed by CNN encounters certain difficulty in identifying the fittest set of network parameters because the number of trained parameters greatly outnumbers the data size. This fact is partly reflected in the stability of the predictive outcomes of the deep learning models.

To quantify the stability of the model prediction, this study has employed the coefficient of variation (COV) [100]. This index is defined as the ratio of the standard deviation to the mean. Generally speaking, a small COV value indicates a

small variation of prediction result and is associated with a reliable model. The COV indices of the proposed model, RFC, and the two CNN models are reported in Figure 16. Considering the metrics of CAR, $F1$ score, and AUC, the COV of JSO-SVC (with $COV_{CAR} = 4.07\%$, $COV_{F1\text{-}score} = 4.54\%$, and $COV_{AUC} = 2.04\%$) is significantly lower than that of the CNN-Adam ($COV_{CAR} = 6.96\%$, $COV_{F1\text{-}score} = 8.35\%$, and $COV_{AUC} = 6.65\%$) and CNN-RMSprop ($COV_{CAR} = 10.48\%$, $COV_{F1\text{-}score} = 12.28\%$, and $COV_{AUC} = 9.36\%$).

On the other hand, the proposed approach based on the SVC is the pattern recognizer that lends itself to learning with small or medium-size datasets because the SVC focuses on sparseness property when building a classification model
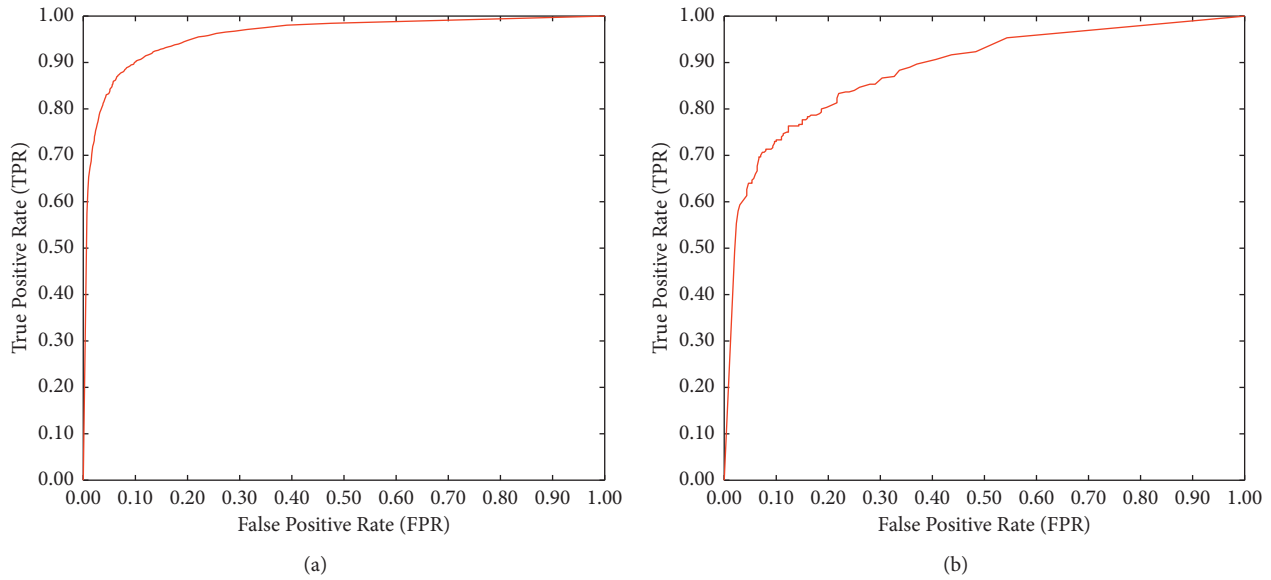
FIGURE 13: ROCs of CNN-Adam: (a) training phase and (b) testing phase.
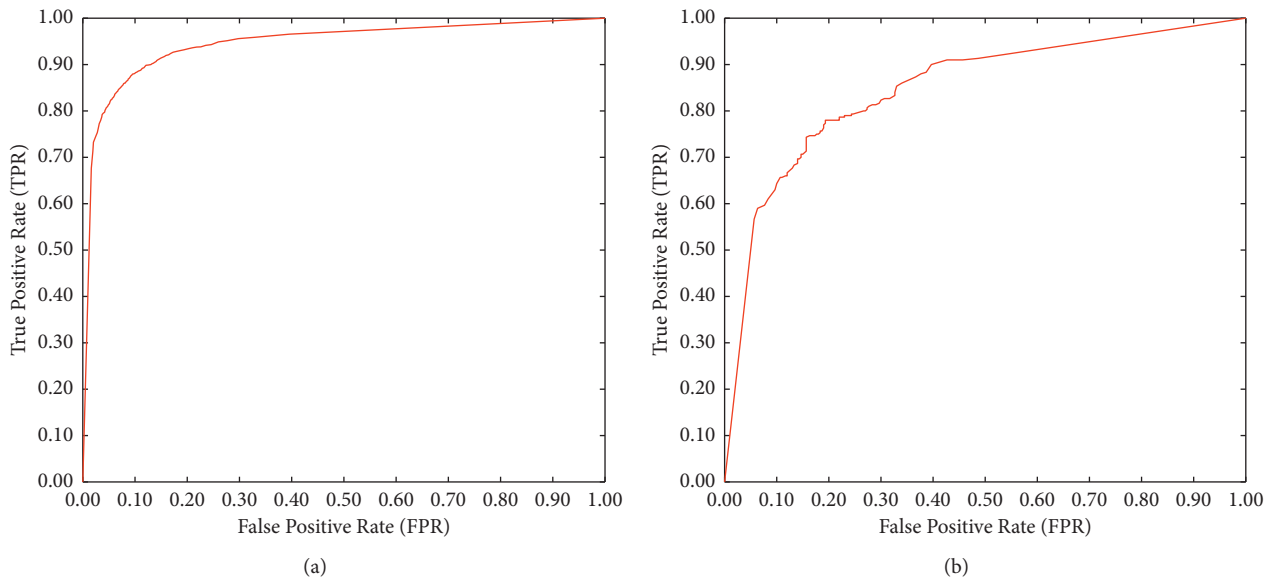
FIGURE 14: ROCs of CNN-RMSprop: (a) training phase and (b) testing phase.

from data. Put differently, the final SVC model only resorts to a small subset of the dataset to construct the classification boundary. The data points contained in such small subset are called support vectors, and they are highly relevant and informative for carrying out the task of concrete spall severity classification. This is a significant advantage of the JSO-SVC because a sparse concrete spall severity classification model is less likely to suffer from data overfitting. This point is clearly demonstrated via the learning performance (CAR = 95.926%) and testing performance (93.333%) of JSO-SVC. The accuracy rates of the proposed approaches in the training and testing phases are relatively close to each other.

The classification model based on the integration of JSO and SVC also features a high degree of learning stability due to its sparseness property because the sparse model is capable of mitigating the effect of noisy samples within the collected dataset. Moreover, the SVC model construction boils down to solving a quadratic programming problem which can guarantee a learning convergence to a global optimal solution. This feature of the JSO-SVC also facilitates the reliability and stability of the spall severity recognition performance. The aforementioned analysis on COV has revealed these facts. The COV of JSO-SVC, which is less than 5%, is comparatively lower than that of other benchmark models.
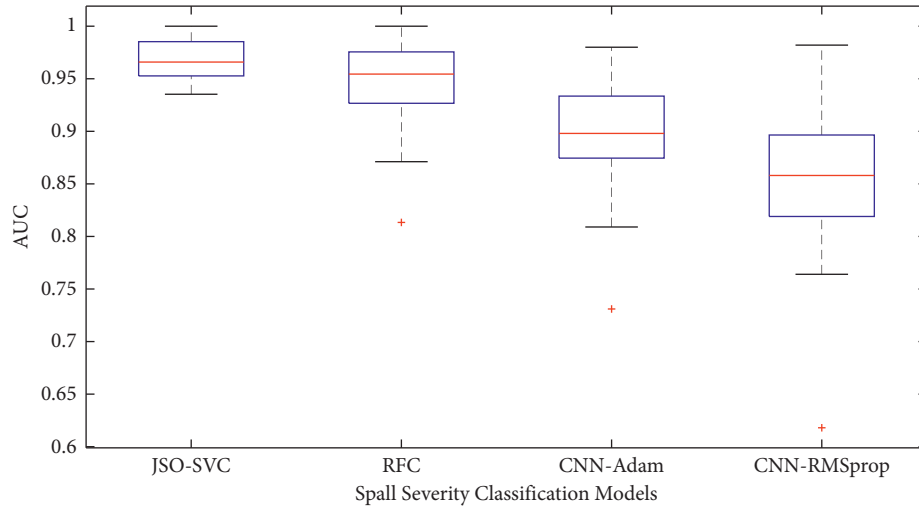
Figure 15: Boxplot of AUC values obtained from the employed machine learning models.

Table 3: p values obtained from the Wilcoxon signed-rank test results with CAR index.

Models	JSO-SVC	RFC	CNN-Adam	CNN-RMSprop
JSO-SVC	x	0.0022	0.0001	0.0002
RFC	0.0022	x	0.0043	0.0023
CNN-Adam	0.0001	0.0043	x	0.1744
CNN-RMSprop	0.0002	0.0023	0.1744	x

Table 4: p values obtained from Wilcoxon signed-rank test results with $F1$ score index.

Models	JSO-SVC	RFC	CNN-Adam	CNN-RMSprop
JSO-SVC	x	0.0028	0.0001	0.0003
RFC	0.0028	x	0.0025	0.0012
CNN-Adam	0.0001	0.0025	x	0.6274
CNN-RMSprop	0.0003	0.0012	0.6274	x

Table 5: p values obtained from Wilcoxon signed-rank test results with AUC index.

Models	JSO-SVC	RFC	CNN-Adam	CNN-RMSprop
JSO-SVC	x	0.0859	0.0002	0.0001
RFC	0.0859	x	0.0137	0.0007
CNN-Adam	0.0002	0.0137	x	0.0793
CNN-RMSprop	0.0001	0.0007	0.0793	x

However, one disadvantage of the proposed spall severity recognition model is that the optimization process required determining an optimal set of parameters of the SVC can be costly. The reason is that the SVC-based model training and prediction phases operate inside the cost function computing phase of the utilized JSO. Another limitation of the JSO-SVC-based spall severity classifier is that it has not been equipped with advanced feature selection. Such drawbacks ought to be addressed in future extensions of the current work.
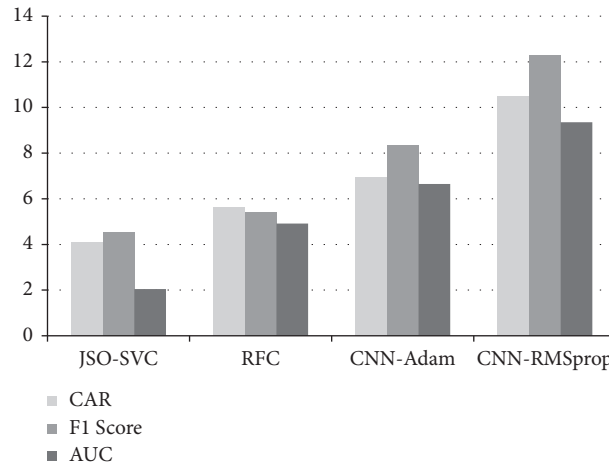
FIGURE 16: Model comparison in terms of the coefficient of variation (COV).

5. Concluding Remarks

This study has proposed and verified a computer vision-based approach for automatic classification of concrete spalling severity. The proposed approach is an integration of image texture analysis methods, metaheuristic optimization, and machine learning-based pattern recognition. The texture descriptors of statistical measurement of color channels, GLRL, and CS-LBP are used to characterize images of concrete surface with respect to color, gray pixel run length, and local structure. With such extracted features, the SVC machine learning optimized by JS metaheuristic is employed to construct a decision boundary that separates the input data into two classes of deep spalling and shallow spalling.

A dataset including 300 image samples has been collected to train the proposed computer vision method. Experimental results point out that the integrated model can help to attain the most desired spall severity classification with CAR = 93.333%, precision = 0.932, recall = 0.936, NPV = 0.963, $F1$ score = 0.933, and AUC = 0.969. These results are significantly better than those of the benchmark methods including RFC and CNN models. Therefore, the newly developed JSO-SVC can be a potential tool to assist building maintenance agencies in the task of periodic structural heath survey. Further improvements of the current approach may include the following:

(i) The utilization of the hybrid model to detect other concrete surface defects such as crack, bughole, algal colonization, and so on.

(ii) The employment of other sophisticated texture descriptors for representing characteristics of concrete surface and better dealing with noise in the surface background.

(iii) Increasing the size of the current dataset to meliorate the applicability of the current method.

(iv) Investigating the possibility of combing handcrafted texture-based features with deep learning models used for concrete spalling severity classification.

(v) Employing advanced techniques of metaheuristic-based model optimization and feature selection to enhance the performance of the spall severity recognition task.

Data Availability

The dataset used to support the findings of this study has been deposited in the repository of GitHub at https://github.com/NDHoangDTU/ConcreteSpallSeverity_JSO_SVC. The first 78 columns of the data are texture-based features extracted from image samples. The last column is the label of the data instances with 0 = "shallow spalling" and 1 = "deep spalling."

Conflicts of Interest

The authors declare that they have no conflicts of interest.

Acknowledgments

References

[1] K. Mostafa and T. Hegazy, "Review of image-based analysis and applications in construction," *Automation in Construction*, vol. 122, Article ID 103516, 2021.

[2] M. Nain, S. Sharma, and S. Chaurasia, "Safety and compliance management system using computer vision and deep learning," *IOP Conference Series: Materials Science and Engineering*, vol. 1099, no. 1, Article ID 012013, 2021.

[3] H. Sun, H. V. Burton, and H. Huang, "Machine learning applications for building structural design and performance assessment: state-of-the-art review," *Journal of Building Engineering*, vol. 33, Article ID 101816, 2021.

[4] S. German, I. Brilakis, and R. DesRoches, "Rapid entropy-based detection and properties measurement of concrete spalling with machine vision for post-earthquake safety

assessments," *Advanced Engineering Informatics*, vol. 26, no. 4, pp. 846–858, 2012.

[5] T. Dawood, Z. Zhu, and T. Zayed, "Machine vision-based model for spalling detection and quantification in subway networks," *Automation in Construction*, vol. 81, pp. 149–160, 2017.

[6] N.-D. Hoang, "Image processing-based recognition of wall defects using machine learning approaches and steerable filters," *Computational Intelligence and Neuroscience*, vol. 2018, Article ID 7913952, 18 pages, 2018.

[7] H. Wu, X. Ao, Z. Chen, C. Liu, Z. Xu, and P. Yu, "Concrete spalling detection for metro tunnel from point cloud based on roughness," *Descriptor Journal of Sensors*, vol. 2019, Article ID 8574750, 12 pages, 2019.

[8] N.-D. Hoang, Q.-L. Nguyen, and X.-L. Tran, "Automatic detection of concrete spalling using piecewise linear stochastic gradient descent logistic regression and image texture analysis," *Complexity*, vol. 2019, Article ID 5910625, 14 pages, 2019.

[9] E. M. Abdelkader, O. Moselhia, M. Marzoukb, and T. Zayedc, "Evaluation of spalling in bridges using machine vision method," in *Proceedings of the 37th International Symposium on Automation and Robotics in Construction (ISARC 2020)*, Kitakyushu, Japan, 2020.

[10] N.-D. Hoang, "Image processing-based spall object detection using gabor filter, texture analysis, and adaptive moment estimation (Adam) optimized logistic regression models," *Advances in Civil Engineering*, vol. 2020, Article ID 8829715, 16 pages, 2020b.

[11] E. Abdelkader, O. Moselhi, M. Marzouk, and T. Zayed, "Entropy-based automated method for detection and assessment of spalling severities in reinforced concrete bridges," *Journal of Performance of Constructed Facilities*, vol. 35, no. 1, Article ID 04020132, 2021.

[12] Z. Zhao, T. Liu, and X. Zhao, "Variable selection from image texture feature for automatic classification of concrete surface voids," *Computational Intelligence and Neuroscience*, vol. 2021, pp. 1–10, 2021.

[13] J. K. Chow, Z. Su, J. Wu, P. S. Tan, X. Mao, and Y. H. Wang, "Anomaly detection of defects on concrete structures with the convolutional autoencoder," *Advanced Engineering Informatics*, vol. 45, Article ID 101105, 2020.

[14] B. Kim and S. Cho, "Automated multiple concrete damage detection using instance segmentation deep learning model," *Applied Sciences*, vol. 10, no. 22, p. 8008, 2020.

[15] C. Zhang, C. c. Chang, and M. Jamshidi, "Concrete bridge surface damage detection using a single-stage detector," *Computer-Aided Civil and Infrastructure Engineering*, vol. 35, no. 4, pp. 389–409, 2019.

[16] F. Wei, G. Yao, Y. Yang, and Y. Sun, "Instance-level recognition and quantification for concrete surface bughole based on deep learning," *Automation in Construction*, vol. 107, Article ID 102920, 2019.

[17] G. Yao, F. Wei, Y. Yang, and Y. Sun, "Deep-learning-based bughole detection for concrete surface image," *Advances in Civil Engineering*, vol. 2019, Article ID 8582963, 12 pages, 2019.

[18] H. Perez, J. H. M. Tah, and A. Mosavi, "Deep learning for detecting building defects using convolutional neural networks," *Sensors*, vol. 19, no. 16, p. 3556, 2019.

[19] N.-D. Hoang and Q.-L. Nguyen, "A novel approach for automatic detection of concrete surface voids using image texture analysis and history-based adaptive differential evolution optimized support vector machine," *Advances in Civil Engineering*, vol. 2020, Article ID 4190682, 15 pages, 2020.

[20] C. Koch, K. Georgieva, V. Kasireddy, B. Akinci, and P. Fieguth, "A review on computer vision based defect detection and condition assessment of concrete and asphalt civil infrastructure," *Advanced Engineering Informatics*, vol. 29, no. 2, pp. 196–210, 2015.

[21] D. Feng and M. Q. Feng, "Computer vision for SHM of civil infrastructure: from dynamic response measurement to damage detection - a review," *Engineering Structures*, vol. 156, pp. 105–117, 2018.

[22] C.-Z. Dong and F. N. Catbas, "A review of computer vision-based structural health monitoring at local and global levels," *Structural Health Monitoring*, vol. 20, no. 2, pp. 692–743, 2020.

[23] R. Yadhunath, S. Srikanth, A. Sudheer, C. Jyotsna, and J. Amudha, "Detecting surface cracks on buildings using computer vision: an experimental comparison of digital image processing and deep learning," in *Proceedings of the Soft Computing and Signal Processing*, pp. 197–210, Springer Singapore, Hyderabad, India, July 2021.

[24] P. Asadi, M. Gindy, and M. Alvarez, "A machine learning based approach for automatic rebar detection and quantification of deterioration in concrete bridge deck ground penetrating radar B-scan images," *KSCE Journal of Civil Engineering*, vol. 23, no. 6, pp. 2618–2627, 2019.

[25] G. M. Hadjidemetriou, P. A. Vela, and S. E. Christodoulou, "Automated pavement patch detection and quantification using support vector machines," *Journal of Computing in Civil Engineering*, vol. 32, no. 1, Article ID 04017073, 2018.

[26] T.-T. Le, V.-H. Nguyen, and M. V. Le, "Development of deep learning model for the recognition of cracks on concrete surfaces," *Applied Computational Intelligence and Soft Computing*, vol. 2021, Article ID 8858545, 10 pages, 2021.

[27] M. H. Ahmadi, M. A. Ahmadi, M. A. Nazari, O. Mahian, and R. Ghasempour, "A proposed model to predict thermal conductivity ratio of Al2O3/EG nanofluid by applying least squares support vector machine (LSSVM) and genetic algorithm as a connectionist approach," *Journal of Thermal Analysis and Calorimetry*, vol. 135, no. 1, pp. 271–281, 2019.

[28] J.-S. Chou and N.-M. Nguyen, "Metaheuristics-optimized ensemble system for predicting mechanical strength of reinforced concrete materials," *Structural Control and Health Monitoring*, vol. 28, no. 5, p. e2706, 2021.

[29] S. Fan, S. Cao, and Y. Zhang, "Temperature prediction of photovoltaic panels based on support vector machine with pigeon-inspired optimization," *Complexity*, vol. 2020, Article ID 9278162, 12 pages, 2020.

[30] N.-D. Hoang, T.-C. Huynh, and V.-D. Tran, "Computer vision-based patched and unpatched pothole classification using machine learning approach optimized by forensic-based investigation metaheuristic," *Complexity*, vol. 2021, Article ID 3511375, 17 pages, 2021.

[31] E. Li, J. Zhou, X. Shi et al., "Developing a hybrid model of salp swarm algorithm-based support vector machine to predict the strength of fiber-reinforced cemented paste backfill," *Engineering with Computers*, vol. 37, no. 4, pp. 3519–3540, 2020.

[32] Y.-k. Pan, K.-w. Xia, W.-j. Niu, and Z.-p. He, "Semi-supervised SVM by hybrid whale optimization algorithm and its application in oil layer recognition," *Mathematical Problems in Engineering*, vol. 2021, Article ID 5289038, 19 pages, 2021.

[33] P. Parsa and H. Naderpour, "Shear strength estimation of reinforced concrete walls using support vector regression

improved by Teaching-learning-based optimization, Particle Swarm optimization, and Harris Hawks Optimization algorithms," *Journal of Building Engineering*, vol. 44, Article ID 102593, 2021.

[34] V. N. Vapnik, *Statistical Learning Theory*, John Wiley & Sons, New Jersey USA, 1998.

[35] J. Cervantes, F. Garcia-Lamont, L. Rodríguez-Mazahua, and A. Lopez, "A comprehensive survey on support vector machine classification: applications, challenges and trends," *Neurocomputing*, vol. 408, pp. 189–215, 2020.

[36] A. Çevik, A. E. Kurtoğlu, M. Bilgehan, M. E. Gülşan, and H. M. Albegmprli, "Support vector machines in structural engineering: a review," *Journal of Civil Engineering and Management*, vol. 21, no. 3, pp. 261–281, 2015.

[37] R. Y. Goh and L. S. Lee, "Credit scoring: a review on support vector machines and metaheuristic approaches," *Advances in Operations Research*, vol. 2019, Article ID 1974794, 30 pages, 2019.

[38] R. Gupta, M. A. Alam, and P. Agarwal, "Modified support vector machine for detecting stress level using EEG signals," *Computational Intelligence and Neuroscience*, vol. 2020, Article ID 8860841, 14 pages, 2020.

[39] N. Naicker, T. Adeliyi, and J. Wing, "Linear support vector machines for prediction of student performance in school-based education," *Mathematical Problems in Engineering*, vol. 2020, Article ID 4761468, 7 pages, 2020.

[40] J. Zhou, Y. Qiu, S. Zhu et al., "Optimization of support vector machine through the use of metaheuristic algorithms in forecasting TBM advance rate," *Engineering Applications of Artificial Intelligence*, vol. 97, Article ID 104015, 2021.

[41] S. Theodoridis and K. Koutroumbas, *Pattern Recognition*, Academic Press, Printed in the United States of America, 2009, https://en.wikipedia.org/wiki/Cambridge,_Massachusetts.

[42] M. M. Galloway, "Texture analysis using gray level run lengths," *Computer Graphics and Image Processing*, vol. 4, no. 2, pp. 172–179, 1975.

[43] T. Xiaoou Tang, "Texture information in run-length matrices," *IEEE Transactions on Image Processing*, vol. 7, no. 11, pp. 1602–1609, 1998.

[44] M. Heikkilä, M. Pietikäinen, and C. Schmid, "Description of interest regions with local binary patterns," *Pattern Recognition*, vol. 42, no. 3, pp. 425–436, 2009.

[45] D. Barnat-Hunek, Z. Omiotek, M. Szafraniec, and R. Dzierżak, "An integrated texture analysis and machine learning approach for durability assessment of lightweight cement composites with hydrophobic coatings modified by nanocellulose," *Measurement*, vol. 179, Article ID 109538, 2021.

[46] Y. Cai, G. Xu, A. Li, and X. Wang, "A novel improved local binary pattern and its application to the fault diagnosis of diesel engine," *Shock and Vibration*, vol. 2020, Article ID 9830162, 15 pages, 2020.

[47] N.-D. Hoang and V.-D. Tran, "Image processing-based detection of pipe corrosion using texture analysis and metaheuristic-optimized machine learning approach," *Computational Intelligence and Neuroscience*, vol. 2019, Article ID 8097213, 13 pages, 2019.

[48] A. Humeau-Heurtier, "Texture feature extraction methods: a survey," *IEEE Access*, vol. 7, pp. 8975–9000, 2019.

[49] N. Kayhan and S. Fekri-Ershad, "Content based image retrieval based on weighted fusion of texture and color features derived from modified local binary patterns and local neighborhood difference patterns," *Multimedia Tools and Applications*, vol. 80, no. 21-23, pp. 32763–32790, 2021.

[50] L. Liu, P. Fieguth, Y. Guo, X. Wang, and M. Pietikäinen, "Local binary features for texture classification: t," vol. 62, pp. 135–160, 2017.

[51] N.-D. Hoang, "Image processing-based pitting corrosion detection using metaheuristic optimized multilevel image thresholding and machine-learning approaches," *Mathematical Problems in Engineering*, vol. 2020, Article ID 6765274, 19 pages, 2020a.

[52] N. Tadi Bani and S. Fekri-Ershad, "Content-based image retrieval based on combination of texture and colour information extracted in spatial and frequency domains," *The Electronic Library*, vol. 37, no. 4, pp. 650–666, 2019.

[53] S. Dash and M. R. Senapati, "Gray level run length matrix based on various illumination normalization techniques for texture classification," *Evolutionary Intelligence*, vol. 14, no. 2, pp. 217–226, 2018.

[54] A. Chu, C. M. Sehgal, and J. F. Greenleaf, "Use of gray value distribution of run lengths for texture analysis," *Pattern Recognition Letters*, vol. 11, no. 6, pp. 415–419, 1990.

[55] B. V. Dasarathy and E. B. Holder, "Image characterizations based on joint gray level-run length distributions," *Pattern Recognition Letters*, vol. 12, no. 8, pp. 497–502, 1991.

[56] T. Ojala and M. Pietikäinen, "Unsupervised texture segmentation using feature distributions," *Pattern Recognition*, vol. 32, no. 3, pp. 477–486, 1999.

[57] T. Ojala, M. Pietikäinen, and D. Harwood, "A comparative study of texture measures with classification based on featured distributions," *Pattern Recognition*, vol. 29, no. 1, pp. 51–59, 1996.

[58] Y. El merabet, Y. Ruichek, and A. El idrissi, "Attractive-and-repulsive center-symmetric local binary patterns for texture classification," *Engineering Applications of Artificial Intelligence*, vol. 78, pp. 158–172, 2019.

[59] C. M. Bishop, *Pattern Recognition and Machine Learning (Information Science and Statistics*, Springer, /Heidelberg, Germany, 2011, https://www.google.com/search?rlz=1C1GCEB_enIN980IN980&q=Berlin&stick=H4sIAAAAAAAAAAONgVuLQz9U3MDQ1K1zEyuaUWpSTmQcAUzZQwhUAAAA&sa=X&ved=2ahUKEwj2io2ZvKL0AhVJzDgGHfm7DWsQmxMoAXoECEMQAw April 6, 2011).

[60] M. S. Nixon and A. S. Aguado, *Feature Extraction & Image Processing for Computer Vision*, Academic Press, Elsevier, Cambridge, Massachusetts, 2012.

[61] M. Heikkila and M. Pietikainen, "A texture-based method for modeling the background and detecting moving objects," *IEEE Transactions on Pattern Analysis and Machine Intelligence*, vol. 28, no. 4, pp. 657–662, 2006.

[62] M.-Y. Cheng and N.-D. Hoang, "Typhoon-induced slope collapse assessment using a novel bee colony optimized support vector classifier," *Natural Hazards*, vol. 78, no. 3, pp. 1961–1978, 2015.

[63] L. H. Hamel, *Knowledge Discovery with Support Vector Machines*, John Wiley & Sons, New Jersey USA, 2009.

[64] J.-S. Chou and T. T. H. Truong, "Sliding-window metaheuristic optimization-based forecast system for foreign exchange analysis," *Soft Computing*, vol. 23, no. 10, pp. 3545–3561, 2019.

[65] T. V. Dinh, H. Nguyen, X.-L. Tran, and N.-D. Hoang, "Predicting rainfall-induced soil erosion based on a hybridization of adaptive differential evolution and support vector machine classification," *Mathematical Problems in Engineering*, vol. 2021, Article ID 6647829, 20 pages, 2021.

[66] H. Luo and S. G. Paal, "Metaheuristic least squares support vector machine-based lateral strength modelling of

reinforced concrete columns subjected to earthquake loads," *Structure*, vol. 33, pp. 748–758, 2021.

[67] D. Prayogo, M.-Y. Cheng, Y.-W. Wu, and D.-H. Tran, "Combining machine learning models via adaptive ensemble weighting for prediction of shear capacity of reinforced-concrete deep beams," *Engineering with Computers*, vol. 36, pp. 1135–1153, 2019.

[68] C. Qi and X. Tang, "Slope stability prediction using integrated metaheuristic and machine learning approaches: a comparative study," *Computers & Industrial Engineering*, vol. 118, pp. 112–122, 2018.

[69] D. Segera, M. Mbuthia, and A. Nyete, "Particle swarm optimized hybrid kernel-based multiclass support vector machine for microarray cancer data analysis," *BioMed Research International*, vol. 2019, Article ID 4085725, 11 pages, 2019.

[70] D. Tien Bui, H. Shahabi, A. Shirzadi et al., "A novel integrated approach of relevance vector machine optimized by imperialist competitive algorithm for spatial modeling of shallow landslides," *Remote Sensing*, vol. 10, no. 10, p. 1538, 2018.

[71] Z.-Z. Zhu, Y.-W. Feng, C. Lu, and C.-W. Fei, "Reliability optimization of structural deformation with improved support vector regression model," *Advances in Materials Science and Engineering*, vol. 2020, Article ID 3982450, 8 pages, 2020.

[72] J.-S. Chou and D.-N. Truong, "A novel metaheuristic optimizer inspired by behavior of jellyfish in ocean," *Applied Mathematics and Computation*, vol. 389, Article ID 125535, 2021b.

[73] G. L. Mariottini and L. Pane, "Mediterranean jellyfish venoms: a review on scyphomedusae," *Marine Drugs*, vol. 8, no. 4, pp. 1122–1152, 2010.

[74] D. Zavodnik, "Spatial aggregations of the swarming jellyfish Pelagia noctiluca (Scyphozoa)," *Marine Biology*, vol. 94, no. 2, pp. 265–269, 1987.

[75] MathWorks, *Statistics and Machine Learning Toolbox User's Guide*, Matwork Inc., Massachusetts USA, 2017, https://www.mathworks.com/help/pdf_doc/stats/stats.pdfDate of last access.

[76] J.-S. Chou and D.-N. Truong, *Jellyfish Search Optimizer (JS) MATLAB Central*, https://wwwmathworkscom/matlabcentral/fileexchange/78961-jellyfish-search-optimizer-js>, 2021a.

[77] Accord, "Accord.NET framework," 2019, http://accord-frameworknet/Last Access Date.

[78] F. Chollet, *Deep Learning with Python*, Manning Publications, New York USA, 2015.

[79] H. Tin Kam Ho, "The random subspace method for constructing decision forests," *IEEE Transactions on Pattern Analysis and Machine Intelligence*, vol. 20, no. 8, pp. 832–844, 1998.

[80] Y. LeCun, Y. Bengio, and G. Hinton, "Deep learning," *Nature*, vol. 521, no. 7553, pp. 436–444, 2015.

[81] P.-j. Chun, I. Ujike, K. Mishima, M. Kusumoto, and S. Okazaki, "Random forest-based evaluation technique for internal damage in reinforced concrete featuring multiple nondestructive testing results," *Construction and Building Materials*, vol. 253, Article ID 119238, 2020.

[82] S. Dorafshan, R. J. Thomas, and M. Maguire, "Comparison of deep convolutional neural networks and edge detectors for image-based crack detection in concrete," *Construction and Building Materials*, vol. 186, pp. 1031–1045, 2018.

[83] T.-C. Huynh, "Vision-based autonomous bolt-looseness detection method for splice connections: design, lab-scale evaluation, and field application," *Automation in Construction*, vol. 124, Article ID 103591, 2021.

[84] M. Sharma, M. K. Sharma, N. Leeprechanon, W. Anotaipaiboon, and K. Chaiyasarn, "Digital image patch based randomized crack detection in concrete structures," in *2017 International Conference on Computer Communication and Informatics (ICCCI)*, vol. 5-7, pp. 1–7, Coimbatore, India, January 2017.

[85] W. R. L. d. Silva and D. S. d. Lucena, "Concrete cracks detection based on deep learning image classification," *Proceedings*, vol. 2, no. 8, p. 489, 2018.

[86] S. Ullah, M. Jeong, and W. Lee, "Nondestructive inspection of reinforced concrete utility Poles with ISOMAP and random forest," *Sensors*, vol. 18, no. 10, p. 3463, 2018.

[87] H. Wan, L. Gao, M. Su, Q. Sun, and L. Huang, "Attention-based convolutional neural network for pavement crack detection," *Advances in Materials Science and Engineering*, vol. 2021, Article ID 5520515, 13 pages, 2021.

[88] W. Wang, W. Hu, W. Wang et al., "Automated crack severity level detection and classification for ballastless track slab using deep convolutional neural network," *Automation in Construction*, vol. 124, Article ID 103484, 2021.

[89] D. P. Kingma and J. Ba, "Adam: a method for stochastic optimization," in *Proceedings of the 3rd International Conference on Learning Representations (ICLR)*, San Diego, January 2015.

[90] T. Tieleman and G. Hinton, *Lecture 6.5 - RMSProp COURSERA: Neural Networks for Machine Learning*, Technical report, 2012.

[91] MathWorks, *Deep Learning Toolbox the MathWorks, Inc*, https://wwwmathworkscom/help/deeplearning/index(Last Access Date, 2019.

[92] V. López, A. Fernández, S. García, V. Palade, and F. Herrera, "An insight into classification with imbalanced data: empirical results and current trends on using data intrinsic characteristics," *Information Sciences*, vol. 250, pp. 113–141, 2013.

[93] L. Yu, C. Wang, H. Chang, S. Shen, F. Hou, and Y. Li, "Application research of intelligent classification Technology in enterprise data classification and gradation system," *Complexity*, vol. 2020, Article ID 6695484, 9 pages, 2020.

[94] A. R. van Erkel and P. M. T. Pattynama, "Receiver operating characteristic (ROC) analysis: basic principles and applications in radiology," *European Journal of Radiology*, vol. 27, no. 2, pp. 88–94, 1998.

[95] B. T. Pham, D. Tien Bui, and I. Prakash, "Bagging based Support Vector Machines for spatial prediction of landslides," *Environmental Earth Sciences*, vol. 77, no. 4, p. 146, 2018.

[96] M. Hollander and D. A. Wolfe, *Nonparametric Statistical Methods*, John Wiley & Sons, Hoboken, NJ, 1999.

[97] W. J. Conover, *Practical Nonparametric Statistics*, John Wiley & Sons, Hoboken, NJ, 1999.

[98] J. Chen, V. M. Patel, L. Liu et al., "Robust local features for remote face recognition," *Image and Vision Computing*, vol. 64, pp. 34–46, 2017.

[99] C.-X. Ren, Z. Lei, D.-Q. Dai, and S. Z. Li, "Enhanced local gradient order features and discriminant analysis for face recognition," *IEEE Transactions on Cybernetics*, vol. 46, no. 11, pp. 2656–2669, 2016.

[100] B. Everitt, *The Cambridge Dictionary of Statistics*, Cambridge University Press, Cambridge, UK New York, 1998.

Research Article

Experimental Study and Prediction Model of the Flexural Strength of concrete Containing Fly Ash and Ground Granulated Blast-Furnace Slag

Hua Zhang [ID], **Qing-Fu Li** [ID], **Hua-De Zhou, and Zong-Ming Song**

School of Water Conservancy Engineering, Zhengzhou University, Zhengzhou 450001, China

Correspondence should be addressed to Qing-Fu Li; lqflch@zzu.edu.cn

Orthogonal experiments were performed to study the flexural strength of an eco-friendly concrete containing fly ash (FA) and ground granulated blast-furnace slag (GGBFS). The effects of different test parameters, such as water-binder ratio (W/B), FA content, GGBFS content, sand ratio, gravel gradation, and curing time, on the flexural strength of the concrete were analyzed. The significance level of each influencing factor and the optimal mixing proportion of the concrete were determined by range analysis and hierarchy analysis. It was found that the W/B ratio had the greatest influence on the flexural strength of the concrete. The flexural strength of the concrete decreased gradually with the increase of W/B. The GGBFS content and the sand ratio had a greater influence in the early stage of concrete curing. The middle and later stages of concrete curing were mainly affected by gravel gradation and the FA content. A flexural strength prediction model of the concrete was developed based on a backpropagation neural network (BPNN) and a support vector machine (SVM) model. It was noticed that the BPNN and SVM models both had higher accuracy than the empirical equation, and the BPNN model was more accurate than the SVM model.

1. Introduction

Concrete is one of the most widely used building materials due to its good quality and low price [1]. Concrete structures are mainly subjected to bending rather than axial tension. However, the flexural properties of concrete are poor, and cracks easily appear under tensile stress conditions. Therefore, it is of great significance to improve the flexural strength of concrete [2]. Supplementary cementitious materials, such as fly ash, ground granulated blast-furnace slag, and silica powder, are generally used to improve the performance of concrete, reduce the waste stock, and lower the construction cost [3].

Fly ash (FA) is a waste discharged after pulverized coal combustion. It has a high storage cost and can cause environmental pollution [4, 5]. Nili M et al. [6] studied the influences of FA on concretes of different ages and noticed that FA greatly enhanced the concrete strength in the later stage of curing. Golewski [7] studied the compressive

strength and fracture toughness of concrete with FA contents of 20% and 30%. It was reported that the compressive strength and fracture toughness of concrete were significantly improved when the FA replacement ratio was 20%. When the FA replacement ratio was 30%, the improvement of material properties did not appear until six months after curing. Golewski [8] found that the optimal FA content to improve the fracture toughness of concrete was 17% (by weight). The fracture toughness of concrete began to decrease when the FA content exceeded 23% of the total cementitious material. Atis [9] reported that the flexural strength of 70% FA-replaced concrete after 7, 28, 90, and 365 days was reduced by 46.83%, 24.71%, 26.2%, and 35.16%, respectively, as compared to that of 50% FA-replaced concrete.

Ground granulated blast-furnace slag (GGBFS) is a by-product of iron smelting [10]. Extensive research has been performed on GGBFS-substituted concrete. Hogan et al. [11] conducted a comparative study on ordinary concrete and

GGBFS-substituted concrete with 40% and 60% replacement ratios. The compressive strength of the GGBFS-substituted concrete was found to be lower than that of the ordinary concrete in the first three days. However, the compressive strength of the GGBFS-substituted concrete increased at a higher rate than that of the normal concrete after three days, especially when the GGBFS replacement ratio was 40%. The GGBFS-substituted concrete had the same or higher flexural strength than the ordinary concrete after seven days. Sivasundaram et al. [12] studied the variation of the flexural strength of GGBFS-substituted concrete with 50%–75% replacement ratios. The flexural strength of the GGBFS-substituted concrete after 14 days was higher than that of common concretes. However, some studies have reported opposite results. For example, Khatib et al. [13] studied the effects of different GGBFS replacement ratios (0%, 40%, 60%, and 80%) on the flexural strength of concrete. It was found that the concrete flexural strength with a GGBFS replacement ratio of 60% was significantly higher than that of the control group and decreased slightly when the replacement ratio was 40%. A significant decrease in flexural strength was noticed when the replacement ratio was 80%. Bharatkumar et al. [14] reported a reduction in the flexural strength of GGBFS-substituted concrete. When the total amount of cementitious material was $472 \, \text{kg/m}^3$ and the water-cement ratio was 0.36, the addition of 50% of GGBFS decreased the 56-day bending strength by 7.2%. When the total amount of cementitious material was $430 \, \text{kg/m}^3$ and the water-cement ratio was 0.4, this drop reached 11.29%. Nazari and Riahi [15–18] found that the 7-day flexural strength of concrete was reduced by 24.32% and 32.43%, respectively, when cement was partially replaced with 45% and 60% of GGBFS. On the contrary, the addition of GGBFS increased the 28-day and 90-day flexural strengths of the concrete.

Machine learning methods are also widely used in the field of concrete strength prediction. Zheng et al. [19] developed a stable concrete compressive strength development over time (CCSDOT) model by combining conventional methods with artificial intelligence. Chithra et al. [20] used multiple regression analysis and an artificial neural network to predict the compressive strength of concrete containing silica and copper slag and reported that the artificial neural network model had higher accuracy and relevance. Chou et al. [21] predicted the compressive strength of a high-performance concrete by a support vector machine (SVM) model based on mean absolute percentage error (MAPE). Omran et al. [22] predicted the compressive strength of concrete containing lightweight aggregates and Portland limestone cement by seven different models—three advanced predictive models, four regression tree models, and two ensemble methods. The SVM model was based on sequential minimum optimization, and test results revealed that all models acquired acceptable prediction performance, except for decision stump. Thi Mai et al. [23] developed a random forest model to predict the compressive strength of concrete based on artificial neural network (ANN) and adaptive-network-based fuzzy inference system models (ANFIS) and noticed that these two machine learning methods had high accuracy. Palika Chopra et al. [24] used a decision tree (DT) model, a random forest (RF) model, and a neural network to predict the compressive strength of concrete, and the neural network model was found to have higher prediction accuracy.

With the growing environmental pollution problems and the urgent demand for green construction, environment-friendly concretes need to be developed. In the present work, orthogonal experiments were performed to study the flexural strength of an eco-friendly concrete containing FA and GGBFS. The effects of different test parameters, such as water-binder ratio (W/B), FA content, GGBFS content, sand ratio, gravel gradation, and curing time, on the flexural strength of the concrete were analyzed. The significance level of each influencing factor was determined by range analysis and hierarchy analysis. Moreover, a flexural strength prediction model of the concrete was developed based on a backpropagation neural network (BPNN) model and an SVM model, and the prediction accuracies of these two machine learning models and an empirical equation were compared.

2. Materials and Methods

2.1. Materials.
Water, cement, river sand, gravel, FA, GGBFS, and a water reducer were used as raw materials. Portland cement 42.5 R was used in this research, and its initial and final setting times were 145 and 211 min, respectively. According to the Chinese Building Code GB/T 14684-2011 "Natural River Sand for Construction," natural river sand with a fineness modulus of 2.8 was used as the fine aggregate. According to the Chinese standard GB/T 14685-2011 "Gravel and Crushed stone for Construction," two types of gravels with different grades were used (maximum particle sizes were 20 mm (G1) and 40 mm (G2)). First-grade FA was selected according to the Chinese standard GB/T1596-2005 "Fly Ash Used in Cement and Concrete." GGBFS with a density of $2.88 \, \text{g/cm}^3$ and a specific surface area of $463 \, \text{m}^2/\text{kg}$ was used. The gradation curves of different mixtures are shown in Figure 1. The chemical compositions of FA and GGBFS are presented in Table 1, and their properties are listed in Table 2.

2.2. Mixing Proportions.
The W/B ratio, the contents of FA and GGBFS, the sand ratio (mass ratio of sand to the total mass of aggregates (mass sum of sand and coarse aggregate) [25]), and gravel gradation were considered as the main influencing factors, and each factor had four levels. Therefore, 16 different mixing proportions were determined based on the orthogonal design method. The levels were determined by literatures [7, 8, 26–28]: W/B ratio = 0.35, 0.375, 0.40, 0.425, sand ratio = 33%, 35%, 37%, 39%, FA and GGBFS contents = 5%, 10%, 15%, 20%, gravel gradation with small stones (5–20 mm) and medium stones (20–40 mm) = 30%:70%, 40%:60%, 50%:50%, 60%:40% (Table 3).

2.3. Test Procedure.
Specimens with different mixing proportions were cured for 1 day, 3 days, 7 days, 14 days, 28
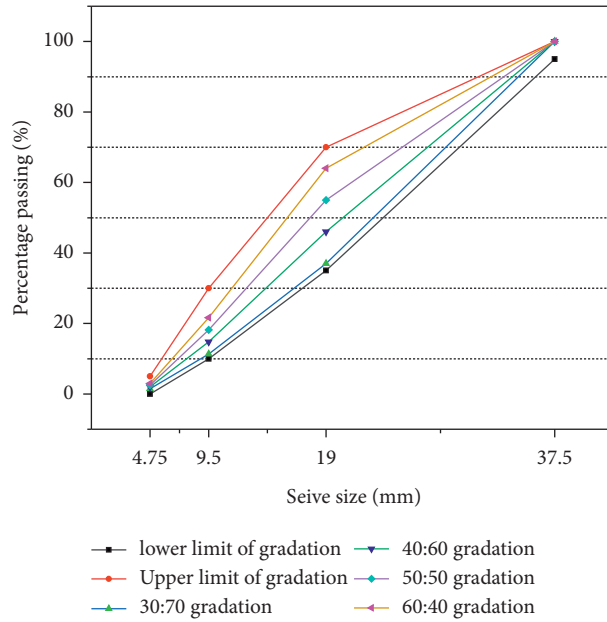
FIGURE 1: Gradation curves of different mixtures.

TABLE 1: Chemical compositions of FA and GGBFS.

Constituent (%)	SiO_2	Al_2O_3	CaO	MgO	SO_3	Fe_2O_3	Na_2O	K_2O	H_2O
FA	58	30	2.8	1.5	1.22	4.3	0.00	1.36	0.5
GGBFS	33.84	13.27	40.8	6.08	0.29	0.28	0.2	0.36	0.3

TABLE 2: Main properties of FA and GGBFS.

Properties	Fineness	Water demand ratio (%)	Loss on ignition (%)	Density(g/cm^3)	Fluidity ratio (%)
FA	9.22	91	5.0	2.252	—
GGBFS	—	—	1.236	0.88	95

TABLE 3: Mix proportions.

Specimen number	Mix proportions (kg/m^3)						
	Water	Binder	FA	GGBFS	Sand	Small gravel	Middle gravel
S1	135	386	19.3	19.3	620	378	881
S2	135	386	38.6	38.6	658	488	733
S3	135	386	57.9	57.9	695	592	592
S4	135	386	77.2	77.2	733	688	458
S5	135	360	18	36	629	766	510
S6	135	360	36	18	667	619	619
S7	135	360	48	72	705	480	720
S8	135	360	72	48	743	349	813
S9	135	338	16.9	50.7	636	516	775
S10	135	338	33.8	16.9	674	376	877
S11	135	338	50.7	67.6	713	728	486
S12	135	338	67.6	33.8	752	588	588
S13	135	318	15.9	63.6	643	652	652
S14	135	318	31.8	44.7	681	760	506
S15	135	318	44.7	31.8	720	368	859
S16	135	318	63.6	15.9	759	475	713

days, and 45 days under standard conditions. Three specimens were formed in each age, and the size of the specimens was 150 mm × 150 mm × 550 mm. The side of each specimen was placed on a support, and the placement position was checked to ensure that the stress position of the specimen met the specified requirements. The loading speed was varied between 0.05 and 0.08 MPa/s. When a specimen was at the edge of failure, the throttle of the testing machine was kept stable until the test ended, and the failure load was recorded. During the processing of test results, 115% and 85% of the mean values of three measured values were taken as the upper and lower limits, respectively. When only one of the measured values did not meet the specified requirements, the average value of the other two measured values was taken as the final result. When more than one of the measured values did not meet the specified requirements, the test was reperformed [29]. The test device is shown in Figure 2. The flexural strength of the concrete was calculated as

$$f_t = \frac{Fl}{bh^2}, \qquad (1)$$

where f_t is the flexural strength of the concrete, F is the maximum load at the time of concrete failure, l is the distance of the support (span; $l = 3h$), b is the width of the specimen section, and h is the height of the specimen section.

3. Results and Discussion

3.1. Test Results. The flexural strengths of the concrete specimens of different ages are shown in Figure 3 and Table.4.

It can be seen from Figure 3 that the flexural strengths of the concrete specimens with different mixing proportions increased with the extension of the curing time. The flexural strength of the specimens varied significantly between 1 and 3 d and slightly between 28 and 45 d, indicating that the increment of flexural strength gradually became smaller with the extension of the curing time [30].

3.1.1. Influence of W/B Ratio on Concrete Flexural Strength. It is clear from Figure 4 that the flexural strength of the concrete decreased gradually with the increase of the W/B ratio. The increase of the W/B ratio was equivalent to the reduction of cementitious materials in the concrete. The shortage of cementitious materials led to an upward migration of the remaining water after the hydration reaction, forming a water film on coarse aggregates and reducing the bond strength between coarse aggregates and the cement mortar. Moreover, the loss of water formed a small water passage inside the concrete, leading to the formation of microcracks. Consequently, the compactness and interfacial bond strength of the structure were reduced, causing a decline in the flexural strength of the concrete [31].

3.1.2. Influence of FA Content on Concrete Flexural Strength. It is observable from Figure 5 that the flexural strength of the concrete first increased and then decreased with the increase

of the FA content. When the FA content was 15%, the flexural strength of the concrete reached a maximum, except for the specimen with 1-d curing age. This was because FA mainly participated in the hardening process of cementitious materials through the formation of microaggregates and particles [32]. The increase of the FA content reduced the proportion of cement and decreased the hydration rate of cement, causing a reduction in the flexural strength of the concrete.

3.1.3. Influence of GGBFS Content on Concrete Flexural Strength. After the addition of GGBFS into the concrete, gaps between cement particles were filled, the compactness was improved, and the flexural resistance was strengthened. GGBFS improved the early flexural strength of cement after the hydration reaction. GGBFS also reduced the calcium ion concentration between cement and coarse aggregates and increased the cementing performance between them. Thus, the flexural strength of the concrete was improved after the addition of GGBFS [6]. However, after a certain amount, GGBFS indirectly affected the hydration reaction of cement and reduced the flexural resistance (Figure 6).

3.1.4. Influence of Sand Ratio on Concrete Flexural Strength. It is observable from Figure 7 that the flexural strength of the concrete gradually increased with the increase of the sand ratio. With the increase of the sand ratio, micropores in the concrete were gradually filled with sand, and the compactness was also gradually improved; thus, the stiffness of the concrete was enhanced. However, the difference between the flexural strengths of the concrete specimens with the sand proportions of 37% and 39% was not very big. Taking the flexural strength of the 28 d specimen as an example, the flexural strengths for the sand proportions of 37% and 39% were 6.26 and 6.35 MPa (only 1.44% increment), respectively. It indicates that the compactness of the concrete did not increase significantly when the sand ratio increased from 37% to 39%.

3.1.5. Influence of Gravel Gradation on Concrete Flexural Strength. It is observable from Figure 8 that when gravel gradation increased from 3 : 7 to 4 : 6, the flexural strength of the concrete increased, and when it exceeded 4 : 6, the flexure strength gradually decreased. A proper gravel gradation could completely wrap the cement mortar on the surface of large and small gravels, enhance the adhesiveness between cement particles, make the internal distribution of each component of the concrete uniform, and improve the compactness by reducing the gap between cement particles. When there were insufficient small gravels and too many large gravels in coarse aggregates, the bonding strength between coarse aggregates and cement particles was affected, resulting in a reduction in the flexural strength [33]. However, when there were too many small gravels, coarse aggregates were affected; thus, the flexural strength of the concrete began to decrease.
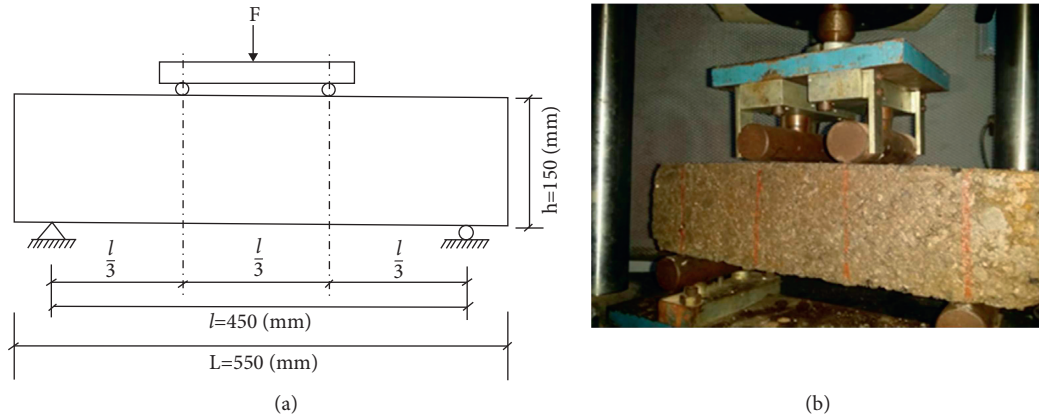
(a)

(b)

FIGURE 2: Flexural strength test setup. (a) Schematic diagram. (b) Test device.
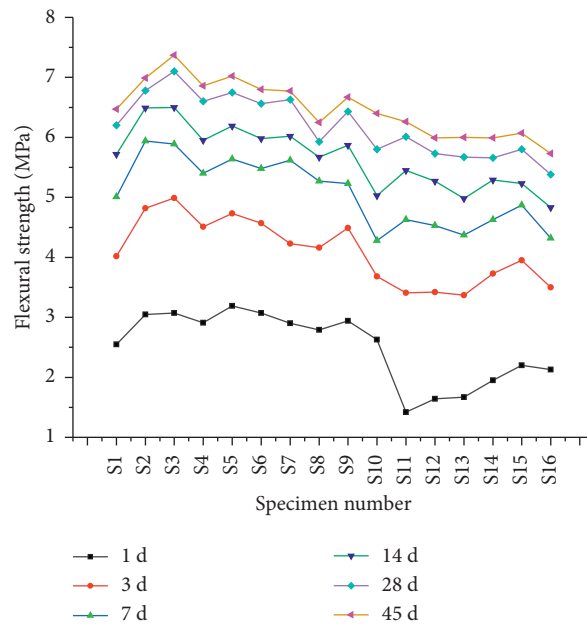

FIGURE 3: Variation of the flexural strengths of concrete specimens with different ages.

TABLE 4: Flexural strength of concrete at various ages.

Specimen number	Flexural strength (MPa)					
	1 d	3 d	7 d	14 d	28 d	45 d
S1	2.55 (0.01)	4.02 (0.12)	5.01 (0.14) (0.06)	5.72 (0.10)	6.20 (0.06)	6.47 (0.06)
S2	3.05 (0.03)	4.82 (0.14)	5.94 (0.12)	6.49 (0.15)	6.78 (0.09)	6.99 (0.06)
S3	3.07 (0.09)	4.99 (0.15)	5.89 (0.10)	6.50 (0.07)	7.10 (0.20)	7.37 (0.18)
S4	2.91 (0.01)	4.51 (0.08)	5.40 (0.14)	5.95 (0.07)	6.60 (0.06)	6.86 (0.14)
S5	3.19 (0.02)	4.73 (0.10)	5.64 (0.15)	6.19 (0.14)	6.75 (0.12)	7.02 (0.20)
S6	3.07 (0.11)	4.57 (0.06)	5.48 (0.10)	5.98 (0.07)	6.56 (0.10)	6.80 (0.09)
S7	2.90 (0.04)	4.23 (0.05)	5.62 (0.12)	6.02 (0.14)	6.63 (0.15)	6.77 (0.15)
S8	2.79 (0.06)	4.16 (0.07)	5.27(0.14)	5.67 (0 .07)	5.93 (0.09)	6.25 (0.06)
S9	2.94 (0.03)	4.49 (0.06)	5.23 (0.06)	5.87 (0.15)	6.43 (0.14)	6.67 (0.20)
S10	2.63 (0.02)	3.68 (0.09)	4.28 (0.08)	5.03 (0.08)	5.80 (0.08)	6.40 (0.12)
S11	1.42 (0.01)	3.41 (0.06)	4.63(0.14)	5.45 (0.14)	6.01(0.09)	6.26 (0.09)
S12	1.64 (0.02)	3.42 (0.04)	4.53 (0.10)	5.27 (0.10)	5.73 (0.14)	5.99 (0.12)

TABLE 4: Continued.

Specimen number	Flexural strength (MPa)					
	1 d	3 d	7 d	14 d	28 d	45 d
S13	1.67 (0.01)	3.37 (0.06)	4.37 (0.09)	4.98 (0.07)	5.67 (0.15)	6.00 (0.14)
S14	1.95 (0.03)	3.73 (0.07)	4.63(0.14)	5.29 (0.06)	5.66 (0.06)	5.99 (0.10)
S15	2.20 (0.05)	3.95 (0.03)	4.87 (0.10)	5.23 (0.07)	5.80 (0.09)	6.07 (0.20)
S16	2.13 (0.04)	3.50 (0.05)	4.32 (0.08)	4.83 (0.10)	5.38 (0.08)	5.73 (0.08)
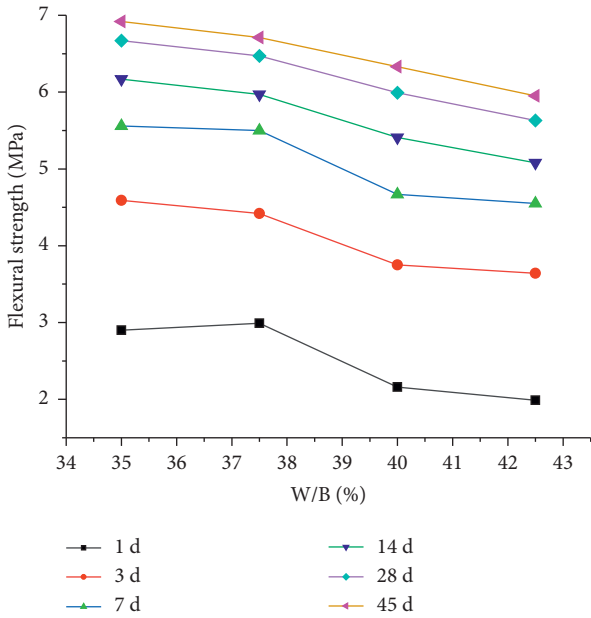
FIGURE 4: Influence of W/B ratio on concrete flexural strength.

FIGURE 6: Influence of GGBFS content on concrete flexural strength.

FIGURE 5: Influence of FA content on concrete flexural strength.
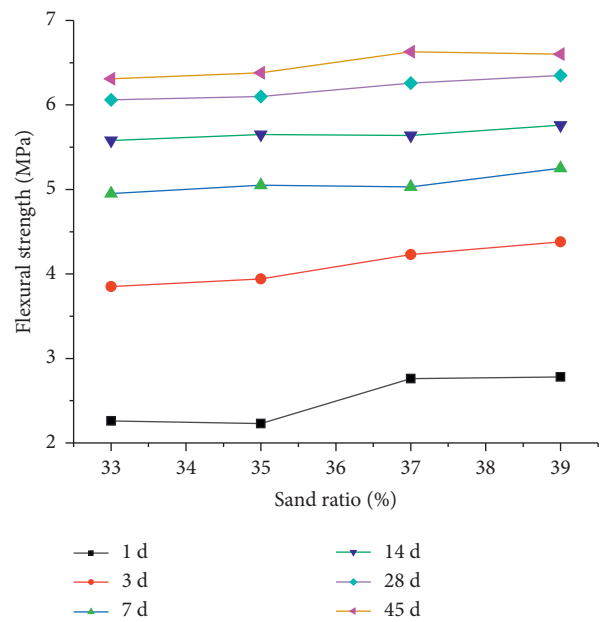
FIGURE 7: Influence of sand ratio on concrete flexural strength.

3.2. *Range Analysis.* Range analysis was carried out based on orthogonal test results, and the corresponding observations are presented in Table 5, where the W/B ratio, the FA content, the GGBFS content, the sand ratio, and gravel gradation are termed as A, B, C, D, and E, respectively.

Now, comparing the R values of different influencing factors after 1 d of aging, it is detectable that $R_A > R_D > R_E = R_C > R_B$; thus, the order of the five influencing factors is W/B ratio > Sand ratio > Gravel

FIGURE 8: Influence of gravel gradation on concrete flexural strength.

gradation > GGBFS content > FA content. Similarly, after 3, 7, 14, 28, and 45 d of aging, the trends were W/B ratio > Sand ratio > GGBFS content > Gravel gradation > FA content, W/B ratio > Gravel gradation > GGBFS content > FA content > Sand ratio, W/B ratio > Sand ratio > Gravel grad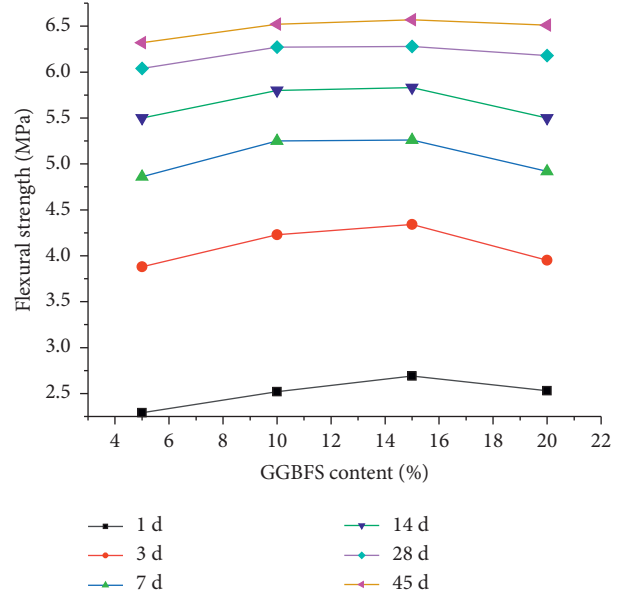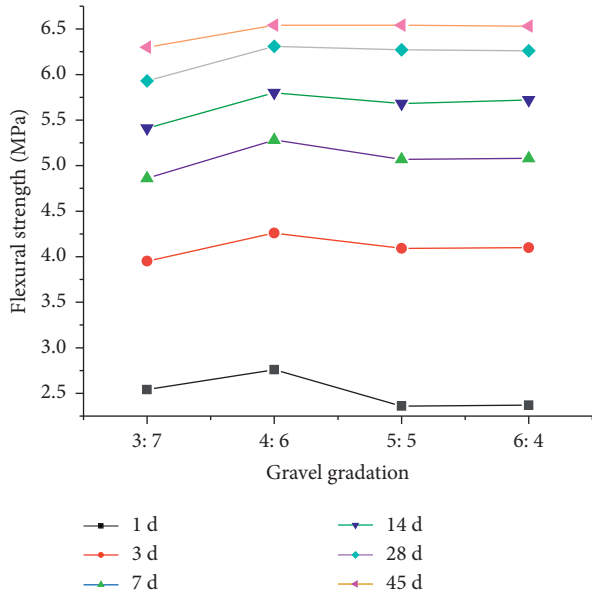ation > GGBFS content > FA content > Sand ratio, W/B ratio > Gravel gradation > FA content > GGBFS content > Sand ratio, W/B ratio > Gravel gradation > FA content > Sand ratio > GGBFS content, and W/B ratio > FA content > Sand ratio > GGBFS content > Gravel gradation, respectively.

Further, by comparing the K_i values, it was found that $K_2 > K_1 > K_3 > K_4$ in the level of factor A, indicating that the flexural strength of the concrete reached a maximum when factor A was on the second level. Similarly, the optimal levels of factors B, C, D, and E were second, third, fourth, and second, respectively. Therefore, when the horizontal combination was A2B2C3D4E2, the flexural strength of the concrete was the greatest under the consideration of a single action of the factors; therefore, this horizontal combination was the optimal preparation process combination to improve the flexural strength of the concrete after 1 d of aging. Similarly, the optimal mixing proportions of the concrete after 3, 7, 14, 28, and 45 d of aging were A1B2C3D4E2, A1B3C3D4E2, A1B3C3D4E2, A1B3C3D4E2, and A1B3C3D4E2, respectively. However, the A1B3C3D4E2 mixing proportion is recommended for engineering applications.

3.3. Analytic Hierarchy Process.

The analytic hierarchy process (AHP) turns complex problems into easy-to-understand hierarchies. Range analysis used for orthogonal tests cannot obtain the influence level of each factor on test results. AHP can obtain the influence level of each factor and also the influence weight of each level [31]. Figure 9 shows the AHP model used in this experiment. The model was divided into three layers—the first layer contained the index of the test, the second layer consisted of different influencing factors, and the third layer was composed of the levels of different factors.

It was assumed that the average value of the sum of test data under the j level of factor $N^{(i)}$ was K_{ij} (Table 5), and it was called the effect of the j level of factor $N^{(i)}$ on the test $(i = 1\,(A), 2\,(B), 3\,(C), 4\,(D), 5\,(E); \ j = 1, 2, 3, 4)$. Moreover, $M_{ij} = K_{ij}$; thus, three matrices were derived. Matrix a presents the influence of horizontal layers on the test, matrix s is the normalization of each column of matrix a, and matrix c is a weight matrix representing the influences of different factors on the test.

$$a = \begin{bmatrix} M_{11} & 0 & 0 & 0 & 0 \\ M_{21} & 0 & 0 & 0 & 0 \\ M_{31} & 0 & 0 & 0 & 0 \\ M_{41} & 0 & 0 & 0 & 0 \\ 0 & M_{12} & 0 & 0 & 0 \\ 0 & M_{22} & 0 & 0 & 0 \\ 0 & M_{32} & 0 & 0 & 0 \\ 0 & M_{42} & 0 & 0 & 0 \\ 0 & 0 & M_{13} & 0 & 0 \\ 0 & 0 & M_{23} & 0 & 0 \\ 0 & 0 & M_{33} & 0 & 0 \\ 0 & 0 & M_{43} & 0 & 0 \\ 0 & 0 & 0 & M_{14} & 0 \\ 0 & 0 & 0 & M_{24} & 0 \\ 0 & 0 & 0 & M_{34} & 0 \\ 0 & 0 & 0 & M_{44} & 0 \\ 0 & 0 & 0 & 0 & M_{15} \\ 0 & 0 & 0 & 0 & M_{25} \\ 0 & 0 & 0 & 0 & M_{35} \\ 0 & 0 & 0 & 0 & M_{45} \end{bmatrix},$$

$$s = \begin{bmatrix} \dfrac{1}{t_1} & 0 & 0 & 0 & 0 \\ 0 & \dfrac{1}{t_2} & 0 & 0 & 0 \\ 0 & 0 & \dfrac{1}{t_3} & 0 & 0 \\ 0 & 0 & 0 & \dfrac{1}{t_4} & 0 \\ 0 & 0 & 0 & 0 & \dfrac{1}{t_5} \end{bmatrix},$$

$$c = \begin{bmatrix} \dfrac{R_1}{\sum_{i=1}^{5} R_i} & \dfrac{R_2}{\sum_{i=1}^{5} R_i} & \dfrac{R_3}{\sum_{i=1}^{5} R_i} & \dfrac{R_4}{\sum_{i=1}^{5} R_i} & \dfrac{R_5}{\sum_{i=1}^{5} R_i} \end{bmatrix}.$$

(2)

TABLE 5: Range analysis of concrete flexural strength.

| 1 d	A	B	C	D	E
K_1	2.90	2.59	2.29	2.26	2.54
K_2	2.99	2.68	2.52	2.23	2.76
K_3	2.16	2.40	2.69	2.76	2.36
K_4	1.99	2.37	2.53	2.78	2.37
R	1.00	0.31	0.40	0.55	0.40
Better scheme (BS)	A2	B2	C3	D4	E2
Factor priority (FP)			ADECB/ADCEB		
3 d	A	B	C	D	E
K_1	4.59	4.15	3.88	3.85	3.95
K_2	4.42	4.20	4.23	3.94	4.26
K_3	3.75	4.15	4.34	4.23	4.09
K_4	3.64	3.90	3.95	4.38	4.10
R	0.95	0.30	0.47	0.53	0.31
BS	A1	B2	C3	D4	E2
FP			ADCEB		
7 d	A	B	C	D	E
K_1	5.56	5.06	4.86	4.95	4.86
K_2	5.50	5.08	5.25	5.05	5.28
K_3	4.67	5.25	5.26	5.03	5.08
K_4	4.55	4.88	4.92	5.25	5.08
R	1.01	0.37	0.40	0.30	0.42
BS	A1	B3	C3	D4	E2
FP			AECBD		
14 d	A	B	C	D	E
K_1	6.17	5.69	5.50	5.58	5.41
K_2	5.97	5.70	5.80	5.65	5.80
K_3	5.41	5.80	5.83	5.64	5.68
K_4	5.08	5.43	5.50	5.76	5.72
R	1.08	0.37	0.34	0.18	0.39
BS	A1	B3	C3	D4	E2
FP			AEBCD		
28 d	A	B	C	D	E
K_1	6.67	6.26	6.04	6.06	5.93
K_2	6.47	6.20	6.27	6.10	6.31
K_3	5.99	6.39	6.28	6.26	6.27
K_4	5.63	5.91	6.18	6.35	6.26
R	1.04	0.48	0.24	0.29	0.33
BS	A1	B3	C3	D4	E2
FP			ABEDC		
45 d	A	B	C	D	E
K_1	6.92	6.54	6.32	6.31	6.30
K_2	6.71	6.55	6.52	6.38	6.54
K_3	6.33	6.62	6.57	6.63	6.54
K_4	5.95	6.21	6.51	6.60	6.53
R	0.98	0.41	0.26	0.33	0.24
BS	A1	B3	C3	D4	E2/E3
FP			ABDCE		
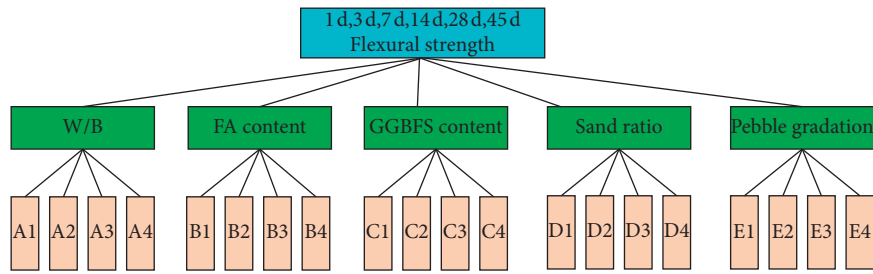
FIGURE 9: AHP model for the flexural strength test.

Now, $t_j = \sum_{i=1}^{5} M_{ij}$ ($j = 1, 2, 3, 4$); hence, the weight of each factor level of the test index was $\omega = \mathrm{asc}^T$. The data presented in Table 4 were substituted into the matrix. Among the four levels of the W/B ratio, A1 (35%) had the largest weight. Among the four levels of FA content, when the age was 1 d, B2 (10%) had the largest weight. When the ages were 7 and 14 d, B4 (20%) and B3 (15%) had the largest weight, respectively. As the curing time increased, the weight of the influence of FA on flexural strength gradually increased. Among the four levels of GGBFS content, when the age was 1 d, C3 (15%) had the largest weight. When the age was 7 d, C2 (10%) and C4 (20%) had the largest weight. When the age reached 14 d, the weight of C3 again (15%) became the largest. Among the four levels of sand ratio, D4 (39%) had the largest weight, and among the four levels of gravel gradation, E2 (40%:60%) had the largest weight. Therefore, the optimal values of W/B ratio, FA content, GGBFS content, sand ratio, and gravel gradation were 35%, 15%, 15%, 39%, and 40%:60%, respectively.

Range analysis and AHP were used to analyze the influences of different factors on the flexural strength of the concrete. It is clear that the effects of each factor on concrete flexural strength were significantly different at different ages. Among the five factors, the W/B ratio had the greatest influence on the flexural strength of the concrete. With the increase of the W/B ratio, the flexural strength of the concrete gradually decreased. FA mainly played a role in the later stage of concrete setting and hardening, and with the increase of the FA content, the flexural strength of the concrete first increased and then decreased. GGBFS played a role mainly in the early stage of concrete curing. With the increase of the GGBFS content, concrete flexural strength first increased and then decreased. The sand ratio also played a more obvious role in the early stage of concrete curing. The flexural strength of the concrete also increased as the sand ratio increased. Gravel gradation mainly played a role in the middle stage of concrete curing. The flexural strength of the concrete first increased and then decreased with the increase of the amount of small gravels.

It is clear from Figure 10 that the flexural strength change of the concrete caused by the W/B ratio was always the largest in all six ages [34], indicating that the effect of W/B was the greatest among the five influencing factors. This was because cementitious materials included cement, FA, and GGBFS. These three materials constantly changed their form and characteristics with the extension of the aging period and "actively" participated during concrete hardening [33]. Cement in cementitious materials continuously underwent a hydration

reaction and generated compounds to improve the flexural strength of the concrete. GGBFS played a role in the early stage of curing and enhanced the early flexural strength of the concrete. The positive role of FA was noticed in the later stage of curing, and it improved the flexural strength.

The influence of FA content on the flexural strength of the concrete was not significant during 1–7 d of curing. However, with the extension of the aging time, FA greatly influenced the flexural strength, and this phenomenon was related to the mineral composition of FA. FA mainly consisted of SiO_2, Al_2O_3, Fe_2O_3, CaO, and other components. These elements had certain activities and reacted with Ca^{2+} ions after cement hydration to form C-S-H, which coated FA and formed a porous structure between cement and fly ash. Therefore, FA could not completely react with the cement hydration products in the early stage and manifested a low influencing degree on the flexural strength. However, a secondary reaction began, because the coated FA was gradually decomposed and formed more stable compounds, thus enhancing the flexural strength of the concrete [6, 32].

The influence level of GGBFS was always higher than that of FA in the early stage. This was because Ca^{2+} ions produced by the hydration reaction became enriched at internal interfaces of the concrete. Active SiO_2 atoms of GGBFS reacted with Ca^{2+} ions and generated stable C-S-H, thus increasing the flexural strength of the concrete. However, with the extension of the curing time, the content of GGBFS decreased continuously; thus, its influence level began to decline. At this time, FA gradually replaced GGBFS and reacted with unstable compounds in the concrete, improving the flexural strength. Therefore, the influence level of GGBFS was less than that of FA in the later stage.

Fine sand particles filled the gaps between the cementitious materials and coarse aggregates and increased the flexural strength by improving the internal compactness of the concrete [35, 36]. In the early stage, the cement hydration reaction was slow; thus, the cement slurry and coarse aggregates could not set well with each other. Therefore, the sand ratio played a significant role in improving the flexural strength during 1–3 d of curing. The internal integrity of the concrete was gradually improved with the extension of the curing time; thus, the cementing performance between materials was continuously enhanced, and the effects of FA and gravels were gradually revealed. In the later stage, the flexural strength of the concrete increased steadily, and the importance of W/B, coarse aggregates, and other materials decreased slightly; however, the influence of the sand ratio increased.
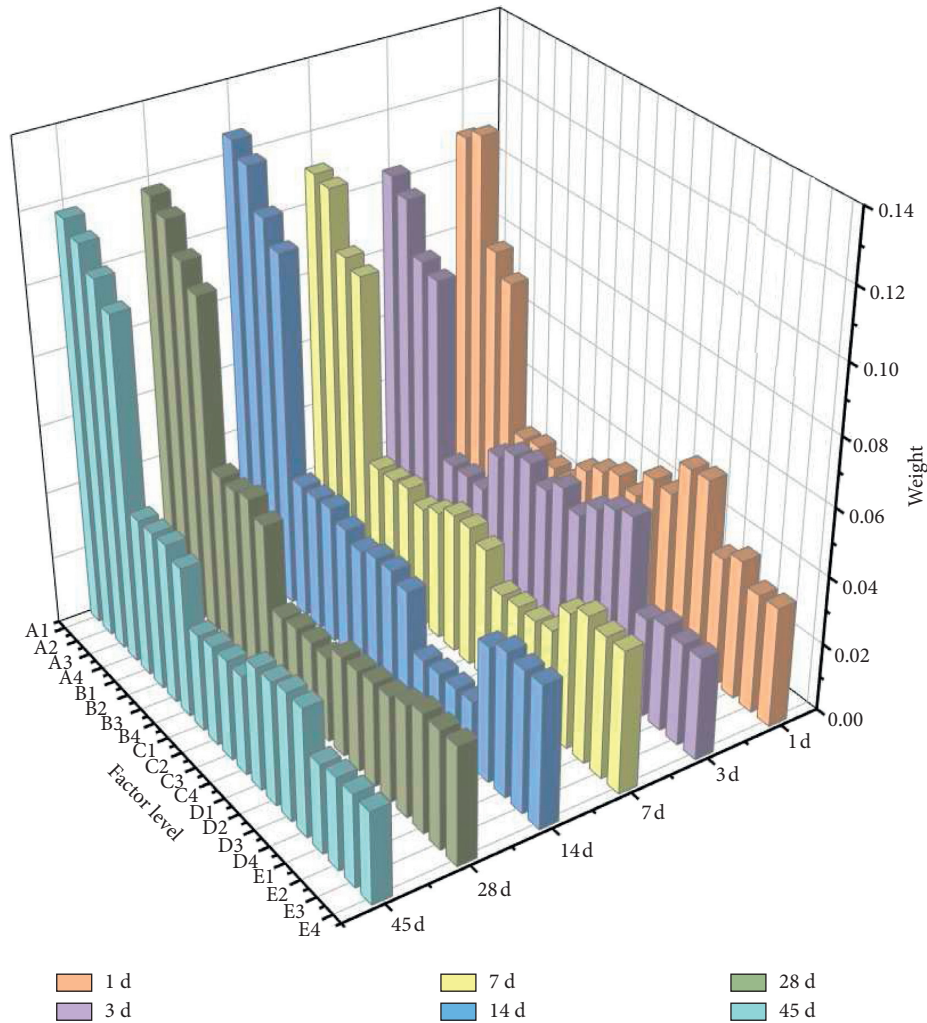
FIGURE 10: Influence weight of each factor level on the test index.

The influence of gravel gradation first increased and then decreased with the extension of the curing time. The increase and decrease of the proportion of coarse aggregates were closely related to the increase of flexural strength. The bond strength between coarse aggregates and cement stones manifested a significant effect on the interfacial bond strength. With the extension of the curing time, the amount of stable materials generated in the concrete gradually increased, and the growth range of the bond strength between coarse aggregates and cement stones also increased, thus improving the flexural strength of the concrete. After 28 d of curing, the growth rate of the bond strength between coarse aggregates and cement stones slowed down; thus, the effect of coarse aggregates on flexural strength decreased.

4. Prediction Model for Concrete Flexural Strength Based on Machine Learning

It is discernible from Figures 6–10 that the relationship between the five factors and the flexural strength of the concrete was nonlinear; therefore, it is necessary to establish a multivariate nonlinear regression model to quantify the influences of these five factors on the flexural strength of the concrete. In this analysis, BPNN and SVM were used to optimize the prediction model by adjusting relevant parameters and functions. The W/B ratio, FA content, GGBFS content, sand ratio, gravel gradation, and aging time were used as input data of the input layer, and the flexural strength of the concrete was the output layer data. A total of 96 sets of data were used to form a database; in order to avoid the overfitting of data, a stratified 20-fold cross-validation was used to set the training model; Figure 11 showed a schematic description of the cross-validation. The designing and testing of these two machine learning models were performed in Matlab 2018b.

4.1. Prediction Model Structure

4.1.1. SVM. SVM, as an intelligent algorithm, can overcome nonlinear problems and is suitable for small samples [37]. The process of flexural strength prediction was performed using a kernel function to learn the relationship between the input index and the output index. In the SVM model, the kernel function defined in the high-dimensional feature
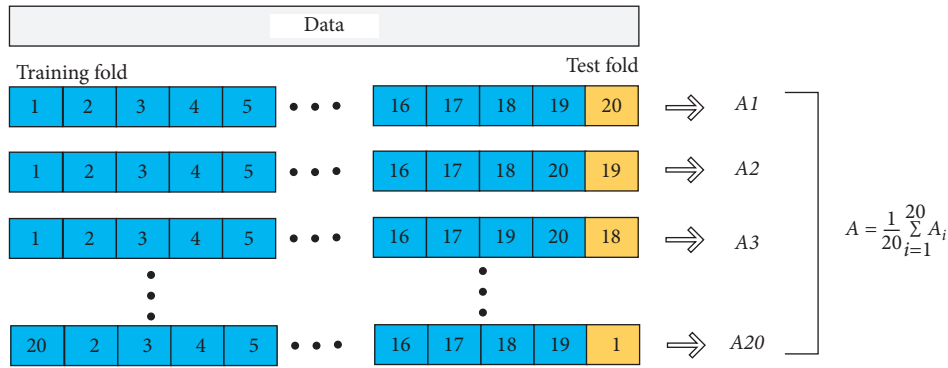
FIGURE 11: Schematic description of 20-fold validation.

space was used to estimate regression. The kernel function was mapped from the low-dimensional space to the high-dimensional space, so that the input had a nonlinear performance (Figure 12). Based on statistical learning theory, the SVM model performed regression estimation through risk minimization. Vapnik's ε-insensitive loss function was used to measure the risk. The risk function consisting of an empirical error and a confidence level value was minimized by the structural risk minimization principle [38].

4.1.1.1. Kernel Function. The Kernel function has a great influence on the prediction accuracy of SVM. In different prediction models, an appropriate kernel function should be selected according to research characteristics [39]. The Gaussian kernel function was used for the prediction model due to its advantages of radial basis kernel function and good antijamming ability.

4.1.1.2. Implementation Steps. First, a sample dataset of the model with N degrees of freedom was given: (x_1, y_1), $(x_2, y_2), \ldots, (x_n, y_n)$}, where x_i is the input vector (prediction vector), and y_i is the output vector (target vector). The set of x_i and y_i was a subset of the population $P(x, y)$ of unknown probability density distribution. Moreover, x_i was mapped to a high-dimensional feature space by the nonlinear function $\varphi(x_i)$, and linear regression was then carried out in the high-dimensional space. The relationship between the prediction vector and the target vector was simulated by the fitting function $f(x) = \omega^T \times \varphi(x) + b$, where ω and b are parameters.

4.1.2. BPNN. BPNN was mainly composed of two processes: signal forward propagation and error backpropagation. The input layer was processed by the hidden layers and then propagated to the output layer. The error between the output value and the actual value was transmitted to the input layer through the hidden layer, so that each unit could share the error. Further, through repeated weight adjustments, the required prediction accuracy was achieved [35]. The structure of the BPNN model shown in Figure 13 includes one input layer, one output layer, and several hidden layers [40].

(1) Hidden Layer of BPNN. Generally, a hidden layer has one or two layers. According to the Kolmogorov theorem,

a simple BPNN with only one hidden layer can approximate a nonlinear continuous function of any complexity degree with arbitrary accuracy on a closed set. In practical applications, the number of hidden layers is generally determined by comparing network training accuracies under different hidden layers [41]. After repeated tests, a hidden layer was used in this analysis, constituting a network structure of "1 + 1 + 1."

The number of hidden layer nodes was determined as $N = \sqrt{n + m} + a$, where N is the number of hidden layer nodes, n is the number of input layer nodes, m is the number of output layer nodes, and a is a constant between 1 and 10 [42]. This equation was used in combination with a trial-and-error method to improve the network performance. The hidden layer was iterated with the number of nodes from 3 to 13 until an optimal network performance was achieved. The optimal minimize number of nodes in the hidden layer was selected as 10.

(2) Determination of Transfer Function and Training Algorithm. (1) Transfer function: in order to select the transfer function, a typical design of BPNN was adopted. The log-Sigmoid function was adopted as the transfer function in the hidden layer, and the output layer used a linear transfer function, because its output value could be arbitrarily assigned as an output function [42]. (2) Training algorithm: a traditional BPNN belongs to the fastest descent method, which has a low learning efficiency and easily falls into a local minimum point. The Levenberg–Marquardt rule is suitable for solving large- and medium-scale problems, because one iteration can significantly reduce the error [43].

4.2. Analysis of Prediction Results. In order to verify the prediction accuracy of the model, the mean square error (MSE), root mean square error (RMSE), and the goodness of fit (R^2) were evaluated. The MSE reflected the degree of dispersion between predicted and actual values, and RMSE is the standard value of MSE, whereas R^2 verified the degree of fit between predicted and actual values.
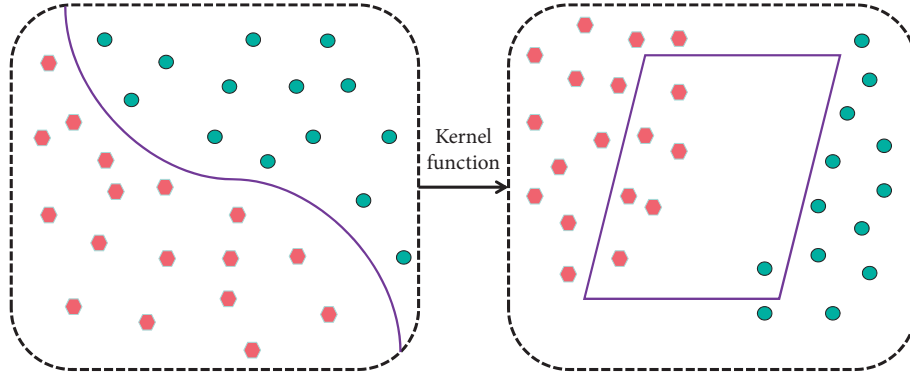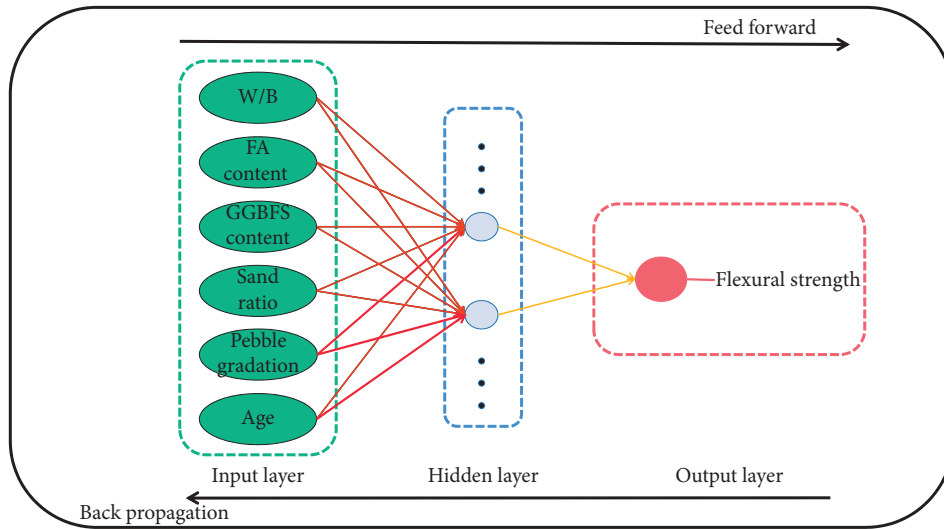
FIGURE 12: Nonlinear mapping in SVM.

FIGURE 13: BPNN structure.

$$\text{MSE} = \frac{\sum_{i=1}^{n} \left(y_{\text{obs}} - y_{\text{pred}} \right)^2}{n},$$

$$\text{RMSE} = \sqrt{\frac{\sum_{i=1}^{n} \left(y_{\text{obs}} - y_{\text{pred}} \right)^2}{n}}, \qquad (3)$$

$$R^2 = 1 - \frac{\sum_{i=1}^{n} \left(y_{\text{obs}} - y_{\text{pred}} \right)^2}{\sum_{i=1}^{n} \left(y_{\text{obs}} - \overline{y_{\text{obs}}} \right)^2},$$

where y_{obs} is the observed value, $\overline{y_{\text{obs}}}$ is the average observed value, and y_{pred} is the predictive value.

4.2.1. Prediction Results Comparison between BPNN and SVM. The performance of the BPNN model was verified by comparing it with the SVM model. From Table 6 and Figure 14, it can be seen that both the SVM model and the BPNN model have high accuracy, but in comparison, the R^2 for the SVM training set is 0.883, the R^2 for the BPNN training set is 0.888, the MSE for the SVM testing set is 0.332,

and R^2 is 0.841, and the MSE for the BPNN testing set is 0.143, and R^2 is 0.927. Based on these observations, it can be concluded that BPNN outperforms the SVM model in predicting the data in both the training and testing sets.

Table 7 and Figure 15 show the number of samples and corresponding percentage in the error range from BPNN and SVM, and the model with the most frequent value of misprediction rate was taken as the model presented in the paper. These key statistics showed that the BPNN model has higher predictive ability compared with SVM model. The percentages of BPNN model training set and test set prediction error range of 5% are 93.9% and 92.7%, respectively, while the SVM model values are 89.25 and 88.5.

Because the basic principles of BPNN and SVM are different, and the operating mechanism is also inconsistent, the significant difference analysis of the model prediction results can better analyze and compare the results. The SPSS 21.0 software was used to test the significance of the difference in the prediction results, the *t*-test method was selected to compare the significant difference between the two methods, and the P value was $0.28 > 0.05$, indicating that there is no significant difference in the fitting results of the two methods. Although there is no significant difference in

TABLE 6: Evaluation parameters of machine learning methods.

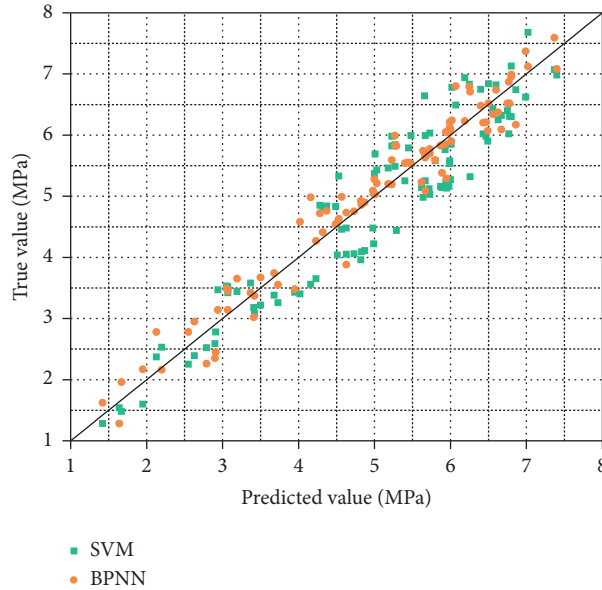|	MSE	RMSE	R^2
BPNN train	0.250	0.500	0.888
BPNN test	0.143	0.364	0.927
SVM train	0.262	0.507	0.883
SVM test	0.322	0.547	0.841

■ SVM
● BPNN

FIGURE 14: The correlation between actual and predicted output using the machine learning methods.

TABLE 7: Number of samples and corresponding percentage in the error range from machine learning predictions.

Error range(%))	SVM				BPNN			
	No of train	%	No of test	%	No of train	%	No of test	%
5	1628	89.25	85	88.5	1712	93.9	89	92.7
10	121	6.63	5	5.2	89	4.88	8	8.33
15	45	2.47	4	4.2	17	0.93	4	4.17
20	30	1.64	2	2.1	6	0.32	3	0.31

the results between the two modeling methods, BPNN was more suitable for the prediction of the flexural strength of the concrete, because there are higher requirements for prediction accuracy of concrete strength.

4.2.2. Prediction Results Comparison with the Empirical Equation. Existing flexural strength prediction models are mainly determined by the compressive strength of concretes. The Chinese code [44] presents a relationship between the compressive strength and flexural strength of concrete, and we compared the prediction accuracy of machine learning methods and empirical formulas for the 28-day flexural

strength of concrete, which was calculated from the machine learning method and the compressive strength in literature [45], respectively. The test results are shown in Table 8.

Since only the relationship between compressive strength and flexural strength of concrete at 28 days of age is given in the specification, the predicted results of 28-day concrete flexural strength in machine learning methods are also chosen for comparison, and the results showed that the BPNN model still has the highest accuracy. Meanwhile, the *t*-test results indicated that there is a significant difference between the machine learning prediction results and the empirical equation prediction results. Furthermore, the use of machine learning methods can avoid complicated
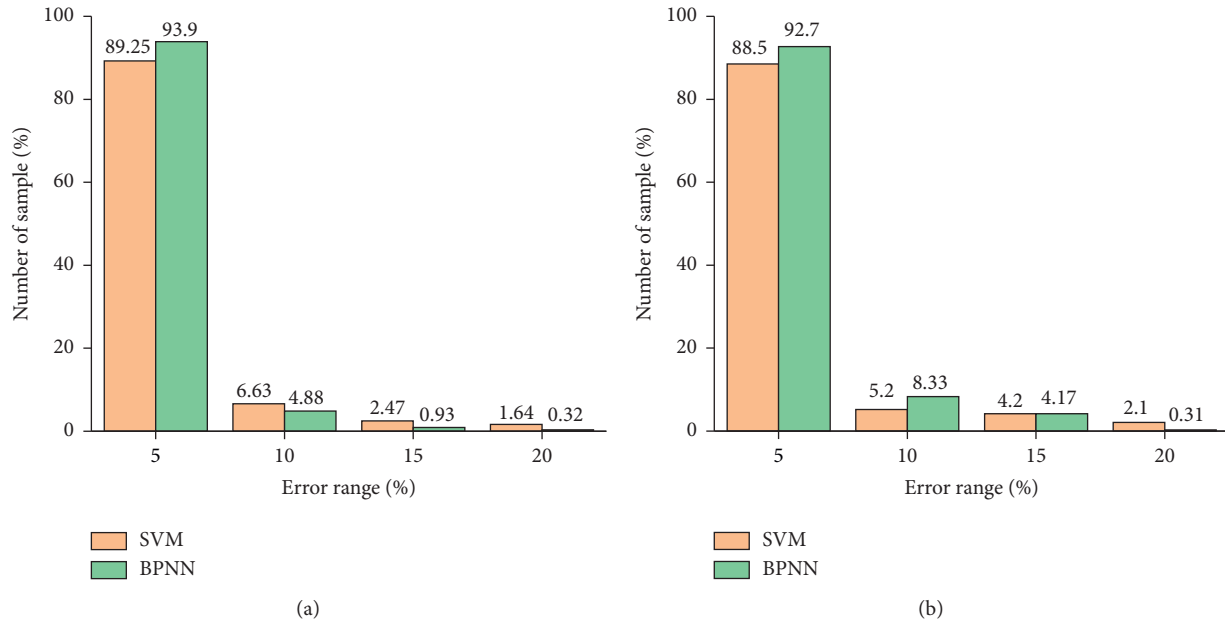
(a)

(b)

FIGURE 15: Distribution of the errors from machine learning methods. (a) Training. (b) Testing.

TABLE 8: Evaluation parameters of machine learning methods and empirical equation.

	MSE	RMSE	R^2
Empirical equation	0.114	0.338	0.720
SVM	0.050	0.223	0.876
BPNN	0.037	0.193	0.909

experiments and reduce the error of human intervention, so the BPNN model is recommended as a prediction tool for the flexural strength of concrete when the data type is similar to this research.

5. Conclusions

Orthogonal experiments were performed to study the flexural strength of an eco-friendly concrete containing FA and GGBFS. The effects of W/B ratio, FA content, GGBFS content, sand ratio, and gravel gradation on the flexural strength of the concrete were investigated by range analysis and hierarchy analysis. In addition, two machine learning models were proposed to predict the flexural strength of the concrete. The main observations of this research are summarized below.

The effects of different factors and different levels of each factor on the flexural strength of the concrete were analyzed, and the optimal mixing proportions of the concrete for six different ages were also determined. The optimal values of W/B ratio, FA content, GGBFS content, sand ratio, and gravel gradation were 35%, 15%, 15%, 39%, and 40%:60%, respectively.

The W/B ratio had the greatest effect on the flexural strength of the concrete. With the increase of W/B, the flexural strength of the concrete decreased gradually. The early stage of concrete curing was mainly influenced by the GGBFS content and the sand ratio. GGBFS manifested a strong activity by consuming Ca^{2+} ions in the concrete. The flexural strength of the concrete first increased and then decreased with the increase of the GGBFS content. The sand ratio had a positive role in the improvement of the flexural strength of the concrete.

Gravel gradation had a greater influence in the middle stage of concrete curing. The flexural strength of the concrete first increased and then decreased with the increase of the content of small gravels. FA mainly played a role in the later stage of concrete curing, because C-S-H initially covered the surface of FA, and the flexural strength of the concrete first increased and then decreased with the increase of the FA content.

The BPNN and SVM models both had higher accuracy than the empirical equation after 20-fold cross-validation. However, the BPNN model was more accurate than the SVM model, while there is no significant difference in the fitting results of the two methods. Thus, BPNN was more suitable for the prediction of the flexural strength of the concrete, because there are higher requirements for prediction accuracy of concrete strength.

The established model has a good adaptability in this research. In the future, future verification of the trained machine learning models on more mix proportions and curing conditions needs to be conducted. Moreover,

some machine learning models with higher prediction accuracy deserve to be built as much as complexity allows.

Data Availability

The data used to support the findings of this study are available from the corresponding author upon request.

Conflicts of Interest

The authors declare no conflicts of interest regarding the publication of this paper.

Acknowledgments

References

[1] P. Rashiddadash, A. A. Ramezanianpour, and M. Mahdikhani, "Experimental investigation on flexural toughness of hybrid fiber reinforced concrete (HFRC) containing metakaolin and pumice," *Construction and Building Materials*, vol. 51, pp. 737-738, 1953.

[2] R. Liu, H. Li, Q. Jiang, and X. Meng, "Experimental investigation on flexural properties of directional steel fiber reinforced rubberized concrete," *Structure*, vol. 27, pp. 1660–1669, 2020.

[3] O. Karahan, "Transport properties of high volume fly ash or slag concrete exposed to high temperature," *Construction and Building Materials*, vol. 152, pp. 898–906, 2017.

[4] D. Ravina and P. K. Mehta, "Properties of fresh concrete containing large amounts of fly ash," *Cement and Concrete Research*, vol. 16, no. 2, pp. 227–238, 1986.

[5] P. K. Mehta, G. M. Giaccio, and V. M. Malhotra, "Concrete incorporating high volumes of ASTM class F fly ash," *Cement, Concrete and Aggregates*, vol. 10, no. 2, 1988.

[6] M. Nili and M. Tadayon, "The relationship between setting time and early age strength of concrete containing silica fume, fly ash and slag," in *Proceedings of the The Third International Conference on Sustainable Construction Materials and Technologies*, pp. 19–21, the University of Kyoto, Kyoto Research Park, Kyoto, Japan, August 2013.

[7] G. L. Golewski, "Estimation of the optimum content of fly ash in concrete composite based on the analysis of fracture toughness tests using various measuring systems," *Construction and Building Materials*, vol. 213, pp. 142–155, 2019.

[8] G. L. Golewski, "Effect of curing time on the fracture toughness of fly ash concrete composites," *Composite Structures*, vol. 185, pp. 105–112, 2018.

[9] C. D. Atis, "High-volume fly ash concrete with high strength and low drying shrinkage, "high-volume fly ash concrete with high strength and low drying shrinkage," *Journal of Materials in Civil Engineering*, vol. 15, no. 2, pp. 153–156, 2003.

[10] P. Wedding, F. Hogan, and J. Meusel, "Evaluation for durability and strength development of a ground granulated blast furnace slag," *Cement, Concrete and Aggregates*, vol. 3, no. 1, p. 40, 1981.

[11] D. M. Roy and D. M. ldorn, "Hydration structure, and properties of blast furnace slag cements,mortars, and concrete," *ACI Journal Proceedings*, vol. 79, pp. 444–457, 1982.

[12] V. Sivasundaram and V. M. Malhotra, "Properties of concrete incorporating low quantity of cement and high volumes of ground granulated slag," *ACI Materials Journal*, vol. 89, pp. 554–563, 1992.

[13] J. M. Khatib and J. J. Hibbert, "Selected engineering properties of concrete incorporating slag and metakaolin," *Construction and Building Materials*, vol. 19, no. 6, pp. 460–472, 2005.

[14] B. H. Bharatkumar, B. K. Raghuprasad, D. S. Ramachandramurthy, R. Narayanan, and S. Gopalakrishnan, "'Effect of fly ash and slag on the fracture characteristics of high performance concrete," *Materials and Structures, A, Structural Materials Properties, Microstructure and Processing*, vol. 528, no. 4-5, pp. 2149–2157, 2011.

[15] Z. Ali, R. Shadi, A. Nazari, and S. Riahi, "Effects of Al_2O_3 nanoparticles on properties of self compacting concrete with ground granulated blast furnace slag (GGBFS) as binder," *Science China Technological Sciences*, vol. 54, no. 9, pp. 2327–2338, 2011.

[16] N. Ali and R. Shadi, "The role of SiO2 nanoparticles and ground granulated blast furnace slag admixtures on physical, thermal and mechanical properties of self compacting concrete," *Materials Science and Engineering*, vol. 528, pp. 2149–2157, 2011.

[17] N. Ali and R. Shadi, "The effects of TiO2 nanoparticles on physical, thermal and mechanical properties of concrete using ground granulated blast furnace slag as binder," *Materials Science and Engineering*, vol. 528, pp. 085–2092, 2011.

[18] N. Ali and R. Shadi, "The effects of ZnO_2 nanoparticles on properties of concrete using ground granulated blast furnace slag as binder," *Journal of Composite Materials*, vol. 46, no. 9, pp. 1079–1090, 2011.

[19] J. Zheng and G. Liu, "The influence and application of slag, fly ash, and limestone flour on compressive strength of concrete based on the concrete compressive strength development over time (CCSDOT) model," *Applied Sciences*, vol. 10, Article ID 3572, 3572 pages, 2020.

[20] S. Chithra, S. R. R. Senthil Kumar, K. Chinnaraju, and F. Alfin Ashmita, "A comparative study on the compressive strength prediction models for High Performance Concrete containing nano silica and copper slag using regression analysis and Artificial Neural Networks," *Construction and Building Materials*, vol. 114, pp. 528–535, 2016.

[21] J. S. Chou, C. K. Chiu, M. Farfoura, and I. Al-Taharwa, "Optimizing the prediction accuracy of concrete compressive strength based on a comparison of data-mining techniques," *Journal of Computing in Civil Engineering*, vol. 9, no. 3, pp. 242–253, 2011.

[22] B. A. Omran, Q. Chen, and R. Jin, "Comparison of data mining techniques for predicting compressive strength of environmentally friendly concrete," *Journal of Computing in Civil Engineering*, vol. 30, no. 6, Article ID 04016029, 2016.

[23] H.-V. T. Mai, T.-A. Nguyen, Ly Hai-Bang, and V. Q. Tran, "Prediction compressive strength of concrete containing GGBFS using random forest model," *Advances in Civil Engineering*, vol. 2021, p. 12, Article ID 6671448, 2021.

[24] P. Chopra, R. K. Sharma, M. Kumar, and T. Chopra, "Comparison of machine learning techniques for the prediction of compressive strength of concrete," *Advances in Civil Engineering*, vol. 2018, pp. 1–9, 2021.

[25] *Code for Mix Design of Hydraulic concrete; DL/T5330-2005*, Development and Reform Commission of the People's Republic of China, Beijing, China, 2005.

[26] M. Nili, M. Tadayon, and M. Nili, "The relationship between setting time and early age strength of concrete containing silica fume, fly ash and slag," in *Proceedings of the Third International Conference on Sustainable Construction Materials and Technologies*, pp. 18–21, the University of Kyoto, Kyoto Research Park, Kyoto, Japan, August 2013.

[27] S. M. Zhao and J. X. Gong, "Experimental study on the strength and shrinkage of high performance concrete with dual mineral admixtures," *Concrete*, vol. 02, pp. 81–86+89, 2016, (in Chinese).

[28] *Specification for Mix Proportion Design of Ordinary concrete; JGJ 55-2011*, Ministry of Housing and Urban-Rural Development of the People's Republic of China, Beijing, China, 2011.

[29] *Test Code for Hydraulic concrete; SL352—2006*, Ministry of Water Resources of the People's Republic of China, Beijing, China, 2006.

[30] P. Zhang, Q. Li, and H. Wei, "Investigation of flexural properties of cement-stabilized macadam reinforced with polypropylene fiber," *Journal of Materials in Civil Engineering*, vol. 22, no. 12, pp. 1282–1287, 2010.

[31] P. C. Aïtcin, "The importance of the water–cement and water–binder ratios," in *Science and Technology of Concrete Admixtures*, pp. 3–13, Woodhead Publishing, Sawston, UK, 2016.

[32] J. W. Bullard, H. M. Jennings, R. A. Livingston et al., "Mechanisms of cement hydration," *Cement and Concrete Research*, vol. 41, pp. 1208–1223, 2011.

[33] D. Sari and A. G. Pasamehmetoglu, "The effects of gradation and admixture on the pumice lightweight aggregate concrete," *Cement and Concrete Research*, vol. 35, pp. 936–942, 2005.

[34] D. A. Abrams, *Design of concrete Mixtures. Structural Materials Research Laboratory, Lewis Institute*, Lewis Institute, Chicago, Illinois, 1919.

[35] Q. Y. Zhang, "Experimental study on concrete material performance of concrete face slab dam in high cold region," Master's Thesis, Zhengzhou University, Zhengzhou, China, 2016.

[36] C. C. Gong, J. Zhang, S. D. Wang, and L. C. Lu, "Effect of aggregate gradation with fuller distribution on properties of sulphoaluminate cement concrete," *Journal of Wuhan University of Technology*, vol. 30, pp. 1029–1035, 2015.

[37] H. Yan, J. Zhang, S. S. Rahman, N. Zhou, and Y. Suo, "Predicting permeability changes with injecting CO2 in coal seams during CO2 geological sequestration: a comparative study among six SVM-based hybrid models," *The Science of the Total Environment*, vol. 705, 2020.

[38] B. Dong, C. Cao, and S. E. Lee, "Applying support vector machines to predict building energy consumption in tropical region," *Energy and Buildings*, vol. 37, no. 5, pp. 545–553, 2005.

[39] T. Y. Liu, P. Zhang, J. Wang, and Yi-F. Ling, "Compressive strength prediction of PVA fiber- reinforced cementitious composites containing nano-SiO2 using BP neural network," *Materials*, vol. 13, p. 521, 2020.

[40] F. Niloufar, Y. Wei-Mon, M. T. Mohammad, and K. Alibakhsh, "The application of artificial neural networks to predict the performance of solar chimney filled with phase change materials," *Design of concrete mixtures*, vol. 171, pp. 1255–1262, 2018.

[41] Z. Z. Zhang, X. M. Ma, and Y. X. Yang, "Bounds on the number of hidden neurons in three-layer binary neural networks," *Neural Networks*, vol. 17, no. 7, pp. 995–1002, 2004.

[42] K. L. Zhou and Y. H. Kang, *Neural Network Model and MATLAB Simulation Program Design*, Tsinghua University Press, Beijing, China, (in Chinese), 2005.

[43] B. Huang and C. Ma, "A Shamanskii-like self-adaptive Levenberg–Marquardt method for nonlinear equations," *Computers and Mathematics with Applications*, vol. 77, no. 2, pp. 357–373, 2018.

[44] *Code for Design of Highway Cement Concrete Pavement*, Ministry of Communications of the People's Republic of China, Beijing, China, 2003.

[45] Q. F. Li and Q. Y. Zhang, "Experimental study on the compressive strength and shrinkage of concrete containing fly ash and ground granulated blast-furnace slag," *Structural Concrete*, vol. 20, pp. 1551–1560, 2019.

[46] S. Haruna, B. Mohammed, M. M. A. Wahab, and M. S. Liew, "Effect of paste aggregate ratio and curing methods on the performance of one-part alkali-activated concrete," *Construction and Building Materials*, vol. 261, Article ID 120024, 2020.

[47] C. B. Cheah, L. L. Tiong, E. P. Ng, and C. W. Oo, "The engineering performance of concrete containing high volume of ground granulated blast furnace slag and pulverized fly ash with polycarboxylate-based superplasticizer," *Construction and Building Materials*, vol. 202, pp. 909–921, 2019.

Review Article

Relationship between the Dynamic Parameters of a Structure's Vibration Process and the Loading Model Moving on a Bridge

Thanh. Q Nguyen [1,2]

^{1}Faculty of Engineering and Technology, Thu Dau Mot University, Thu Dau Mot, Binh Duong, Vietnam
^{2}Thu Dau Mot University, Thu Dau Mot, Binh Duong, Vietnam

Correspondence should be addressed to Thanh. Q Nguyen; nguyenquangthanh@tdmu.edu.vn

A sufficiently strict conduction of supervision during bridge operation is a crucial matter for many countries, including the underdeveloped country of Viet Nam. In recent times, the budgets in developed countries used for funding the implementation of quality-assessment procedures are quite high compared to the lower budgets in underdeveloped countries. The plan proposed in this work addresses the current lack of information available in the process of structure-quality evaluation. The vibration signals will be acquired from the random circulation status to determine the structure's behavior so as to utilize the signal information during the bridge span's operation. The study's main goal is to find various parameters that can be used to evaluate the actual bridge performance. These parameters must meet certain criteria, such as high sensitivity, low measurement cost, and efficiency in the measurement process, but must not affect the itinerary of vehicles moving on the bridge. The actual structural vibration signals used in this work currently serve as a best trend model for evaluating the operation of the bridge span structure. This study will focus on determining the relationship among deflection, acceleration, and vehicle load so as to evaluate the structure's working process. This study has also fabricated an experimental model to evaluate and test the sensitivity of the parameters utilized in this study in order to verify the results obtained. The results obtained in this research will be applied for the quality-control process in several bridge models with span structures built with the composite steel concrete cross section of the beam. Many developing countries, including Viet Nam, will receive benefit in the future from the useful advantages presented in this study.

1. Introduction

Viet Nam is similar to other Southeast Asian countries [1, 2] located in the region, in that it has an interlace system of rivers and canals. Most major cities in Viet Nam are located in areas near rivers or river junctions. After conducting extensive surveys in the Ho Chi Minh City area [3, 4], it was determined that there are more than 1000 bridges [5, 6] and safe operations of these bridges are especially considered as a key focus because of their important role in so many socioeconomic activities. The normal measures of assessing the quality conditions of the bridge structure will be undertaken through an assessment of the bridge structure's concrete beams and the composite steel concrete cross section of the beam [7, 8]. At present, the inspection, monitoring, and verification of bridge quality are commonly implemented through three main measures as follows:

(i) The first measure is a system of human monitoring, giving information that is often more qualitative than quantitative, and that can be somewhat subjective. The techniques of this measure include inspection and monitoring by manual methods, visual inspection, and use of specialized equipment [9–11]. This measure has significant advantages and is simple and easy to implement, and the inspection cost for initial investment is low, but it has disadvantages as well: the damages in the details of the bridge structure cannot be detected in a timely fashion, and the bridge material mechanical changes cannot be evaluated. Most of the information obtained from a structure with these methods is of a qualitative nature, acquired through the subjective evaluation of human observations.

(ii) The second measure consists of methods for collecting quantitative data for bridge vibrations generated by an applied periodic force. The bridge quality inspection [12–14] includes the following activities: the quality is either merely checked or thoroughly determined, the project quality is formally assessed, and the quality is compared to the design's original requirements. The aim of this measure is to assess the bridge's actual working ability under the actual load effect. Some parameters are used for a quantitative evaluation process during implementation [15], including deformation, deflection, vibration amplitude, and specific frequency. The advantage of this measure is that it can give us a clear understanding of the different quantitative values and the load's impact options. These methods can shed light on the factors responsible for putting the structure in some of the most dangerous situations during its operation. This measure's disadvantage is that the measurement data are obtained in a static state, except for few of the following dynamic parameters: specific frequency, damping coefficient, and vibration amplitude, which are determined by generating the vibration pattern with a periodic force. The amount of information received from this method is too low; therefore, it cannot fully reflect the operation status of the structure, nor fully explain the structure's behavior.

(iii) The third measure surveys the structure's behavior during the actual operation through vibration measurement [16–19]. This measure has been widely applied to bridge abutments in recent times. This measure allows the acquisition of much data regarding bridge behavior under diverse actual loads. This measure allows the advantages of characterizing the actual situation of the load, detecting changes in mechanical parameters, locating weakened portions of the structure, and determining the weakening rate over time. These advantages can help in making reasonable decisions and plans when evaluating a project's quality. However, for the cases of difficult economic situations in underdeveloped countries, these testing systems are not economically feasible and so cannot be widely applied.

Assessing the advantages and disadvantages of all three methods above, this study proposes several methods for building relationships between important parameters in the bridge structure's vibration process so as to collect data for the vibrations and deformation of the structure under the effects of random loads during operation and utilization. The data obtained in this study will supplement the bridge's existing database system and, at the same time, will add new parameters having a higher sensitivity than traditional parameters. This can serve in making the most suitable plan for

quality assessment, inspection, and regular maintenance for a project. This study has practical significance in monitoring and evaluating a project's working status over time. This study also helps management agencies form a basis for making important decisions about the structure's operation. Furthermore, the results in this study, which have been implemented in practice, will establish a database source facilitating the application of these advanced methods in quality assessment and project management. This is the basis for expanding these research methods and conducting future bridge evaluations.

2. Theoretical Basis

Many studies have already carried out the modeling of bridge structures, which are categorized by type according to the structure's bearing status. Many models have simulated the structure of a bridge span in the form of force-bearing beams, models which are presently popular [20–22]. For a load applied under static conditions, the span structure model is generally depicted as shown in Figure 1.

For the case of the span model shown in Figure 1, if P is the static load, the beam's deflection y is given by the following formulas as

$$y = \begin{cases} \dfrac{Pbz}{6EJl}\left(l^2 - z^2 - b^2\right), & 0 \le z \le a, \\[4mm] \dfrac{Pa(l-z)}{6EJl}\left(2lz - z^2 - a^2\right), & a \le z \le l, \end{cases} \tag{1}$$

in which l is the length of the beam and a and b are the positions to determine the set point of the load P. EJ is the flexural stiffness; E is the elastic modulus; P is the load on the beam; and J is the area inertia moment to the principal axis of inertia, which is coincident with the x-axis direction.

If the load p moves with speed v along the beam length with $Q = Q_0 \cos(\Omega t)$, as shown in Figure 2, the beam's forced vibration is demonstrated through the deflection equation, shown as follows:

$$y = \frac{2gPl^3}{A\gamma\pi^2} \sum_{i=1}^{i=\infty} \frac{\sin i\pi x/l}{i^2\left(i^2\pi^2 a^2 - v^2 l^2\right)} \sin \frac{i\pi x}{l} \\ - \frac{2gPl^4 v}{A\gamma\pi^3 d} \sum_{i=1}^{i=\infty} \frac{\sin i\pi x/l}{i^3\left(i^2\pi^2 a^2 - v^2 l^2\right)} \sin \frac{i^2\pi^2 at}{l^2}, \tag{2}$$

where g is the gravity acceleration, ρ is the specific weight per structure's unit volume, A is the cross-sectional area, $d = \sqrt{EJ/A\rho}$, and t is the time. The forces actually acting on the structure are, however, often in the form of a harmonic force.

For the case shown in Figure 3, in which Q is the variable force given by the expression $Q = Q_0 \cos \Omega t$ and moving with speed v, the beam's forced vibration [23, 24] is presented as follows:
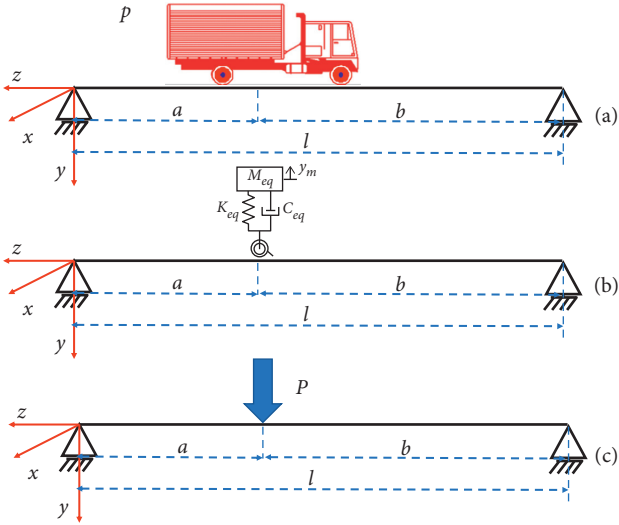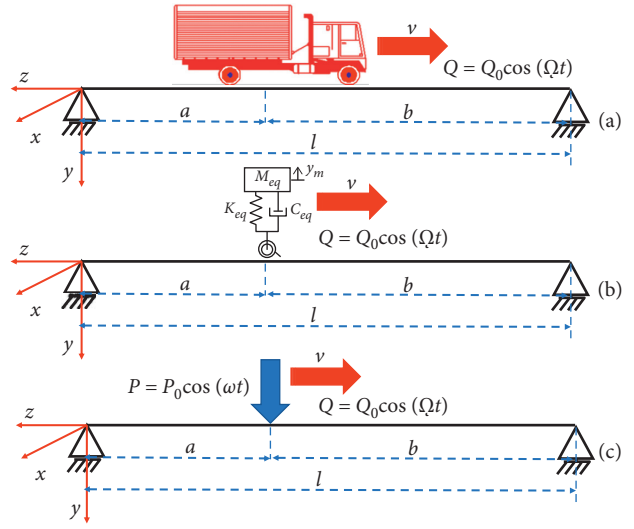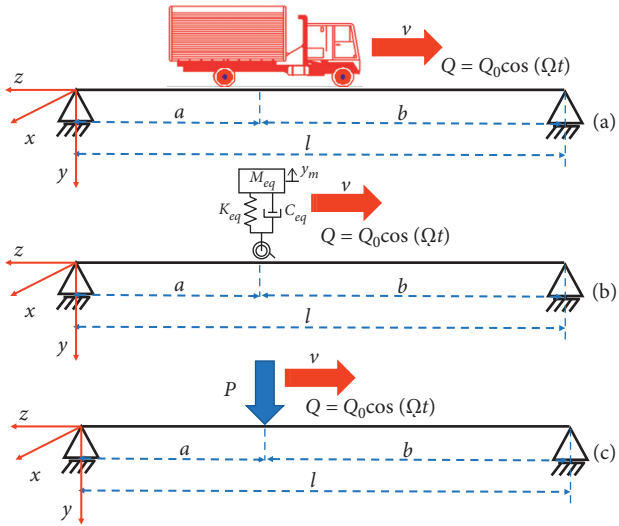
FIGURE 1: Single beam borne with static load.

FIGURE 2: Single beam is under load moving with velocity v along the beam bar.

$$y = \frac{Pl^3}{EJ\pi^4} \sum_{i=1}^{i=\infty} \sin \frac{i\pi x}{l} \left\{ \frac{\sin(i\pi v/l + \Omega)t}{i^4 - (\beta + i\beta)^2} + \frac{\sin(i\pi v/l - \Omega)t}{i^4 - (\beta - i\beta)^2} \right\}$$

$$- \frac{Pl^3}{EJ\pi^4} \sum_{i=1}^{i=\infty} \sin \frac{i\pi x}{l} \left\{ \frac{\alpha}{i} \left(\frac{\sin i^2 \pi^2 at/l^2}{-i^2\alpha^2 + (i^2 - \beta)^2} + \frac{\sin i^2 \pi^2 at/l^2}{-i^2\alpha^2 + (i^2 + \beta)^2} \right) \right\},$$

(3)

in which $\alpha = vl/\pi a$; $\beta = \tau/\tau_2$; $\tau = 2l^2/\pi a$; $\tau_1 = l/v$; and $\tau_2 = 2\pi/\Omega$. The nondamped free vibration of a single support beam has the following form:

$$y = \sum_{i=1}^{i=\infty} \sin \frac{i\pi z}{l} (C_i \cos p_i t + D_i \sin p_i t),$$

(4)

where C_i and D_i are constants and p_i is the ith-specific frequency in the following equation:

FIGURE 3: Single beam is under the harmonically variable load moving with velocity v along the beam bar.

$$p_i = \left(\frac{i\pi}{l}\right)^2 \sqrt{\frac{EJ}{A\rho}}.$$

(5)

This study introduces the concept of "dynamic coefficient" so as to determine the relationship between the structure's load impact and the specific vibration frequency, in order to evaluate the changes in bridge span structure during the vibration process. The dynamic coefficient model has demonstrated that this coefficient is used for evaluating the bridge's load capacity through the deflection and the vibration frequency, as shown in equations (2) and (3), and the abridged model of the dynamic coefficient, as shown in the following equation:

$$\delta = 1 + \frac{Q}{P} \frac{\omega_{(1)}^2}{\Omega^2} \frac{1}{\left(\omega_{(1)}^2/\Omega^2 - 1\right)^2 + 4\left(\omega^2/\Omega^2 + \omega_b^2/\Omega^2\right)}$$

$$\cdot \left\{ \left[\left(\frac{\omega_{(1)}^2}{\Omega^2} - 1\right)^2 + 4\frac{\omega_b^2}{\Omega^2} \right]^{1/2} + 2\frac{\omega}{\Omega} e^{-\omega_b l/(2v)} \right\},$$

(6)

in which δ is the dynamic coefficient, ω is the excitation frequency of vehicle load, Ω is the excitation frequency of the load under the action of velocity v, $\omega_{(1)}$ is the first excitation frequency of vehicle load, and ω_b is the bending frequency.

3. Results

3.1. Building the Experimental Models.
Considering the methods implemented by us, this study examines the actual model of the Thang Long Bridge, as shown in Figure 4, which has the following specifications: the bridge is 60 m long; it includes 5 spans, each span being 12 m long; it has a simple steel concrete; the span cross-section includes 5 steel I-beams with dimensions $550 \times 250 \times 9 \times 22$ mm; the abutments and pillars are made of reinforced concrete; the bridge deck for vehicles is made of reinforced concrete of thickness
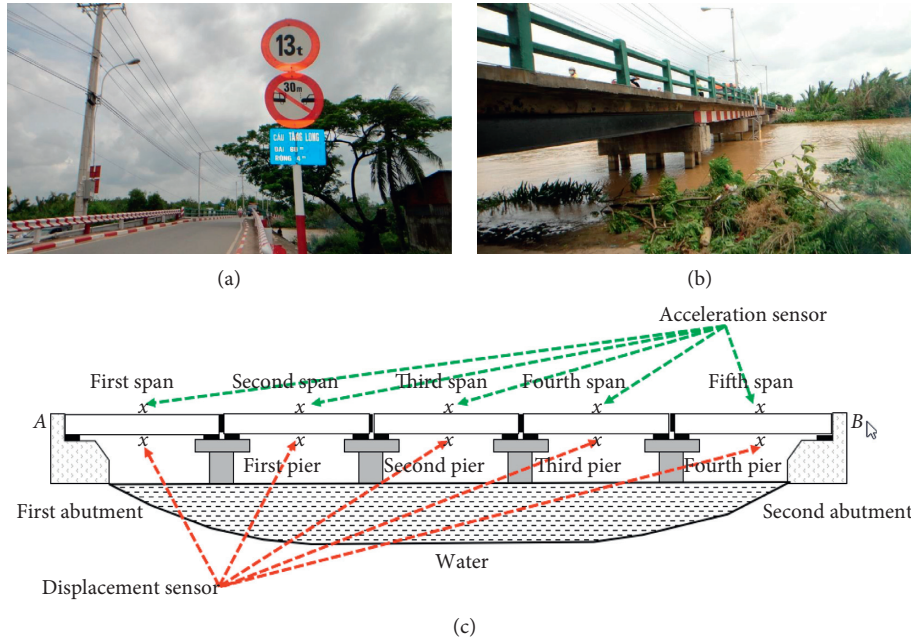
(a)

(b)

(c)

FIGURE 4: Actual model and longitudinal section of Thang Long Bridge.

18 cm; the bridge deck for pedestrians has a thickness of 20 cm; the current operating load is 13 tons; and the bridge was built before 1990. The modeling process used in this study for the Thang Long Bridge, which is located on Thang Long Street, District 9, Ho Chi Minh City, is shown in Figure 5.

The bridge span is narrow; therefore, only one vehicle at a time can cross the bridge. The study models the Thang Long Bridge's mechanical force-bearing system, as shown in Figure 5, with a load consisting of two contributing components: the concentrated load P and the moving load $Q_0 \sin \Omega t$, with forced frequency Ω, as originally analyzed.

In this research, the displacement signals are measured using a displacement sensor and the vibrations are measured with an accelerometer sensor. These sensors are permanently mounted and in contact with the beams' underside surfaces. The signal acquisition model is demonstrated in Figure 6.

In fact, the frequency of the constraining force Ω often depends on the mechanism and Q depends on the velocity v as in Table 1. This study assumes that $Q = k * v^2$ and $\Omega = v/R$, where Q is the amplitude of the harmonic force, k is the experimental coefficient, Ω is the force's angular frequency, and R is the wheel radius, as shown in Table 2. This study will consider the change of load P in the range of load limit for each type of vehicle, as in Table 3, due to the harmonically constraining force influenced by the vehicle structure.

With the parameters of the load P, the velocity v, and the frequency Ω of the constraining force, this study has built a workable model through the actual measurement process so as to determine the maximum deflection at given locations on the bridge span. This study has calculated the maximum stress value during the beams' vibration for the locations at which the deflection value is measured. The graph of the relationship between deflection and stress is given in Figure 7.

We can see the linear relationship between deflection and stress with the results in Figures 7 and 8. The linear regression

equation is $y = 6 \times 10^{-12}x - 8 \times 10^{-9}$ with a correlation coefficient of $R^2 = 1$. When the load, velocity, and frequency of the constraining force change, the slope coefficient in Figure 8 remains constant; the deflection linearly increases when the load increases, regardless of the change in velocity or the change in frequency of the constraining force. The relationship between displacement and stress is often expressed as the structure's stress-deformation relationship. The results shown in Figure 9 [25, 26] were obtained from a study that used the linear material model to demonstrate the stress-deformation relationship of a concrete-reinforced beam structure with two required parameters: the elastic modulus of steel E_s and the yield intensity of steel f_y. This concrete structure's simple stress-strain relationship curve has a multilinear isotropic form, proposed by Kachlakev [27], with two required parameters: the concrete's elastic modulus E_c and its compressive strength f_c'. In this material model, the von Mises criterion was used for determining the stress threshold so as to convert the concrete's linear behavior into nonlinear behavior, as shown in Figure 10, in which ε_0 is the stress at the peak of the material structure and β is a material parameter depending on the shape of the stress-deformation diagram. The stress-deformation relationship is given by equation (7a). For the case of [25], the stress-deformation relationship is as shown in equation (7b).

$$\sigma = E\varepsilon, \tag{7a}$$

$$\sigma_i = E_i \varepsilon_i. \tag{7b}$$

With the models being studied in [25–27], we can see in the results that the relationship between stress and deformation is either always a linear function during a process [28, 29] or it is only a linear function in each defined space [25, 26]. An evaluation model that exhibits both the influence of the elastic modulus E, which is a structural characteristic,
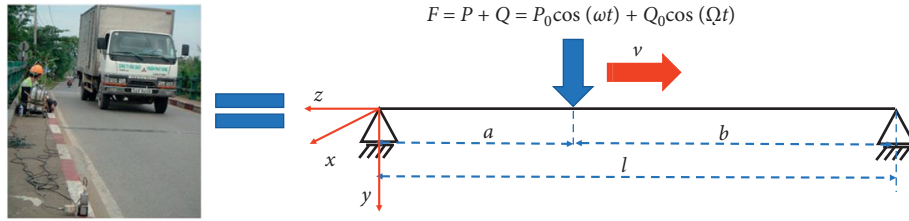
FIGURE 5: Actual load model of Thang Long Bridge.

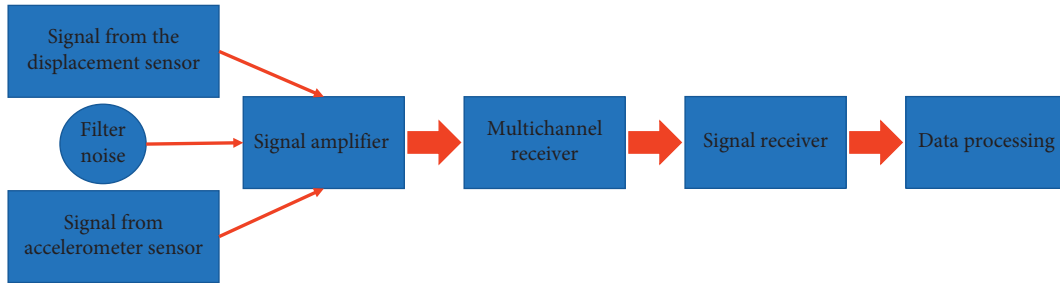

FIGURE 6: Diagram of data acquisition from the displacement sensor and vibration accelerometer.

TABLE 1: Deflection data and elongation with load P, as the experimental velocity v changes.

P	v	Deflection (m)	Stress (N/m^2)
5,700	13	0.0056461	9.93×10^8
5,800	6	0.0052025	9.15×10^8
5,900	6	0.0052897	9.31×10^8
6,100	6	0.0054634	9.61×10^8
6,200	14	0.0066553	1.17×10^8
6,500	6	0.0058087	1.02×10^9
7,100	15	0.0071237	1.25×10^9
8,200	13	0.0080203	1.41×10^9
8,300	15	0.0083693	1.47×10^9
8,500	8	0.0079308	1.40×10^9
8,600	8	0.0080177	1.41×10^9
8,800	6	0.0086454	1.52×10^9
9,000	8	0.0083818	1.47×10^9
10,100	9	0.01011	1.78×10^9
10,200	8	0.0094648	1.67×10^9
10,300	9	0.010372	1.82×10^9
10,400	4	0.010212	1.80×10^9
10,500	5	0.010266	1.81×10^9
10,600	3	0.010262	1.81×10^9
10,900	16	0.010373	1.82×10^9
11,000	5	0.010795	1.90×10^9
11,200	5	0.010946	1.93×10^9

TABLE 2: Load parameters corresponding to different radii of vehicle wheels.

Wheel radius R (m)	Load index	Weight (kg)
0.330	83	487
0.356	88	560
0.381	96	710
0.406	100	800
0.432	104	900
0.457	108	1,000
0.483	109	1,030
0.508	110	1,060
0.533	111	1,090
0.559	112	1,120

TABLE 3: Increased range of P force value corresponding to each type of wheel radius.

R-wheel radius (m)	P value (N)
0.008382	4,500–4,800
0.009042	4,800–5,600
0.009677	5,600–7,100
0.010312	7,100–8,000
0.010973	8,000–9,000
0.011608	9,000–10,000
0.012268	10,000–10,300
0.012903	10,300–10,600
0.013538	10,600–10,900
0.014199	10,900–11,200

and the antiviscosity coefficient C, which is a characteristic property of the material, has not yet been constructed.

3.2. Relationship of Dynamic Parameters

3.2.1. Relationship between Deflection and Vibration Acceleration. For the change of each load P, this study gets the results of both maximum deflection and maximum acceleration. When the velocity v changes in the model, this study changes the velocity v from 6 m/s to 16 m/s in order to

either simplify the simulation process or conform to the bridge inspection standards.

We can see from the graphs shown in Figures 11(a)–11(f) that the variable relationship between deflection and acceleration at different load levels is relatively similar in terms of shape. Generally, when the acceleration increases, the deflection also increases and the difference in loads may be due to the masses of the loads that have influenced the beam's vibration
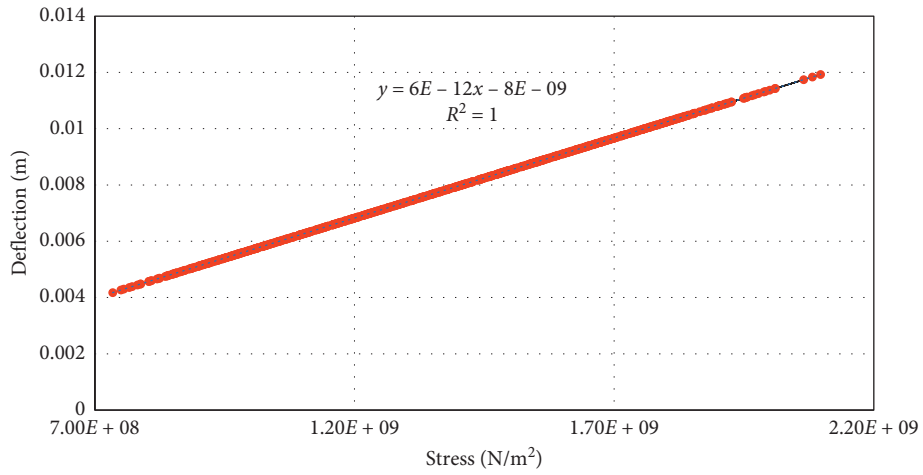
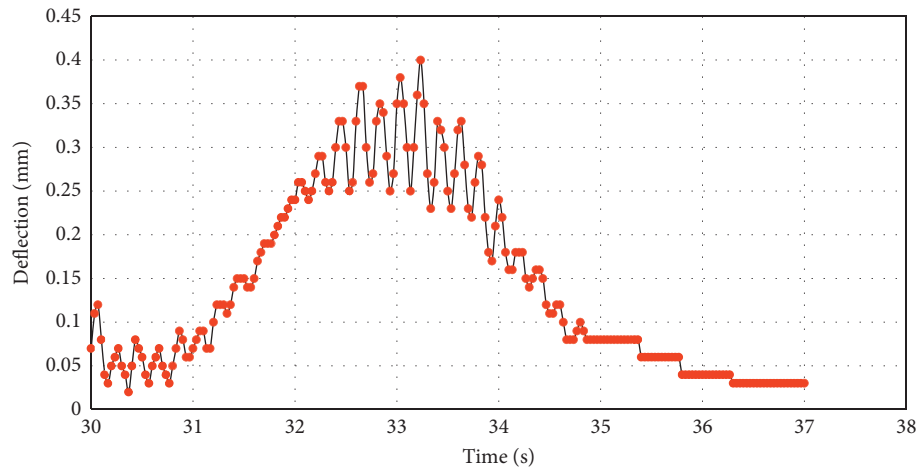FIGURE 7: Graph showing the relationship between deflection and stress.

$$y = 6E - 12x - 8E - 09$$
$$R^2 = 1$$
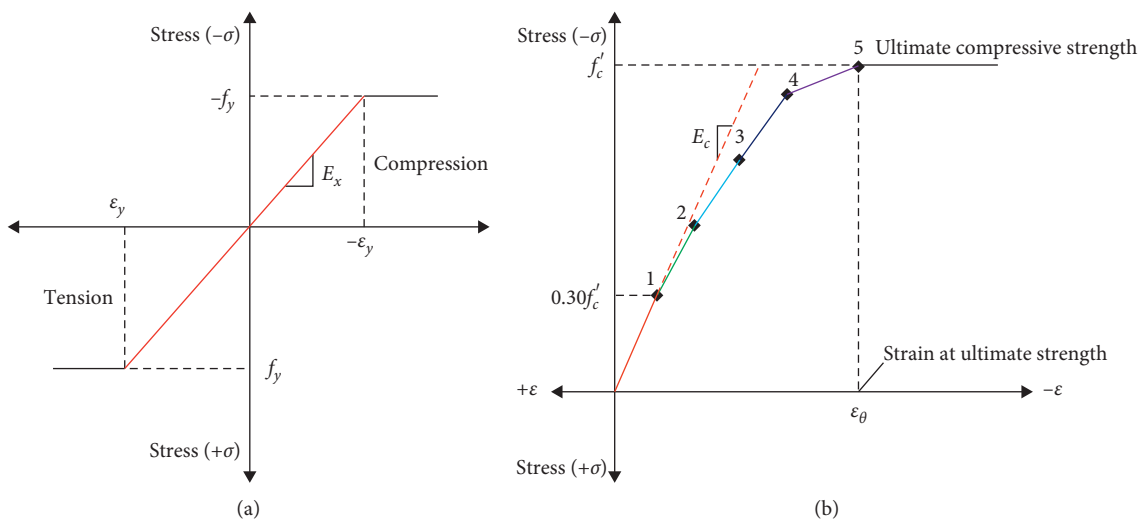

FIGURE 8: Signal deflection over time.

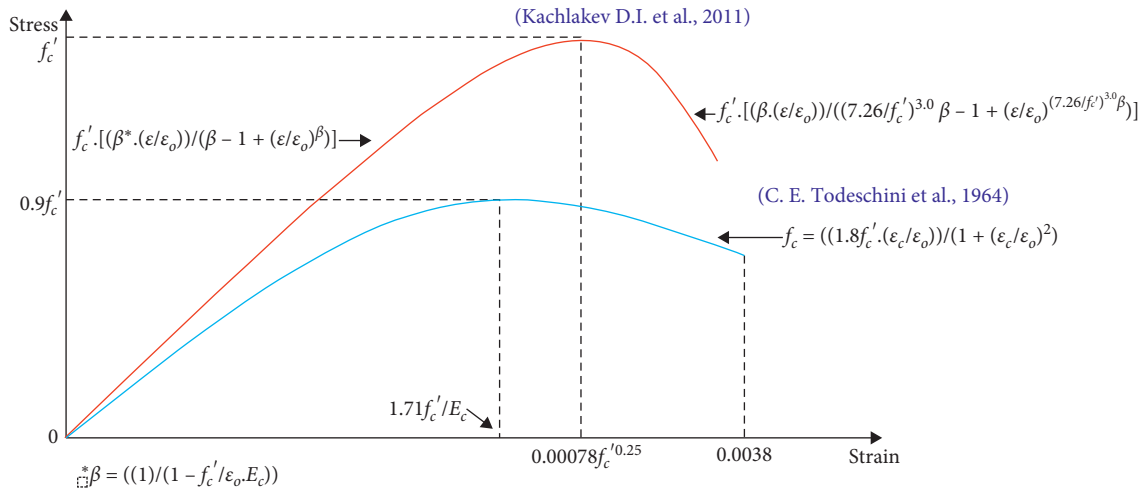FIGURE 9: Stress-deformation relationship between reinforcement and concrete beams' concrete [25] and [26].

$$f_c'.[(\beta^*.(\varepsilon/\varepsilon_o))/(\beta - 1 + (\varepsilon/\varepsilon_o)^\beta)] \rightarrow$$

(Kachlakev D.I. et al., 2011)

$$\leftarrow f_c'.[(\beta.(\varepsilon/\varepsilon_o))/((7.26/f_c')^{3.0}\,\beta - 1 + (\varepsilon/\varepsilon_o)^{(7.26/f_c')^{3.0}\beta})]$$

(C. E. Todeschini et al., 1964)

$$\leftarrow f_c = ((1.8f_c'.(\varepsilon_c/\varepsilon_o))/(1 + (\varepsilon_c/\varepsilon_o)^2)$$

$$1.71f_c'/E_c$$

$$0.00078f_c'^{0.25} \qquad 0.0038$$

$$\dashbox{}\beta = ((1)/(1 - f_c'/\varepsilon_o.E_c))$$

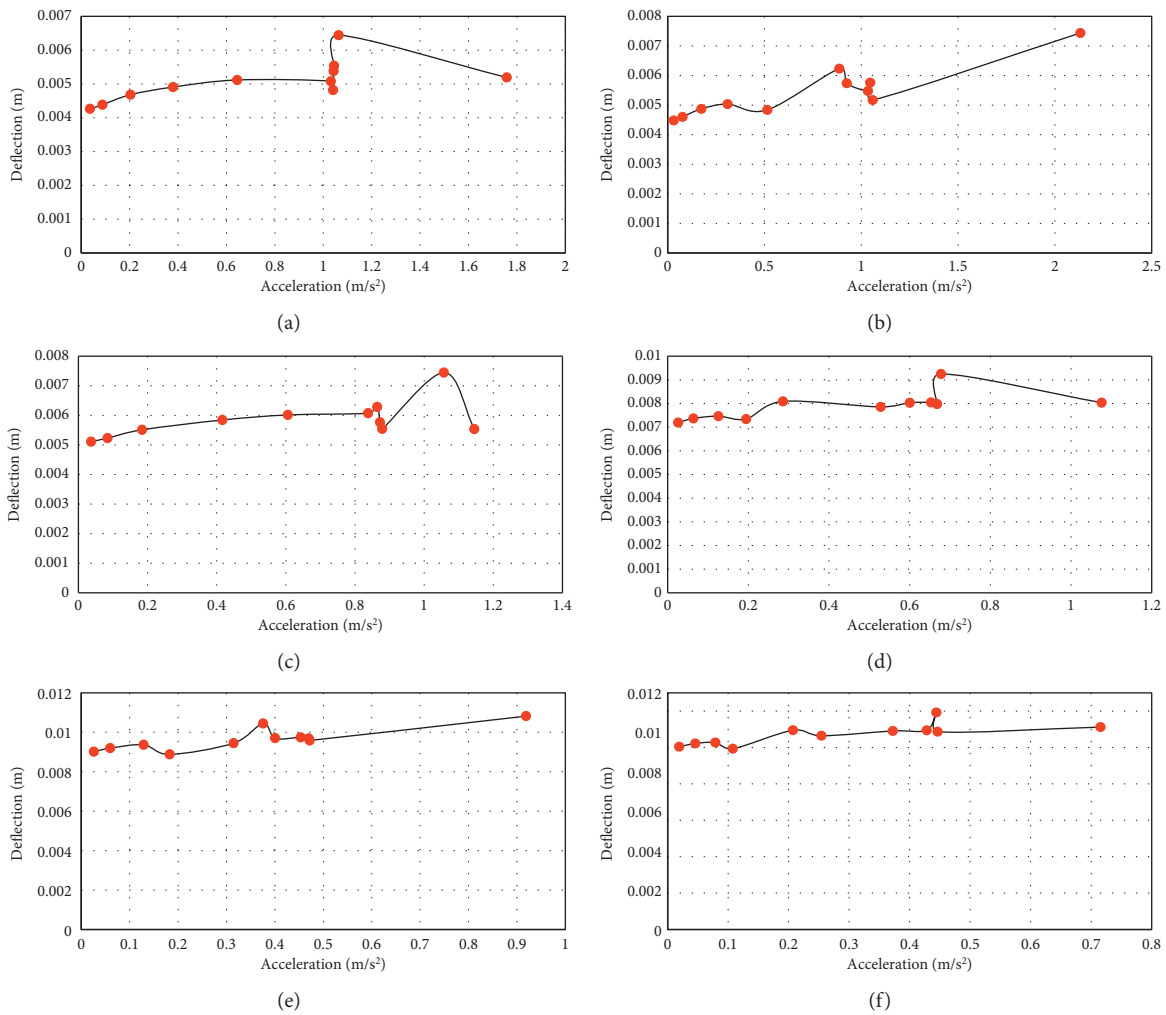FIGURE 10: Concrete stress-strain models [27] and [28].

FIGURE 11: Graph of deflection versus acceleration with load of (a) $P = 4{,}600$ N, (b) $P = 4{,}900$ N, (c) $P = 5{,}600$ N, (d) $P = 8{,}000$ N, (e) $P = 10{,}00$ N, and (f) $P = 11{,}200$ N, all enclosed with the change of velocity v.

frequencies according to equation (6). Thus, when the speed changes from 6 m/s to 16 m/s with the same P load value, the study gets both the maximum deflection in this speed range and the frequency of the corresponding coercive force. From this, the study gets a graph that demonstrates the relationship between the deflection and the coercive force frequency
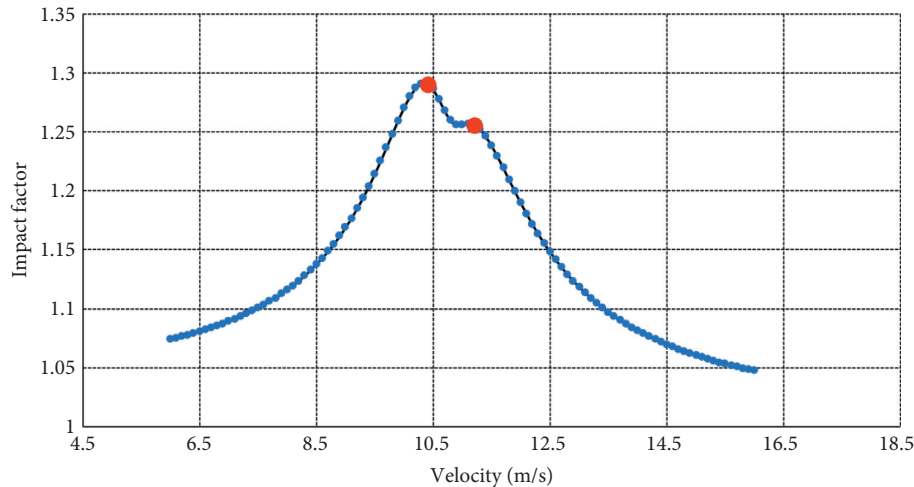
FIGURE 12: Relationship between the dynamic coefficient and velocity.

corresponding to the load P, as shown in Figures 11(a)–11(f), where the deflection reaches the maximum value for the case in which the vibration gradually approaches closer to the beam's first specific frequency.

3.2.2. Building the Relationship between the Dynamic Coefficient and the Excitation Conditions.

The curve has demonstrated the relationship between the dynamic coefficient δ and the velocity v, as represented in equation (6). When the force P is constant, this study shows a dynamic coefficient δ corresponding to each velocity v, with v varying from 6 m/s to 16 m/s. In the graph, the dynamic coefficient δ and the velocity v appear as two neighboring peaks, the distance between the two peaks being about 1 m/s, as shown in Figure 12. This can be explained because δ is affected by Ω in equation (6). Theoretically, the larger the dynamic coefficient is, the closer the coercive force frequency will be to the system's specific frequency. When referring to the actual spectrum analysis graph for a bridge, the frequency graph of the free vibrations shows two frequency peaks, which is called the "beat" phenomenon. This will be clearly analyzed in the following points:

(1) The influence of P on the dynamic coefficient of fixed v.

Because of the fixed speed and the increased load, the dynamic coefficient δ increases due to the force P affecting the beam's first natural frequency, according to equation (6). Therefore, when P increases, the beam's specific frequency ω_1 decreases, with a value close to the coercive frequency generated by the vehicle, and the dynamic coefficient δ also increases. Because of the increased load P, the dynamic coefficient δ also increases in each specified load interval. In Figure 13, each new segment will linearly increase and then a sudden decrease is shown at the segment's end. At that moment, the dynamic coefficient δ linearly increases according to the original relationship; this process continues in many different force intervals, forming a graph that is not entirely linear, according to the theory

originally given. This can be explained: When the force P increases, the dynamic coefficient δ linearly increases, but when Ω decreases, the dynamic coefficient δ also decreases because it corresponds to each frequency of the coercive force Ω. At certain locations, the δ value suddenly decreases because the coercive force frequency Ω abruptly changes under the original sine-cosine period, as shown in Figures 14(a)–14(f).

Table 4 shows that in the experimental model, the slope coefficient a, which is calculated as the ratio of the dynamic coefficient δ to the coercive force Ω, is nearly constant during the experiment process. This can be explained by the fact that the coefficient a does not depend on the angular frequency of the coercive force at constant velocity. In addition, when the coercive force frequency Ω increases, the coefficient of b decreases. Table 4 shows the result that the more the Ω decreases in value, the faster the coefficient of b increases. When the actual speed of the experimental model is $v = 9$ m/s, the relationship between the load P and the dynamic coefficient δ given by the equation $\delta = aP + b$ is $\delta = 0.000003 \ast P + 1.041517$. In this experiment, the average deviation for coefficient a is 0, and for coefficient of b, it is 0.004117. With this deviation level, the obtained results have given a high convergence.

(2) The influence of P impacted on the dynamic coefficient in the case of changed velocity v.

With the increase in speed, the load value increases and the δ value also increases in each specified load interval. However, when all load ranges are considered in the same graph, the δ value tends to decrease, as shown in Figure 15. This study can see the conformity with equation (6) when the P load value is in inverse ratio to the δ coefficient. This is similar to the previous survey, which showed that when the speed increases, the dynamic coefficient in each P value segment increases and the δ value increases linearly, as shown in Figures 16(a)–16(e).
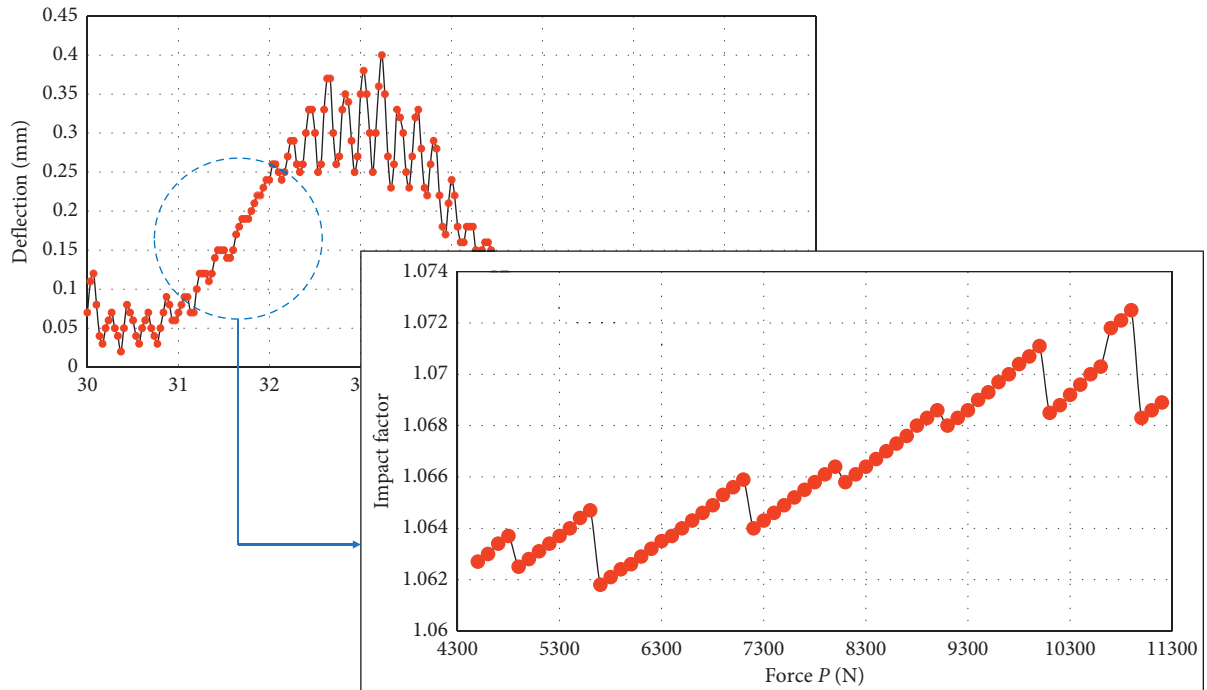
FIGURE 13: Graph showing relationship between P and δ corresponding to $v = 9$ m/s.
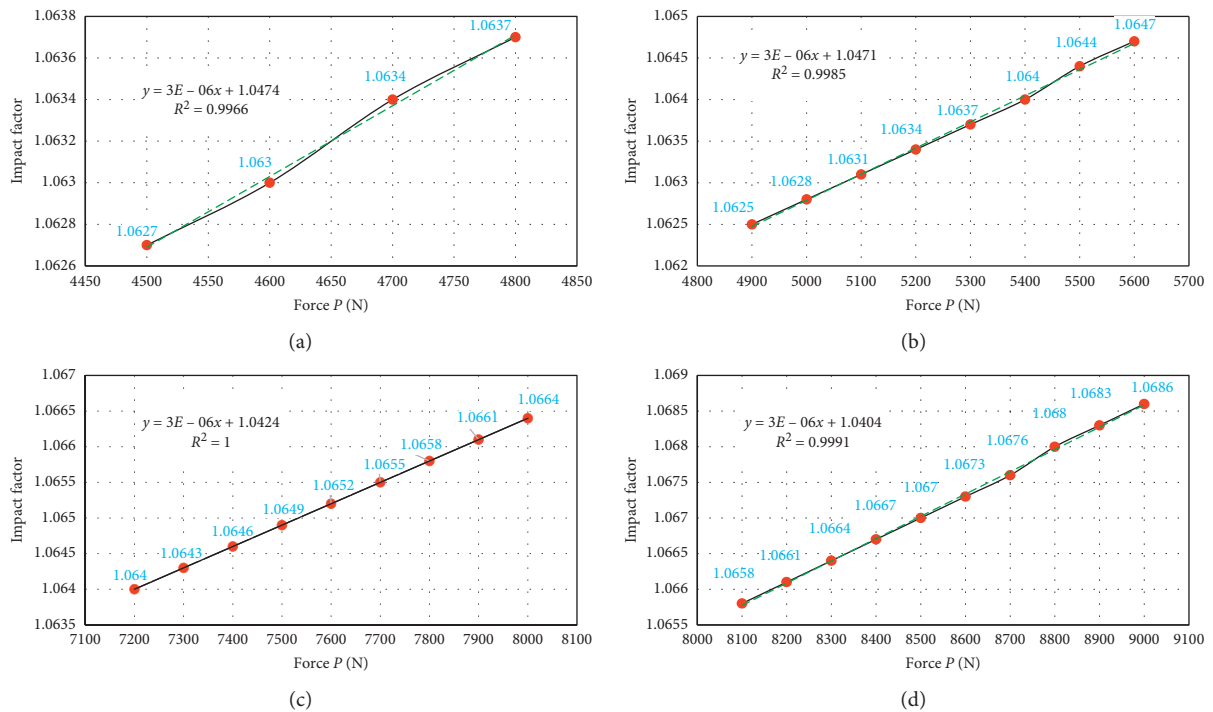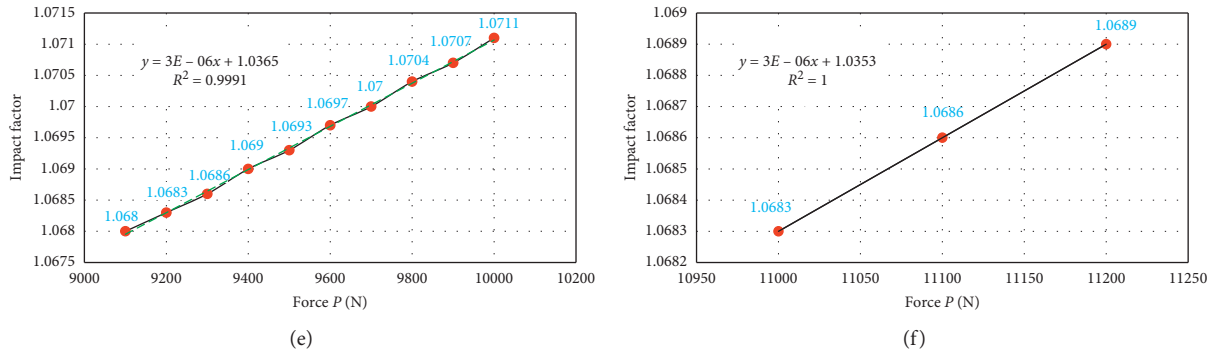

FIGURE 14: Continued.

(e)

(f)

FIGURE 14: δ value graph when force P ranges (a) from 4,500 N to 4,800 N with $\Omega = 19.47209$ rad/s, (b) from 4,900 N to 5,600 N with $\Omega = 18.55288$ rad/s, (c) from 7,200 N to 8,000 N with $\Omega = 15.7784$ rad/s, (d) from 8,100 N to 9,000 N with $\Omega = 15.39646$ rad/s, (e) from 9,100 N to 10,000 N with $\Omega = 15.06402$ rad/s, and (f) from 9,100 N to 10,000 N with $\Omega = 15.06402$ rad/s.

TABLE 4: Regression coefficients of $\delta = aP + b$ corresponding to each Ω.

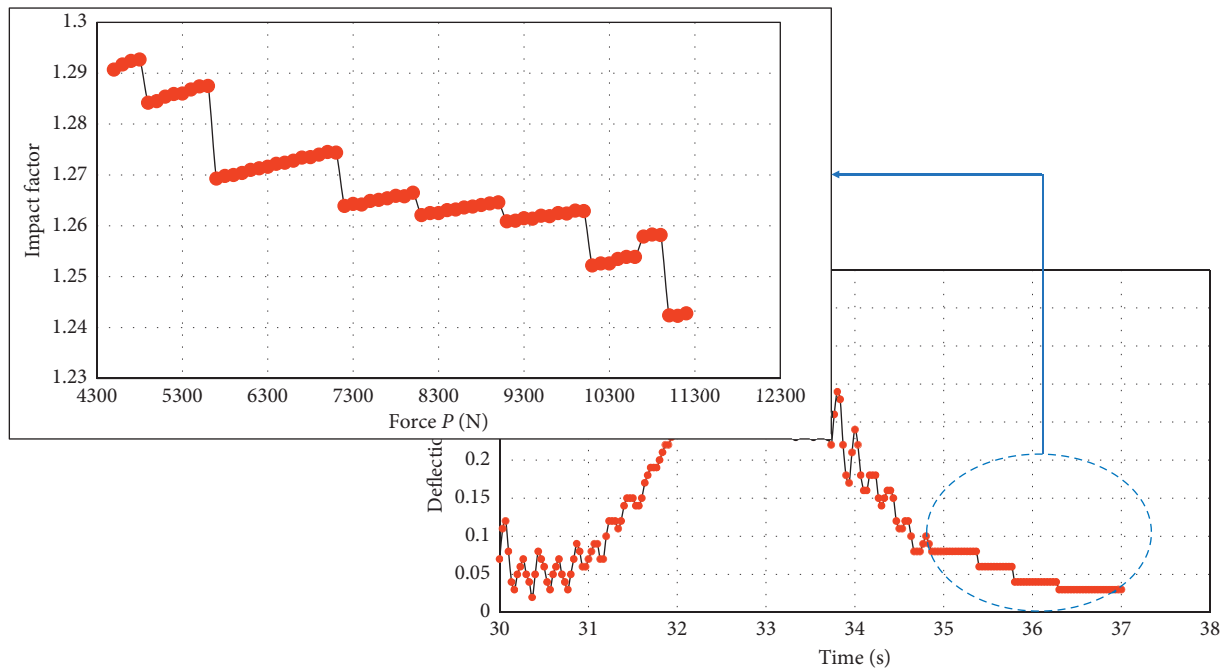| Ω	a	b	R^2
13.29787	0.000003	1.0353	1
15.06402	0.000003	1.0365	0.9991
15.39646	0.000003	1.0404	0.9991
15.7784	0.000003	1.0424	1
18.55288	0.000003	1.0471	0.9985
19.47209	0.000003	1.0474	0.9966
Average	0.000003	1.041517	0.998883
Average deviation	0	0.004117	0.000889

FIGURE 15: Graph showing relationship between P and δ corresponding to v varying from 6 m/s to 16 m/s.

In Table 5, we can see that the equation showing the relationship between the dynamic coefficient δ and the load P, when the velocity v changes, gives $\delta = 0.000004 \ast P + 1.24804$ with an average deviation of 0.0000016 for the coefficient of a and of 0.009768 for the coefficient b. Thus, the value of the dynamic coefficient δ depends on both the velocity v and the load P as well as the frequency of coercive force Ω. As v increases, the δ value changes according to the linear relationship, as shown in the diagrams for δ and v. Corresponding to each Ω value, P and δ increase linearly.
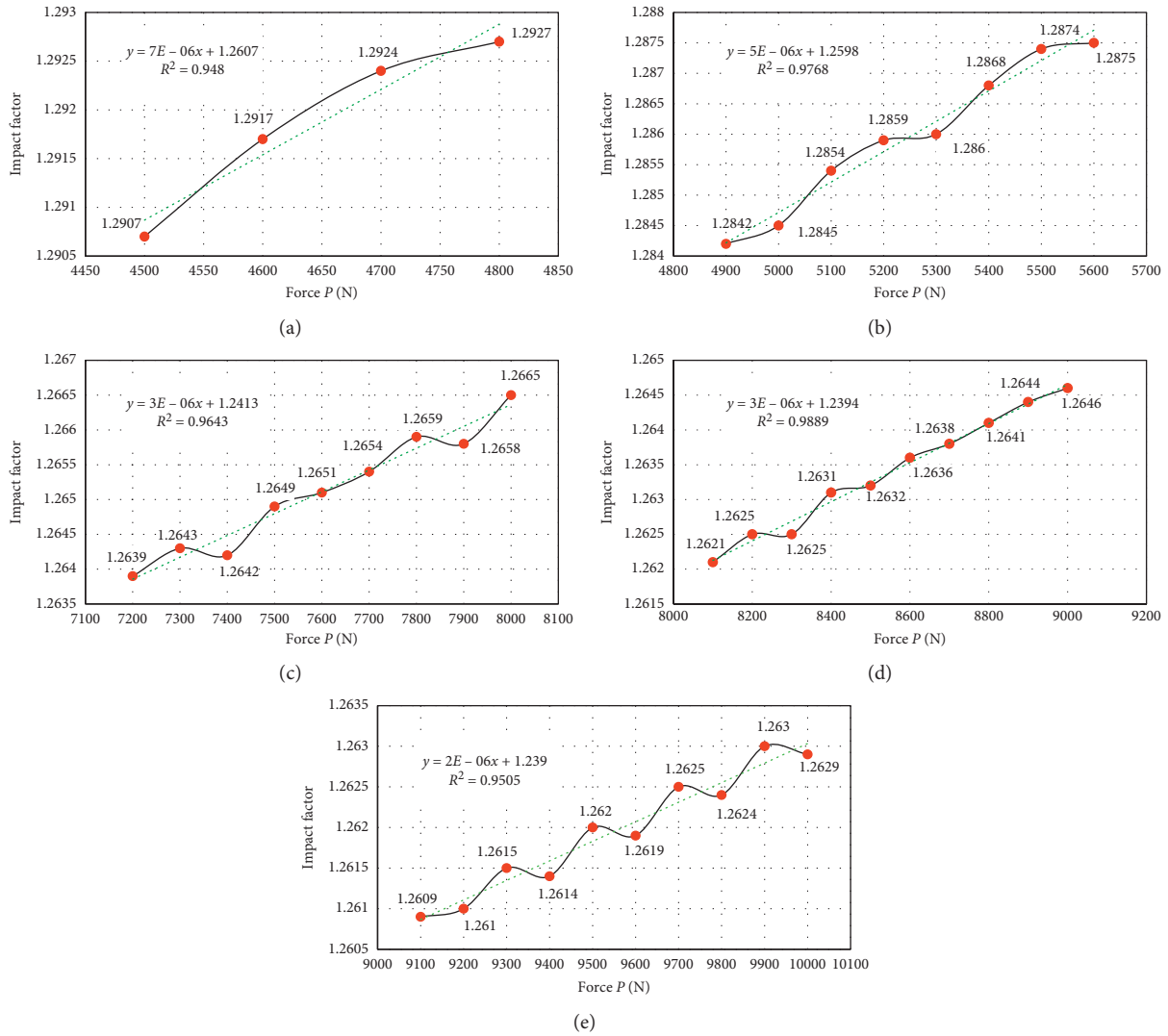
Figure 16: The diagram of the maximum δ value, when the velocity v changes corresponding to P (a) from 4,500 N to 4,800 N, (b) from 4,900 N to 5,600 N, (c) from 7,200 N to 8,000 N, (d) from 8,100 N to 9,000 N, and (e) from 9,100 N to 10,000 N.

Table 5: Regression coefficients $\delta = a * P + b$ corresponding to each P value range.

P (N)	a	b	R^2
4500–4800	0.000007	1.2607	0.948
4900–5600	0.000005	1.2598	0.9768
7200–8000	0.000003	1.2413	0.9643
8100–9000	0.000003	1.2394	0.9889
9100–10000	0.000002	1.239	0.9505
Average	0.000004	1.24804	0.9657
Average deviation	0.0000016	0.009768	0.01372

4. Conclusion

The experimental testing model has been applied in this study so as to find the relationships between the characteristic mechanical parameters during the measurement and testing process. From this manuscript, we can build an experimental model in the field that is most suitable for the actual moving load model, with some conclusions as follows:

(1) From either theory or experiment, the deflection values obtained under the load influence moving on the beams are relatively similar in terms of shape. As the deflection increases along with the velocity increase of the accelerating load, it can be seen that the difference in results with the varying loads may be due to the loads' mass influence on the beam's vibration frequencies. With a constant P load value, but with speed increasing from 6 m/s to 16 m/s, the study finds that the maximum deflection of frequency of the corresponding coercive force either remains unchanged or shows an insignificant change. From this study, we get the relationship between the deflection and the frequency of the corresponding coercive force. And, the deflection reaches the maximum value when the vibration

frequency approaches closer to the beam's first specific frequency.

(2) Vehicle velocity has almost no influence on deflection values in both theoretical and experimental cases. It can be shown that for varying velocities, the differences in the results obtained for deflection values are insignificant and a structure's quality verification process is based primarily on deflection values.

(3) As P increases, the beam's specific frequency ω_1 decreases, so the dynamic coefficient δ increases accordingly. As the load P increases, however, the dynamic coefficient δ increases only for each specified load interval. The value of the dynamic coefficient δ appears as a relationship, showing a linear increase at each segment, with a sudden decrease between segments. This process continues for many different force intervals, resulting in an incompletely linear diagram, according to the originally given theory. It can be shown that at certain locations, the δ value suddenly decreases because the coercive force frequency Ω suddenly changes, according to the initially given period.

Data Availability

The data used to support the findings of this study are included within the article.

Conflicts of Interest

The author declares no conflicts of interest.

References

[1] M. F. Van Staveren, J. P. M. Van Tatenhove, and J. F. Warner, "The tenth dragon: controlled seasonal flooding in long-term policy plans for the Vietnamese Mekong delta," *Journal of Environmental Policy and Planning*, vol. 20, no. 3, pp. 267–281, 2018.

[2] O. Husson, P. H. Verburg, M. Thanh Phung, and M. E. F. Van Mensvoort, "Spatial variability of acid sulphate soils in the plain of reeds, Mekong delta, Vietnam," *Geoderma*, vol. 97, no. 1-2, pp. 1–19, 2000.

[3] T. D. Nguyen, T. Q. Nguyen, T. N. Nhat, H. Nguyen-Xuan, and N. K. Ngo, "A novel approach based on viscoelastic parameters for bridge health monitoring: a case study of Saigon bridge in Ho Chi Minh City-Vietnam," *Mechanical Systems and Signal Processing*, vol. 141, Article ID 106728, 2020.

[4] T. Q. Nguyen, T. D. Nguyen, L. Q. Tran, and N. K. Ngo, "A new insight to vibration characteristics of spans under random moving load: case study of 38 bridges in Ho Chi Minh city Vietnam," *Shock and Vibration*, vol. 2020, Article ID 1547568, 20 pages, 2020.

[5] A. Atkinson, "Asian urbanisation," *City*, vol. 19, no. 6, pp. 857–874, 2015.

[6] N. T. Viet, T. T. Dieu, and N. Loan, "Current status of sludge collection, transportation and treatment in Ho Chi Minh city," *Journal of Environmental Protection*, vol. 4, no. 12, p. 40550, 2013.

[7] T. Q. Nguyen, H. C. Doan, L. C. Vuong, H. Nguyen-Xuan, and N. K. Ngo, "Fretting fatigue damage nucleation and propagation lifetime using a central point movement of power spectral density," *Shock and Vibration*, vol. 2020, Article ID 4985134, 16 pages, 2020.

[8] T. Q. Nguyen, T. D. Nguyen, H. Nguyen-Xuan, and N. K. Ngo, "A correlation coefficient approach for evaluation of stiffness degradation of beams under moving load," *Computers, Materials & Continua*, vol. 61, no. 1, pp. 27–53, 2019.

[9] D. Agdas, J. A. Rice, J. R. Martinez, and I. R. Lasa, "Comparison of visual inspection and structural-health monitoring as bridge condition assessment methods," *Journal of Performance of Constructed Facilities*, vol. 30, no. 3, Article ID 04015049, 2016.

[10] B. F. Spencer, V. Hoskere, and Y. Narazaki, "Advances in computer vision-based civil infrastructure inspection and monitoring," *Engineering*, vol. 5, no. 2, pp. 199–222, 2019.

[11] A. Mufti, F. Raeisi, H. Khalid, A. Horosko, and B. Bakht, "A case for adding an inspection level related to structural health monitoring (SHM) for bridge evaluation," *Canadian Journal of Civil Engineering*, vol. 48, no. 4, pp. 1–14, 2021.

[12] S. Farhangdoust and A. Mehrabi, "Health monitoring of closure joints in accelerated bridge construction: a review of non-destructive testing application," *Journal of Advanced Concrete Technology*, vol. 17, no. 7, pp. 381–404, 2020.

[13] A. Sriram and S. Sritharan, "Quantifying bonding characteristics between UHPC and normal-strength concrete for bridge deck application," *Journal of Bridge Engineering*, vol. 24, no. 6, Article ID 04019041, 2019.

[14] S. Yehia, O. Abudayyeh, S. Nabulsi, and I. Abdelqader, "Detection of common defects in concrete bridge decks using nondestructive evaluation techniques," *Journal of Bridge Engineering*, vol. 12, no. 2, pp. 215–225, 2007.

[15] T. Q. Nguyen, L. C. Vuong, C. M. Le, N. K. Ngo, and H. Nguyen-Xuan, "A data-driven approach based on wavelet analysis and deep learning for identification of multiple-cracked beam structures under moving load," *Measurement*, vol. 162, Article ID 107862, 2020.

[16] C. C. Tung, "Random response of highway bridges to vehicle loads," *Journal of the Engineering Mechanics Division*, vol. 93, pp. 73–94, 1967.

[17] R. Iwankiewicz and P. Śniady, "Vibration of a beam under a random stream of moving forces*," *Journal of Structural Mechanics*, vol. 12, no. 1, pp. 13–26, 1984.

[18] H. S. Zibdeh and R. Rachwitz, "Moving loads on beams with general boundary conditions," *Journal of Sound and Vibration*, vol. 195, no. 1, pp. 85–102, 1996.

[19] S. F. Rastehkenari and M. Ghadiri, "Nonlinear random vibrations of functionally graded porous nanobeams using equivalent linearization method," *Applied Mathematical Modelling*, vol. 98, no. 2, pp. 847–1859, 2021.

[20] J. Zhan, F. Zhang, M. Siahkouhi, X. Kong, and X. He, "A damage identification method for connections of adjacent box-beam bridges using vehicle–bridge interaction analysis and model updating," *Engineering Structures*, vol. 228, Article ID 111551, 2020.

[21] Y. Zhang, L. Jiang, W. Zhou, Y. Feng, Z. Tan, and X. Chai, "Study of bridge-subgrade longitudinal constraint range for high-speed railway simply-supported beam bridge with CRTSII ballastless track under earthquake excitation,"

Construction and Building Materials, vol. 241, Article ID 118026, 2020.

[22] Z. Zhao, L. Yuan, and S. He, "Analysis of the failure mechanism of multi-beam steel–concrete composite bridge under car explosion," *Advances in Structural Engineering*, vol. 23, no. 3, pp. 538–548, 2020.

[23] W. Weaver, S. P. Timoshenko, and D. H. Young, *Vibration Problems in Engineering*, Wiley, Hoboken, NJ, USA, 5th edition, 1990.

[24] J. B. Roberts and P. D. Spanos, "Stochastic averaging: an approximate method of solving random vibration problems," *International Journal of Non-Linear Mechanics*, vol. 21, no. 2, pp. 111–134, 1986.

[25] T. T. Nguyen, H. H. Pham, Q. H. Luu, and H. C. Ho, "Finite element model and experiment verification of testing steel-concrete structures," in *Proceedings of the Science and Technology Conference 12th*, Rhodes, Greece, October 2011.

[26] A. J. Wolanski, "Flexural behavior of reinforced and pre-stressed concrete beams using finite element analysis," Master thesis, Marquette University, Milwaukee, WI, USA, 2004.

[27] D. I. Kachlakev, T. Miller, S. Yim, K. Chansawat, and T. Potisuk, "Finite element modeling of reinforced concrete structures strengthened with FRP laminates," SPR, 316, Oregon Department of Transportation, Salem, OR, USA, 2011.

[28] C. E. Todeschini, A. C. Bianchini, and C. E. Kesler, "Behavior of concrete columns reinforced with high strength steels," *International Concrete Abstracts Portal*, vol. 61, no. 6, pp. 704–716, 1964.

[29] T. H. Wee, M. S. Chin, and M. A. Mansur, "Stress-strain relationship of high-strength concrete in compression," *Journal of Materials in Civil Engineering*, vol. 8, no. 2, pp. 70–76, 1996.